Quantum dot based mode locked lasers for optical frequency combs

Cosimo Calo

THÈSE DE DOCTORAT CONJOINT DE TÉLÉCOM SUDPARIS ET DE L'UNIVERSITÉ PIERRE ET MARIE CURIE

Spécialité

Électronique et Télécommunications

École doctorale Informatique, Télécommunications et Électronique (Paris)

Présentée par

Cosimo CALÒ

Pour obtenir le grade de

DOCTEUR de l'UNIVERSITÉ PIERRE ET MARIE CURIE et TÉLÉCOM SUDPARIS

Sujet de la thèse :

Lasers à blocage de modes à base de boîtes et bâtonnets quantiques pour les peignes de fréquences optiques

soutenue le 18 décembre 2014
devant le jury composé de :

M. Abderrahim Ramdane	Directeur de recherche, CNRS-LPN	Directeur de thèse
M. Badr-Eddine Benkelfat	Professeur, Télécom SudParis	Co-directeur de thèse
M. Pascal Besnard	Professeur, ENSSAT	Rapporteur
M. Guillaume Huyet	Senior Research Scientist, Tyndall National Institute, Irlande	Rapporteur
M. Philippe Gallion	Professeur, Télécom ParisTech	Examinateur
M. Aziz Benlarbi-Delaï	Professeur, UPMC	Examinateur
M^{me} Béatrice Dagens	Directrice de recherche, CNRS-IEF	Examinatrice
M. François Lelarge	Ingenieur de Recherche, III-V Lab	Examinateur

Thèse n° 2014TELE0034

PhD DISSERTATION
TÉLÉCOM SUDPARIS – UNIVERSITÉ PIERRE ET MARIE CURIE

Discipline: Electronics and Telecommunications

Doctoral School: EDITE de Paris

Presented by

Cosimo CALÒ

Quantum dot based mode locked lasers for optical frequency combs

Doctoral Committee:

Prof. Abderrahim Ramdane	Research Director, CNRS-LPN
Prof. Badr-Eddine Benkelfat	Professor, Télécom SudParis
Prof. Pascal Besnard	Professor, ENSSAT
Dr. Guillaume Huyet	Senior Research Scientist, Tyndall National Institute, Irlande
Prof. Philippe Gallion	Professor, Télécom ParisTech
Prof. Aziz Benlarbi-Delaï	Professor, UPMC
Prof. Béatrice Dagens	Research Director, CNRS-IEF
Dr. François Lelarge	Research Engineer, III-V Lab

Thèse n° 2014TELE0034

Résumé

Introduction

La croissance exponentielle du trafic Internet demande de nouvelles solutions techniques afin d'augmenter la capacité des réseaux optiques existants à des couts raisonnables. Dans les systèmes de communication actuels, les principales limitations de capacité se rapprochent de plus en plus des utilisateurs finaux, touchant en particulier les réseaux optiques d'accès et les interconnexions à l'intérieur des centres de traitement de données. Dans ces scénarios, la longueur des liens optiques est typiquement assez courte, étant de l'ordre de quelque centaine de mètres jusqu'à plusieurs dizaines de kilomètres. Par conséquent, pour ce type d'applications, les systèmes de transmission doivent être optimisés afin d'assurer des hauts débits à faible coût, sur des plages relativement courtes.
Une solution très prometteuse dans l'optique d'une augmentation substantielle de la capacité des interconnexions consiste à utiliser la technique de multiplexage en longueur d'onde (WDM) en combinaison avec des formats de modulation avancés. Cependant, la complexité intrinsèque d'une telle architecture et surtout le fait d'employer un laser stabilisé en fréquence optique par canal WDM ne rendent cette solution praticable que dans le cas de transmissions à longue-distance. La situation pourrait toutefois changer si les différents canaux WDM pouvaient être générés par un seul composant. À cet égard, les peignes de fréquences optiques, produisant des dizaines de porteuses régulièrement espacées à partir d'une seule source laser, présentent un grand intérêt pour les systèmes de communication à haut débit [1]. Dans ce cas, chaque raie du peigne peut être opportunément filtrée et modulée indépendamment des autres, avant d'être transmise sur la fibre optique.

La façon la plus simple et couramment utilisée pour générer des peignes de fréquences consiste à utiliser un laser à verrouillage de modes. Ces lasers, émettant des trains réguliers d'impulsions courtes, présentent un spectre optique constitué d'une série de raies ayant un intervalle spectral libre (ISL) qui correspond à la fréquence de répétition des impulsions. Bien que les meilleurs peignes de fréquences en termes de stabilité et de largeur spectrale sont ceux générés par des lasers à état solide [2, 3], les

lasers à blocage de modes basés sur des milieux semi-conducteurs de type III-V sont particulièrement intéressants pour les applications télécom. Leur taille réduite, aussi bien que leurs faibles coûts de fabrication et basse consommation en puissance, sont des atouts incontournables pour les communications optiques de nouvelle génération. Dans les dernières années, la recherche en optoélectronique s'est focalisée sur les lasers à blocage de modes à base de nanostructures semi-conductrices à faible dimensionnalité. En particulier, les boîtes quantiques (BQs) d'InGaAs/InAs sur GaAs et les bâtonnets d'InAs sur InP ont fait l'objet de plusieurs études [4,5] grâce à leurs propriétés uniques, comme par exemple leur meilleur stabilité en température [6], leurs faibles densités de courant de seuil [7], les dynamiques ultra-rapides des porteurs de charge [8], ou encore le faible couplage entre le bruit d'émission spontanée amplifiée et les modes guidés du laser [9]. Ces caractéristiques ont permis le développement de lasers à blocage de modes émettant des impulsions aussi courtes que quelques centaines de femto-secondes à des taux de répétition de plusieurs dizaines de gigahertz, avec des spectres d'émission plus larges que 10 nm [10,11].

Typiquement les diodes lasers à blocage de modes sont constitués de deux sections séparées: une première section amplificatrice polarisée en directe et la deuxième, polarisée en inverse, agissant comme absorbant saturable. Dans ces structures, le délicat équilibre entre le gain fourni par la section amplificatrice et les pertes produites par l'absorbant est responsable de la création de trains d'impulsions stables dans le temps à la sortie du laser. Comme les impulsions les plus courtes dans ces lasers sont obtenues près du seuil, ce mécanisme de verrouillage de modes en général comporte un compromis entre la puissance moyenne et la durée d'impulsion. Par conséquent, ce type de configuration ne permet pas d'avoir des puissances moyennes très élevées pour les différents modes optiques.
Une autre manière d'obtenir des peignes de fréquences optiques à partir de lasers à semi-conducteur consiste à exploiter le régime de blocage de modes dans les lasers mono-section. Ce régime, fréquemment observé dans les composants à base de puits quantiques [12–15] aussi bien que dans les matériaux à BQs [16–19] et à bâtonnets [20–24], implique une forte corrélation de phase entre les modes Fabry-Perot du laser, même si les impulsions émises sont particulièrement étendues. Le phénomène, étant très efficace dans les matériaux à faible facteur de confinement optique comme les boîtes et bâtonnets quantiques, est souvent attribué aux effets optiques non-linéaires ayant lieu dans le milieu à gain et, plus particulièrement, au mélange à quatre ondes entre les modes laser [12,14]. Cependant, une description exhaustive du mécanisme d'un point de vue théorique et expérimental n'est toujours pas disponible.

Le présent travail de thèse a l'objectif de fournir plus d'éléments pour la compréhension du régime de blocage de modes dans les diodes laser mono-section basées sur des nanostructures semi-conductrices à basse dimensionnalité. Dans cette étude,

les performances en verrouillage de modes de lasers Fabry-Perot mono-section, basés sur différents systèmes de matériaux, sont comparées sur la base de la largeur du spectre optique d'émission et de la capacité à produire des impulsions courtes à faible gigue temporelle. Cette dernière quantité, en particulier, est évalué sur la base de la largeur à mi-hauteur du battement radiofréquence des modes laser sur une photodiode rapide [25].
En remarquant que les lasers à base de bâtonnets quantiques d'InAs sur InP présentent de meilleures caractéristiques par rapport aux autres matériaux examinés, leurs propriétés spécifiques en termes de stabilité des peignes de fréquences optiques et de chirp des impulsions sont étudiées plus en détail. Le chirp est d'abord étudié par la technique FROG (*Frequency-resolved optical gating*). Ensuite, la dispersion chromatique du matériau laser est évaluée afin de vérifier si elle peut expliquer les grandes valeurs de chirp mesurées par FROG. Pour cela, la technique de réflectométrie optique dans le domaine fréquentiel est utilisée et ses capacités uniques de mesure ont été étudiées et validées. Enfin, ces lasers sont employés avec succès pour les transmissions à haut débit à l'aide de la technique de modulation optique OFDM en détection directe. Débits de l'ordre du térabit par seconde, ainsi que le faible coût de l'architecture du système, sont particulièrement prometteurs pour les futures applications datacom.

Structures laser et fabrication des diodes laser

Dans le présent travail, les caractéristiques spécifiques de différentes structures lasers émettant à 1,3 µm et à 1,55 µm pour les télécommunications optiques ont été analysées. Pour la fenêtre de transmission autour de 1,3 µm, une structure commerciale fournie par Innolume GmbH, à base de 10 plans de boîtes quantiques d'InGaAs/InAs sur GaAs, a été utilisée, alors que pour une émission autour de 1,55 µm, nous avons considéré des structures laser à base de BQs d'InAs sur un substrat d'InP (311)B [26, 27] et de bâtonnets quantiques d'InAs sur InP (100) [28]. Ces dernières sont constituées de 9 plans de boîtes/bâtonnets inclus dans des barrières d'InGaAsP et fournies respectivement par INSA Rennes et Alcatel-Lucent-Thales III-V Lab. En outre, une structure à un seul puits quantique InGaAsP sur InP (100), fabriquée par III-V Lab et spécialement conçue pour avoir un facteur de confinement optique comparable à celui des structures à boîtes et bâtonnets quantiques, a été prise en compte comme référence.
À partir de ces structures, des lasers à ruban large (50 µm) on été fabriqués avec les technologies de salle blanche disponibles au LPN, ce dans le but d'évaluer leurs propriétés optiques principales. En particulier, le gain modal Γg_0, les pertes internes α_i, la densité de courant de seuil pour une longueur de cavité infinie J_{th_∞} et le rendement quantique interne η_i^d peuvent être calculés sur la base des caractéristiques puissance-courant de ces lasers (voir le tableau 1) [29]. Les valeurs obtenues sont en accord avec

la littérature sur le sujet [28, 30] et montrent, en particulier, que des gains modaux plus élevés peuvent être obtenus à partir de structures à bâtonnets, même s'ils sont accompagnés par des pertes internes plus significatives.

Structure laser	$\boldsymbol{\Gamma g_0}$ **(cm^{-1})**	$\boldsymbol{\alpha_i}$ **(cm^{-1})**	$\boldsymbol{J_{th_\infty}}$ **(A/cm^2)**	$\boldsymbol{\eta_i^d}$
BQs d'InGaAs/InAs sur GaAs	22	3.5	280	0.54
BQs d'InAs sur InP (311)B	25	5.6	504	0.46
Bâtonnets d'InAs sur InP (100)	56	15	1285	0.27
Puits d'InGaAsP sur InP (100)	13	3.3	97	0.10

Table 1 – Gain modal Γg_0, pertes internes α_i, densité de courant de seuil pour une longueur de cavité infinie J_{th_∞} et rendement quantique interne η_i^d pour les structures laser considérées.

Après avoir vérifié la qualité des structures considérées, nous avons procédé à la conception et à la fabrication en salle blanche de rubans laser monomodes transverses. Le procédé de fabrication se compose de plusieurs étapes, schématisées dans la figure 1 et listées ci-dessous :

1. retrait de la couche d'oxide natif ;
2. définition par lithographie optique du masque pour la gravure des rubans laser ;
3. gravure des guides d'ondes laser ;
4. retrait du masque de gravure ;
5. planarisation de la structure laser à l'aide d'une couche épaisse de Benzo Cyclo Buthène (BCB) ;
6. gravure du BCB afin de dégager le sommet des rubans ;
7. dépôt des contacts électriques de type p par évaporation de Ti/Au et lift-off ;
8. amincissement de substrat, dépôt de l'électrode de type n et clivage des barrettes laser.

Le résultat final de cette procédure de fabrication est montré dans la figure 2, prise à l'aide d'un microscope électronique à balayage (MEB). Les barrettes laser ainsi fabriquées sont, ensuite, testées et triées sur la base de leurs caractéristiques puissance-courant et tension-courant à température ambiante. Les meilleurs lasers sont montés sur des embases en cuivre pour une évacuation plus efficace de la chaleur, avant d'être caractérisés sur des bancs de mesure dédiés à l'analyse des performances en verrouillage de modes.

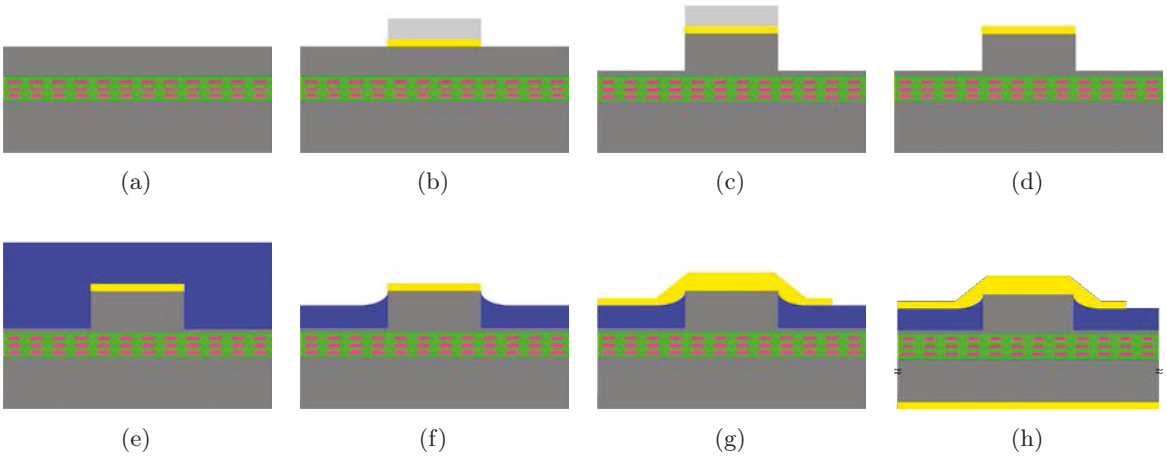

Figure 1 – Étapes de fabrication pour les lasers à semi-conducteur utilisés dans cette étude.

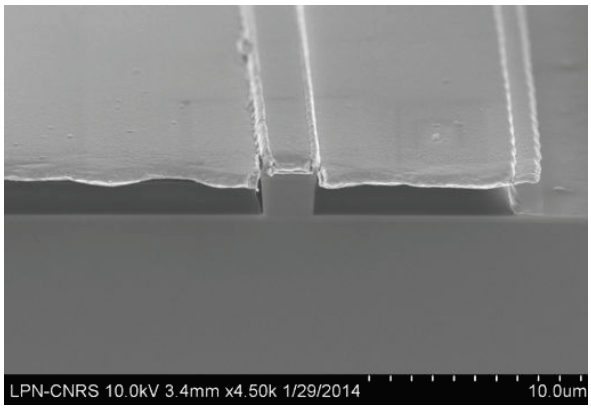

Figure 2 – Image MEB d'un ruban laser après fabrication.

Blocage de modes dans les lasers mono-section

A partir des diodes lasers fabriquées des structures présentées ci-dessus, les caractéristiques spécifiques de chaque milieu à gain sont identifiées à travers une investigation systématique de trois aspects principaux : le spectre optique d'emission, le spectre radiofréquence généré par battement des modes Fabry-Perot sur une photodiode rapide et la capacité de générer des impulsions courtes. Comme nous avons remarqué que les lasers issus de la même plaque (ou de plaques comparables) présentent des performances similaires, pour des raisons de simplicité, nous allons considérer, par la suite, un seul dispositif pour chaque structure.

Lasers à puits quantique InGaAsP sur InP (100)

Le premier composant étudié est un laser avec une longueur de cavité de 1 mm, issu de la structure ayant un seul puits quantique d'InGaAsP sur InP. Le laser, émettant autour de 1,56 µm, présente un spectre assez plat avec une largeur à mi-hauteur d'environ

4-6 nm relativement constante en fonction du courant d'injection (voir fig. 3a). Le spectre RF à la fréquence de répétition du laser ($f_r = 37,6$ GHz) est constitué d'une raie fine avec une largeur à mi-hauteur toujours inférieure à 100 kHz, ce qui indique une faible gigue temporelle du train d'impulsions généré. Un comportement assez régulier est observé pour le pic RF en fonction du courant, avec des sauts de fréquence qui ont lieu en correspondance des décalages du spectre optique vers les plus hautes longueurs d'onde, comme montré dans la figure 3b. Ces décalages sont souvent attribués en littérature au gain non-linéaire du milieu laser [31, 32], même si leur origine est encore objet de débat [33]. Des impulsions courtes d'environ 1.2 ps ont été mesurées par autocorrélation, après compensation de la dispersion de retard de groupe normale des impulsions, au moyen de la propagation du signal optique à travers 250 mètres de fibre optique monomode standard (SMF-28).

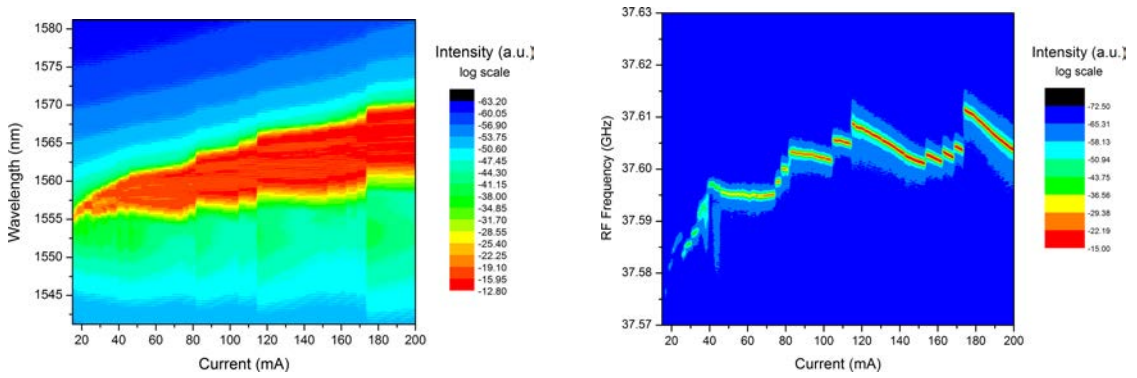

(a) (b)

Figure 3 – Evolution du spectre optique (a) et du spectre RF (b) en fonction du courant d'injection mesurés à 20°C pour le laser mono-section à puits quantique avec une longueur de cavité de 1 mm.

Lasers à boîtes et bâtonnets quantiques d'InAs sur InP

Un comportement similaire à celui des lasers à puits quantique a été observé pour les composants à base de BQs d'InAs sur un substrat d'InP (311)B et de bâtonnets d'InAs sur InP (100). Pour ces dispositifs, des largeurs de battement RF de l'ordre de la dizaine de kHz sont fréquemment atteintes, grâce aux faibles facteurs de confinement optique des structures, permettant un couplage réduit entre le bruit d'émission spontanée amplifiée et les modes guidés du laser. De plus, des spectres optiques qui s'élargissent régulièrement en fonction du courant d'injection sont typiques pour ces lasers. Dans ce sens, des meilleures performances peuvent être obtenues en utilisant des lasers à base de bâtonnets quantiques, qui présentent des spectres optiques très plats avec une largeur à mi-hauteur supérieure à 15 nm, comme montré dans la figure 4a pour un laser avec une longueur de cavité de 890 µm. Les largeurs spectrales maximales mesurées pour les lasers à BQs InAs/InP (311)B sont, en effet, de l'ordre de 4 nm.

Pour les deux types de lasers, une évolution assez irrégulière du spectre RF est observée en fonction du courant d'injection (voir figure 4b). Des plages de courants pour lesquelles des raies RF fines peuvent être identifiées, aussi bien que d'autres pour lesquelles la largeur à mi hauteur du battement devient de d'ordre de plusieurs centaines de kHz. Dans tous les cas, des impulsions avec durées inférieures à la picoseconde ont été mesurées par autocorrélation, après compression à l'aide d'une bobine de fibre optique monomode de longueur convenable. Les impulsions ultracourtes générées par les lasers à bâtonnets quantiques ont fait l'objet d'une étude plus détaillée utilisant la technique FROG, dont les résultats seront présentés ultérieurement dans ce travail.

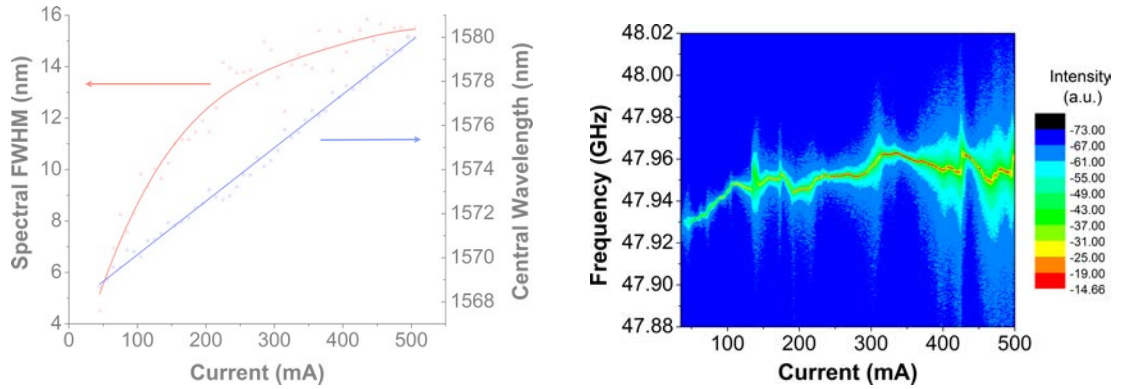

(a) (b)

Figure 4 – Evolution de la longueur d'onde centrale et de la largeur du spectre optique (a), ainsi que du spectre RF (b) en fonction du courant d'injection pour le laser mono-section à bâtonnets quantiques avec une longueur de cavité de 890-µm.

Lasers à boîtes quantiques d'InGaAs/InAs sur GaAs

Outre les lasers basés sur des substrats d'InP, aussi une structure commerciale à base de boîtes quantiques d'InGaAs/InAs sur GaAs émettant à 1,3 µm a été considérée. Les composants issus de cette structure présentent un comportement très singulier pour les spectres optiques et RF, en fonction du courant d'injection, comme on peut le voir dans la figure 5 pour un laser avec une longueur de cavité de 1.4 mm. Pour ce laser, une forte corrélation entre l'enveloppe du spectre optique et le spectre RF est observée. Plus particulièrement, quand le premier est constitué d'un seul lobe, un très large battement RF se produit. Au contraire, quand pour certaines plages de courant (autour de 180 et 310 mA) le laser émet de la lumière sur deux gammes de longueurs d'onde distinctes, une réduction de la largeur de la raie RF a lieu. Cette réduction devient beaucoup plus marquée pour des valeurs de courant au-dessus de 450 mA, pour lesquelles le laser émet simultanément sur l'état fondamental et sur l'état excité des boîtes quantiques.

La génération d'impulsions courtes à partir de ce laser est possible seulement dans

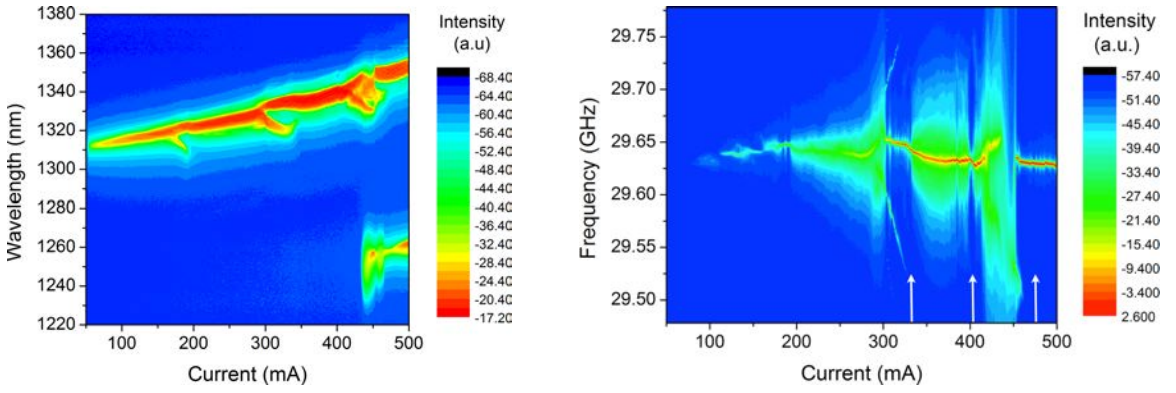

(a) (b)

Figure 5 – Evolution du spectre optique (a) et du spectre RF (b) en fonction du courant d'injection mesurés à 20°C pour le laser mono-section à boîtes quantiques d'InGaAs/InAs sur GaAs avec une longueur de cavité de 1.4 mm. Les regions pour lesquelles ont été observées des meilleures performances en verrouillage de modes sont indiquées au moyen de flèches.

cette dernière gamme de courants, pour laquelle nous avons pu obtenir des durées d'impulsion de l'ordre de 4 ps. Cette génération d'impulsion a été, encore une fois, réalisée en compensant la dispersion normale du signal laser avec celle anormale d'une fibre optique monomode standard SMF-28 de 2.1 km, en exploitant le fait que le spectre d'émission laser dépasse la longueur d'onde de dispersion nulle de la fibre.

La comparaison entre les performances en verrouillage de modes des différentes structures considérées, nous a permis de conclure que les lasers mono-section basés sur InP sont plus performants que ceux à base de BQs d'InAs sur GaAs. En particulier, les structures à base de bâtonnets quantiques, permettant d'obtenir des plus larges spectres optiques avec des largeurs de raie RF de l'ordre de la dizaine de kHz, présentent un grand intérêt pour les peignes de longueurs d'onde aussi bien que pour la génération d'impulsions courtes à faible gigue temporelle. Dans la section suivante, les caractéristiques des ces impulsions sont étudiées, plus en détail, au moyen de la technique FROG.

Caractérisation d'impulsions courtes par autocorrélation résolue en fréquence

La technique FROG (*Frequency resolved optical gating*) est une méthode avancée de caractérisation qui, contrairement à l'autocorrélation optique, permet de déterminer avec précision la forme et le chirp d'un train d'impulsions. La technique consiste à effectuer une autocorrélation optique résolue en fréquence et, ensuite, à reconstruire le champ électrique complexe du signal optique à partir de la trace enregistrée, dite

spectrogramme. À cette fin, un algorithme itératif est utilisé, indiquant la qualité de la reconstruction au moyen d'un paramètre d'erreur ε qui dépend de la taille de la trace [34].

Dans une étude menée en collaboration avec l'équipe du Prof. Bimberg à TU Berlin, la technique FROG a été employée pour la caractérisation des impulsions générées par les lasers à bâtonnets quantiques d'InAs sur InP. Avant d'être analysées par FROG, les impulsions sont d'abord comprimées à l'aide d'une longueur convenable de fibre optique monomode, car la technique ne se prête pas à la mesure d'impulsions trop étendues. Ensuite, le chirp des impulsions à la sortie du laser est déterminé à partir de la dispersion du retard de groupe introduit par la fibre et de celle mesurée par FROG. Un exemple de mesure FROG effectuée sur le composant considéré dans la figure 4, pour un courant d'injection de 300 mA et une longueur de fibre de 66 mètres, est présenté dans la figure 6. En outre, les caractéristiques principales des impulsions en fonction du courant pour le même échantillon sont montrées dans la figure 7.

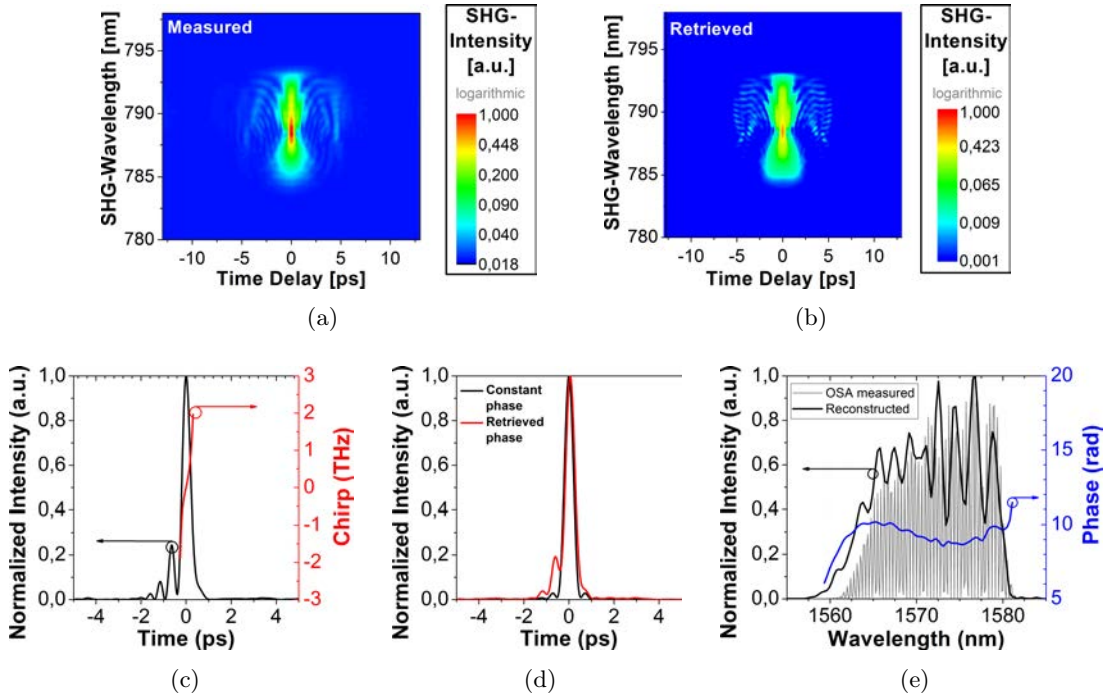

Figure 6 – Exemple de mesure FROG des impulsions générées par le laser mono-section à bâtonnets quantiques avec une longueur de cavité de 890-µm pour un courant d'injection de 300 mA, après propagation du signal optique à travers une fibre SMF-28 longue 66 mètres. (a) Spectrogramme mesuré et (b) reconstruit par l'algorithme FROG ; (c) forme et chirp de l'impulsion reconstruite ; (d) formes d'impulsions simulées pour un profil de phase constant et pour le profil de phase reconstruit par FROG et (e) intensité et phase spectrales mesurées par FROG en comparaison avec le spectre optique mesuré à l'aide d'un analyseur de spectre optique standard.

Nous pouvons remarquer que grâce au large spectre d'émission du laser des impulsions ayant des durées de l'ordre de 400 fs peuvent être obtenues, à condition que leur chirp soit entièrement compensé. L'asymétrie des impulsions est causée par la composante

Pulse Intensity and Phase	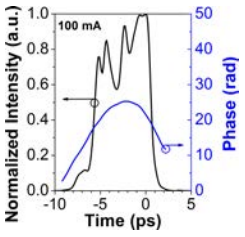	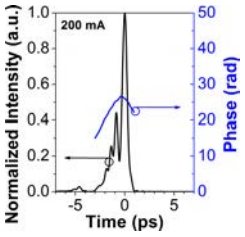	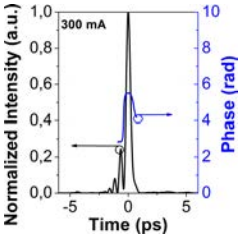	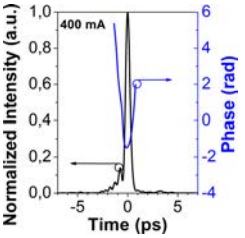
$\Delta\tau$	6.188 ps	576 fs	423 fs	519 fs
ε	0.0297	0.0095	0.0061	0.0088
λ_c	1561.39 nm	1566.89 nm	1575.0 nm	1582.81 nm
$\Delta\lambda_{FWHM}$	9.32 nm	12.45 nm	13.76 nm	14.65 nm
GDD_p	0.65 ps^2	0.16 ps^2	0.01 ps^2	-0.12 ps^2
GDD_{SMF-28}	-1.43 ps^2	-1.46 ps^2	-1.52 ps^2	-1.57 ps^2
GDD_{tot}	2.08 ps^2	1.62 ps^2	1.53 ps^2	1.45 ps^2
$\Delta\tau_{min}$	567 fs	439 fs	423 fs	374 fs

Figure 7 – Profils d'intensité et de phase des impulsions pour des courants d'injection (de gauche à droite) de 100, 200, 300 et 400 mA. Pour chaque mesure, les valeurs de durée d'impulsion $\Delta\tau$, d'erreur de reconstruction FROG ε, de longueur d'onde centrale λ_c, de largeur du spectre optique à mi-hauteur $\Delta\lambda_{FWHM}$, de dispersion de retard de groupe (*GDD – group delay dispersion*) de l'impulsion, de la fibre et totale GDD_p, GDD_{SMF-28} et GDD_{tot} et de durée d'impulsion minimale qui peuvent être obtenues sont indiquées.

non-linéaire du chirp qui n'est pas compensé par la fibre optique monomode (voir la figure 6d). Le parfait accord entre le spectrogramme mesuré par FROG (figure 6a) et celui obtenu par l'algorithme de reconstruction (figure 6b) dénote une instabilité réduite de la forme des impulsions tout au long de la mesure [35]. De plus, la forte correspondance entre le spectre optique mesuré à l'aide d'un analyseur de spectre optique standard et celui reconstruit à travers la technique FROG indique que tous les modes longitudinaux du laser contribuent à la formation d'impulsions. Enfin, nous avons observé que la durée minimale d'impulsion, qui peut être obtenue en compensant entièrement la dispersion du retard de groupe du signal laser, diminue en fonction du courant d'injection. Cela est lié à l'élargissement du spectre d'émission avec le courant. Néanmoins, aussi le chirp total du signal laser diminue en fonction du courant, en accord avec des études précédentes sur ce sujet de recherche [24]. Par conséquent, des hauts niveaux d'injection sont favorables pour l'obtention d'impulsions courtes, même si, pour ce but, des valeurs de dispersion plutôt élevées (de l'ordre de la ps^2) doivent être compensées.

Différentes études sur les lasers à verrouillage de modes à une seule section ont indiqué qu'un tel chirp peut être produit par la dispersion chromatique du matériau laser [13,36]. Afin de vérifier cette hypothèse, la dispersion du milieu à gain à base de bâtonnets quantiques est étudiée au moyen de la technique de réflectométrie optique dans le domaine fréquentiel, comme présenté dans la section suivante.

Caractérisation de la dispersion chromatique par réflectométrie optique dans le domaine fréquentiel

Dans une étude menée en collaboration avec Télécom SudParis, la technique de réflectométrie optique dans le domaine fréquentiel [37] est utilisée pour la mesure de la dispersion chromatique des matériaux pour deux raisons principales. Tout d'abord, parce que très peu d'études ont été présentées en littérature sur la possibilité de mesurer les propriétés de phase des composants optiques à travers cette technique [38, 39]. En deuxième lieu, parce que cette méthode présente un grand intérêt pour les caractérisations optiques, vue la facilité de mise en œuvre du système de mesure. Dans cette étude, nous avons évalué, dans un premier moment, les limites de la technique en estimant les valeurs les plus faibles de dispersion qui peuvent être mesurées. Ensuite, une fois que la méthode est validée, elle est utilisée pour mesurer la dispersion chromatique du milieu à gain à base de bâtonnets quantiques.

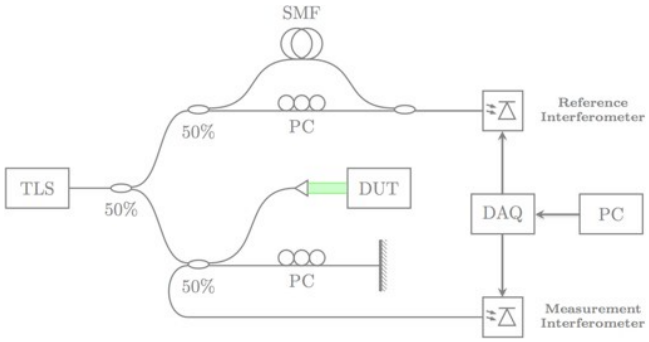

Figure 8 – Montage expérimental pour la technique de réflectométrie optique dans le domaine fréquentiel.

La technique de réflectométrie optique dans le domaine fréquentiel consiste à sonder le composant optique sous test, situé sur l'un des deux bras d'un interféromètre, avec la lumière provenant d'un laser accordable linéairement en fréquence (voir figure 8). Les franges d'interférence, générées à l'aide d'une photodiode placée à la sortie de l'interféromètre, sont ensuite échantillonnées et traitées numériquement afin d'extraire la réponse en amplitude et en phase du composant sous test. L'échantillonnage des franges est fait à pas constant en fréquence, en utilisant le signal de sortie d'un deuxième interféromètre comme déclencheur [37, 40]. En ce qui concerne le traitement numérique du signal échantillonné, il consiste à déterminer les fonctions de transfert en amplitude et en phase du composant sous test encodées, respectivement, dans l'enveloppe et dans la phase des franges d'interférence enregistrées. Pour récupérer ces informations, il faut se servir du signal analytique des franges, qui peut être déterminé à partir d'une version opportunément filtrée du pic correspondant au composant sous test dans la transformée de Fourier des franges (*réflectogramme*) [41].

Afin d'évaluer les capacités de mesure de la technique, dans un premier temps,

nous avons considéré comme composant sous test un filtre optique programmable en amplitude et en phase dans la bande 1530-1625 nm (Finisar Waveshaper 1000 S/X). Dans le cadre de notre analyse, le filtre est utilisé en tant qu'étalon d'amplitude et de phase ; par conséquent, l'évaluation des capacités de la technique se traduit par le fait de pouvoir récupérer précisément la fonction de transfert programmée sur le composant. Grace à un algorithme que nous avons développé pour extraire la réponse en phase du filtre, des mesures de dispersion ont pu être effectuées, comme montré dans la figure 9. Nous pouvons remarquer que des valeurs de dispersion aussi faibles que 0,02 ps/nm peuvent être mesurées par la technique sur une plage spectrale de 1 THz, ce qui indique une très grande sensibilité de la méthode aux caractéristiques de phase des composants optiques. Nous avons pu aussi vérifier que la valeur minimale de dispersion mesurable est limitée par les vibrations mécaniques à proximité du système de mesure, auxquelles cette technique est particulièrement sensible. Toutefois, cette caractéristique présente un grand potentiel pour l'analyse des propriétés dynamiques des composants optiques.

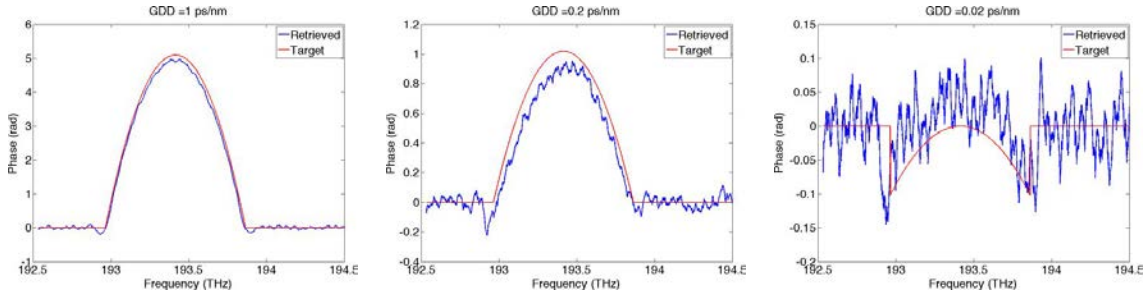

(a) GDD = 1 ps/nm (b) GDD = 0.2 ps/nm (c) GDD = 0.02 ps/nm

Figure 9 – Exemples de mesure de dispersion pour des valeurs différentes de dispersion de retard de groupe programmées sur le filtre optique.

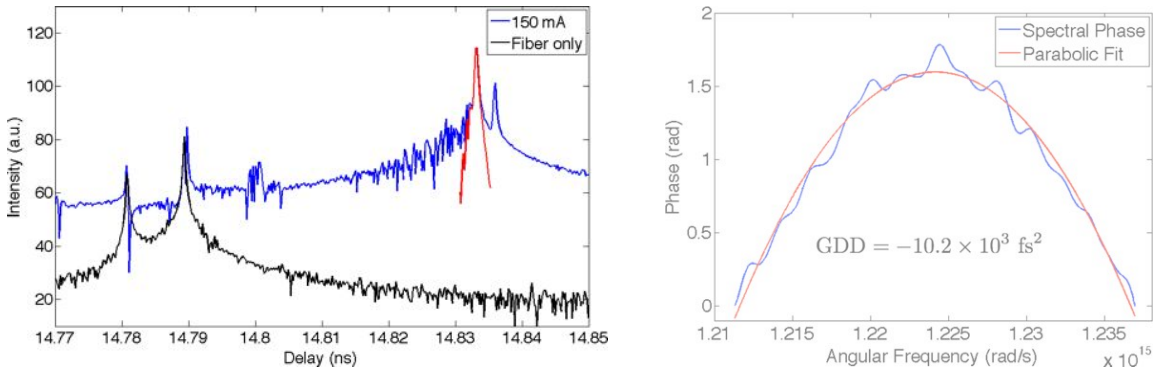

Figure 10 – Mesure de la dispersion chromatique d'un amplificateur à semi-conducteur à base de bâtonnets quantiques pour un courant d'injection de 150 mA. (a) Réflectogramme mesuré en présence (en bleu) et en absence (en noir) du composant. Le pic correspondant à un aller-retour dans l'amplificateur à semi-conducteur, après filtrage numérique est indiqué en rouge. (b) Réponse en phase de l'amplificateur avec ajustement parabolique pour l'extraction de la dispersion du retard de groupe.

Après avoir validé la technique pour la mesure de la réponse en phase des composants

optiques, nous avons utilisé la réflectométrie optique dans le domaine fréquentiel pour déterminer la dispersion chromatique du matériau à bâtonnets quantiques. À ce propos, un amplificateur à semi-conducteur, fabriqué à partir d'une structure à 9 plans de bâtonnets d'InAs sur InP et long 2 mm, a été utilisé comme composant sous test. Sa dispersion est mesurée en utilisant deux mesures successives : sans et avec le composant (voir figure 10a). Pour ces deux mesures, les profils de phase encodés dans les pics correspondant à la fibre optique lentillée utilisée pour le couplage de la lumière dans le composant et à un aller-retour dans l'amplificateur sont calculés. Ensuite, ces deux courbes sont soustraites afin d'obtenir le profil de phase final relatif à la dispersion de l'amplificateur. Le résultat de ces calculs est montré dans la figure 10b, pour un courant d'injection dans le composant de 150 mA. Une valeur de dispersion de retard de groupe de l'ordre de -10×10^3 fs^2 a été estimée en utilisant un ajustement parabolique de la courbe. Cette valeur, correspondant à une dispersion de vitesse de groupe anormale d'environ -2.5×10^3 fs^2/mm, n'est pas compatible avec les larges valeurs de dispersion normale mesurées par FROG. Par conséquent, nous pouvons affirmer que le chirp des impulsions émises par les lasers à blocage de modes à base de bâtonnets quantiques n'est pas dû à la dispersion chromatique du milieu à gain, mais plutôt aux dynamiques spécifiques des composants. Ces dernières nécessitent d'une meilleure compréhension d'un point de vue théorique, afin de révéler l'origine du verrouillage de modes dans les lasers mono-section.

OFDM optique pour les communications optiques à très haut débit

Indépendamment des causes à la base du blocage de modes dans les lasers mono-section, leurs propriétés uniques en termes de largeur de spectre optique et de bruit peuvent être exploitées avec succès dans les systèmes de communication optiques. Dans une étude menée en collaboration avec l'équipe du Prof. Barry à la Dublin City University (DCU), nous avons démontré la possibilité d'utiliser les peignes de fréquences optiques générés par les lasers à base de puits et bâtonnets quantiques sur InP comme source multi-longueur d'onde pour les communications WDM. Dans cette étude, le format de modulation multi-porteuse OFDM à bande latérale unique et à détection directe est utilisé pour moduler l'intensité de chaque raie du peigne. Ce format de modulation, permettant d'obtenir des efficacités spectrales et des débits élevés tout en gardant une architecture de système simple et à faible coût, est très prometteur pour les réseaux datacom de nouvelle génération. De plus, la résistance du format OFDM à la dispersion chromatique de la fibre est un atout incontournable pour les télécommunications optiques [42].

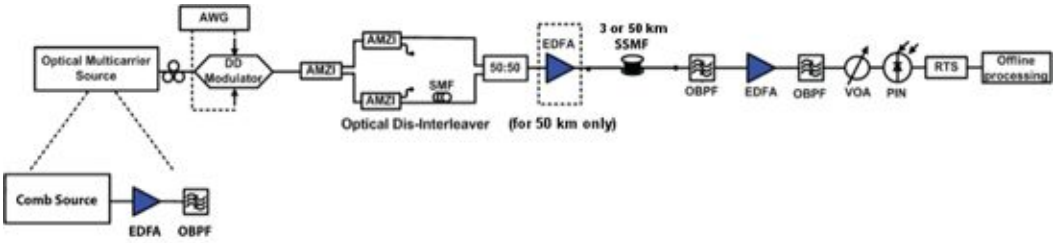

Figure 11 – Montage expérimental pour les mesures de transmission WDM en utilisant le format de modulation OFDM à bande latérale unique et à détection directe.

Pour les mesures de transmission effectuées à DCU, un système de communication similaire à celui présenté en [43] a été utilisé (voir fig. 11). Dans ce système, un signal OFDM électrique est produit par un générateur de formes d'onde arbitraires et utilisé pour moduler tout le peigne de fréquences à l'aide d'un modulateur Mach-Zehnder. Le signal est constitué d'un certain nombre de sous-porteuses RF séparées de 97.65 MHz, qui dépend de la bande passante totale désirée. Chaque sous-porteuse est modulée selon le format de modulation 16-QAM, pour un débit individuel d'environ 390.6 Mb/s. Les raies du peigne ainsi modulées sont ensuite décorrelées entre elles, avant d'être transmises à travers 3 ou 50 km de fibre optique monomode standard SMF-28. Du côté du récepteur, chaque raie est individuellement filtrée et détectée à l'aide d'une photodiode rapide et d'un oscilloscope en temps réel, avant de procéder à la démodulation du signal reçu et au comptage des erreurs binaires avec Matlab.

Dans cette étude, nous avons considéré plusieurs diodes laser : le composant à puits quantique dont les caractéristiques ont été présentées en figure 3 et des lasers à base de bâtonnets quantiques avec des longueurs de cavité différentes. Pour le dispositif à puits quantique avec fréquence de répétition de 37.6 GHz, 16 modes longitudinaux du spectre d'émission laser ont été filtrés, modulés à 25 Gb/s avec un signal OFDM constitué de 80 sous-porteuses, et transmis à travers 50 km de fibre. Dans cette transmission, le taux d'erreur binaire pour les différents modes du laser est toujours inférieur à la limite imposée par la convergence des algorithmes de correction d'erreur sans voie de retour (7% FEC), comme montré dans la figure 12a. Cependant, ces performances sont inférieures à celles qui peuvent être obtenues en utilisant un laser en cavité externe pour chaque canal WDM. Cette dégradation des performances est liée au bruit d'intensité à basse fréquence de chaque raie du laser Fabry-Perot, comme nous avons pu le remarquer en considérant la variation du spectre de bruit d'intensité et de l'EVM (*error vector magnitude*) en fonction de la fréquence RF (voir figure 12b). Néanmoins, en utilisant ce laser à puits quantique un débit agrégé net de 400 Gb/s a été obtenu avec une seule polarisation de la lumière.

Des débits beaucoup plus élevés peuvent être atteints en utilisant comme sources multi-longueur d'onde pour le WDM des lasers à base de bâtonnets quantiques. En

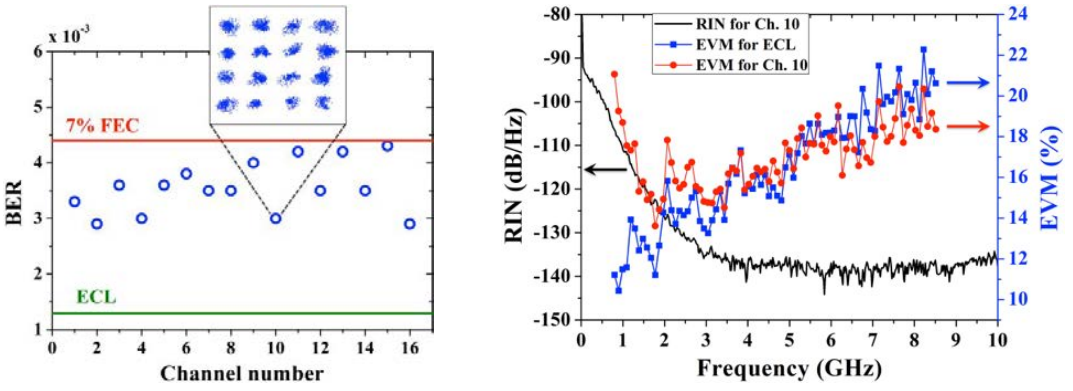

(a) (b)

Figure 12 – (a) Taux d'erreur binaire pour les différentes porteuses optiques générées par le laser à puits quantique en comparaison avec celui obtenu pour un laser en cavité externe. Dans l'encart : diagramme de constellation 16-QAM pour la porteuse optique numéro 10, comprenant la contribution de tous les 80 sous-porteuses RF. (b) Magnitude du vecteur d'erreur (EVM - *Error-vector magnitude*) de la constellation 16-QAM des 80 sous-porteuses OFDM pour le mode optique numéro 10 du laser à puits quantique et pour le laser en cavité externe. Le bruit relatif d'intensité du mode numéro 10 est aussi inclus pour comparaison.

effet, leur large spectre d'emission permettrait d'avoir davantage de modes pour la transmission de données. Pour les mesures de transmission à l'aide de lasers à bâtonnets quantiques, nous avons utilisé deux signaux OFDM constitués, respectivement, de 72 et de 86 sous-porteuses RF, en fonction du pourcentage d'*overhead* supposé pour le FEC (*forward error correction*). Ces signaux, permettant des débits de l'ordre de 28.2 Gb/s et de 33.6 Gb/s par canal WDM, sont utilisés pour moduler les raies des peignes de fréquences optiques générés par des lasers avec ISLs de 44.7 et de 22.7 GHz. Les performances des transmissions effectuées à travers 3 et 50 km de fibre avec le composant à 44.7 GHz, et à travers 3 km de fibre avec le laser à 22.7 GHz sont montrées dans la figure 13.

Comme dans le cas du laser à puits quantique, aussi pour les composants à bâtonnets la qualité de la transmission est limitée par le rapport signal à bruit de chaque porteuse optique et par le bruit relatif d'intensité des différents modes. Ces caractéristiques sont dégradées pour des valeurs d'ISL plus faibles car, à parité de largeur spectrale du peigne et de puissance optique émise par le laser, le nombre de modes laser augmente et la puissance optique par mode diminue. Cependant, le débit agrégé et l'efficacité spectrale vont augmenter, en vertu du nombre supérieur de porteuses optiques et de l'espacement réduit entre les modes. Dans ce travail, des débits agrégés de l'ordre de 1.128 Tb/s (40×28.2 Gb/s) et de 1.344 Tb/s (40×33.6 Gb/s) ont été obtenus en utilisant le laser avec ISL de 44.7 GHz, alors que des débits de l'ordre de 2.256 Tb/s (80×28.2 Gb/s) peuvent être atteints avec le composant à 22.7 GHz. L'efficacité spectrale la plus large que nous avons obtenue est de 1.25 bit/s/Hz pour le laser à 22.7 GHz, mais des valeurs plus élevées sont possibles en réduisant ultérieurement l'ISL du laser. À ce

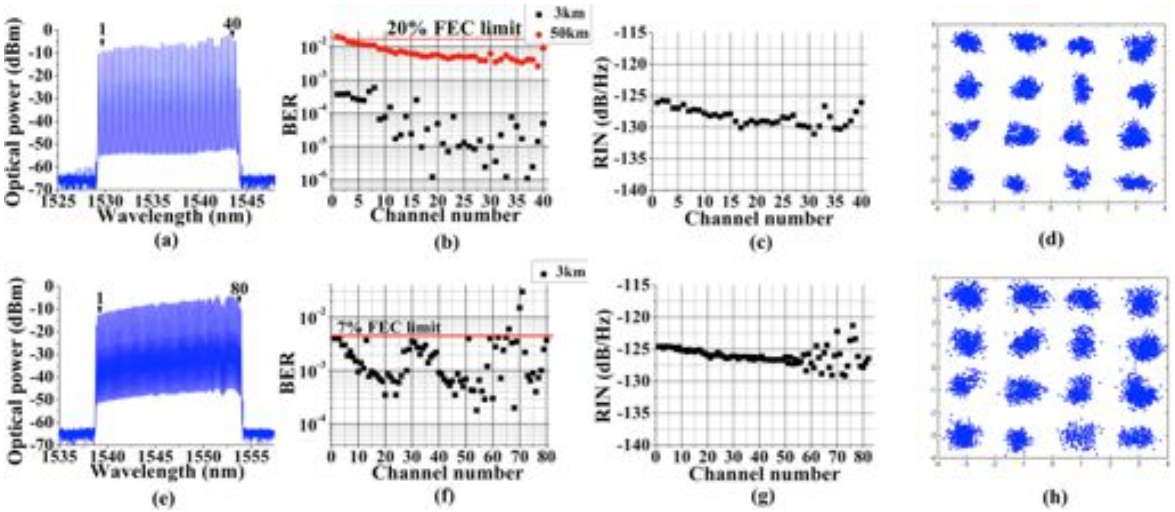

Figure 13 – (a) Spectre optique filtré du laser à blocage de modes à bâtonnets quantiques avec ISL de 44.7 GHz, (b) taux d'erreur binaire pour les différentes porteuses optiques en utilisant les signaux OFDM à 28.2 Gb/s (carrés noirs) et 33.6 Gb/s (cercles rouges), respectivement pour des transmissions à travers 3 et 50 km de fibre SMF-28, (c) bruit relatif d'intensité moyen mesuré dans la bande 0-10 GHz pour tous les modes, et (d) diagramme de constellation 16-QAM pour le mode central, après une transmission à travers 3 km de fibre SMF-28. (e)-(h) Les mêmes quantités que dans (a)-(d), mais pour le laser à blocage de modes à bâtonnets quantiques avec ISL de 22.7 GHz.

propos, des premiers tests effectués avec un composant à 10.8 GHz ont montrés que des débits de l'ordre de 4 Tb/s peuvent être obtenus, avec des efficacités spectrales d'environ 2.6 bit/s/Hz. Ces capacités de transmission semblent être particulièrement prometteuses pour des liens à très haut débit, dans des scénarios compatibles avec les futures applications datacom.

Conclusions

Dans le présent travail de thèse nous avons traité différents aspects relatifs aux peignes de fréquences optiques générés par les lasers à blocage de modes mono-section. Tout d'abord, une comparaison des performances en verrouillage de modes à été effectuée pour des structures laser à base de milieux à gain semi-conducteurs à basse dimensionnalité. Une étude systématique de propriétés telles que la largeur du spectre optique d'émission et l'évolution du battement RF des modes laser sur une photodiode nous a permis de conclure que le matériau à bâtonnets quantiques d'InAs sur InP présente des meilleures caractéristiques par rapport aux autres matériaux considérés. En effet, ce milieu à gain permet d'obtenir des largeurs de spectre d'émission jusqu'à 15 nm et des largeurs de raie RF de l'ordre de la dizaine de kHz, ce qui ne semble pas être possible avec des lasers mono-section à puits quantique ou à boîtes quantiques d'InAs sur GaAs. Le large spectre d'émission des lasers à bâtonnets peut donner lieu à des impulsions ayant des durées allant jusqu'à 400 fs, comme nous avons pu l'observer à l'aide de

la technique FROG. Toutefois, un chirp important du signal optique à la sortie du laser rend nécessaire la présence d'un élément dispersif, comme par exemple une fibre optique de longueur convenable, afin de comprimer les impulsions. Ce chirp semble être dû aux dynamiques spécifiques du milieu à gain et non pas à la dispersion chromatique du matériau à bâtonnets. Une étude de cette dispersion effectuée au moyen de la technique de réflectométrie optique dans le domaine fréquentiel nous a permis, en effet, de conclure que les faibles valeurs de dispersion anormale mesurées pour le milieu à gain ne sont pas compatibles avec le large chirp de type normal déterminé par FROG. La technique de réflectométrie optique dans le domaine fréquentiel, expressément étudiée et validée pour la mesure de la dispersion chromatique dans les composants optiques, s'est révélée être particulièrement sensible aux propriétés dynamiques des composants sous test. Cela ouvre la voie à des nouvelles possibilités de mesure et applications.
Enfin, dans le présent travail de thèse, nous avons montré une utilisation efficace des composants à base de bâtonnets quantiques pour des transmissions WDM à très haut débit, à l'aide de la technique de modulation numérique OFDM en détection directe. Des bandes passantes supérieures au térabit par seconde ont été obtenues en modulant simultanément les différents modes d'un seul laser. Ces remarquables capacités de transmission, ainsi que le faible coût et la simplicité de mise en ouvre rendus possibles par l'utilisation du format de modulation OFDM, sont très intéressantes pour les futures applications télécom. Les technologies étudiées et développées au cours de cette thèse peuvent, plus particulièrement, constituer des solutions prometteuses par rapport à l'émergente problématique des interconnexions optiques à haut débit à l'intérieur des centres de traitement de données.

Références bibliographiques

[1] P. Delfyett, S. Gee, M.-T. Choi, H. Izadpanah, W. Lee, S. Ozharar, F. Quinlan, and T. Yilmaz, "Optical frequency combs from semiconductor lasers and applications in ultrawideband signal processing and communications," Journal of Lightwave Technology **24**(7), 2701–2719 (2006).

[2] J. Ye, H. Schnatz, and L. Hollberg, "Optical frequency combs: From frequency metrology to optical phase control," IEEE Journal of Selected Topics in Quantum Electronics **9**(4), 1041–1058 (2003).

[3] T. Udem, R. Holzwarth, and T. W. Hänsch, "Optical frequency metrology," Nature **416**(6877), 233–237 (2002).

[4] D. Bimberg and U. W. Pohl, "Quantum dots: promises and accomplishments," Materials Today **14**(9), 388–397 (2011).

[5] J. P. Reithmaier, A. Somers, S. Deubert, R. Schwertberger, W. Kaiser, A. Forchel, M. Calligaro, P. Resneau, O. Parillaud, S. Bansropun, M. Krakowski, R. Alizon, D. Hadass, A. Bilenca, H. Dery, V. Mikhelashvili, G. Eisenstein, M. Gioannini, I. Montrosset, T. W. Berg, M. v. d. Poel, J. Mørk, and B. Tromborg, "InP based lasers and optical amplifiers with wire-/dot-like active regions," Journal of Physics D: Applied Physics **38**(13), 2088–2102 (2005).

[6] Y. Arakawa and H. Sakaki, "Multidimensional quantum well laser and temperature dependence of its threshold current," Applied Physics Letters **40**(11), 939–941 (1982).

[7] M. Asada, Y. Miyamoto, and Y. Suematsu, "Gain and the threshold of three-dimensional quantum-box lasers," Quantum Electronics, IEEE Journal of **22**(9), 1915–1921 (1986).

[8] M. Sugawara, *Self-assembled InGaAs/GaAs quantum dots* (Academic, San Diego, CA; London, 1999).

[9] K. Yvind, D. Larsson, J. Mørk, J. M. Hvam, M. Thompson, R. Penty, and I. White, "Low-noise monolithic mode-locked semiconductor lasers through low-dimensional structures," in *Proceedings of SPIE*, A. A. Belyanin and P. M. Smowton, eds., vol. 6909, pp. 69,090A–69,090A–9 (2008).

[10] E. U. Rafailov, M. A. Cataluna, and W. Sibbett, "Mode-locked quantum-dot lasers," Nature Photonics **1**(7), 395–401 (2007).

[11] M. Thompson, A. Rae, M. Xia, R. Penty, and I. White, "InGaAs Quantum-Dot Mode-Locked Laser Diodes," IEEE Journal of Selected Topics in Quantum Electronics **15**(3), 661–672 (2009).

[12] Y. Nomura, S. Ochi, N. Tomita, K. Akiyama, T. Isu, T. Takiguchi, and H. Higuchi, "Mode locking in Fabry-Pérot semiconductor lasers," Physical Review A **65**(4) (2002).

[13] K. Sato, "Optical pulse generation using Fabry-Pérot lasers under continuous-wave operation," IEEE Journal of Selected Topics in Quantum Electronics **9**(5), 1288–1293 (2003).

[14] J. Renaudier, G.-H. Duan, P. Landais, and P. Gallion, "Phase Correlation and Linewidth Reduction of 40 GHz Self-Pulsation in Distributed Bragg Reflector Semiconductor Lasers," IEEE Journal of Quantum Electronics **43**(2), 147–156 (2007).

[15] W. Yang, "Single-Section Fabry-Pérot Mode-Locked Semiconductor Lasers," Advances in OptoElectronics **2011**, 1–11 (2011).

[16] J. Renaudier, R. Brenot, B. Dagens, F. Lelarge, B. Rousseau, F. Poingt, O. Legouezigou, F. Pommereau, A. Accard, P. Gallion, and G.-H. Duan, "45 GHz self-pulsation with narrow linewidth in quantum dot Fabry-Pérot semiconductor lasers at 1.5 µm," Electronics Letters **41**(18), 1007 (2005).

[17] Z. G. Lu, J. R. Liu, S. Raymond, P. J. Poole, P. J. Barrios, and D. Poitras, "312-fs pulse generation from a passive C-band InAs/InP quantum dot mode-locked laser," Opt. Express **16**(14), 10,835–10,840 (2008).

[18] J. Liu, Z. Lu, S. Raymond, P. J. Poole, P. J. Barrios, and D. Poitras, "Dual-wavelength 92.5 GHz self-mode-locked InP-based quantum dot laser," Optics letters **33**(15), 1702–1704 (2008).

[19] R. Rosales, K. Merghem, C. Calo, G. Bouwmans, I. Krestnikov, A. Martinez, and A. Ramdane, "Optical pulse generation in single section InAs/GaAs quantum dot edge emitting lasers under continuous wave operation," Applied Physics Letters **101**(22), 221,113 (2012).

[20] C. Gosset, K. Merghem, A. Martinez, G. Moreau, G. Patriarche, G. Aubin, A. Ramdane, J. Landreau, and F. Lelarge, "Subpicosecond pulse generation at 134GHz using a quantum-dash-based Fabry-Pérot laser emitting at 1.56 µm," Applied Physics Letters **88**(24), 241,105 (2006).

[21] K. Merghem, A. Akrout, A. Martinez, G. Aubin, A. Ramdane, F. Lelarge, and G.-H. Duan, "Pulse generation at 346 GHz using a passively mode locked quantum-dash-based laser at 1.55 µm," Applied Physics Letters **94**(2), 021,107–021,107–3 (2009).

[22] S. Latkowski, R. Maldonado-Basilio, and P. Landais, "Sub-picosecond pulse generation by 40-GHz passively mode-locked quantum-dash 1-mm-long Fabry-Pérot laser diode," Optics Express **17**(21), 19,166–19,172 (2009).

[23] R. Maldonado-Basilio, J. Parra-Cetina, S. Latkowski, and P. Landais, "Timing-jitter, optical, and mode-beating linewidths analysis on subpicosecond optical pulses generated by a quantum-dash passively mode-locked semiconductor laser," Optics letters **35**(8), 1184–1186 (2010).

[24] R. Rosales, S. G. Murdoch, R. T. Watts, K. Merghem, A. Martinez, F. Lelarge, A. Accard, L. P. Barry, and A. Ramdane, "High performance mode locking characteristics of single section quantum dash lasers," Optics Express **20**(8), 8649–8657 (2012).

[25] F. Kéfélian, S. O'Donoghue, M. T. Todaro, J. G. McInerney, and G. Huyet, "RF Linewidth in Monolithic Passively Mode-Locked Semiconductor Laser," IEEE Photonics Technology Letters **20**(16), 1405–1407 (2008).

[26] C. Paranthoen, N. Bertru, O. Dehaese, A. L. Corre, S. Loualiche, B. Lambert, and G. Patriarche, "Height dispersion control of InAs/InP quantum dots emitting at 1.55 µm," Applied Physics Letters **78**(12), 1751–1753 (2001).

[27] P. Caroff, C. Paranthoen, C. Platz, O. Dehaese, H. Folliot, N. Bertru, C. Labbé, R. Piron, E. Homeyer, A. L. Corre, and S. Loualiche, "High-gain and low-threshold InAs quantum-dot lasers on InP," Applied Physics Letters **87**(24), 243,107 (2005).

[28] F. Lelarge, B. Dagens, J. Renaudier, R. Brenot, A. Accard, F. Van Dijk, D. Make, O. Le Gouezigou, J. Provost, F. Poingt, J. Landreau, O. Drisse, E. Derouin, B. Rousseau, F. Pommereau, and G.-H. Duan, "Recent Advances on InAs/InP Quantum Dash Based Semiconductor Lasers and Optical Amplifiers Operating at 1.55 μm," IEEE Journal of Selected Topics in Quantum Electronics **13**(1), 111–124 (2007).

[29] G. P. Agrawal and N. K. Dutta, *Semiconductor Lasers* (Springer US, Boston, MA, 1995).

[30] D. Bimberg and C. Ribbat, "Quantum dots: lasers and amplifiers," Microelectronics Journal **34**(5-8), 323–328 (2003).

[31] G. Gray and G. Agrawal, "Importance of self-induced carrier-density modulation in semiconductor lasers," IEEE Photonics Technology Letters **4**(11), 1216–1219 (1992).

[32] M. Alalusi and B. Darling, "Effects of nonlinear gain on mode-hopping in semiconductor laser diodes," IEEE Journal of Quantum Electronics **31**(7), 1181–1192 (1995).

[33] S. Pralgauskaitė, V. Palenskis, J. Matukas, B. Šaulys, V. Kornijčuk, and V. Verdingovas, "Analysis of mode-hopping effect in Fabry-Pérot multiple-quantum well laser diodes via low frequency noise investigation," Solid-State Electronics **79**, 104–110 (2013).

[34] R. Trebino, *Frequency-resolved optical gating: the measurement of ultrashort laser pulses* (Kluwer Academic, 2000).

[35] J. Ratner, G. Steinmeyer, T. C. Wong, R. Bartels, and R. Trebino, "Coherent artifact in modern pulse measurements," Opt. Lett. **37**(14), 2874–2876 (2012).

[36] Z. Jiao, R. Zhang, X. Zhang, J. Liu, and Z. Lu, "Modeling of Single-Section Quantum Dot Mode-Locked Lasers: Impact of Group Velocity Dispersion and Self Phase Modulation," IEEE Journal of Quantum Electronics **49**(12), 1008–1015 (2013).

[37] U. Glombitza and E. Brinkmeyer, "Coherent frequency-domain reflectometry for characterization of single-mode integrated-optical waveguides," Journal of Lightwave Technology **11**(8), 1377–1384 (1993).

[38] B. J. Soller, D. K. Gifford, M. S. Wolfe, and M. E. Froggatt, "High resolution optical frequency domain reflectometry for characterization of components and assemblies," Optics Express **13**(2), 666–674 (2005).

[39] T.-J. Ahn, Y. Jung, K. Oh, and D. Y. Kim, "Optical frequency-domain chromatic dispersion measurement method for higher-order modes in an optical fiber," Optics Express **13**(25), 10,040–10,048 (2005).

[40] T.-J. Ahn, J. Y. Lee, and D. Y. Kim, "Suppression of nonlinear frequency sweep in an optical frequency-domain reflectometer by use of Hilbert transformation," Applied Optics **44**(35), 7630 (2005).

[41] E. D. Moore, "Advances in Swept-Wavelength Interferometry for Precision Measurements," Ph.D. thesis, University of Colorado (2011).

[42] J. Armstrong, "OFDM for Optical Communications," Journal of Lightwave Technology **27**(3), 189–204 (2009).

[43] V. Vujicic, P. Anandarajah, C. Browning, and L. Barry, "WDM-OFDM-PON Based on Compatible SSB Technique Using a Mode Locked Comb Source," IEEE Photonics Technology Letters **25**(21), 2058–2061 (2013).

Abstract

Optical frequency combs, generating tens of equally spaced optical carriers from a single laser source, are very attractive for next-generation wavelength division multiplexing (WDM) communication systems. This PhD thesis presents a study on the optical frequency combs generated by mode-locked laser diodes based on low-dimensional semiconductor nanostructures. In this work, the mode-locking performances of single-section Fabry-Perot lasers based on different material systems are compared on the basis of the optical spectrum width, the timing jitter and pulse generation capabilities. Then, noticing that InAs quantum dashes grown on InP exhibit on average better characteristics than other examined materials, their unique properties in terms of comb stability and pulse chirp are studied in more detail. Laser chirp, in particular, is first investigated by frequency resolved optical gating (FROG) characterizations. Then, chromatic dispersion of the laser material is assessed in order to verify whether it can account for the large chirp values measured by FROG. For that, a high sensitivity optical frequency-domain reflectometry setup is used and its measurement capabilities are extensively studied and validated. Finally, the combs generated by quantum dash mode-locked lasers are successfully employed for high data rate transmissions using direct-detection optical orthogonal frequency division multiplexing. Terabit per second capacities, as well as the low cost of this system architecture, appear to be particularly promising for future datacom applications.

Acknowledgements

First of all, I would like to thank my thesis director Abderrahim Ramdane and co-director Badr-Eddine Benkelfat for the invaluable support and guidance they have provided me during my research work at the CNRS Laboratory for Photonics and Nanostructure (LPN) and Télécom SudParis, respectively. Their trust and commitment has been of fundamental importance for me to carry out this PhD thesis with passion and self-confidence.

I express my gratitude to the members of the doctoral committee Philippe Gallion, Guillaume Huyet, Pascal Besnard, Béatrice Dagens and Aziz Benlarbi-Delaï for having willingly accepted to examine and judge this PhD dissertation.

Working at LPN has been for me a great pleasure and honor and for this I would like to thank the laboratory director Dominique Mailly. This thesis work would not have been possible without the dedicated support of Anthony Martinez and Kamel Merghem. I am particularly grateful to them for their commitment during the initial training, as well as during cleanroom and laboratory research activities.

I would also like to express my gratitude to all the engineers and the technical staff of the LPN cleanroom, who contributed directly or indirectly to the fabrication and processing of the devices used in this thesis, and to the IT and administrative staff of the LPN for their kind and precious assistance in everyday work. I wish to thank also the entire PHODEV group and in particular Guy Aubin, Jean-Louis Oudar and Sophie Bouchoule for fruitful and stimulating discussions on semiconductor laser physics, fabrication and telecommunication applications.

A special thank goes to Yaneck Gottesman for his valuable advices on the whole thesis work and his passionate and inspiring supervision of the research carried out at Télécom SudParis. My days in Evry would not have been the same without him, as well as the closeness of Bruno Robillart, Abdoulaye Fall and François Lamare.

I would like to acknowledge the EU FP7 Marie Curie Initial Training Network PROPHET and all its partners for fruitful and enriching interactions. In particular, I am very grateful to François Lelarge from III-V lab for providing state-of-the-art quantum dash heterostructures and components employed in this work and for fruitful

discussion during this thesis. I would also like to thank Holger Schmeckebier and Prof. Dieter Bimberg for having welcomed me at TU Berlin during my PROPHET secondment. I owe the results of frequency-resolved optical gating characterizations to their excellent organization and proficiency on the subject. In addition, I would like to express my gratitude to Jean-Guy Provost from III-V lab and Catherine Lepers from Télécom SudParis for having made possible many of the experimental investigations on short-distance feedback sensitivity of single-section lasers presented in chapter 3.

I wish to acknowledge also the ANR TELDOT project and all its partners, in particular Kamil Klaime from INSA Rennes for having provided the InAs/InP (311)B quantum dot laser structure used in the present study. Fruitful collaborations have been developed in the framework of the EU FP7 BIG PIPES project, that I wish to thank together with its partners. In particular, I am very grateful to Prof. Liam Barry, Regan Watts and Vidak Vujicic from Dublin City University (DCU), Ireland, for the stimulating exchanges and the very productive work carried out on optical orthogonal frequency division multiplexing. I owe the results presented in chapter 5 to their outstanding expertise in the domain, as well as to the facilities of the DCU Radio and Optical Communication Lab.

In my unique experience at LPN, I have really appreciated the closeness of many friends and colleagues, in particular my officemates Konstantinos Papatryfonos, Ricardo Rosales and Vivek Panapakkam, as well as Andrea Cattoni, Giacomo Priante, Oriane Mollet, Dimitris Kazazis, Konstantinos Pantzas, Carmen Gomez, Vishnuvarthan Kumaresan and Julie Carimalo from LPN, and Siddharth Joshi and Maria Anagnosti from III-V lab. I thank them for their friendship and for all the good times we spent together.

Last but not the least, I would like to express my immense gratitude to my parents, my brother Nicola and my girlfriend Cristina for their endless love and encouragement, their interest and admiration for my studies and, above all, for having tolerated me in the difficult period of thesis writing. Their support has been invaluable to me during these years.

Contents

List of Figures

List of Tables

Introduction

The exponential growth of the Internet traffic, together with current trends in networking such as Internet of things and cloud storage and computing, requires new solutions to face the increasing demand for communication bandwidth. As the bottleneck of the network approaches the end users and data centers, owing to the increasing number and capacity requirement of them, telecommunication technologies providing high data rates at low cost and high energy efficiency for short-reach transmission (few kilometers down to hundreds of meters) are needed. Fiber optic communications, allowing for superior performances in terms of latency and power consumption at high data rates compared to other technologies, appear to be the only viable solution for this purpose. Moreover, the current efforts toward the integration of several optoelectronic component on InP and Si platforms open the way for potential cost reduction and higher energy efficiency for optical communications.

One of the most effective solutions to increase the communication bandwidth of optical systems is the use of wavelength division multiplexing (WDM) technology, allowing for parallel transmission of high bit-rate signals on separate wavelengths. Additionally, the possibility of combining the advantages of WDM with the use of advanced optical modulation formats and, potentially, coherent detection would lead to unprecedented transmission capacity. Although WDM technology is already widely deployed in core networks and coherent optical communication systems are under development to further increase the capacity of Internet backbone, to date, use of WDM in access networks and intra-/inter-data center communications has been hampered by the high cost of components and by the network planning challenges related to the management of hundreds of wavelengths in the telecommunication system. Consequently, time-division multiple access (TDMA) and encrypted packet broadcasting have been preferred, respectively, for upstream and downstream links in current Gigabit-capable Passive Optical Networks (GPON), over wavelength-separated high-capacity transmission channels of WDM.
Nonetheless, the availability of low-cost laser sources, each capable of generating a number of equally-spaced optical frequency channels, would probably change the scenario in future optical communications. Sources of this kind are known in literature as optical frequency combs (OFCs) and can be obtained in a number of ways, the most popular

one being the use of mode-locked lasers. A mode-locked laser (MLL) is a device capable of emitting a regular train of optical pulses at a repetition period equal to the round-trip time of the laser cavity. In the frequency domain this corresponds to a discrete set of equally-spaced spectral lines, with spacing equal to the pulse repetition rate. For optical communications, OFCs produced by semiconductor-based mode-locked laser diodes are of interest [1, 2], owing to their potential for low cost, low power consumption and monolithic integration in photonic integrated circuits (PICs), compared to frequency comb generators consisting of discrete optical components. Moreover, the possibility of manufacturing millimeter-long components, capable of generating tens of transmission channels compatible with dense-WDM grids, would be beneficial for the realization of compact modules.

In the last decade, research on semiconductor MLLs has been focused on the use of low-dimensional nanostructures, such as quantum dot (QD) and quantum wire (QWR), as laser active material. In particular, self-assembled structures, like InAs QDs on GaAs substrates and InAs dots and dashes (elongated dots) on InP substrates, have received increasing attention, owing to the reduced threshold current densities, the ultrafast carrier dynamics and the low spontaneous emission noise coupled to lasing modes inherent to these material systems. These properties have led to improved mode-locking (ML) performances of semiconductor lasers, such as the generation of low-timing-jitter, sub-picosecond pulse trains with repetition rates of several tens of gigahertz and the production of OFCs with full width at half maximum (FWHM) bandwidth in excess of 10 nm [3].

Typical semiconductor mode-locked laser diodes consist of two sections, a gain section and an absorber one. The interplay between the gain provided by the forward-biased gain region and the saturable absorption obtained from the reverse-biased absorber is responsible for the generation and amplification of a stable pulse train at the cavity round-trip frequency. Additionally, a number of studies have indicated that phenomena analogous to ML in classic two-section devices can also be observed in single-section Fabry-Perot (FP) lasers, under continuous wave (CW) current injection [4–7]. Generation of self-starting pulses and strong phase correlation among the laser longitudinal modes, indicative of low timing jitter operation, exhibited by these devices has been attributed to significant nonlinear optical effects inside the cavity [5, 6]. In particular, four wave mixing (FWM) has been indicated as a possible mechanism responsible for this regime. Nonetheless, complete understanding of the phenomenon is still lacking and further experimental and theoretical investigations are necessary to unveil this laser dynamics. Because, in presence of these phenomena, mode-locking and comb generation can be achieved in single-section lasers without loss of average power, unlike two-section MLLs, study of this operating regime may be beneficial for future use of these devices in telecommunication applications.

Understanding and engineering of ML characteristics of single-section devices based on low-dimensional nanostructures has become one the main research subject of the Photonic Devices (PHODEV) group at the CNRS Laboratory for Photonics and Nanostructures (LPN), that I have joined in November 2011 in the framework of the Marie Curie Initial Training Network (ITN) PROPHET. In this thesis work, we aimed at gaining more insight into the generation of OFCs by means of single-section QD and quantum dash (QDash) based lasers and their use in telecommunication applications. For this purpose, we have considered different aspects of the problem.

First of all, we have studied the ML performance, in terms of pulse generation capability and timing jitter, of single-section FP laser based on different material systems: InAs QDs and quantum dashes (QDash) on InP for emission at 1.55 µm, InAs QDs on GaAs for emission at 1.3 µm, as well as the conventional InGaAsP quantum well (QW) material on InP at 1.55 µm. Noticing that the QDash material, skillfully developed at Alcatel-Lucent-Thales III-V Lab, exhibits on average better lasing and ML characteristics compared to other materials examined in our study, we have focused on QDash based lasers for further investigations in the spectral and temporal domain.

In the spectral domain, optical linewidth and long term stability of the generated combs has been studied in detail. Additionally, in a preliminary study carried out in collaboration with III-V lab, we have demonstrated that FP lasers compatible with monolithic integration on InP platform, with lithographically defined cavity lengths, can be obtained without ML performance degradation.

In the temporal domain, we have investigated the shape and frequency chirping of emitted pulses by frequency-resolved optical gating (FROG), in collaboration with the solid-state physics group of Technical University of Berlin. In agreement with previous works on these devices, FROG measurements reveal that highly up-chirped pulses are emitted at the laser output and a large intra-cavity dispersion is responsible for broad pulse generation. In order to verify whether material dispersion is at the origin of these observations [4], or rather if this behavior is a consequence of the complex laser dynamics, we have turned our attention to the measurement of the chromatic dispersion of optoelectronic components. For this purpose, as a part of this thesis work at Télécom SudParis, we have contributed to the performance analysis of a high-sensitivity optical frequency-domain reflectometry (OFDR) setup for the characterization of optical components. Using OFDR technique, the group velocity dispersion of a semiconductor optical amplifier (SOA) based on QDash material has been determined and the values obtained, being incompatible with the large chirp observed for lasers, have allowed us to exclude the material dispersion as cause of pulse broadening in single-section QDash devices.

Finally, as a further achievement of this work, we have demonstrated, in collaboration with Dublin City University (DCU), successful use of QDash based frequency comb

generators for WDM data transmission using high-spectral efficiency 25 Gbit/s optical orthogonal frequency division multiplexing (OFDM) encoding. Aggregate capacities up to 4 Tb/s from a single device using direct detection OFDM (DD-OFDM) are achievable in transmission scenarios compatible with intra- and inter-data center communications. Transmission results are interpreted on the basis of the relative intensity noise (RIN) performances of QDash FP lasers and specific tradeoffs when using these devices for OFDM transmission are identified.

In accordance with the research strategy outlined above, this thesis is structured as follows. In the first chapter, after an introduction on the concept of optical frequency combs and the existing technologies for combs generation and use in telecommunication applications, we provide a theoretical background on the technique of laser mode-locking. We focus, in particular, on the ML mechanisms in semiconductor lasers and on the special case of single-section devices and we discuss the state of the art of QD and QDash based MLLs.
In chapter 2, we review the physical principles behind the use of low-dimensional nanostructures as gain material for lasers and present the epitaxial structures and the laser fabrication process employed for this study.
Chapter 3 is devoted to the ML characterization of single-section lasers based on QD and QDash material. For the latter, we carry out more detailed investigation in the temporal domain, by means of FROG technique, and in the spectral domain. As a perspective of this work, we conclude the chapter presenting the outcome of a study of ML performances of a QDash distributed Bragg reflector (DBR) laser, markedly conceived at III-V Lab to emulate a single-section comb generator and intended for integration on InP based PICs.
In chapter 4, we present our investigation on dispersion characterization using optical frequency-domain reflectometry (OFDR). Understanding, validation and specific features identification of the technique are performed, and discussed here, before its actual use in the characterization of a QDash based SOA.
Finally, in chapter 5, we report on the use of QW and QDash based frequency comb generators for WDM data transmission, using spectrally efficient OFDM modulation. Conclusion and future perspectives of this work are, then, drawn.

Studies presented in this thesis have been the object of a number of publications. For a complete list, the interested reader is referred to page XX.

Chapter 1

Semiconductor mode-locked lasers for optical frequency combs

Optical frequency combs OFCs generated by mode-locked lasers (MLLs) have become a key technology in different scientific domains, from fundamental physics to optical fiber telecommunications. In this chapter, we review the main technologies devoted to the generation of optical frequency combs, with a major focus on the laser mode-locking (ML) technique. The chapter is organized as follows: after an introduction on OFCs, their implementation and uses in optical fiber telecommunications, presented in sec. 1.1, in sec. 1.2 we will discuss in detail the technique of mode-locking of lasers and the characteristics of MLLs. Finally in sec. 1.4 we will address the mechanisms of ML in semiconductor lasers, including single-section passively mode-locked laser, which constitutes the actual scope of this thesis work.

1.1 Optical frequency combs

An optical frequency comb (OFC) is a light source whose spectrum is composed of a discrete set of equally spaced lines. In the frequency domain an ideal comb would be represented as a series of Dirac delta functions centered at:

$$f(n) = f_0 + nf_r, \tag{1.1}$$

where n in an integer, f_r is the line spacing and $f_0 < f_r$ is the carrier offset frequency. If the comb spans one octave or more, i.e. the highest frequency of the comb is at least double the lowest one, the comb is said to be *self-referenced* and direct measurement (and drift correction) of f_0 is possible. This is performed by detecting the beat-note of two lines of the comb separated by one octave in an *f–2f interferometer*, in which the highest frequency is compared with the lowest one, after frequency-doubling of the latter in a nonlinear crystal, as shown in fig. 1.1. If the comb is frequency stabilized and

f_r and f_0 are precisely known, as referred to the microwave cesium frequency standard which defines the second in the SI system of units, any unknown optical frequency within the comb bandwidth can be measured absolutely by determining the beat-note frequency between the target frequency and its closest line of the comb on a square-law detector, using an electronic frequency counter [8].

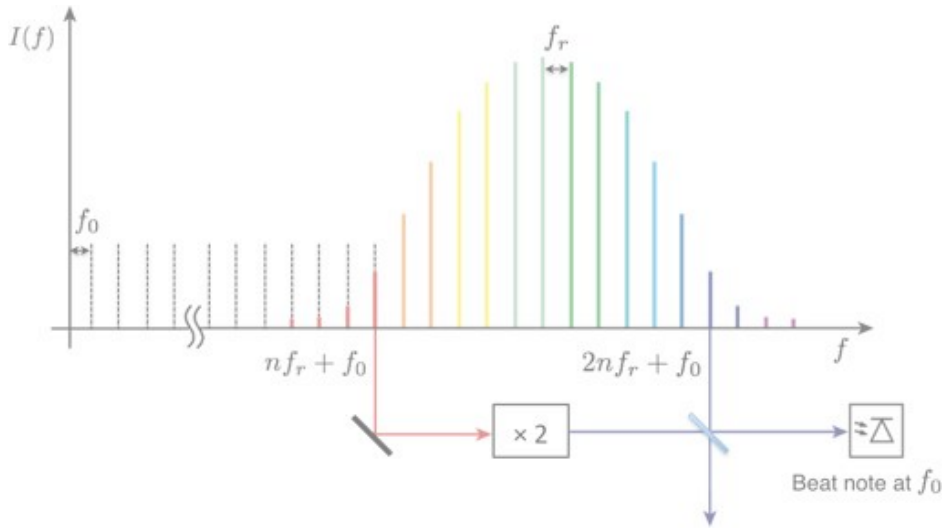

Figure 1.1 – Optical frequency comb with f–$2f$ interferometer for carrier offset frequency measurement (adapted from [8]).

The use of OFCs and comb self-referencing in the context of optical frequency metrology has been introduced at the turn of the 21$^{\text{th}}$ century by the group of T. W. Hänsch at the Max Planck Institute for Quantum Optics (MPQ) in Garching, Germany and that of J. L. Hall at the Joint Institute for Laboratory Astrophysics (JILA) in Boulder, Colorado. The first showed in 1999 that the comb lines of the spectrum of an ultrafast Kerr-lens mode-locked Titanium-Sapphire laser could be used as a ruler for the accurate measurement of optical frequencies [9]. The latter demonstrated that the mode-locked spectrum generated by this laser could be expanded through supercontinuum generation in a microstructured optical fiber to span one octave and, thus, allow for comb self-referencing [10]. The groundbreaking research on OFCs and their use in metrology and spectroscopy allowed for a dramatic simplification of the complex, large-scale metrology setups (frequency multiplication chains [11]) used until then and, ultimately, lead to the attribution of one half of the Nobel Prize in Physics 2005 to J. L. Hall and T. W. Hänsch. More importantly, the theoretical and technological advances in the field of OFCs since 1999 have had a significant impact on several fields of science and frequency comb technologies, initially developed in the context of fundamental physics, are now receiving much attention in the optical fiber communication community. It is, thus, worth reviewing the techniques allowing for the generation of optical frequency combs.

1.1.1 Optical frequency combs technologies

The most popular techniques adopted in literature for the generation of optical frequency combs are the following:

- phase modulation and gain-switching of a single-frequency laser,
- laser mode-locking, and
- parametric frequency conversion in optical microresonators.

We will discuss here each of them in more detail.

Phase modulation and gain-switching of single-frequency laser

The generation of modulation sidebands on a continuous wave (CW) optical carrier is the most straightforward way of producing an optical frequency comb. For this purpose, an electro-optic modulator (EOM) driven by a radio frequency (RF) signal can be used. If large modulation frequency and modulation index are used, the resulting spectrum can be quite wide, although, in general, this scheme does not allow to achieve large fractional bandwidths $\Delta\lambda/\lambda$. Nonetheless, OFCs with tooth spacing in the range from 0.5 to 20 GHz, covering a spectral width of few THz have been obtained by placing the EOM inside a free-space optical cavity, resonant with the modulated carrier and the modulation sidebands [12].
In the context of optical communications, analogous solutions have also been reported, based on phase modulation within amplified fiber loops [13, 14] and cascaded Mach Zehnder modulators (MZM) [15]. All these schemes provide tunability of both the central wavelength and the frequency spacing of the output combs, and some of them are also capable of excellent comb flatness and narrow optical linewidths. On the other hand, the large insertion loss of the modulators along with the large number of components involved has a detrimental impact on the cost and on the power efficiency of these frequency comb generators, making the resulting transmission systems unsuitable for cost-effective access networks and short distance communications.
Alternatively, a promising approach in the sense of complexity reduction consists in the direct modulation an injection-locked FP laser diode so as to produce gain-switching [16], possibly followed by a spectral expansion stage such as a phase modulator or a highly nonlinear optical fiber in order to increase the number of comb lines [17]. In this case, comb spacing tunability is limited by the direct modulation bandwidth of the laser to about 18 GHz, but the narrow optical linewidth across the whole spectrum induced by injection of an external cavity laser (ECL) makes this comb source suitable for use in coherent communication systems.

Laser mode-locking

The most established way of generating an optical frequency comb is using a mode-locked laser (MLL). These lasers produce a periodic train of optical pulses at a period equal to the round-trip time of the laser cavity, leading to a spectrum consisting of discrete lines separated by integer multiples of the pulse repetition frequency. Although laser mode-locking has been achieved in a large variety of wavelength ranges and material systems [18], ultrafast Kerr-lens mode-locked Titanium-Sapphire lasers remain the preferred tools for wide comb generation. Their capability of emitting high peak-power femtosecond pulses, their large fractional bandwidth, expandable in a highly nonlinear microstructured fiber if needed, and the possibility of obtaining octave-spanning [19] or 10 GHz frequency spacing [20] combs directly from the laser, make Titanium-Sapphire MLLs essential in fundamental physics applications.
Nevertheless, the high complexity and cost of such a laser systems make them unsuitable for telecommunication applications, for which III-V semiconductors are the materials of choice for laser sources. In this regard, a number of solutions based on semiconductor MLLs have been proposed: from stabilized optical fiber loop based mode-locked lasers [21, 22] to monolithic semiconductor components [1]. These frequency comb generators allow to achieve sub-picosecond pulses at repetition frequencies ranging from few GHz to several tens of GHz, with locked spectral full width at half maximum (FWHM) in excess of 10 nm [3]. Monolithic MLLs, in particular, appear to be promising for future communication applications, in a philosophy of cost reduction and component integration on emerging III-V semiconductor or Si-based photonic integrated circuits (PICs) platforms [23, 24], even though these advantages come at the expenses of more demanding efforts in order to reduce the linewidth and jitter and increase the free spectral range (FSR) f_r of the generated combs. Issues related to mode-locking in semiconductor lasers will be discussed in more detail further on in this chapter.

Parametric frequency conversion in optical microresonators

A very active field of research in the last decade has been the generation of OFCs by means of nonlinear optical processes in high quality factor optical microresonator, typically whispering gallery mode (WGM) resonators with Q ranging from 10^5 up to 10^{10} [25]. In these components, the ultrahigh Q-factors and the small modal volumes lead to to very low thresholds (down to the µW power level) for nonlinear optical effects, such as four wave mixing (FWM) if the resonator is made from third-order nonlinear material. Frequency comb generation can, then, be obtained by pumping the optical microresonator with a CW laser beam, coupled into the device by means of a tapered optical fiber. Under these conditions, degenerate FWM will occur, leading to

conversion of two pump photons into a "signal" photon at higher frequency and an "idler" photon at lower frequency. Conservation of energy implies that the generated frequencies are equally spaced with respect to the pump frequency. The efficiency of this sideband generation will be higher if the new frequencies correspond to the optical modes of the resonator, resulting in a cavity enhanced process. The generated frequency components may then interact among them or with other pump photons in the $\chi^{(3)}$ medium through non-degenerate FWM. Cascaded wave mixing will, thus, lead to the generation of equidistant sidebands or, equivalently, an optical frequency comb, whose bandwidth is only limited by material transparency and intracavity dispersion [25, 26]. The latter, in particular, inducing a variation of the resonator FSR with wavelength, limits the efficiency of the parametric processes for large detuning with respect to the pump frequency. Nonetheless, suitable selection of materials and dispersion engineering, e.g. by means of surface coatings [27], can be used for wider comb generation.
OFCs generated with this technique exhibit large fractional bandwidth of one octave, or a consistent fraction thereof, and large tooth spacing of several tens of GHz up to THz [25]. Moreover, using CMOS-compatible fabrication processes, on-chip optical frequency comb generators have been demonstrated [28]. This family of comb generators has been indicated by many as a promising solution, enabling a convergence of comb technology with fiber optics [29]. Nevertheless, the watt-range pump powers required to trigger broadband parametric frequency conversion and, above all, the unsuitable phase noise performances, due to a number of processes inside the resonator cavity (e.g. thermo-refractive and thermo-elastic noise), may be limiting factors for use of these combs in communication applications. Yet, long-term stabilization mechanisms can be implemented and, recently, high-speed coherent communications have been demonstrated [30].

A summary of the technologies employed for the generation of optical frequency combs as a function of comb spacing f_r and fractional bandwidth $\Delta\lambda/\lambda$ is reported in fig. 1.2. The focus of this thesis work are OFCs produced by semiconductor MLLs, sitting in the lower right region of the graph in fig. 1.2.

1.1.2 Frequency combs for optical telecommunication applications

Having reviewed the main technologies allowing to generate OFCs, we now aim at briefly discussing their potential applications in the field of optical communications and signal processing. These can be divided into two groups: frequency domain and time domain applications. In the frequency domain, the main areas of interest for use of OFCs are:

- analog and digital wavelength division multiplexing (WDM) communications,

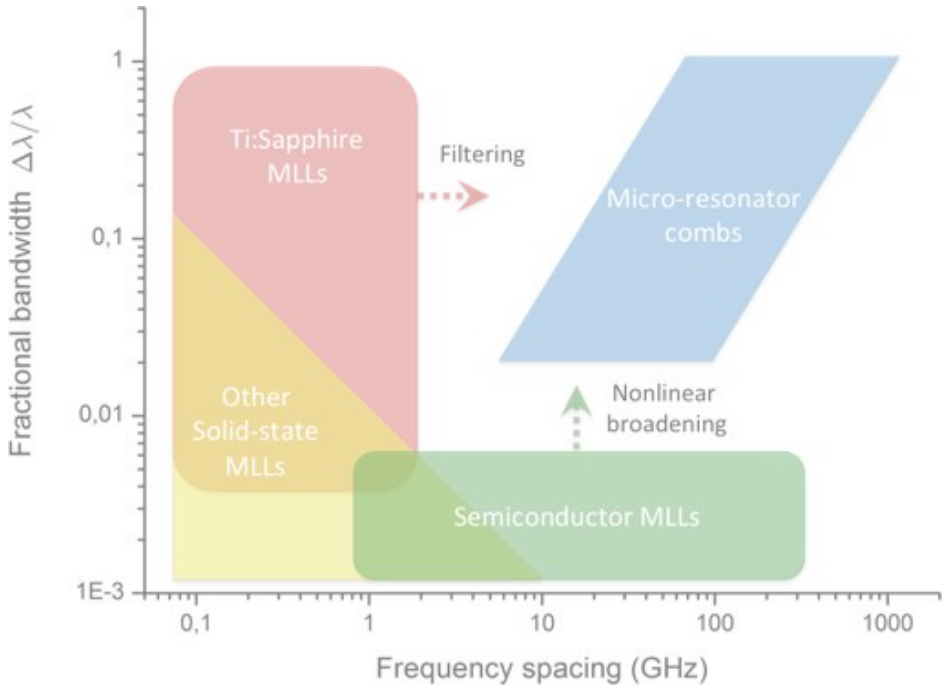

Figure 1.2 – Qualitative summary of optical frequency comb technologies as function of fractional bandwidth $\Delta\lambda/\lambda$ and frequency spacing f_r (adapted from [25]).

- optical and RF arbitrary waveform generator (AWG) and radio over fiber (RoF).

In WDM, equally-spaced lines with comparable powers from the comb can be individually modulated using either analog or digital modulation formats and multiplexed for subsequent transmission over optical fiber. If the optical linewidths of the comb modes are sufficiently narrow, coherent detection can be used in combination with advanced optical modulation formats, for better sensitivity and higher capacity. Among the different modulation formats under investigation, a promising approach is optical orthogonal frequency division multiplexing (OFDM), allowing for large capacities and improved spectral efficiency through the use of multilevel modulation of tightly-spaced orthogonal subcarriers [31]. If the subcarriers are the narrow lines of an OFC, all-optical OFDM based on coherent detection can be implemented to achieve very high capacities, at the expense of system complexity. Alternatively, digitally generated subcarriers modulated onto an optical carrier can be used together with direct-detection in high capacity, cost-effective systems. This approach will be discussed in more detail in chapter 5.

OFCs can also be employed to produce tailored optical and RF waveforms. The former can be obtained by individually modulating in amplitude and phase the different comb lines and spectrally recombining them [32], while the latter are achieved by mixing into a fast photodetectors suitably selected and modulated lines at the desired frequency spacing [33]. This last scheme can be successfully employed for the generation of radio signal for broadband wireless communications in radio over fiber (RoF) systems

at 60 GHz [34]. In RoF, wireless signals are transported over optical links between a central station and multiple base station and hence radiated by antennas, after optical-to-electrical (O/E) conversion. This technology, providing Gb/s speeds with relatively simple and cost-effective architectures, is very promising for future wireless access networks.

In the time domain, ultrashort pulses and combs generated by MLL can be employed in several applications, such as:

- high-speed optical time-division multiplexing (OTDM) transmission,
- optical clock recovery and distribution,
- optical code-division multiple access (OCDMA) systems, and
- optical sampling.

In high-speed OTDM, ultrashort, low-timing-jitter MLL pulse trains are intensity modulated and interleaved at the transmitter and temporally demultiplexed at the receiver, based on pulse arrival time. Using a 40 GHz repetition rate quantum dot (QD) based semiconductor MLL, OTDM data transmission up to 160 Gb/s has been demonstrated [35]. Additionally, still in the context of OTDM, semiconductor MLLs have been proposed as key components at the receiver side for optical clock recovery and optical time demultiplexing of the tributary signals composing the OTDM data stream [36]. For this purpose, optical injection of the data signal into a MLL at the repetition frequency of the tributary streams can be used to retrieve the transmitter's clock, allowing for synchronization of the receiver. If the jitter of the MLL is sufficiently low, high speed OTDM data up to 320 or 640 Gb/s can be successfully demultiplexed [37]. Eventually, the high-power, low-jitter pulse train from a MLLs can be used as clock signal and distributed in high speed switching systems [38].
Using MLLs also OCDMA systems can be implemented by performing spectral phase encoding of on-off keying (OOK) modulated optical pulses at the transmitter, and coherent homodyne detection with a synchronized MLL at the receiver [33]. Despite their high complexity and the poor spectral efficiency, OCDMA systems may be interesting for secure communications and asynchronous, bursty data transmission in metropolitan area network (MAN)s.
Finally, MLLs can be used in optical sampling systems for time-resolved characterization of high-speed, periodic optical waveforms with bandwidth hardly accessible to conventional photodetectors and oscilloscopes. In these systems, a nonlinear interaction between the signal to be measured and an ultrashort pulse train, acting as sampling signal, can be used in combination with low-speed electronics to build an equivalent-time sampling oscilloscope. Specific requirements for this application are the

narrow pulsewidth and the low timing jitter of the pulse source, directly impacting on the temporal resolution and the jitter of the system. Additionally, high-power pulses for improved sensitivity and low pulse repetition rates of few hundreds of MHz to match the bandwidth of acquisition electronics are desirable. For these reasons, low-jitter mode-locked Erbium-doped fiber laser are the preferred pulse sources for optical sampling [39], although extended-cavity semiconductor MLLs have been proposed for compact systems [40].

1.2 Laser mode-locking

Owing to its versatility and its potential for applications, laser mode-locking (ML) is probably the most popular technique for generating OFCs. In this section, we introduce to the concept of laser mode-locking and provide some theoretical bases for the noise characteristics of MLL of interest for OFCs applications.

1.2.1 Introduction to the mode-locking regime

Let us consider a single transverse mode Fabry-Pérot laser with cavity length L and assume that it oscillates on multiple longitudinal modes. The frequency spacing f_r between the modes is determined by the optical length of the cavity and is given by:

$$f_r = \frac{c}{2n_g L} \tag{1.2}$$

with

$$n_g(\omega) = n_{eff}(\omega) + \omega \frac{\mathrm{d}n_{eff}(\omega)}{\mathrm{d}\omega} \tag{1.3}$$

where n_g is the group refractive index and n_{eff} is the mode effective refractive index. As indicated by eq. 1.2, in general, the free spectral range of the FP cavity is not necessarily constant, by virtue of the laser intracavity dispersion. However, if the emission bandwidth FWHM $\Delta\nu$ of the laser is not too wide or the active material dispersion is sufficiently small, we can assume with good approximation an equal frequency spacing between the modes. Under this condition, the output beam can be expressed as a sum of evenly spaced frequencies, as in a Fourier series, resulting in a periodic waveform with period $T_r = 1/f_r$, equal to to the cavity round-trip time. If the phases of the longitudinal modes have random values, the output waveform will be a continuous wave (CW) signal with average power given by the sum of powers of the modes. On the other hand, if a suitable mechanism is in place to make the modes oscillate with a well defined phase relation, a periodic train of short pulses can be produced and the laser is said to be mode-locked.
To clarify this point, let us consider $N = 2M + 1$ modes with equal field amplitude

E_0, separated by f_r within a laser emission bandwidth $\Delta\nu = Nf_r$. Let ν_0 be the optical frequency of the central mode and let us suppose that the n-th mode, with $n = -M, \ldots, M$, at frequency $\nu_n = \nu_0 + nf_r$ oscillate with a phase $\varphi_n = n\varphi$, i.e. the following phase relation is established between the modes:

$$\varphi_{n+1} - \varphi_n = \varphi \tag{1.4}$$

where φ is a constant. Then, assuming a linear polarization for the electric field (so as to consider only one component of it) and neglecting its spatial dependence, the temporal evolution of the total electric field at any point of the output beam, can be written as:

$$\begin{aligned} E(t) &= \mathbf{Re}\left\{\sum_{n=-M}^{M} E_0 \exp\left[j\left(2\pi\nu_n t + \phi_n\right)\right]\right\} \\ &= \mathbf{Re}\left\{A(t)\exp\left(j2\pi\nu_0 t\right)\right\} \end{aligned} \tag{1.5}$$

where $\mathbf{Re}\{\cdot\}$ denotes the real part operator and

$$A(t) = \sqrt{I(t)}\exp\left[-j\phi(t)\right] = \sum_{n=-M}^{M} E_0 \exp\left[jn\left(2\pi f_r t + \phi\right)\right] \tag{1.6}$$

is referred to as the *complex amplitude* of the electric field. In eq. 1.6, $I(t) = |A(t)|^2$ is the electric field intensity profile while $\phi(t)$, known as *temporal phase*, is related to the instantaneous optical frequency $\nu_{\text{inst}}(t)$ along $I(t)$ by:

$$\nu_{\text{inst}}(t) = \nu_0 - \frac{1}{2\pi}\frac{\mathrm{d}\phi(t)}{\mathrm{d}t}, \tag{1.7}$$

as one can deduce by taking the time derivative of the argument of $A(t)\exp\left(j2\pi\nu_0 t\right)$. Note that we have used different symbols to distinguish the temporal phase $\phi(t)$, from the phases of the longitudinal modes in the frequency domain φ_n, i.e. the *spectral phase* $\varphi(\omega)$, with $\omega = 2\pi\nu$.
Setting $2\pi f_r t' = 2\pi f_r t + \phi$ in eq. 1.6 and performing the summation, we obtain:

$$A(t') = E_0\frac{\sin(N\pi f_r t')}{\sin(\pi f_r t')} \tag{1.8}$$

Because the beam intensity is proportional to $|A(t')|^2$, let us consider the quantity $|A(t')|^2/E_0^2$. Fig. 1.3 shows the functional behavior of this quantity for different values of the number of modes N. It can be observed that the ML condition expressed by eq. 1.4 leads to the formation of a regular train of pulses with repetition frequency f_r, pulse width inversely proportional to N and pulse peak power proportional to N^2.

Although these conclusions are drawn from the special case of equal amplitude modes, analogous consideration can be made if different spectrum envelopes are assumed. In particular, it can be shown [41] that, if the condition in eq. 1.4 holds true, the field

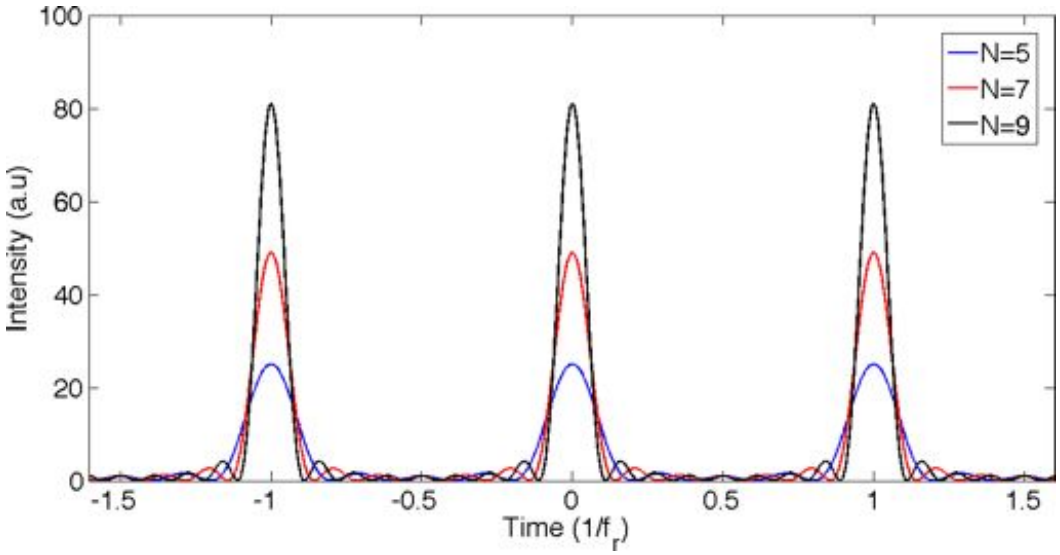

Figure 1.3 – Functional behavior of $|A(t')|^2/E_0^2$ for $N = 5$, 7 and 9.

amplitude $A(t)$ is proportional to the Fourier transform of the spectral amplitude of the modes E_n. In this case, the pulse is said to be *transform-limited* and its duration $\Delta\tau$ is minimum and inversely proportional to the spectrum FWHM $\Delta\nu$, i.e. $\Delta\tau = \beta/\Delta\nu$. The proportionality factor $\beta = \Delta\tau\Delta\nu$ is called time bandwidth product (TBP) and depends on the actual shape of the spectrum. The exact value of the minimum TBP can be determined analytically only for few particular pulse shapes [42], among which the most commonly considered in the context of laser mode-locking are indicated in table 1.1.

Spectrum shape	**Pulse shape**	**TBP**
Gaussian	Gaussian	0.441
Hyperbolic secant squared	Hyperbolic secant squared	0.315
Rectangular	Sinc squared	0.88

Table 1.1 – Minimum time bandwidth product (TBP) for selected spectrum envelope shapes.

If the spectral phases φ_n are locked with a relation different form eq. 1.4, the pulses may be far from being transform-limited and the TBP will be larger than the minimum values reported in table 1.1. This is the case, in particular, for the condition

$$\varphi_n = n\varphi + n^2\theta \tag{1.9a}$$

or, equivalently

$$2\varphi_n - \varphi_{n+1} - \varphi_{n-1} = \Phi \tag{1.9b}$$

when the constants φ, θ and Φ are different from zero. Although, eq. 1.9 has been indicated by some authors as the general condition for acML [5, 7], this phase relation

can lead to very different situations depending on the value of the constants. First of all, it may produce a train of broadened optical pulses in which the instantaneous frequency of the optical field undergoes a linear sweep (*frequency chirp*). Second, if $\theta = -\pi/m$ (or, equivalently, $\Phi = 2\pi/m$) with m integer, pulse generation at a repetition frequency m times larger than the nominal frequency f_r can be achieved [43, 44]. The two cases are considered for equal spectral amplitudes and different values of the parameter θ, respectively in fig. 1.4 and fig. 1.5. While the latter case corresponds to a special ML regime, called *harmonic mode-locking* as opposed to fundamental locking for eq. 1.4, the first situation is generally associated with inferior ML performances, especially for very broad and chirped optical pulses [45]. In presence of chirped pulses from a MLL, the quality of ML regime can be evaluated by measuring the pulse width and calculating the TBP and, in case transform-limited pulses are desired, the parabolic spectral phase profile indicated by eq. 1.9 can be flattened to compensate for chirp. This can be done externally or internally to the laser cavity by propagating light through suitably selected wavelength dispersive elements, such as optical fibers [7, 46], prisms [41] or gratings [35, 47].

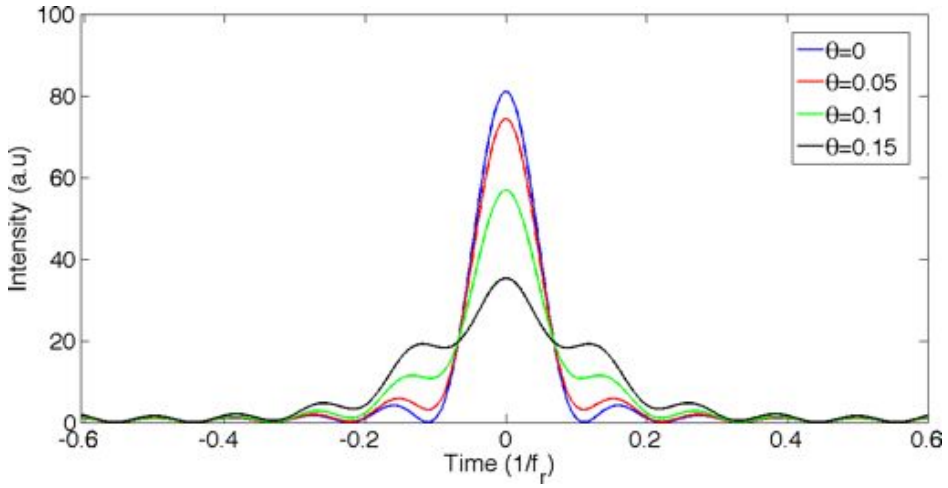

Figure 1.4 – Functional behavior of $|A(t')|^2/E_0^2$ for $N = 9$ and $\theta = 0$, 0.05, 0.1 and 0.15.

1.2.2 Noise characteristics of mode-locked lasers

In actual MLL systems, coupling of amplified spontaneous emission (ASE) with the guided modes leads to fluctuations in both amplitude and phase of the longitudinal modes. While amplitude fluctuations are mostly determined by shot noise [48, 49], which can be assumed to be white and, hence, somehow bounded, phase variations can grow unbounded over time. Indeed, it can be demonstrated [50] that the optical phase $\varphi_{\text{opt}}(t)$ of a free running laser oscillator is subject to a random walk process, i.e. a stochastic process with zero average and variance linearly increasing with time

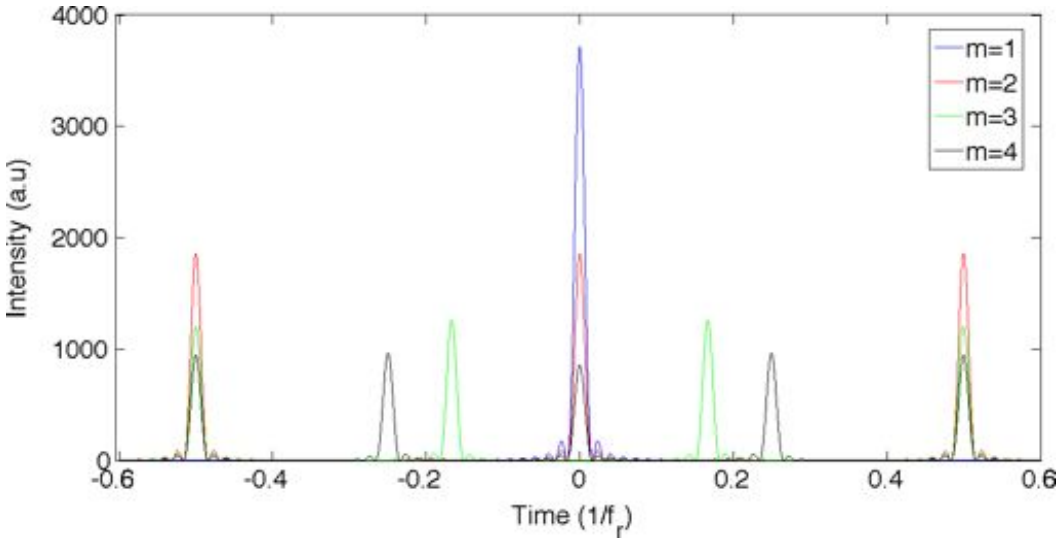

Figure 1.5 – Functional behavior of $|A(t')|^2/E_0^2$ for $N = 61$ and $m = 1$, 2, 3 and 4.

according to the law:

$$\left\langle |\varphi_{\text{opt}}(t+\tau) - \varphi_{\text{opt}}(t)|^2 \right\rangle = D_{\varphi_{\text{opt}}}|\tau| \tag{1.10}$$

where $D_{\varphi_{\text{opt}}}$ is a diffusion coefficient. In a multimode laser, such a relation is verified by all the longitudinal modes φ_n, as the laser can be seen by a set of coupled single-frequency oscillators. This result, known in the theory of oscillators as Leeson's effect and valid both for optical and for electronic resonators [51], has few important consequences.

First of all, the two-sided power spectral density (PSD) of the optical phase noise $S_{\varphi_{\text{opt}}}$, equal to

$$S_{\varphi_{\text{opt}}}(f) = \int_{-\infty}^{\infty} G_{\varphi_{\text{opt}}}(\tau)\, \mathrm{e}^{\mathrm{i}\,2\pi f\tau}\, \mathrm{d}\tau \tag{1.11}$$

by virtue of the Wiener-Khinchin theorem, where $G_{\varphi_{\text{opt}}}(\tau) = \langle \varphi_{\text{opt}}(t)\varphi_{\text{opt}}(t+\tau)\rangle$ is the autocorrelation function of φ_{opt}, is proportional to f^{-2}. Because phase fluctuations induce optical frequency variations with PSD $S_{\nu_{\text{opt}}}$ given by [52]:

$$S_{\nu_{\text{opt}}}(f) = f^2 S_{\varphi_{\text{opt}}}(f) \tag{1.12}$$

the condition $S_{\varphi_{\text{opt}}}(f) \propto f^{-2}$ implies that optical frequency noise is independent on the noise frequency, i.e. it is white. This means that the line-shape of each optical mode will be a Lorentzian with FWHM $\Delta\nu_{\text{opt},n}$ directly proportional to the corresponding diffusion coefficient $D_{\varphi_{\text{opt,n}}}$ [53] and related to $S_{\varphi_{\text{opt},n}}$ by:

$$\Delta\nu_{\text{opt},n} = 2\pi f^2 S_{\varphi_{\text{opt},n}}(f). \tag{1.13}$$

The second consequence, of fundamental importance for MLL, consists in the fact that, in order to achieve stable phase-locking over time, the optical phase noise of different

modes should be correlated. In particular, ML condition expressed by eq. 1.4 requires, for all n:

$$\varphi_{n+1}(t) - \varphi_n(t) = \varphi_t(t) \tag{1.14}$$

where $\varphi_t(t)$ is called timing phase noise [54]. This relation implies that, for efficient ML the phases of all modes should drift by the same amount.

Equation 1.9a has also other important implications. To gain insight on its physical significance, let us consider its time derivative. The derivative of the left hand side of eq. 1.9a is the difference of frequency drift of two adjacent modes separated by f_r or, in other words, the fluctuation of the pulse repetition frequency around the nominal value f_r. The time dependence of $\varphi_t(t)$, thus, determines the variation of temporal position of the pulse with respect to the nominal one, i.e. the pulse timing jitter. If φ_t is nearly constant, very low timing jitter can be achieved. This is the case, for example, when an external RF signal is used to stabilize the repetition frequency. On the other hand, for a free running MLL affected by ASE noise [55], as well as for any other oscillator subject to uncorrelated white noise events [56], the timing phase noise φ_t follows a random walk statistics, with diffusion coefficient D_{φ_t}. As for the optical phase noise φ_{opt}, the PSD of the timing phase noise $S_{\varphi_t}(f)$ produced by spontaneous emission, is proportional to f^{-2}. Moreover, because the PSD of the pulse repetition frequency $S_{f_r}(f)$ is related to S_{φ_t} by

$$S_{f_r}(f) = f^2 S_{\varphi_t}(f), \tag{1.15}$$

also the noise affecting f_r is white [54]. Under this condition, neglecting amplitude fluctuations, the power spectrum of the pulse train recorded using a fast photodiode and an RF spectrum analyzer consists of a set of Lorentzian peaks at integer multiples m of the repetition frequency f_r. Their FWHM can be shown to be directly proportional to the diffusion coefficient D_{φ_t} and to the square of the harmonic order m [57]. In practice, only the linewidth of the first harmonic of the pulse train power spectrum $\Delta\nu_{RF}$ is of interest. The latter is related to $S_{\varphi_t}(f)$ by:

$$\Delta\nu_{RF} = 2\pi f^2 S_{\varphi_t}(f), \tag{1.16}$$

and this relation can be used for direct estimation of the pulse timing jitter [58].

Phase correlation between the longitudinal modes, expressed by eq. 1.9a, also implies a certain relation between the linewidths of the different modes. Referring the optical phase noise of the generic mode n to the phase noise of a given mode $\bar{n}$ at the center of the spectrum, one obtains:

$$\varphi_n(t) = \varphi_{\bar{n}}(t) + (n - \bar{n})\varphi_t(t) \tag{1.17}$$

i.e. common-mode phase noise affects all lines, while excess phase noise induced by timing jitter influences to a larger extent lines in the wings of the spectrum than in the

center. If this common-mode noise and the timing phase noise are uncorrelated and ASE is the only noise source, it can be demonstrated [52] that the PSD of the optical phase noise of mode n is given by:

$$S_{\varphi_{\mathrm{opt}},n}(f) = S_{\varphi_{\mathrm{opt,ST}}}(f) + (n-\bar{n})^2 S_{\varphi_t}(f). \tag{1.18}$$

$S_{\varphi_{\mathrm{opt,ST}}}(f)$ in eq. 1.18 is given by $S_{\varphi_{\mathrm{opt,ST}}}(f) = \Delta\nu_{\mathrm{opt,ST}}/(2\pi f^2)$, where $\Delta\nu_{\mathrm{opt,ST}}$ is the Schawlow-Townes (S-T) limit for the laser linewidth. The latter, following the derivation reported in [53], can be written as:

$$\Delta\nu_{\mathrm{opt,ST}} = \frac{h\nu\, l_{\mathrm{tot}}\, T_{\mathrm{out}}}{4\pi\, {T_r}^2\, P_{\mathrm{out}}}(1+{\alpha_H}^2). \tag{1.19}$$

where:

$h\nu$ is the laser photon energy, h being the Planck's constant,

$l_{\mathrm{tot}} = T_{\mathrm{out}} + l_{\mathrm{par}}$ is the total resonator loss, composed of the output coupler transmission T_{out} and the parasitic cavity loss l_{par},

T_r is the laser cavity round-trip time,

P_{out} is the total laser output power, and

α_H is the linewidth enhancement factor (LEF), or Henry's factor [50].

This last parameter quantifies the coupling between gain g and refractive index n variations induced by charge carriers in the active material. It is defined as:

$$\alpha_H = -\frac{4\pi}{\lambda_0}\frac{\mathrm{d}n(N)/\,\mathrm{d}N}{\mathrm{d}g(N)/\,\mathrm{d}N}, \tag{1.20}$$

where λ_0 is the free-space wavelength and N is the charge density in the gain medium, and it is especially important in semiconductor lasers, for which values on the order of 2 to 6 depending on the laser design and, particularly, on the gain material [59].

Assuming without loss of generality that the minimum linewidth $\Delta\nu_{\mathrm{opt,ST}}$ occurs for mode $\bar{n}$, using eq. 1.13, 1.16 and 1.18, we can write:

$$\Delta\nu_{\mathrm{opt},n} = \Delta\nu_{\mathrm{opt,ST}} + (n-\bar{n})^2\Delta\nu_{RF}. \tag{1.21}$$

Equation 1.21, thus, establishes a parabolic dependence of the optical linewidth with the mode number, with concavity given by the RF linewidth $\Delta\nu_{RF}$. This dependence can be particularly important for free running MLLs [60, 61], for which limited control over the RF linewidth is possible [45]. On the other hand, if synchronization of the pulse repetition frequency with external RF signal is used to reduce timing jitter, very narrow ($<$ 1 kHz) RF linewidths and strong mode correlation can be achieved [62].

Consequently, nearly equal optical linewidths can be obtained for the lines of the mode-locked spectrum. This technique, however, does not allow to reduce the common-mode phase noise leading to $\Delta\nu_{\mathrm{opt,ST}}$, as it acts only on the unbound drift of the timing phase noise $\varphi_t(t)$, i.e. on the low-frequency divergence of $S_{\varphi_t}(f)$.

The argumentation presented above is well-founded if the MLL is affected only by ASE noise. In practice, laser systems are subject to a number of other sources of fluctuations, such as pumping noise or temperature- and vibrations-induced cavity length variations. These disturbances, commonly referred to as technical noise, can lead to optical phase noise far above the S-T limit. Technical noise is, indeed, the main source of instabilities in mode-locked solid-state lasers, where the low repetition rates (typically on the order of few kHz to tens of MHz) and high average powers of several watts make the contribution of quantum noise rather small [55]. On the other hand, semiconductor MLLs are primarily affected by spontaneous emission noise, owing to their multi-gigahertz repetition rates and their low average power of few milliwatts. For this reason, the theoretical predictions formulated under the assumption of quantum limited phase noise discussed above are in good agreement with experimental observations for such devices [58, 60, 61]. Semiconductor lasers, though, are not immune to technical noise which, in combination with laser dynamics, can couple together different kinds of noise supposedly uncorrelated. In fact, intensity fluctuations, producing gain changes, couple through the linewidth enhancement factor to refractive index changes, affecting both the optical phase and timing jitter [63, 64]. Identifying and reducing the impact of technical noise sources is, then, of fundamental importance to approach the quantum-noise-limited MLL operating regime.

1.3 Mode-locking characteristics and characterization techniques

In the previous section, the main figures of merit of MLLs, such as pulse duration $\Delta\tau$, spectrum FWHM $\Delta\nu$, optical linewidth $\Delta\nu_{\mathrm{opt},n}$, RF linewidth $\Delta\nu_{RF}$, pulse repetition rate f_r and its stability have been introduced. Here we discuss these quantities in more detail and present the main characterization techniques to evaluate them.

1.3.1 Pulse shape and duration

As we have seen in sec. 1.2.1, the spectral phase profile $\varphi(\omega)$, together with the optical spectrum, has a strong impact on the resulting pulse shape and duration. If we consider the Taylor expansion of $\varphi(\omega)$ around the central frequency $\omega_0 = 2\pi\nu_0$,

$$\varphi(\omega) = \varphi_0 + \left.\frac{\mathrm{d}\varphi}{\mathrm{d}\omega}\right|_{\omega_0}(\omega-\omega_0) + \frac{1}{2}\left.\frac{\mathrm{d}^2\varphi}{\mathrm{d}\omega^2}\right|_{\omega_0}(\omega-\omega_0)^2 + \ldots, \tag{1.22}$$

we can define the group delay (GD) and the group delay dispersion (GDD), respectively as

$$\mathrm{GD} = \left.\frac{\mathrm{d}\varphi}{\mathrm{d}\omega}\right|_{\omega_0} \tag{1.23}$$

and

$$\mathrm{GDD} = \left.\frac{\mathrm{d}^2\varphi}{\mathrm{d}\omega^2}\right|_{\omega_0}. \tag{1.24}$$

While the GD simply represents a shift of the temporal position of the pulse and it is, in general, of little interest, the GDD, giving rise to parabolic spectral phase, is of fundamental importance in the determination of the actual pulse profile. If GDD = 0, transform limited pulses can be achieved. Conversely, for non-zero GDD values, interference between the longitudinal modes leads to broadened, chirped pulses or even to pulse generation at integer multiples of the nominal repetition frequency f_r [43, 44], as shown above in figures 1.4 and 1.5. Higher dispersion orders in the Taylor expansion of eq. 1.22 may also lead to pulse broadening and/or distortion, however their contribution is significant only for large spectrum FWHM.
Determining spectral amplitude and phase of the MLL output is essential to reconstruct the shape of the emitted pulse train. Often, though, only the pulse duration is of interest for our applications. The most straightforward way of measuring optical pulse duration is direct detection using a fast photodiode and a sampling oscilloscope. However, the limited bandwidth of the detector and, particularly, of sampling electronics result in a resolution of about 10 ps for the fastest commercially available components. Such a resolution is unsuitable for characterization of ps and sub-ps pulses from current semiconductor MLLs. Alternatively, one can use streak cameras or optical sampling oscilloscopes providing ps and sub-ps resolutions [39], even though these systems are very delicate and costly. Excessive jitter from free-running MLLs can also impair pulse duration measurements in equivalent-time oscilloscopes, producing large noise levels in measured traces.

For these reasons, optical methods are the preferred tools for pulse characterization, the most popular one being second harmonic generation (SHG) autocorrelation (AC) for its simplicity. This technique consists in spatially overlapping on an SHG nonlinear crystal the pulse to be measured with a variably delayed version of it, and detecting the SHG signal on a slow detector, as shown in fig. 1.6. The autocorrelation signal, given by

$$A^{(2)}(\tau) = \int_{-\infty}^{-\infty} I(t)I(t-\tau)\,\mathrm{d}t, \tag{1.25}$$

provides a measure of the pulse duration as it is maximum for $\tau = 0$, when the pulses perfectly overlap in time, and decreases for increased detuning. This signal is always symmetric, regardless on the actual pulse shape, and, because it tends to wash out ripples in the pulse structure, multiple pulse shapes can lead to the same

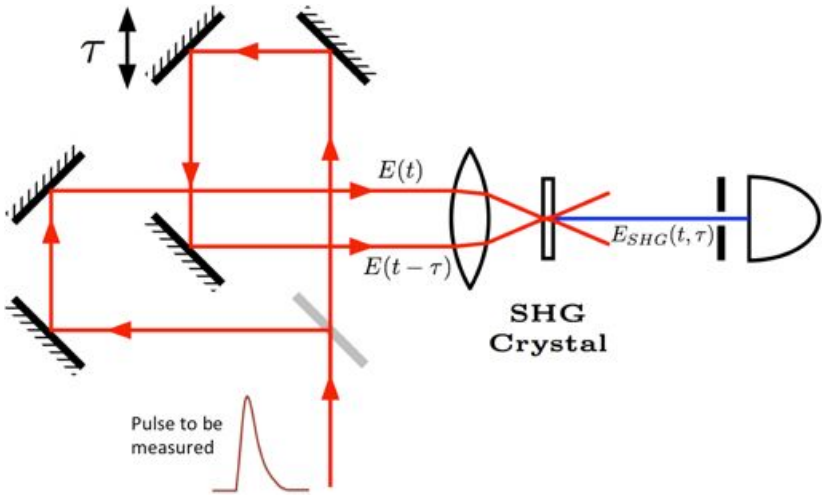

Figure 1.6 – Second harmonic generation SHG autocorrelation AC optical setup.

autocorrelation [65]. Additionally, because AC trace is produced by averaging over many different pulses, it can be shown that, in presence of pulse shape instabilities, this trace consists of a narrow peak on top of a broader pedestal [66]. The peak, representative only of the nonrandom component of the noisy pulse train, is known in literature as *coherent artifact* and it may be indiscriminately mistaken for the measure of the actual pulse duration. Despite of its inherent ambiguities, autocorrelation is often used to estimate the pulse FWHM $\Delta\tau$ by assuming a particular pulse shape and dividing the measured AC FWHM by a numerical factor depending on the given choice. Typical pulse shape assumptions are the Gaussian and $\text{sech}^2(t)$ profiles, yielding a factor of 1.41 and 1.54, respectively. Gaussian shape is, generally, a more conservative choice for such an approximate method, as it results in a slightly larger estimate for the pulse width. Perfectly Gaussian or $\text{sech}^2(t)$ pulses, though, occur very rarely in practice.

In case the actual pulse shape is of interest, advanced characterization techniques should be used, capable of retrieving unambiguously the full complex amplitude $A(t)$ of the electric field. Typical techniques employed for this purpose are SHG frequency-resolved optical gating (FROG) and spectral phase interferometry for direct electric-field reconstruction (SPIDER). The first consists in spectrally resolving with a spectrometer the output of an SHG autocorrelator and retrieving the complex electric field of the pulse from the measured SHG time-frequency map [65]. The latter retrieves the pulse spectral phase $\varphi(\omega)$ by recording and processing the spectral interferogram produced by the interference of two replicas of the pulse to be characterized, with a relative frequency shift between them [67]. Although these techniques are nowadays well-established, both of them rely on nonlinear optics, making necessary the use of high-sensitivity detectors or long signal integration times in case relatively low power pulses are to be measured. A number of linear techniques combining optics with fast electronics

have, thus, been developed in the context of optical communications to achieve higher sensitivity for the characterization of pulse trains and/or periodic modulated waveforms from semiconductor lasers [68–74].
In this work, we have used autocorrelation for fast, first-order characterization of pulses from semiconductor MLLs. Additionally, GDD of pulses generated from InAs/InP quantum dash (QDash) based lasers is characterized using a high-sensitivity SHG-FROG setup, as discussed in chapter 3.

1.3.2 Optical spectrum and linewidth

The emission spectrum, defined as $S(\omega) = |E(\omega)|^2$, is of fundamental importance for MLLs. A key characteristics for ML regime is the spectrum envelope FWHM, which is inversely proportional to the pulse duration in case of transform-limited pulses, as shown in sec. 1.2.1. Spectrum FWHM of MLLs is mostly determined by the homogeneous and inhomogeneous broadening of the gain medium and by the strength of the ML mechanism. Indeed, a broad gain bandwidth, typically resulting from a large inhomogeneous broadening, is beneficial for amplification of short pulses generated by an effective ML process. Additionally, homogeneous broadening has been shown to have a significant impact on the output spectrum shape for lasers based on inhomogeneously broadened media, like InAs quantum dots QDs on GaAs [75].
Another important characteristic of the spectrum of MLLs is the central wavelength. This is determined by the energy levels of the optical transition exploited for laser emission, or by the band-gap of the active material in the case of semiconductor lasers. Suitable material choice and/or band-gap engineering is, thus, required to achieve lasing at the wavelength prescribed for the target application. Optical communications, in particular, require devices operating in the telecom windows around 1.3 µm (*O-band*: 1260-1360 nm) and 1.55 µm (*C+L band*: 1530-1625 nm), where standard single mode fiber (SMF) experiences minimum chromatic dispersion and minimum attenuation, respectively.

Spectrum of MLLs can be characterized using commercially available, grating-based optical spectrum analyzers OSAs. These equipments are typically well-suited for simple measurement of the central emission wavelength and spectrum envelope FWHM. However, in most of the cases, they do not provide suitable resolution to characterize the shape and width of individual comb lines. For this purpose, specific techniques are used, the most popular ones being optical heterodyning [72] and delayed self-heterodyne (DSH) [76], depicted in fig. 1.7 and 1.8, respectively. In optical heterodyning, the beat-note between the mode to be measured and the line of an external cavity laser (ECL) is detected by means of a photodiode and an electrical spectrum analyzer (ESA). Provided that the linewidth of the TLS is much narrower

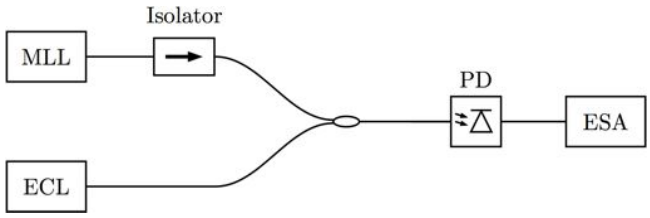

Figure 1.7 – Optical heterodyning setup.

than that of the line under test, the beating provides a measure of shape of the latter. Because both the ECL and the MLL may undergo independent frequency drifts, for reliable characterization this method requires that either both laser are sufficiently frequency stable during the measurement time or that a phase-locked loop (PLL) is used to track the RF beating signal.

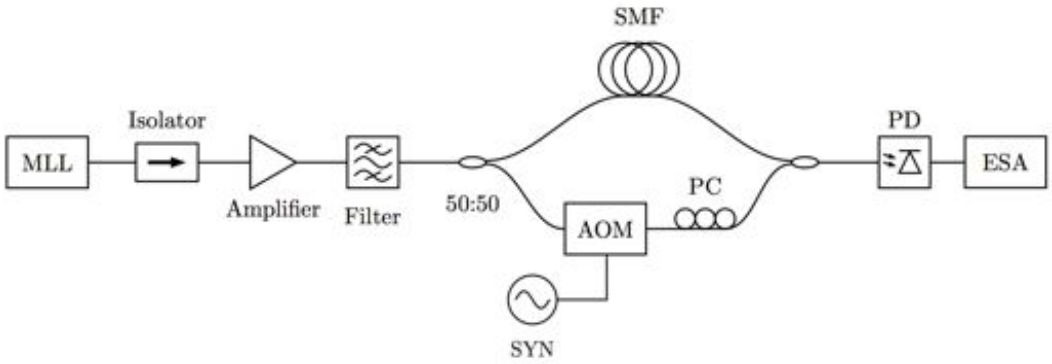

Figure 1.8 – Delayed self heterodyne (DSH) technique setup.

In DSH technique, the line under test itself is used to measure its width. For that, the filtered mode is split in two optical paths with a relative group delay much larger than the coherence time of the laser line $T_{\mathrm{opt},n} = 1/\Delta\nu_{\mathrm{opt},n}$ and an acousto-optic modulator (AOM) on either of them. The two beams are, then, recombined and the beating signal at the frequency of the AOM is detected using a photodiode and an ESA. Because the beam that has experienced the largest delay has lost its coherence with respect to the other, interference cannot occur and the spectrum measured on the ESA will be the auto-convolution of the shape of the line under test. For a Lorentzian line shape, this will be a Lorentzian peak with FWHM twice as large as the FWHM of the mode under test and this relation can be used to deduce its optical linewidth. Measuring the linewidth of individual modes from a MLL with DSH technique is relatively easy if the modes are well separated in frequency. It can be challenging or even impossible, though, if the pass-band of the optical filter becomes comparable or larger than the FSR of the MLL. This fact typically does not constitute a limitation in the case of monolithic semiconductor MLLs with repetition rates above 10 GHz and currently commercially available filters with pass-band of about 10 GHz and out-of-band rejection in excess of 50 dB. Another possible limitation may arise from the condition on the

relative group delay between the two beam path. In case very narrow, sub-kHz laser linewidths are to be measured, recirculating fiber loops can be used to achieve large delays. On the other hand, few kilometers of SMF are typically enough to measure linewidths of few hundreds of kHz and above from semiconductor lasers.
In addition to the techniques discussed above, other methods have been proposed based on the conversion of frequency fluctuations to intensity fluctuations through an optical frequency discriminator, such as an unbalanced interferometer or a high quality factor resonator [77]. However, these approaches do not typically provide high resolution and stability for optical linewidth measurement [64].

1.3.3 Timing jitter and RF linewidth

A very important figure of merit for MLLs is the timing jitter of the generated pulse trains. Timing jitter refers to the random variation of the temporal position of the pulse t_p, defined for each pulse as its center of gravity [54]

$$t_p = \frac{\int_{\text{pulse}} t\, I(t)\, \mathrm{d}t}{\int_{\text{pulse}} I(t)\, \mathrm{d}t}, \tag{1.26}$$

with respect to the nominal position t_{p0} established by the pulse repetition frequency f_r. Typically, timing fluctuations $\Delta t(t) = t_p(t) - t_{p0}(t)$ are converted into phase variations with respect to the pulse repetition frequency using the following relation:

$$\varphi_t(t) = 2\pi f_r\, \Delta t(t) \tag{1.27}$$

where $\varphi_t(t)$ is the timing phase noise, previously introduced in sec. 1.2.2. In accordance with eq. 1.27, the timing jitter can be quantified in terms of the variance of φ_t, $\sigma^2_{\varphi_t} = \langle |\varphi_t|^2 \rangle$, which can be written as

$$\sigma^2_{\varphi_t} = \int_{-\infty}^{+\infty} S_{\varphi_t}(f)\, \mathrm{d}f, \tag{1.28}$$

owing to the Wiener-Khinchin theorem.

Use of eq. 1.28 for jitter characterization requires a certain knowledge on the frequency dependence of the timing phase noise spectrum S_{φ_t}. In practice, useful information can be extracted from the power spectrum of the MLL pulses, detected using a fast photodiode and an ESA. This consists of a number of lines at integer multiples m of the repetition frequency f_r, with noise sidebands, produced by timing jitter, growing in power with m^2 [78]. Additionally, noise pedestals beneath the lines, not scaling with the harmonic number and present even at DC frequencies, occur in the power spectrum due to pulse amplitude fluctuations. Taking advantage of their different behavior with the harmonic number, timing and amplitude noise spectra can be separately deduced using the method proposed by von der Linde in [78]. Timing

jitter can, then, be calculated by integrating over a given frequency interval $[f_L, f_H]$ the timing phase noise PSD extracted from the photocurrent.
This procedure relies on the assumption, not always well satisfied, that amplitude and timing noises are uncorrelated. Moreover, it requires that the power of the noise sidebands is considerably lower than the carrier power at the harmonics of f_r. The last hypothesis, in practice, is verified for MLLs locked to a stable RF oscillator for jitter reduction. On the other hand, in free-running MLLs, the pulse trains may undergo unbound timing fluctuations, leading to broad line shapes at the different harmonics of the power spectrum and, therefore, limiting the applicability of von der Linde's method. Yet, for these system, the intrinsic phase noise properties can be used to determine the frequency dependence of S_{φ_t}.

As discussed in sec. 1.2.2, free-running MLLs are mostly affected by ASE noise coupled to the lasing modes, responsible for a random walk of φ_t and a consequent dependence of S_{φ_t} with f^{-2}. Its effect is proportional to the pulse repetition rate f_r and to the round-trip gain G_{rt}, as these determine how often and in which amount pulses are perturbed per unit time. Quantum noise is, therefore, the major source of fluctuations of monolithic semiconductor MLLs, with pulse repetition rates of several GHz.
Random walk of timing phase is expected to be further enhanced in semiconductor devices by effect of coupling of different types of fluctuations with timing noise [79]. One of such coupling mechanisms is the so-called Gordon-Haus noise, which converts ASE-induced optical frequency fluctuations into pulse repetition frequency changes through the chromatic dispersion of the gain medium [80]. Additionally, coupling of intensity noise with timing phase noise may take place by effect of gain-change-induced refractive index fluctuations. This last phenomenon is quantified by the linewidth enhancement factor α_H, defined in eq. 1.20, and it is more pronounced for narrower gain bandwidths.

The contribution of random walk phase noise to $S_{\varphi_t}(f)$, predominant at low noise frequencies, becomes increasingly smaller at higher frequencies, where the PSD of the timing noise of output pulses tends to a constant value. This value, typically very low, constitutes a fundamental limit for the timing jitter and it is due to photon shot noise [55]. The opposite situation occurs at kHz-range noise frequencies and below, where the $S_{\varphi_t}(f)$ can grow at a rate even larger than f^{-2} by effect of technical noise. In fact, if the laser undergoes cavity length fluctuations, induced by mechanical vibrations and/or thermal changes of the refractive index, random walk of repetition frequency takes place, resulting in an f^{-4} dependence of $S_{\varphi_t}(f)$ at low noise frequencies [51, 55].

If the effect of technical noise is strongly reduced and an f^{-2} dependence of $S_{\varphi_t}(f)$ can be assumed over a broad frequency range, the power spectrum of the MLL pulses

will consist of Lorentzian lines. In particular, the line at the first harmonic f_r will have a FWHM $\Delta\nu_{RF}$ related to $S_{\varphi_t}(f)$ by $\Delta\nu_{RF} = 2\pi f^2 S_{\varphi_t}(f) = \pi f^2 S^{\mathrm{SSB}}_{\varphi_t}(f)$, where $S^{\mathrm{SSB}}_{\varphi_t}(f) = 2S_{\varphi_t}(f)$ is the single sideband phase noise (SSBPN) of φ_t, non-zero only for positive frequencies.
Starting from eq. 1.28 and 1.27 and using the previous expression for $\Delta\nu_{RF}$, one can define the root-mean-square (rms) timing jitter, integrated over the frequency interval $[f_L, f_H]$ as [58]:

$$\sigma_t^i(f_L, f_H) = \frac{T_r}{2\pi}\sqrt{\int_{f_L}^{f_H} S^{\mathrm{SSB}}_{\varphi_t}(f)\,\mathrm{d}f} = \frac{T_r\sqrt{\Delta\nu_{RF}}}{2\pi^{3/2}}\sqrt{\frac{1}{f_L} - \frac{1}{f_H}}. \tag{1.29}$$

Therefore, in the hypothesis of random walk of timing phase only, the RF linewidth $\Delta\nu_{RF}$ can provide a direct measure of the pulse timing jitter.
Additionally, in case the jitter cumulated over successive pulses is of interest, the pulse-to-pulse rms timing jitter can be calculated as [58, 81]:

$$\sigma_t^{pp}(N) = \frac{T_r}{\pi}\sqrt{\int_0^{+\infty} \sin^2(\pi N f T_r)\; S^{\mathrm{SSB}}_{\varphi_t}(f)\,\mathrm{d}f} = T_r\sqrt{\frac{\Delta\nu_{RF} N T_r}{2\pi}}, \tag{1.30}$$

where N is the number of repetition periods between the pulses considered for calculation.

Pulse-to-pulse timing jitter, apart from being estimated from the RF linewidth, is typically measured directly using SHG cross-correlation (XC) [81, 82]. This consists in modifying the SHG-AC setup, shown in fig. 1.6, so as to induce a delay longer than the pulse repetition period on one of the two autocorrelation beam paths. For that, a spool of optical fiber can be used. Each MLL pulse will, thus, be correlated with N pulses ahead in time, where N depends on the extra-delay, and, because of timing instability and integration on many pulse pairs, an XC trace larger than the AC one will occur. The variation of trace FWHM can, then, be used to quantify the jitter. In particular, the timing variance σ_j^2 will be given by $\sigma_j^2 = \tau_{XC}^2 - (\tau_{AC1}^2 + \tau_{AC2}^2)/2$, where τ_{XC} is the FWHM of the XC trace and τ_{AC1}, τ_{AC2} are the FWHM of the AC traces recorded with an without the delay line, to account for the GDD introduced by the latter in the setup.

1.3.4 Repetition frequency stability

Inherently related to the pulse timing jitter is the time stability of the repetition frequency f_r. As this is of fundamental importance for applications like optical clock generation and distribution and microwave photonics, we aim at introducing the main statistical tools used to characterize frequency stability.
In the context of frequency metrology, frequency fluctuations $\Delta f(t)$ are typically normalized to their nominal value. Thus, for the pulse repetition rate f_r, we can define

the fractional frequency fluctuation as $y(t) = \Delta f(t)/f_r$. Using eq. 1.15, the PSD of $y(t)$ is related to $S_{\varphi_t}(f)$ by:

$$S_y(f) = \frac{f^2}{f_r^2} S_{\varphi_t}(f). \tag{1.31}$$

In practice, absolute frequency $f(t)$ (or a down-converted version of it, using a suitable reference) is measured using a frequency counter [83]. The k-th sample recorded by the counter over a time interval of duration τ is the time average

$$\bar{f}_k(\tau) = \frac{1}{\tau} \int_{k\tau}^{(k+1)\tau} f(t)\, \mathrm{d}t. \tag{1.32}$$

Fractional frequency samples can then be obtained from $\bar{f}_k(\tau)$, using $\bar{y}_k(\tau) = (\bar{f}_k(\tau) - f_r)/f_r$. From the $\bar{y}_k(\tau)$ samples, in principle one can quantify the frequency instability using the classical N-samples variance:

$$\sigma_y^2 = \frac{1}{N-1} \sum_{k=1}^{N} [\bar{y}_k - \langle \bar{y} \rangle_N]^2, \tag{1.33}$$

where $\langle \bar{y} \rangle_N$ is the average value of the samples. However, by effect of dephasing mechanisms in oscillators and, in particular, technical-noise-induced frequency drift, σ_y^2 diverges for large measurement times, with an undetermined dependence on N and τ. More suitable statistical tools are, thus, required for characterization and comparison of oscillators. For this purpose, the Allan variance $\sigma_y^2(\tau)$ has been developed, defined by [51]:

$$\sigma_y^2(\tau) = \mathbb{E}\left\{ \frac{1}{2} [\bar{y}_{k+1} - \bar{y}_k]^2 \right\}, \tag{1.34}$$

i.e. as the expectation of the two-sample variance. As in the case of classical variance, Allan deviation $\sigma_y(\tau)$ can be defined as $\sigma_y(\tau) = \sqrt{\sigma_y^2(\tau)}$.
In practice, evaluation of the statistical expectation is unrealistic and an estimator of the Allan variance should be used instead. The simplest estimator consists in replacing $\mathbb{E}\{\cdot\}$ with the mean operator, i.e.

$$\sigma_y^2(\tau, M) = \frac{1}{2(M-1)} \sum_{k=1}^{M-1} [\bar{y}_{k+1} - \bar{y}_k]^2, \tag{1.35}$$

where M is the number of frequency samples. Such an estimator, however, is only capable of providing the value of σ_y^2 at the time interval $\tau = \tau_0$ at which subsequent frequency measurements are performed. New frequency samples are, thus, needed to calculate σ_y^2 for a different τ. On the other hand, if a suitable estimator for the Allan variance is introduced, the time series recorded for an interval τ_0 can be used to calculate $\sigma_y^2(\tau)$ for values $\tau = n\tau_0$, integer multiples of τ_0. The preferred estimator for this purpose is the overlapping Allan variance estimator, defined as:

$$\sigma_y^2(n\tau_0, M) = \frac{1}{2n^2(M-2n+1)} \sum_{j=0}^{M-2n} \left(\sum_{i=j}^{j+n-1} \bar{y}_{i+n} - \bar{y}_i \right)^2. \tag{1.36}$$

This definition can be shown to be equivalent to the following:

$$\sigma_y^2(N\tau_0/2) = \frac{1}{2}\left(\frac{\bar{y}_{N/2+1} + \ldots + \bar{y}_N}{N/2} - \frac{\bar{y}_1 + \ldots + \bar{y}_{N/2}}{N/2}\right) \tag{1.37}$$

i.e. blocks on n subsequent frequency samples should be averaged prior to computing two-sample variance, in order to determine $\sigma_y^2(\tau)$.

The Allan variance is intrinsically related to the PSD of the fractional frequency fluctuations. Indeed, it can be show [83] that if the samples $\bar{f}_k(\tau)$ are defined as in eq. 1.32, $\sigma_y^2(\tau)$ can be calculated from $S_y(f)$ using the following relation:

$$\sigma_y^2(\tau) = 2\int_0^{+\infty} S_y(f)\frac{\sin^4(\pi f\tau)}{(\pi f\tau)^2}\,\mathrm{d}f. \tag{1.38}$$

For actual oscillators $S_y(f)$, as well as $S_{\varphi_t}(f)$ (through eq 1.31), can be conveniently described with a power law model:

$$S_y(f) = \sum_{\alpha=-2}^{2} h_\alpha f^\alpha \tag{1.39}$$

or, equivalently,

$$S_{\varphi_t}(f) = \sum_{\beta=-4}^{0} b_\beta f^\beta, \tag{1.40}$$

where $b_\beta = f_r^2 h_\alpha$, with $\beta = \alpha - 2$, and only few terms, representative of the most often encountered types of noise, are included. Using eq. 1.38, it can be shown that each term of eq. 1.39 (or eq. 1.39) leads to a variance $\sigma_y^2(\tau)$ given by:

$$\sigma_y^2(\tau) = K_\alpha h_\alpha \tau^\gamma, \tag{1.41}$$

where the coefficients K_α and the relation between α, β and γ for the different types of noise of interest are indicated in table 1.2.

Noise type	$\boldsymbol{\alpha}$	$\boldsymbol{\beta}$	$\boldsymbol{\gamma}$	$\boldsymbol{K_\alpha}$
Random walk frequency modulation	-2	-4	1	$2\pi^2/3$
Flicker frequency modulation	-1	-3	0	2ln2
White frequency modulation	0	-2	-1	1/2
Flicker phase modulation	1	-1	-2	$[1.038 + 3\ln(2\pi f_h\tau)]/4\pi^2$
White phase modulation	2	0	-2	$3f_h/4\pi^2$

Table 1.2 – Power coefficients mapping between spectral densities in the frequency domain to Allan variance in the time domain [84]. f_h is the cutoff frequency of an ideal low-pass filter introduced to avoid noise power divergence at $f = 0$.

One can notice that Allan variance does not distinguish between white and flicker $(1/f)$ phase noise, as both lead to a τ^{-2} dependence of $\sigma_y^2(\tau)$. If this is a required

feature a modified version of the Allan variance can be defined [51]. On the other hand, we remark that white and random walk frequency noise, typically encountered in laser systems, lead to γ coefficient of different signs. Impact of technical noise resulting in random walk of frequency can, thus, be readily evaluated from the change of slope of the plot of $\sigma_y^2(\tau)$ vs. τ in bi-logarithmic scale, as it will be shown in chapter 3.

1.4 Mode-locking mechanisms in semiconductor lasers

Having discussed the principles of MLLs, their noise properties and figures of merit with particular reference to semiconductor lasers, we now aim at reviewing the main mechanisms to achieve ML regime in these devices. We will focus especially on monolithic MLLs, in which pulse generation is achieved directly at the output of the semiconductor chip, without the need of external optical components. These devices are very attractive for communication applications, owing to their compactness, low cost, high pulse repetition rates and potential for integration in photonic integrated circuits (PICs).
The most common design for semiconductor MLLs is Fabry-Perot (FP) cavity consisting of an optical waveguide delimited by cleaved mirror facets. By virtue of their *p-i-n* diode structure, the lasers are electrically pumped by current injection. Additionally, the bias electrode is very often separated into two electrically isolated sections. This configuration allows for different operating regimes along the laser cavity, the most interesting one occurring for reverse bias of the smaller section to act as an intracavity absorber. Suitable modulation of the gain or loss can then be used to achieve ML in single-section and two-section devices. This may involve the presence of an external RF signal, as in active and hybrid ML techniques, or just CW bias, as in the case of passive ML. These schemes will be discussed in more detail below.

1.4.1 Active and hybrid mode-locking

Active ML is a technique that can be applied to both single-section and two-section devices and consists in directly modulating the injection current in the gain section at a frequency equal to the cavity longitudinal mode spacing f_r. Hybrid ML, on the other hand, is intended for use in two-section devices only and involves the modulation of the absorber loss at the pulse repetition frequency, through a suitable RF voltage signal applied at its terminals. These schemes are illustrated in fig. 1.9.
ML regime produced using these techniques can be considered both in the time domain and in the frequency domain. In the time domain, gain/loss modulation will produce at each round-trip a well-defined time window where intracavity pulse amplification is favored over attenuation. The width of this window is governed by external modulation

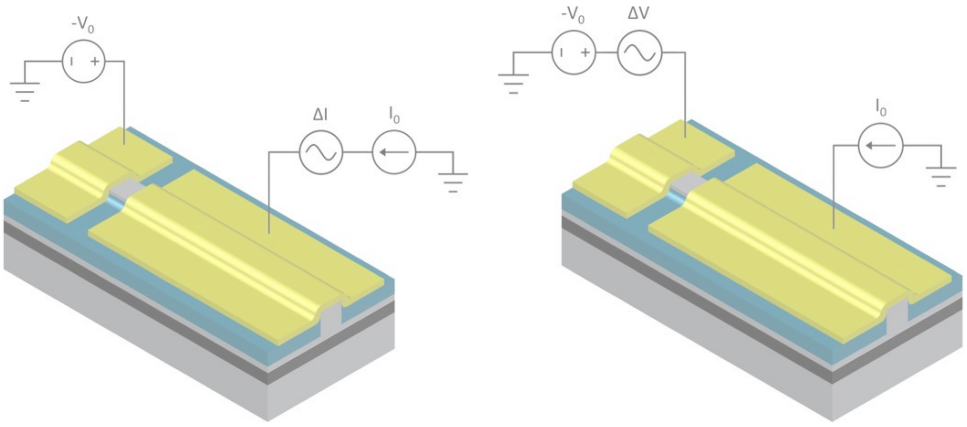

(a) Active ML (b) Hybrid ML

Figure 1.9 – Biasing condition for active and hybrid mode-locking.

and laser dynamics and it will ultimately determine the output pulse duration. In the frequency domain, the modulation sidebands produced at each longitudinal mode will force the neighboring modes to oscillate in phase at a fixed frequency spacing. This mechanism, stronger for larger RF powers, will prevent the phases of the longitudinal modes to drift apart under the effect of ASE noise, resulting in a much reduced timing jitter. The latter can be determined using von der Linde's method [78], as the power spectrum of photodetected pulses will consist of delta-function like lines on top of a broad pedestal due to residual timing phase noise [85]. Integrated jitter values on the order of few hundreds of fs are usual for current actively and hybridly MLLs [35, 86].

Active and hybrid ML techniques can also be used to tune the pulse repetition frequency, allowing to compensate to a certain extent for the frequency error resulting from the uncertainty in the device cleaving process [36]. Typical tuning ranges are on the order of few tens of MHz, the larger values being achieved for higher modulation powers [87]. Additionally, optical injection locking in combination with RF modulation has been shown to yield tuning ranges in excess of 100 MHz [88, 89].
Despite their inherent advantages, active and hybrid ML techniques are increasingly complex and costly for shorter devices, as higher pulse repetition frequencies pose more stringent limitations in terms of availability of suitable RF oscillators and design of impedance matching circuitry. For these reasons, passive ML techniques are often preferred for repetition rates above 10 GHz.

1.4.2 Passive mode-locking in two-section devices

Mode-locking in two-section devices can be achieved without the need of RF signals, by taking advantage of the nonlinear dynamics of the intracavity absorber. To gain insight into this mechanism, let us consider a laser diode as in fig. 1.10a, where a

negative voltage is applied to the absorber section of the laser and current is injected into the gain section. For injection currents above the threshold value I_{th}, an optical waveform is allowed to propagate inside the cavity, being amplified in the gain section and attenuated in the absorber. If the waveform includes a sharp temporal feature with enough energy to induce loss saturation at the absorber, the latter will become transparent during a short time interval before loss recovery takes place. This will lead to the formation of a pulse that, propagating into the gain section, will deplete the carrier population of the inverted medium, causing gain saturation. If the absorption recovers faster than the gain and recovery times of both are shorter than the cavity round-trip time, then a window of net amplification is produced at each round-trip and generation of a stable pulse train will eventually occur after a certain transient.
The steady-state ML regime resulting from this process is represented in fig. 1.10b. It can be noticed that the width of the net gain window, and hence the pulse duration, is intrinsically governed by the relative dynamics of gain and loss saturation. In particular, if loss saturation and recovery is much faster than that of gain, very short pulses can be achieved. On the other hand, if dynamics in the two sections become comparable, broadened pulses are emitted. Also important is the pulse amplification per round-trip, that will be larger for a lower saturation depth of the gain compared to the absorption one.

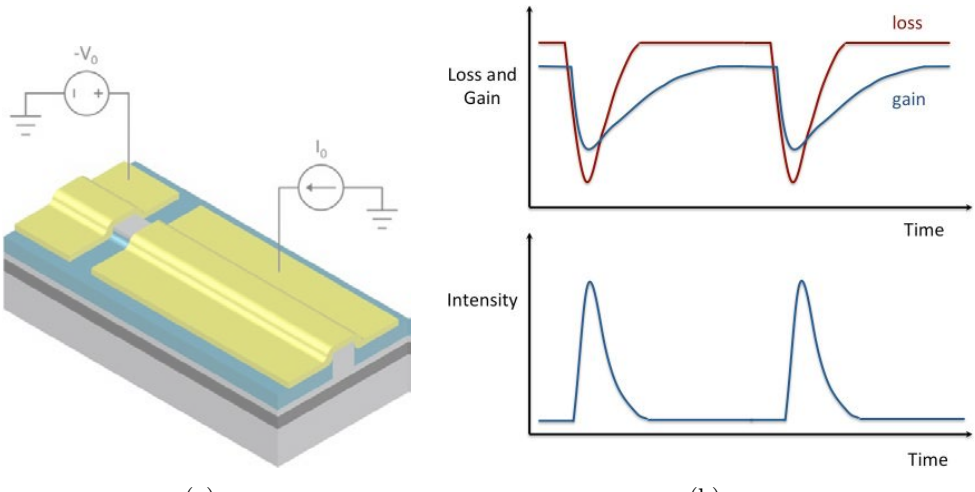

(a) (b)

Figure 1.10 – (a) Biasing condition for a passively MLL. (b) Steady-state loss and gain dynamics in a passively MLL.

Saturation depth and recovery velocities of gain and loss depend on a number of factor, that can vary with bias conditions, laser design and active material. More specifically, recovery times are determined by the carrier lifetimes in the gain and absorber sections, while saturation depth in each region is controlled by the saturation

energy E_{sat}, defined as,

$$E_{\text{sat}} = \frac{h\nu A}{\Gamma \, \mathrm{d}g/\,\mathrm{d}n}, \tag{1.42}$$

where $h\nu$ is the photon energy, A is the transverse mode area, Γ is the optical confinement factor, and $\mathrm{d}g/\,\mathrm{d}n$ is the material differential gain.
For stable pulse emission, the saturation energy of the absorber should be smaller than that of the gain section, so that the first saturates more for a given pulse energy [90]. This condition can, in principle, be fulfilled by reverse-biasing the absorber and forward-biasing the gain section, as shown in fig. 1.10a. Indeed, if the values of A and Γ are the same in the two sections, larger differential gain is expected in the absorption regime than in the gain regime, as in semiconductors this quantity decreases with increased carrier density [91].
Nonetheless, in practice, simultaneous optimization of saturation energies and recovery times for best ML performances can be rather challenging. Increasing current in the gain section, in the attempt of maximizing E_{sat} and pulse peak power, in fact, would lead to a faster gain recovery and a consequent pulse broadening. This effect can be compensated by applying higher reverse voltages on the absorber, so as to attain faster loss recovery through a more efficient carrier extraction. However, the larger cavity loss induced would result in a higher laser threshold. Additionally, an increase of the absorber saturation energy may occur, owing to the detuning with voltage of the absorption band-gap with respect to the lasing wavelength. In the extreme case, if the laser is operated too close to threshold, it may fall into regimes such as Q-switching instabilities or Q-switched mode-locking, in which either very unstable or nearly stable pulse bursts are produced by low frequency modulation of the cavity loss [92].
One can conclude that optimal biasing of a two-section MLL implies a delicate balance between different competing phenomena. This results in a limited range of current/voltage values for which short pulses can be obtained, typically found in the vicinity of laser threshold.

Laser bias is not the only way of controlling pulse duration and stability. Device geometry and active material, in fact, can be suitably engineered to improve ML performances. Regarding laser geometry, a common design parameter is the gain-to-absorber length ratio. Lower values for this ratio typically result in shorter pulses, by virtue of the increased saturable absorption. However, the larger intracavity losses induced by a longer absorber cause higher lasing thresholds and enhanced optical and timing phase noise [91]. Another design solution consists in using a tapered waveguide for the gain section, so as to increase the gain saturation energy by increasing the mode area A. This approach may be very useful for high power MLLs, as such a configuration for the gain section would provide large pulse amplification and a more efficient saturation of a narrow waveguide absorber [93].

Concerning active material engineering, MLL optimization through the use different layer stacks for the gain and absorbing media has been proposed [94,95] for the already extensively studied QW devices [1, 2]. However, the complexity of this approach, involving epitaxial regrowth steps during fabrication, may be incompatible with low-cost requirement. Alternatively, a promising solution to improve ML performances is use of low-dimensional nanostructures, such as semiconductor quantum dots (QDs) as laser active material. As it will be discussed in chapter 2, notable features of self-assembled In(Ga)As dots grown on GaAs and InP substrates, such as ultrafast carrier dynamics and broad gain bandwidths, are ideal characteristics for short pulse generation [3]. In addition, low values of internal loss and optical confinement factor in QD laser structures help reducing the ASE noise coupled to lasing modes, resulting in lower timing jitter [96]. Specific features of semiconductor QDs

Superior ML performances in two-section devices are achieved, to date, for InGaAs QDs grown on GaAs emitting at 1.3 µm. For this material system, sub-ps pulse trains [3,93], ps-range integrated timing jitter [86,93] and operation above 100 °C [97] have been demonstrated. Additionally, a number of theoretical models have been able to suitably describe the unique dynamics observed for these devices [98–102].
On the hand, MLLs based on InAs dots and dashes (elongated dots) on InP for 1.55 µm emission generally do not exhibit comparable performances in the two-section configuration. Reduced absorption saturation in these material systems, in fact, pose more stringent limitations on the absorber reverse bias compared to InGaAs/GaAs QD-MLLs [103–105]. Improved ML characteristics are, nonetheless, observed for the single-section configuration, which appears to be the most suitable for InAs/InP QDs and QDashes [7].

1.4.3 Passive mode-locking in single-section devices

Operating regimes compatible with mode-locking have also been observed in simple FP lasers consisting of just a gain section (see fig. 1.11a) [4–7, 106–115]. As in ML mechanisms described above, such regimes imply regular pulse emission at a rate equal to the cavity round-trip frequency and relatively narrow RF linewidths in the pulse power spectrum. Here, however, no mechanism is in place to control pulse duration and timing other than carrier and gain dynamics in the device. As a consequence, pulses emitted by single-section lasers are, in general, far from the Fourier transform limit. Yet, the blue chirp typically observed for these devices can be externally compensated to achieve ps and sub-ps pulse durations [4,7,107,108]. In addition, the absence of extra losses from an intracavity absorber allows for larger average output power and reduced optical linewidths compared to two-section passively MLLs with similar characteristics. The occurrence of ML phenomena in single-section lasers appears to be independent on

the dimensionality of the gain material, as it has been observed for bulk material [106], multiple quantum wells [4–6, 107, 108], quantum dashes [7, 109–112] and quantum dots [113–115]. Even so, single-section devices based on low-dimensional nanostructures have shown to outperform conventional bulk and QW lasers. Indeed, the larger spectrum FWHM exhibited by QDs and QDashes allows for shorter pulse duration after GDD compensation. Additionally, the narrower RF linewidths demonstrated for these materials indicate improved mode coherence. This last property, in particular, has been ascribed to the low optical confinement factor of QD and QDash structures [116], leading to a reduced spontaneous emission noise coupled to the longitudinal modes.

Despite the numerous reports on mode-locking in single-section lasers, a theoretical model capable of explaining a reasonable number of features observed in practice is still missing. So far the most accredited mechanism yielding phase coherence and equal distances between the longitudinal modes is four wave mixing (FWM) in the gain medium [5, 117, 118]. According to this interpretation, nonlinear interaction of adjacent modes through FWM results in the generation of sidebands, that will cause mutual injection locking of the cavity modes, stabilizing the laser (see fig. 1.11b) [6, 118].

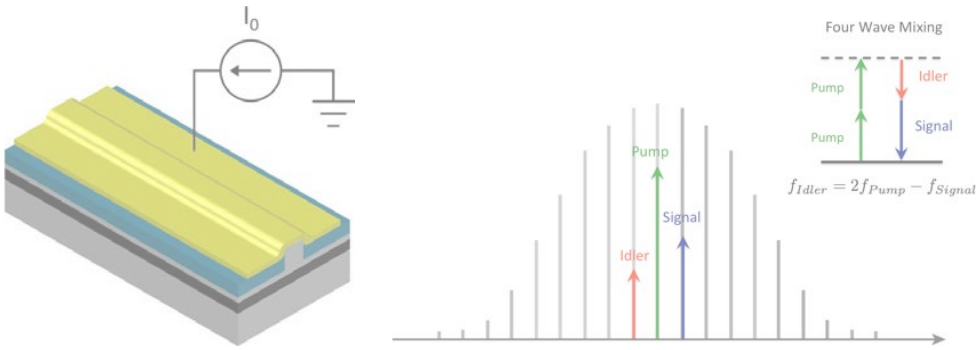

Figure 1.11 – (a) Single-section passively MLL. (b) Mutual injection locking provided by degenerate four wave mixing (FWM).

FWM in the active region may arise from optical transitions occurring between the conduction band (CB) and the valence band (VB) (interband effects) and within the sole CB or VB (intraband effects) [119]. Interband contribution to FWM comes from carrier density modulation (CDM), i.e. the oscillation of electrons and holes population at the beating frequencies of the modal fields. carrier density modulation (CDM) response time is typically on the order of hundreds of ps, comparable to the carrier lifetime in the gain region. As for intraband transitions, the main effects are spectral hole burning (SHB) and carrier heating (CH), which redistribute electrons and holes within they respective bands and respond with sub-ps relaxation times.
Interband effects have been shown to have a larger impact on nonlinear gain compared to intraband ones [119, 120]. In particular, CDM is expected to enhance the gain on

the long-wavelength side of the spectrum and to reduce it on the short-wavelength side, the asymmetry of this process being more pronounced for larger values of the linewidth enhancement factor α_H [120]. This phenomenon, often pointed out as the principal cause of ML in single-section lasers [4–6,117,118], is also commonly associated to mode-hopping in FP lasers, i.e. sudden wavelength jumps sometimes observed for changes in injection current, temperature and/or optical back reflections [119,121,122]. Mode-hopping events are typically accompanied by increased levels of relative intensity noise, that can couple to phase noise through the LEF. This may lead to larger and/or unstable RF linewidths, corresponding to worse ML performances. As a consequence, it is still unclear whether nonlinear gain is beneficial or detrimental for ML in single-section lasers or, instead, both phase-locking and mode-hopping are produced by CDM, depending on the operating conditions of the devices.
In addition to FWM, other mechanisms have been proposed to explain self-pulsation in single-section devices, such as spatial mode coupling in a multiple transverse mode laser [108,123] or saturable absorption induced by random carrier populations in QD lasers [124]. Cavity group velocity dispersion (GVD) has also been indicated recently as the cause of pulse chirp in single-section QD MLLs [125]. Nevertheless, most of theoretical models proposed so far for single-section devices pay little attention on the spectrum shape for the output pulse train. In practice, broad and flat optical spectra with FWHM of several nanometers are observed for best QW and QD/QDash based single-section MLL [4,7,114].

In our work on QD and QDash based single-section lasers, special emphasis is posed on the optical spectrum and on the power spectrum of the emitted light, as these quantities are of fundamental importance for frequency combs for telecommunications. In chapter 3 we show that optical spectrum and power spectrum in these device are closely related and their characteristics depend on the particular laser active material. As for the pulses generated by single-section devices, we verify whether the GVD of the laser waveguide can account for the large chirp observed and reported in chapter 3. For this purpose, optical frequency-domain reflectometry (OFDR) technique is first validated and, then, used for component dispersion measurement, as presented in chapter 4.

Chapter 2

Quantum dot and quantum dash based lasers: physics and fabrication

The introduction of III-V semiconductor nanostructures, such as quantum well (QW) and quantum dots (QDs), as active material for lasers and optical amplifiers has been one of the major breakthroughs in the field of optoelectronics. In this chapter, we discuss the physical principles behind the performance improvement in optoelectronic devices based on low-dimensional nanostructures and, in particular, the specific features of InAs QDs grown on GaAs and InAs QDs and QDashes grown on InP. The laser structures and the fabrication procedure followed for the realization of the devices considered in this study are also presented.

2.1 Low-dimensional nanostructures as laser active material

Size reduction of semiconductor material down to the nanometer scale strongly affects the electronic and optical properties of the physical system. More specifically, if the electron or hole wave-function is confined in one or more directions by a potential well whose width is comparable to or smaller than the de Broglie wavelength, its allowed set of energy values will be reduced. In other words, a low-dimensional density of states (DOS) will result. DOS is defined as the number of states per unit energy per unit volume that are available for electrons occupation at each energy level and it is directly related to the dimensionality of the system. The DOS as function of energy for 3D (bulk), 2D (quantum well), 1D (quantum wire) and 0D (quantum dot) electronic systems is schematically shown in fig. 2.1.

Because gain and absorption of semiconductors depend on the *joint density of states* of conduction band (CB) and valence band (VB), which exhibit the same functional behavior as the curves reported in fig. 2.1, a number of optical properties of the system will depend on its dimensionality [41]. In particular, low dimensional structure such as

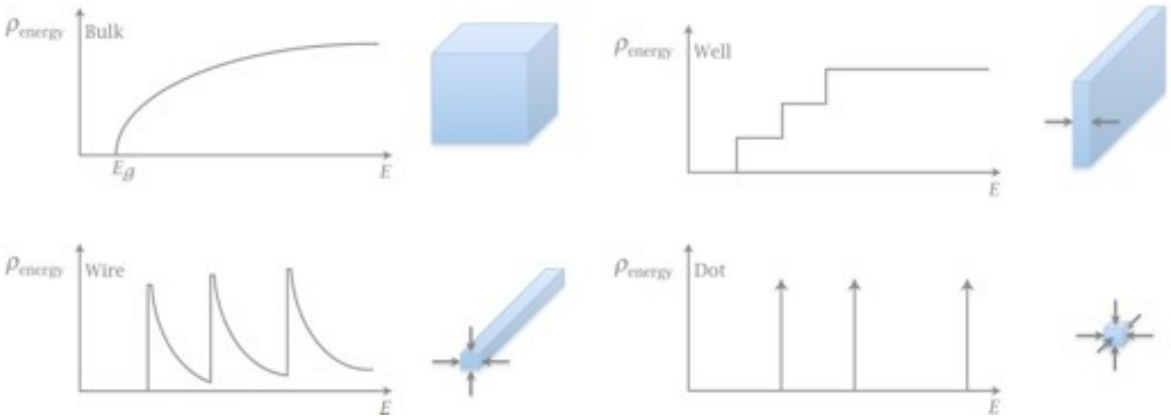

Figure 2.1 – Density of states for bulk material, quantum well, quantum wires and quantum dots.

quantum wires and quantum dots have been predicted to exhibit lower temperature sensitivity [126] and lasing threshold [127], and higher differential gain and direct modulation bandwidth [128] compared to bulk and quantum well material. These predictions arise from the fact that for smaller dimensionalities carriers injected by electrical pumping concentrate in a narrower energy range, leading to a larger optical gain and higher temperature stability. Following this reasoning, QDs would exhibit ultimate lasing performances, as their delta function-like DOS would imply that all the injected carrier contribute to the population inversion at the lasing energy.

In practice, the most effective way of realizing QD laser structures, to date, is the heteroepitaxial growth of self-assembled dots on III-V substrates in the so-called Stranski-Krastanov (S-K) regime. This takes advantage of the large lattice mismatch between the substrate and the material to be grown, to promote the formation of defect-free three-dimensional islands on top of a few-monolayer-thick film, the *wetting layer* (WL). Self-assembled growth of QDs induces a certain dispersion of the composition and the size (in particular the height) of the dots, ultimately leading to a finite distribution of the transition energies of the dot ensemble. The resulting gain spectrum will, thus, be determined by the superposition of the homogeneous lineshapes of single QDs in the ensemble, leading to an inhomogeneous broadening typically on the order of few tens of millielectronvolts (meV), depending on the growth process. Consequently, the temperature-independent carrier distribution expected from theory turns into a Fermi function at room temperature in real dots [129,130]. Further deviations from theoretical expectations for QD laser performances arise from the presence of multiple states inside the CB and VB of the dots [75,129–132] and, above all, from the existence of a wetting layer (WL) state, acting as a common carrier reservoir for the dots in the ensemble. Carrier relaxation and escape rates in these levels strongly impact on laser dynamics and on the final laser properties [132–134].

Despite these facts, a number of technological and design advances on QD and QDash lasers and epitaxial growth have led to performances comparable, and in some

cases superior to those of QW lasers [135]. Indeed, regardless of the debate on the lasing threshold of QD lasers as compared to QW devices [136], QDs and QDashes have demonstrated unique features in terms of low temperature sensitivity [97, 137], ultrafast carrier dynamics and recovery of gain and absorption [129, 138], wide emission spectra [139] and low spontaneous emission noise coupled to lasing modes [140]. The superior temperature stability of QD lasers with respect to QW is a result of a technological breakthrough which consists in the *p*-doping of grown QDs. With this technique, the extra holes provided from the dopant atoms compensate for the thermal smearing of hole population among the many VB states of the QDs, preventing lasing performance drop at high temperature [128, 137]. Yet, this approach seems to be particularly effective only for InAs QDs on GaAs substrate, but not so much for dots and dashes on InP [116]. The ultrafast carrier dynamics and the consequent fast recovery of gain and absorption in QDs and QDashes at room temperature is attributable to the rapid carrier-phonon and carrier-carrier scattering mechanisms that take places within the nanostructures and in the surrounding WL and barrier regions [141]. The wide emission spectra observed for QD and, particularly, for QDash lasers is made possible by the inhomogeneous broadening of the ensemble, even though homogeneous broadening is predicted to play a major role in determining the final lasing spectrum [75]. Finally, the low spontaneous emission noise coupled to lasing modes is a consequence of the small overall volume of the active region, leading to low values of the optical confinement factor achieved in QD and QDash laser structures [116].

The optical confinement factor Γ of a semiconductor laser has a large impact on a number of device characteristics and, thus, merits more attention. It is a measure of the overlap of the optical field with the active material and, in its more general formulation, is defined as:

$$\Gamma = \frac{\int_{V_A} |E(\boldsymbol{r})|^2 \, \mathrm{d}V}{\int_{V_{Tot}} |E(\boldsymbol{r})|^2 \, \mathrm{d}V} \tag{2.1}$$

where V_A is the volume of the QD active region and V_{Tot} is the total volume of the laser waveguide. While for bulk and QW lasers, Γ depends only on the waveguide geometry and on the layer stack of the epitaxial structure, due to the in-plane homogeneity of the latter, for the case of quantum wire (QWR) and QD lasers the confinement factor also depends on the areal density of the nanostructures. Following the definition provided by Bimberg *et al.* [142, p. 183], equation 2.1 can thus be written as:

$$\Gamma = \Gamma_{xy} \Gamma_z \tag{2.2}$$

with

$$\Gamma_{xy} = \frac{N_D A_D}{A} = \xi \tag{2.3}$$

$$\Gamma_z = \frac{1}{A} \iint_A \int_{dot} |E(z)|^2 \, \mathrm{d}z \Big/ \int_{-\infty}^{+\infty} |E(z)|^2 \, \mathrm{d}z \tag{2.4}$$

where N_D is the number of QDs/QDashes over the in-plane area of the waveguide A, A_D is the average base size of the nanostructures and ξ is the area coverage of QDs/QDashes. For typical laser structures, with electronically uncoupled QD/QDash layers, the optical confinement factor increase linearly with the area coverage ξ and with the number of active layers in the epitaxial structure. Typical areal densities in QD/QDash laser structures are on the order of 10^{10}-10^{11} dots/cm^2, and Γ values of 1% or less are common. Larger values of Γ are expected for dashes than for dots, owing to their larger area coverage ξ [130].

One of the main characteristics affected by the optical confinement factor is the lasing threshold current density. This point can be made clear by considering the fundamental condition for laser emission. This requires that, at threshold, the modal gain equals the total cavity losses, i.e.:

$$g_{\mathrm{mod}}(J_{\mathrm{th}}) = \Gamma g_{\mathrm{mat}}(J_{\mathrm{th}}) = \alpha_{\mathrm{tot}} = \alpha_{\mathrm{i}} + \frac{1}{2L}\log\left(\frac{1}{R_1 R_2}\right) \tag{2.5}$$

where g_{mod} and g_{mat} are the modal gain and the material gain, respectively, α_{tot} is the total internal losses, J_{th} is threshold current density, L is the laser cavity length and R_1, R_2 are the laser mirror reflectivities. We can deduce from eq. 2.5 that, for a given cavity loss, a higher confinement factor would allow for a lower material gain needed to achieve threshold or, equivalently, for a lower J_{th}. On the other hand, if the large material gain of QD/QDash (on the order of 10^5 cm^{-1}) is not supported by a sufficient Γ, limited lasing performance will result, especially for short cavity lengths.

Another property influenced by the low confinement factor is the saturation energy of the gain material E_{sat}, whose importance for MLLs has already been discussed in sec. 1.4.2. Because E_{sat} is inversely proportional to Γ, as indicated by eq. 1.42 on page 32, use of QD/QDash based gain material would be beneficial for several high-power applications, such as linear amplification of large input power signals in semiconductor optical amplifiers (SOAs) [140] and high peak power pulse generation in MLLs [93]. In this last case, a low Γ would also allow for a reduced ML destabilization due to nonlinear refractive index variations produced by high energy pulses traveling inside the laser cavity [143].

From the above discussion, it can be deduced that area density of self-assembled nanostructures and number of active layers are fundamental design parameters in order to achieve low lasing threshold current density, without compromising noise and gain saturation performances. Although the most straightforward way of controlling Γ consists in stacking more active layers, for better laser performances it is preferable to optimize nanostructures growth in order to achieve large densities and reduced size dispersion, rather than using a large stack of QD/QDash layers. In fact, strain fields propagating along the epitaxial structure during growth impact on the nanostructure

density and size distribution in subsequent layers, leading to a larger inhomogeneous broadening. This effect is more severe for larger laser stacks, although strain relaxation techniques can be adopted and growth parameters optimized for thicker structures [116].

Further considerations on the number of active layers and on the total thickness of the active region are related to the design of single transverse mode optical waveguides for lasers and the injection current density required to achieve material transparency. The latter, in particular, will increase with the number of QD/QDash layers, as for the case of QW devices [144], limiting the advantages, in terms of high Γ, arising from large stacks of active layers.

Optimized laser structures grown according the design guidelines outlined above have been used for this study and will be discussed in section.

2.2 Laser structures investigated

For laser emission at 1.3 µm and 1.55 µm, we have used, respectively, two different material systems: InAs/GaAs QDs and InAs/InP QDs and QDashes. Additionally, as a benchmark for our study, we have considered a single InGaAsP/InP QW structure emitting at 1.55 µm, with an optical confinement factor comparable to that of QD/QDash active regions. The investigated structures are presented in more detail hereafter.

2.2.1 InAs/GaAs quantum dots for 1.3 µm emission

$In_xGa_{1-x}As$/InAs QDs grown on GaAs by molecular beam epitaxy (MBE) and metal-organic chemical vapor deposition (MOCVD) techniques are one of the most studied material systems in research for nanostructures based active regions. [141, 145, 146]. Also, industrial development of QD material for lasers and amplifiers has been carried out in companies such as Innolume GmbH [147] and QDLaser, Inc. [148]. In our work we have employed both epitaxial structures grown by MBE at LPN and commercial substrates provided by Innolume GmbH. Although the former exhibit good static performances (modal gain up to 19 cm^{-1}, photoluminescence (PL) FWHM down to 35 meV) and ML in single-section devices, wider and more reproducible mode-locking regions have been observed for FP lasers based on one of the commercial structures. In the following, we will, thus, focus on the latter. The laser stack, grown by solid source molecular beam epitaxy (MBE) on an n^+-GaAs (100) substrate, is reported in table 2.1. It consists of 10 $In_{0.85}Ga_{0.15}As$/InAs QD layers embedded into a GaAs matrix, surrounded by 1.5-µm-thick $Al_{0.35}Ga_{0.65}As$ cladding layers. In order to improve the temperature stability of lasing characteristics, *p*-doping of QD layers has also been

performed.

Function	Material	Thickness (nm)	Comment
Contact	GaAs	200	p^+-doped (C)
Upper cladding	$Al_{0.35}Ga_{0.65}As$	1520	graded p-doped (C)
Barrier	GaAs	9	×10
QD doping	GaAs	10	×10, p-doped (C)
Barrier	GaAs	14	×10
QD	$In_{0.15}Ga_{0.85}As$	5	×10
QD	InAs	0.8	×10
Barrier	GaAs	33	
Lower cladding	$Al_{0.35}Ga_{0.65}As$	1520	graded n-doped (Si)
Buffer	GaAs	500	n^+-doped (Si)
Substrate	GaAs		n^+-doped, 3 inch

Table 2.1 – $In_{0.15}Ga_{0.85}As$/InAs QD laser structure for emission at 1.3 µm.

2.2.2 InAs/InP quantum dots and quantum dashes for 1.55 µm emission

For lasing operation in the 1.55 µm telecommunication, InAs nanostructures grown on the InGaAsP/InP material system are considered. In case standard InP (001) substrates are used, MBE growth leads to the formation of elongated dots along the $[1\bar{1}0]$ direction, known as quantum dashes. Alternatively, in order to achieve truly 3D confined structures, MBE growth of InAs dots on InP (311)B [149, 150] and optimized processes for MOCVD growth on InP (001) [151] have been proposed. In this work, fruitful collaborations with Alcatel-Lucent-Thales III-V Lab and Laboratoire FOTON / INSA - Rennes have allowed us to process and investigate, respectively, optimized QDash based epitaxial structures and InAs/InP (311)B QD based structures, described below.

Concerning InAs/InP (311)B QD lasers, the structure considered in this study is presented in fig. 2.2a. It consists of 9 InAs QD layers embedded into $In_{0.8}Ga_{0.2}As_{0.435}P_{0.565}$ barriers (Q1.18), surrounded by InP claddings. A 20-nm-thick etch-stop layer is grown 250 nm above the active region to act as a reference point for the interruption of the etching process that allows to pattern the laser waveguide. QD active layers feature a large areal density of about 10^{11} dots/cm^{-2}, as deduced from atomic force microscopy (AFM) characterizations, and supposedly reduced inhomogeneous broadening, as a result of the double-cap growth procedure devised to control the height fluctuation of QDs [149]. Nonetheless, PL spectra, centered around 1.52 µm with FWHM varying from 82 to 95 meV (153 to 177 nm) along the wafer, as shown in fig. 2.2b, indicate significant

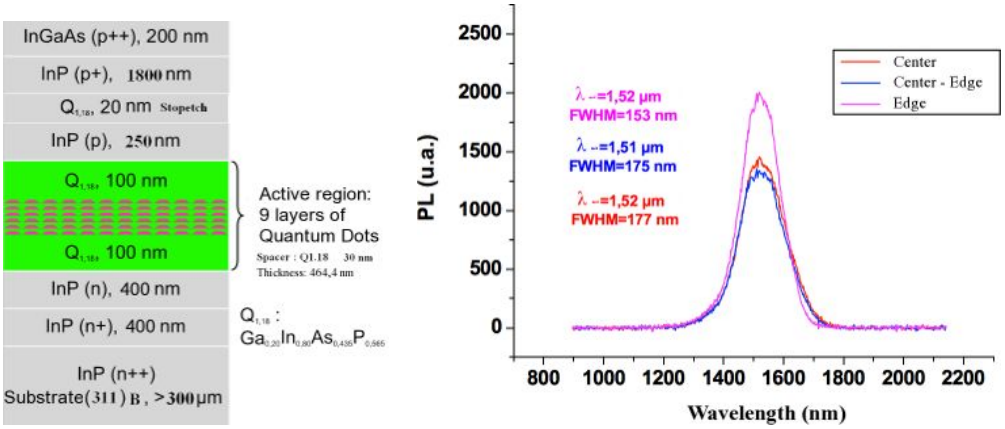

(a) (b)

Figure 2.2 – (a) InAs/InP (311)B QD laser structure and (b) PL spectra measured at different positions along the wafer (courtesy of K. Klaime, INSA Rennes).

size/composition fluctuation of the grown dots.

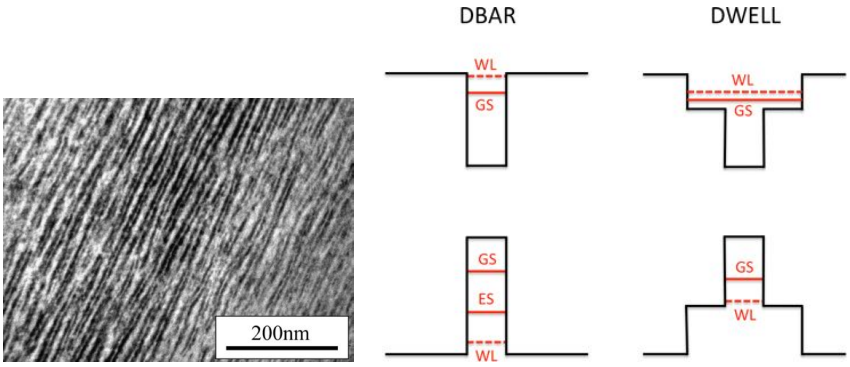

(a) (b)

Figure 2.3 – (a) In-plane transmission electron microscopy (TEM) picture of as-grown quantum dashes (courtesy of F. Lelarge, III-V Lab). (b) Comparison of band diagrams of DBAR and DWELL structures, where the qualitative position of the WL and QDash states is indicated, as shown in [152].

The other material system widely studied in this work is InAs QDashes grown on InGaAsP/InP (001) by gas source molecular beam epitaxy (GSMBE) at III-V Lab. Figure 2.3a shows an in-plane view of a QDash based active layer, recorded by transmission electron microscopy (TEM). Quantum dashes have a typical height of about 2 nm and width of 15-20 nm, while their length ranges between 40 and 300 nm, depending on growth conditions. Surface densities on the order of 1-4 $\times$ 10^{10} dashes/cm^{-2} result in an optical confinement factor of about 0.15 % per dash layer [116]. Growth optimization of QDash material has allowed the realization of laser structures comprising up to 15 active layers [153], with reduced size dispersion and large modal gain, as large as 100 cm^{-1} [154]. Nonetheless, the advantages in terms of modal gain and confinement factor achieved by stacking such a large number of QDash layer are somewhat compensated by an increased absorption in the active layers. The

best tradeoff is found for structures consisting of 9 layers of InAs dashes embedded into $In_{0.8}Ga_{0.2}As_{0.4}P_{0.6}$ barriers (dash-in-a-barrier (DBAR) design) [155]. Although other designs, such as the dash-in-a-well (DWELL) one, have demonstrated slightly lower threshold current densities and larger direct modulation bandwidths over DBAR structures [116], the latter exhibit better reproducibility and reduced phase noise [155]. This is most likely due to a better growth control and a higher carrier confinement of DBAR structures with respect to DWELL (see fig. 2.3b), allowing for a reduced impact of spontaneous emission noise on the lasing modes. For the reasons discussed above, in our study we will mostly focus on 9 DBAR epitaxial structures.

2.2.3 InGaAsP/InP single quantum well for 1.55 µm emission

In addition to the QD and QDash material described above, we have considered a single quantum well structure especially designed to have an optical confinement factor of 1%, comparable to that of QD/QDash based lasers. The structure, grown at III-V Lab, has a PL peak centered at 1558 nm and its layer stack is reported in table 2.2.

Function	**Material**	**Thickness (nm)**	**Comment**
Contact	InGaAs	300	MOCVD, p^+-doped (Zn)
Upper cladding	InP	1500	MOCVD, graded p-doped (Zn)
Top	InP	30	p-doped (Be)
Etch stop	$In_{0.8}Ga_{0.2}As_{0.4}P_{0.6}$	35	p-doped (Be)
Top	InP	100	p-doped (Be)
SCH	$In_{0.8}Ga_{0.2}As_{0.4}P_{0.6}$	214	
QW	InGaAsP	6	
SCH	$In_{0.8}Ga_{0.2}As_{0.4}P_{0.6}$	214	
Lower cladding	InP	1000	n-doped (Si)
Substrate	InP		n^+-doped, 2 inch

Table 2.2 – InGaAsP/InP single QW laser structure for emission at 1.56 µm.

2.3 Laser fabrication

In this section we present the fabrication process followed for the realization of the devices studied in this thesis. Additionally, we discuss the method used to characterize the quality of epitaxial structures, starting from the light-current characteristics of broad area (BA) lasers processed from the latter.

2.3.1 Broad area lasers

Prior to realization of MLL diodes, BA lasers for material characterization are fabricated from the considered epitaxial structure using cleanroom technologies available at LPN. A sketch of a BA laser is shown in fig. 2.4, while the steps followed for this purpose are reported below.

Figure 2.4 – Sketch of a broad area laser for material characterization.

1. *Native oxide removal*

   At first, deoxidation of the substrate surface is performed in a 1 min bath of 40% HF in the case of InP and of 37% HCl in the case of GaAs, followed by a 3-min rinse in deionized (DI) water.

2. *Definition of openings for p-type contacts deposition*

   50-µm-wide stripe openings are produced in image reversal resist AZ 5214E by optical lithography. For that a 1.4-µm-thick film is spin-coated on the sample at 4000 rpm for 30 s and baked for 1 min 30 s at 125 °C on a hot-plate. After sample exposure using Suss MicroTec MJB4 mask aligner and 1 min 30 s image reversal bake at 125 °C, flood exposure without mask followed by 1 min development in AZ 726 MIF allow for negative sidewall profiles, suitable for lift-off.

3. *Electrodes deposition*

   Electron beam evaporation of a Ti/Au (200/2000 Å) bilayer in a Plassys MEB 550 SL equipment, followed by lift-off in acetone is, then, used to define the BA laser p-contact.

4. *Etching of the p^+-doped contact layer*

   The p^+-doped InGaAs (GaAs) contact layer of the InP (GaAs) based structure is chemically etched in a bath of $H_3PO_4/H_2O_2/H_2O$ in a ratio of 1:1:8, at an etching rate of $\approx$ 3000 Å/min, using the Ti/Au electrode as mask.

5. *Substrate thinning and deposition of n-type contacts*

   Finally, the substrate is thinned down to about 120 µm using an alumina based slurry, in order to facilitate laser bars cleaving, and backside polishing with a solution of 5% HBr in methanol is performed, prior to evaporation of n-contact. This consists of a Ti/Au (200/2000 Å) bilayer for InP samples, while for GaAs samples, deposition of a stack of Ni (100 Å) / Ge (600 Å) / Au (1200 Å) / Ni (200 Å) / Au (2000 Å), followed by a 2-min rapid thermal annealing (RTA) at 400 °C is required to achieve an ohmic contact on n-GaAs. In both cases, surface preparation

by Ar^+ ion bombardment is performed in the metal evaporation equipment, prior to contact deposition.

After fabrication, laser bars with different cavity lengths are hand-cleaved and light-current measurements are carried out in order to deduce material properties. In particular, modal gain Γg_0, internal loss α_i, threshold current density for infinite cavity length J_{th_∞} and internal quantum efficiency η_i^d of the structure can be extracted from the following relations:

$$\log(J_{th}) = \frac{L^{-1}}{\Gamma g_0} \log\left(\frac{1}{R}\right) + \log(J_{th_\infty}) \tag{2.6}$$

$$\frac{1}{\eta_{ext}^d} = \frac{1}{\eta_i^d}\left(1 + \frac{\alpha_i L}{\log(1/R)}\right) \tag{2.7}$$

where

$$\eta_{ext}^d = \frac{q\lambda}{hc}\frac{\Delta P}{\Delta I} \tag{2.8}$$

is the external differential quantum efficiency, $R = 0.3$ is the cleaved facet reflectivity, c and h are respectively the speed of light and the Planck's constants, λ is the central emission wavelength of the laser diode and $\Delta P/\Delta I$ is the slope of the light-current characteristics, also known as slope efficiency. More specifically, once J_{th} is calculated for each laser diode by dividing the measured threshold current by the electrode area, Γg_0 and J_{th_∞} are deduced from the slope and the intercept of $\log(J_{th})$ vs. the inverse cavity length L^{-1}. On the other hand, α_i and η_i^d are estimated from the slope and the intercept of $1/\eta_{ext}^d$ vs. L, using for each laser the measured value of the slope efficiency and eq. 2.8 to calculate η_{ext}^d.

Although the validity of this well-established method [156] has been questioned, especially in the case of QD/QDash laser [157], because of the possible dependence of α_i with L due to incomplete pinning of the quasi-Fermi levels at threshold [158], the technique still provides good indications about the material quality. In fig. 2.5 we report an example of modal gain and internal loss extraction performed for a 9 DBAR InAs/InP (001) QDash structure, while a summary of material properties measured for the other structures considered in this study is presented in table 2.3 on page 46. Regarding structures emitting at 1.55 µm, a large modal gain in excess of 50 cm^{-1} and relatively low internal loss on the order of 12 cm^{-1} are observer for an optimized QDash structure. Conversely, lower values for the modal gain ($\approx$ 25 cm^{-1}) and internal loss ($\approx$ 6 cm^{-1}) have been extracted for the QDs on InP (311)B. This is most likely due to the lower area coverage of QDs with respect to dashes, but also to the detrimental effect of inhomogeneous broadening, that is expected to affect more severely QDs than wire-like nano structures [159]. Values extracted for the QD structure at at 1.3 µm are in line with other literature reports [160].

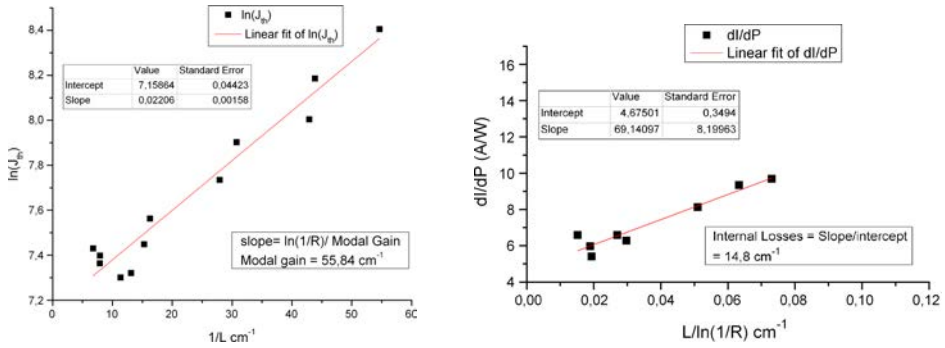

(a) (b)

Figure 2.5 – (a) Modal gain and (b) internal loss extraction for a 9 DBAR InAs/InP (001) QDash structure.

Laser structure	Γg_0 **(cm^{-1})**	α_i **(cm^{-1})**	J_{th_∞} **(A/cm^2)**	η_i^d
InGaAs/InAs QDs on GaAs	22	3.5	280	0.54
InAs QDs on InP (311)B	25	5.6	504	0.46
InGaAsP QW on InP	13	3.3	97	0.10

Table 2.3 – Modal gain Γg_0, internal loss α_i, threshold current density for infinite cavity length J_{th_∞} and internal quantum efficiency η_i^d for the investigated laser structures.

2.3.2 Shallow ridge lasers

Once the static performances of the epitaxial structures in exam are validated, we proceed with cleanroom fabrication of shallow ridge waveguide lasers. As first step, before the actual processing of the laser structure, we determine the ridge width and etching depth in the upper cladding layer necessary to allow for single transverse mode operation. For this purpose, effective refractive index simulations are performed using the proprietary software ALCOR, developed by France Telecom/CNET. Typically, ridge width of $\approx$ 2 µm and residual cladding thickness values of about 50-200 nm above the active region are used to achieve single transverse mode lasing, with a guided mode profile as shown in fig. 2.6. Because contact photolithography with resolution of about 0.5 µm is generally used for ridge patterning, sufficient tolerances are considered in the design of the waveguide geometry.

The procedure adopted for the fabrication of ridge waveguide lasers is composed of different steps, summarized in fig. 2.7 and presented in detail below.

1. *Native oxide removal*

   Deoxidation of the wafer surface is performed using HF and HCl, respectively in the case of InP and GaAs samples, as described in sec. 2.3.1.

2. *Definition of mask for ridge waveguide etching*

   For this purpose, different processes are used for GaAs and InP substrates. For GaAs, Ti/Au

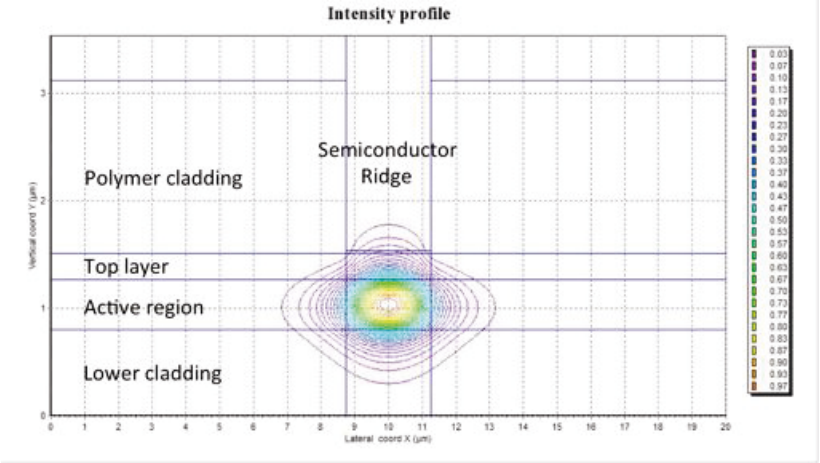

Figure 2.6 – Alcor simulation of ridge waveguide laser for single transverse mode operation.

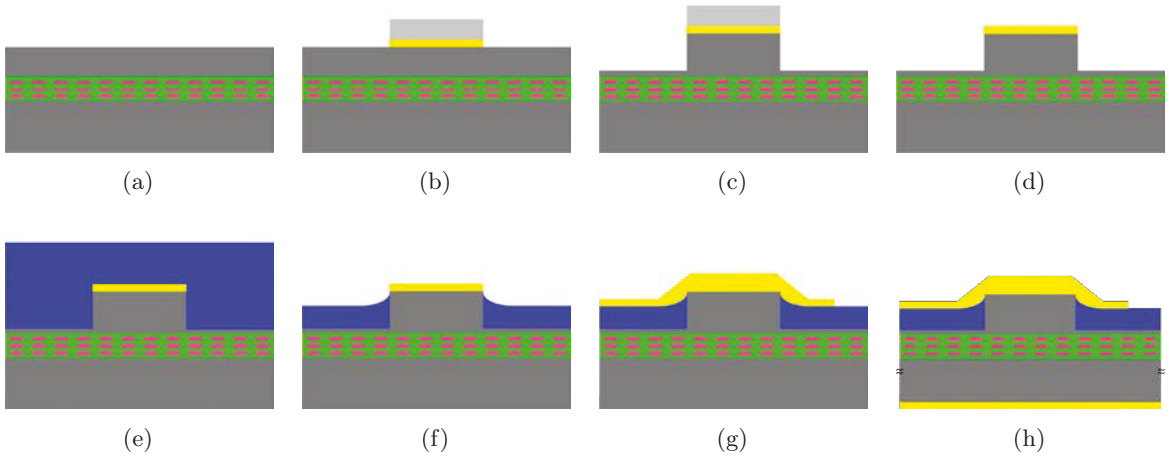

Figure 2.7 – Fabrication steps for shallow ridge waveguide lasers: (a) Deoxidation, (b) etching mask patterning, (c) ridge waveguide etching, (d) etching mask removal, (e) BCB planarization, (f) etching of BCB covering the top of the ridges, (g) deposition of p-type contacts and (h) substrate thinning and deposition of n-type contacts.

(200/3000 Å) 2-µm-large ribbons separated by 400 µm are deposited by lift-off to act both as etching mask and as laser p-contact. On the other hand, for InP, a 700-nm-thick SiN_x mask is patterned on top of a Ti/Au (200/2000 Å) bilayer, uniformly evaporated on the sample. The SiN_x layer is deposited at a rate of ≈ 20 nm/min in an Unaxis D200 plasma-enhanced chemical vapor deposition (PECVD) equipment, using SiH_4 and NH_3 precursors. It is, then, etched in a plasma of CHF_3/SF_6 in a ratio 2:1 at a pressure of 10 mTorr, using a capacitively coupled plasma reactive ion etching (CCP-RIE) Nextral NE100 equipment endowed with an interferometric monitoring system. A 100-nm-thick Al layer, deposited by lift-off, is used as etching mask for SiN_x. For both GaAs and InP processes, contact photolithography using AZ 5214E resist (see sec. 2.3.1) has been carried out prior to metal lift-off.

3. *Patterning of ridge waveguides*

   For InP samples, this consists of ion beam etching (IBE) of the p^+-InGaAs/Ti/Au contact layers,

followed by etching of InP upper cladding, while for GaAs only p^+-GaAs/AlGaAs cladding etching is needed. Physical etching of contact layer is carried out in a Roth&Rau IBE equipment. An etching angle of 20°between the sample, glued on a cooled holder, and the Ar^+ ion beam ensures an average etching rate of ≈ 40 nm/min for the contact layer stack and of 15-20 nm/min for the dielectic mask.

Regarding the etching of the upper cladding, this is typically performed by inductively coupled plasma reactive ion etching (ICP-RIE), using an ICP Sentech SI500 equipment endowed with interferometric process monitoring (see fig. 2.8). Different optimized recipes, based on HBr and H_2/Cl_2 plasmas, are used, respectively for the etching of GaAs and InP. The recipes take advantage of Si-based radicals, introduced in the reaction chamber by the use of a 4-inch silicon substrate underneath the sample to etch, to achieve better anisotropy through sidewall passivation [161, 162]. Alternatively, only in the case of InP (001), crystallographic etching in 37% HCl solution fo 1 min can be used to define ridges oriented in the [110] direction. A comparison of the ridge profiles obtained with wet and dry etching is shown in fig. 2.9.

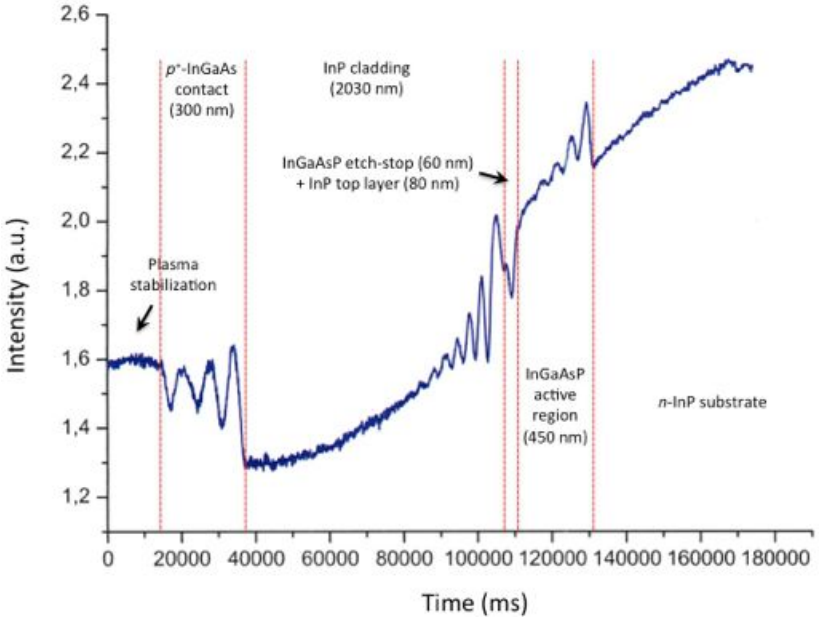

Figure 2.8 – ICP-RIE interferogram of an etching test on a QDash structure. Phase shifts in the interferogram indicate material transitions. Ridge etching should be interrupted around the etch-stop + top layers in order to ensure single transverse mode operation of the lasers.

4. *Etching mask removal and ridge waveguide passivation*

   Residual SiN_x mask is etched by CCP-RIE in a plasma of SF_6 at a pressure of 30 mTorr. Surface cleaning is performed in a bath of 95% H_2SO_4 for 1 min, followed by a 3-min rinse in DI water. A conformal deposition of ≈ 100 nm of SiN_x is, then, carried out by PECVD in order to passivate the ridge sidewalls so as to reduce carrier surface recombination.

5. *Laser structure planarization*

   For this purpose benzocyclobutene (BCB) resin (Dow cyclotene 3022-46) is used. Because adhesion of BCB is hampered by the possible presence of water droplet on the sample surface,

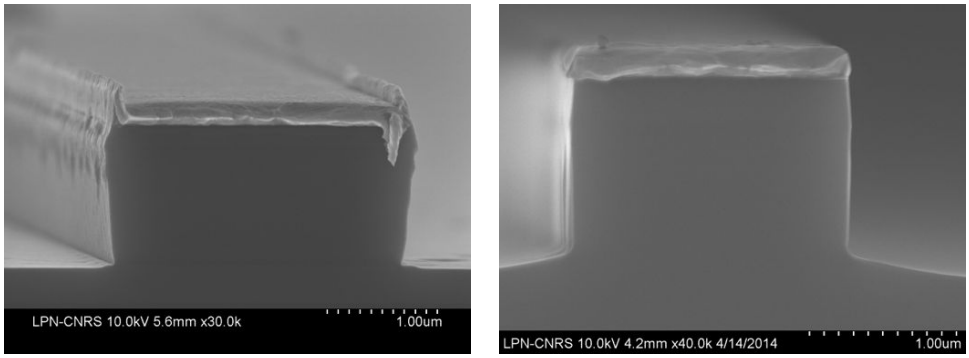

(a) HCl Etching (b) ICP-RIE Etching

Figure 2.9 – Comparison of InP etching profiles obtained with (a) wet and (b) dry etching. While the latter offers more vertical sidewalls, the former provides a smoother bottom, resulting in reduced propagation losses.

the sample is annealed at 120 °C for 5 min and an adhesion promoter (Dow AP3000) is used before resin coating. Both AP3000 and BCB are spin coated on the sample at 2000 rpm for 30 s, yielding an overall thickness above 3.5 µm. Soft cure of BCB is, then, performed on a hot plate at 120 °C for 1 min before a 2-hour hard bake at 250 °C under nitrogen atmosphere in a quartz tube furnace.

6. *Etching of BCB covering the top of ridge waveguides*

   This step is performed by CCP-RIE, prior to deposition of *p*-type electrode. For that a 5:1 O_2/SF_6 gas mixture at 100 mTorr is used, together with interferometric monitoring of the process. In order to control the height of the ridge portion emerging from the BCB, etching is carried out in multiple steps, alternated by profilometry measurements an microscopy inspections. The procedure concludes when 500 to 700 nm ridges emerge from the resin and no BCB residues are observed on the top of the waveguides, at least over an area of 80-90 % of the sample. Indeed, a potion of the sample periphery will be unexploitable, as BCB planarization results in a larger resin thickness on the sample edges than on the center and BCB etching by more than 1 µm from the top of the ridge may lead to inefficient current injection in the laser diode. CCP-RIE recipe used for BCB etching also attacks the SiN_x passivation layer with a selectivity of about 1:1. We take advantage of this fact to remove from the ridge top both BCB and SiN_x cappings at the same time, gaining access to the underlying Ti/Au *p*-contact.

7. *Deposition of p-type contacts*

   For this step 100-µm-wide stripe openings are produced in negative resist AZ nLOF 2070 by photolithography. The resist is spin-coated on the sample at 4000 rpm for 30 s and baked for 1 min 15 s at 97 °C on a hot-plate, resulting a 5-µm-thick film. Prior to sample exposure, 100-µm stripes are aligned on previously patterned ridge waveguides so as to produce large openings of more than 80 µm on one of the sides of the ridges. Post-exposure bake for 1 min 15 s at 97 °C is then performed, followed by 1 min development in AZ 726 MIF to allow for negative sidewall profiles. Next, just before contact deposition, further etching of about 100 nm of BCB is carried out in order to remove the portion of resin possibly affected by water absorption, that may

hinder electrode adhesion. A Ti/Au (200/3000 Å) bilayer is, then, evaporated on the sample at an angle of 10°to allow for conformal deposition on the ridge side facing the ≈ 80 µm-wide opening in nLOF resist. Lift-off in a dimethyl sulfoxide (DMSO) bath is then performed to achieve *p*-type contacts.

8. *Substrate thinning and deposition of n-type contacts*

   Substrate thinning down to about 120 µm and backside metallization is performed for InP and GaAs based samples as described in sec. 2.3.1 on page 44 for broad area lasers. Eventually, in order to facilitate device cleaving, the BCB layer between adjacent *p*-type electrodes is etched down to the semiconductor by CCP-RIE.

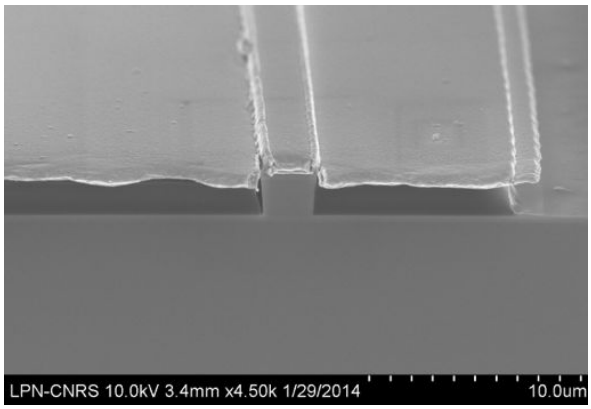

Figure 2.10 – SEM picture of a processed laser structure.

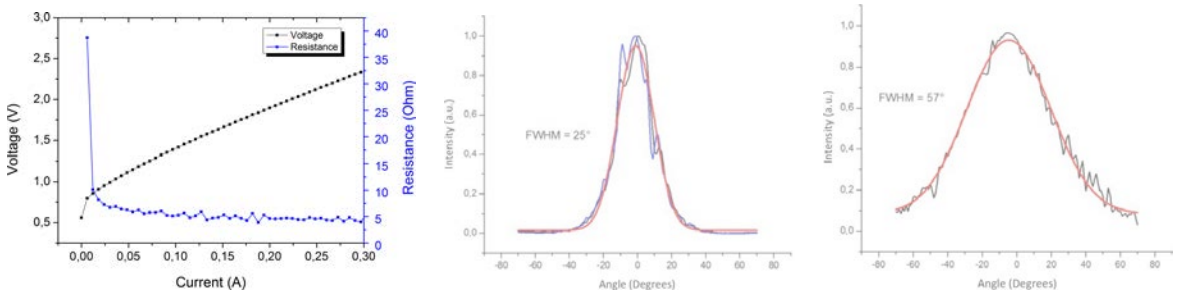

(a) (b) (c)

Figure 2.11 – (a) Current-voltage characteristic of a 9 DBAR QDash laser, far-field intensity profile (b) in the horizontal direction for different values of injection current, and (c) in the vertical direction.

An SEM picture of the final planarized laser structure is reported in fig. 2.10. After wafer processing, laser bars with different cavity length are hand-cleaved and tested. Best devices are selected on the basis of the light-current and current-voltage characteristics at room temperature and mounted on copper bases for thermal management purposes, for subsequent mode-locking (ML) characterizations. Typical knee voltages of about 0.7 V and series resistance on the order of 2 to 6 Ω indicate good electrical characteristics of the fabricated devices, as shown in fig. 2.11a. Additionally, in order to verify the single transverse mode operation of the realized lasers, we measure the far-field intensity profile at different

injection current values. Typically observed gaussian profiles, with larger beam divergence in the vertical direction than on the horizontal one (see fig. 2.11b and 2.11c), indicate single mode behavior of the shallow ridge waveguide. In the presence of such a far-field pattern, a lensed fiber with a suitable spot-size should be used for laser-to-fiber coupling, as indicated in sec. 3.1.1.

2.3.3 Buried ridge stripe lasers

The fruitful collaboration with III-V Lab has allowed us, not only to process optimized QDash epitaxial structures, but also to characterize numerous QDash devices fabricated using buried ridge stripe (BRS) technology. A brief description of the technology is, thus, provided in this section. Fabrication process of BRS lasers starts from an epitaxial structure consisting just of the InAs QDash/InGaAsP active region, capped with a top stack of InP/InGaAsP/InP layers, whose overall thickness does not exceed 200 nm. Ribbons with widths of 1 up to 1.5 µm, separated by 250 µm are defined by electron beam lithography and patterned into an SiO_2 layer. The latter will serve as mask for ICP-RIE etching of the laser active region. After mask removal, the etched ridges are buried by an MOCVD regrowth of InP with optimized doping profile for effective current injection in the laser diode. MOCVD growth of a p^+-InGaAs contact layer and lift-off of Ti/Pt/Au deposited by ion beam sputtering allow to define the p-type electrodes. Then, proton implantation is carried out on both sides of the ridges, in order to ensure lateral localization of the injected carrier. Finally, substrate thinning and deposition of backside n-type Ti/Pt/Au contact are performed. An SEM image of a BRS laser fabricated on a 6 DBAR structure is shown in fig. 2.12. Compared to shallow ridge lasers, BRS design is more rugged and provides a smaller beam divergence in the vertical direction, owing to the nearly circularly-symmetric refractive index profile. This last feature enables an improved coupling of the emitted power in optical fibers, due to reduced mismatch between the laser mode and the fiber mode shapes [163]. On the other hand, larger parasitic capacitances are expected for BRS lasers compared to shallow ridge design, potentially limiting the direct modulation bandwidth of these devices. Concerning mode-locking characteristics, practically no difference is observed between the two technologies that, consequently, will be treated indistinctly in this work.

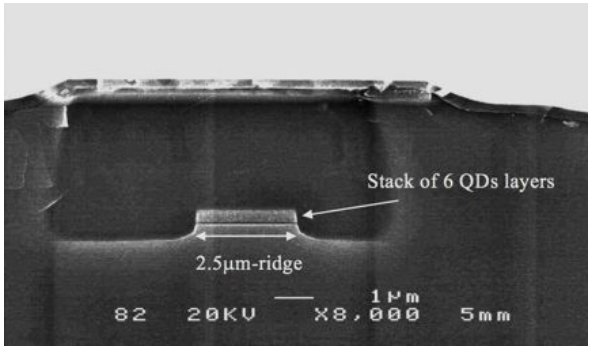

Figure 2.12 – SEM picture of a 6 DBAR buried ridge stripe (BRS) laser (courtesy of F. Lelarge, III-V Lab).

Chapter 3

Characterization of QD and QDash mode-locked lasers

In this chapter, we present the ML characteristics of single-section Fabry-Perot (FP) lasers based on InAs/GaAs QD and InAs/InP QD/QDash material, as compared to InGaAsP/InP QW devices. ML regime in these systems is studied in sec. 3.1 and investigated in more detail in the rest of the chapter for QDash based lasers for two main reasons: firstly, their broad and flat emission spectra and their low phase noise, secondly, the larger availability of high-quality material provided by III-V Lab. QDash MLLs characterization in the time domain are carried out by frequency-resolved optical gating (FROG) technique to gain insight on the chirp of emitted pulses and results are shown in sec. 3.2. Additionally, frequency domain characteristics of these devices, in particular the time stability of repetition frequency, the optical linewidth and their dependence on bias conditions and measurement setup, are studied in detail in sec. 3.3. Finally, demonstration of optical frequency comb generators suitable for integration on InP photonic integrated circuits (PICs), without performance degradation compared to single-section FP lasers, is reported in sec. 3.4.

3.1 Mode-locking performances of single-section lasers

In this section, we review the ML properties of single-section lasers based on InGaAsP/InP QW, InAs/InP QD/QDash and InAs/GaAs QD material. With respect to previous researches on ML in single-section devices presented in sec. 1.4.3, this study is intended to identify the specific characteristics of each material through a systematic investigation of all the main aspects: RF spectrum, optical spectrum, pulse generation and their evolution with injection current. As we have remarked that lasers issued from the same (or a comparable) structure exhibit similar performances, in the following, for the sake of simplicity, we consider only one representative device for each material. After a description of the characterization setup employed, MLLs comparison is performed on the basis of optical and RF spectrum features.

3.1.1 Characterization setup

Fundamental mode-locking characteristics of single-section lasers, such as optical spectrum, pulse power spectrum and autocorrelation are investigated using the setup shown in fig. 3.1. The devices, fabricated as described in chapter 2 and mounted on copper bases, are clamped on a copper heat sink for thermal management purposes. The latter is kept at a constant temperature of 20 °C using a Peltier cooler and a commercially available thermistor-based temperature controller (Thorlabs TED200C), with a stability of 1 mK. Light coupling into the fiber-optic setup is carried out with a hemisphere-lensed fiber [164] with working distance d of about 50 µm and spot-size of 4 µm. The fiber is held on a piezo-electrically driven XYZ-translation stage for fine tuning of the coupling distance d. Additionally, an automated alignment control system (Thorlabs NanoTrack TNA001) is in place to ensure long term stability of fiber coupling in the transverse plane and compensate for possible laser beam steering with injection current and/or temperature. The entire coupling stage, mounted on a floating optical table, is enclosed by a plexiglass box to minimize the effect of environmental fluctuations.

Concerning laser biasing, the devices are contacted using DC needle probes, connected to the current source through shielded cables. Depending on the specific experiment, either a low-noise battery-based laser driver (ILX Lightwave LDX 3620) or a GPIB-controllable current source (Keithley 2400) is used. Although the larger low-frequency noise exhibited by the latter has shown to have a detrimental effect on the optical linewidth, no evident dependence on the noise of the current source has been remarked for the laser regimes discussed hereafter. Therefore, systematic assessment of general ML characteristics of single-section devices is carried out using the GPIB-controllable source and a LabVIEW based acquisition routine.

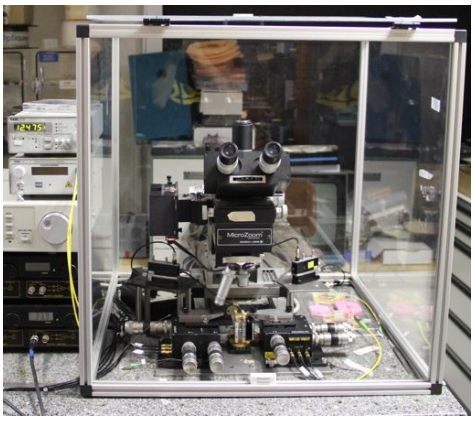

(a)

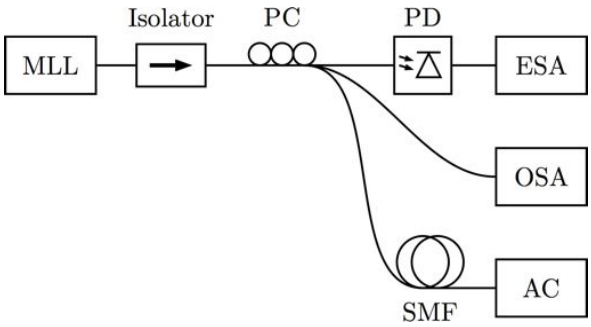

(b)

Figure 3.1 – Coupling stage (a) and fiber optic setup (b) used for MLL characterization.

Light coupled into single mode fiber (SMF) is passed through an optical isolator and split into multiple measurement paths, using fused-fiber couplers. Optical spectrum is characterized using a standard grating-based optical spectrum analyzer (OSA) (Ando AQ6319) with resolution of 10 pm, while the pulse power spectrum is detected with a 50-GHz-bandwidth

photodiode (U^2T) and an ESA (HP 8565E). Finally, pulse autocorrelation is recorded using a rotating-mirror, background-free autocorrelator (Femtochrome Research – FR-103HS) and a sampling oscilloscope. If necessary, a spool of SMF for GDD compensation and/or a fiber amplifier for signal boost are inserted before the autocorrelator. Pulse width can then be evaluated, after correction of the AC timescale with a specific polynomial regression that compensates for the time-delay sweep nonlinearity of the tool.

3.1.2 InGaAsP/InP single quantum well lasers at 1.55 µm

As already discussed in chapter 2, as benchmark for our study, we have considered a 1-mm-long ridge waveguide laser based on a single InGaAsP quantum well structure grown on InP, especially designed to exhibit a low optical confinement factor Γ. The device, emitting around 1.56 µm, has as-cleaved facets and features a threshold current of 16 mA and maximum output power of 21 mW, as shown in the light-current characteristic in fig. 3.2a. The optical and RF spectra recorded at 155 mA are shown, respectively, in fig. 3.2b and 3.2c, while a full mapping of these quantities as function of injection current is reported in fig. 3.3. One can observe that a relatively flat comb spectrum with FWHM on the order of 4 to 6 nm is generated for currents above 50 mA. Strong phase correlation between the longitudinal modes is demonstrated by the narrow RF line shape at the MLL repetition frequency $f_r = 37.6$ GHz. Indeed, RF linewidth FWHM on the order of 100 kHz and below is observed for a current range as large as 150 mA. For comparison, the minimum RF linewidth reported for multiple quantum well lasers is about 200 kHz [4], suggesting that better noise performances achievable with a structure with lower Γ.

As correlated optical phase drifts occur for the lines of the spectrum, phase-locked modes are typically treated as a unique entity, called *supermode* [45]. In general, a supermode has its own repetition frequency and its own evolution with current and temperature. In case the laser emits light on multiple super-modes at a certain bias point, these will compete between them for gain, resulting in repetition frequency instability and larger RF linewidths [45].
For the device under test, little competition between supermodes has been observed. In fact, sharp transitions between different mode-locked states are observed with injection current. These transitions involve jumps of both the RF frequency and the central wavelength. In particular, shifts of the emission spectrum toward longer wavelengths are accompanied by larger values of the beat-note frequency. This trend, already observed in [4], has been attributed to the normal chromatic dispersion of semiconductor material, resulting in lower group refractive indices for longer wavelengths. On the other hand, the origin of wavelength and RF frequency jumps remains a subject of debate. Because this phenomenon resembles the well-known mode-hopping in DBR lasers, junction heating and the consequent temperature rise in the component has been indicated as a possible cause [4]. In addition, several authors attribute this hopping effect to nonlinear gain [119, 121, 122] (cf. sec. 1.4.3), while others ascribe it to carrier generation and recombination events mediated by defects in the barrier

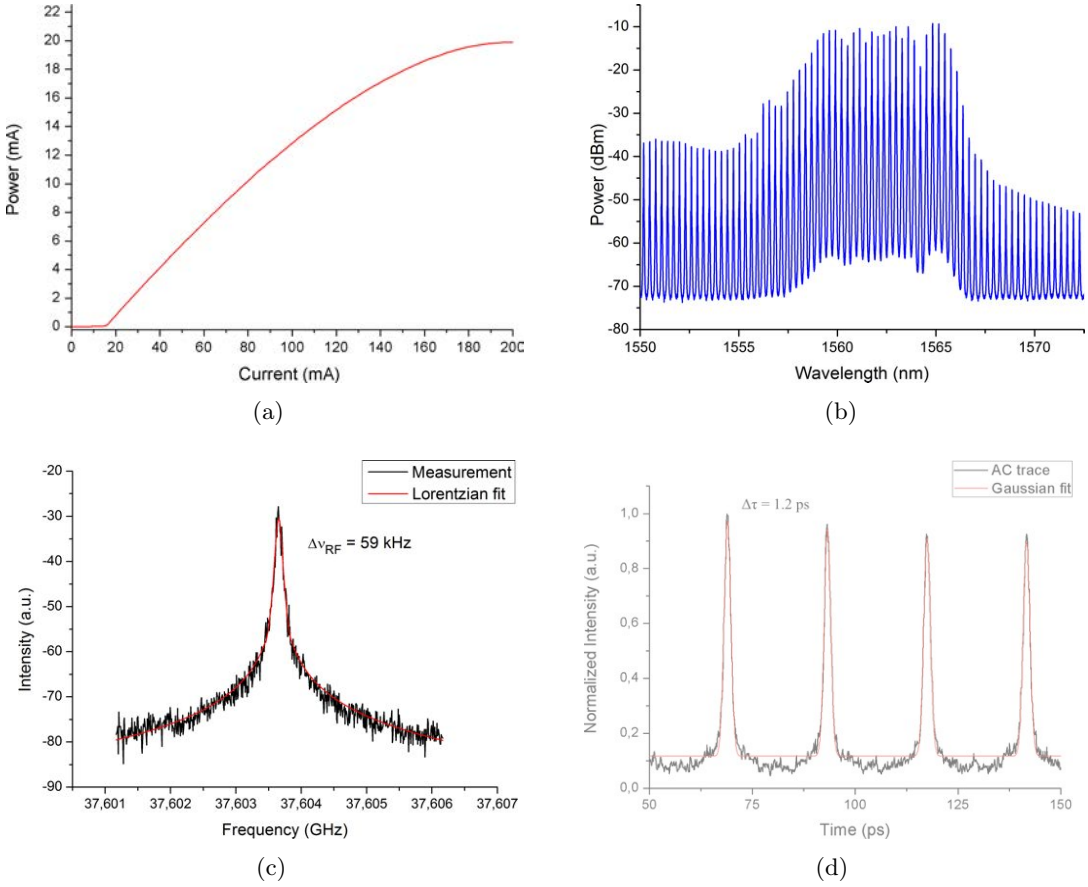

Figure 3.2 – (a) Light-current characteristic and (b)-(d) mode-locking properties of the 1-mm-long, single-section QW laser at 155 mA: (b) optical spectrum, (c) RF spectrum and (d) pulse autocorrelation.

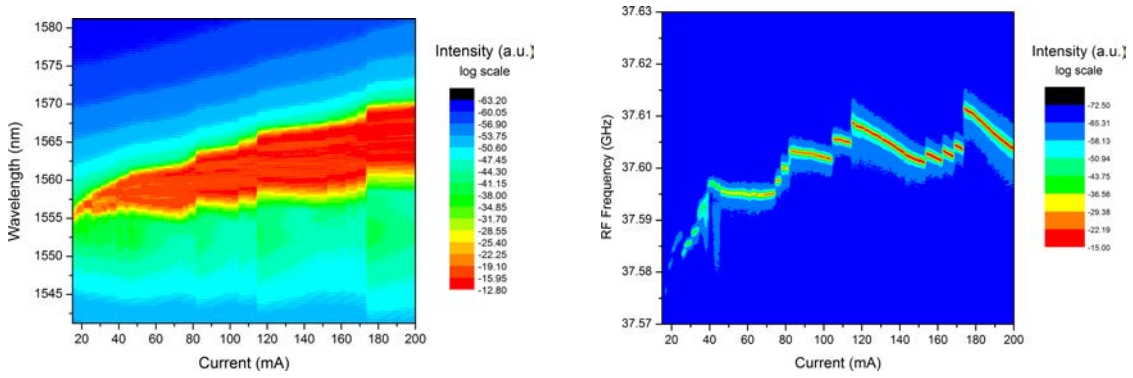

Figure 3.3 – Optical spectrum (a) and RF spectrum (b) mapping as a function of current for the 1-mm-long, single-section QW laser.

layers [165].

Regardless of mode hopping, pulse generation from this device can be achieved by compensating the normal group delay dispersion (GDD) of the laser signal using the anomalous dispersion of standard single mode fiber (SMF-28) at 1.55 µm. More specifically, pulse FWHM of about 1.2 ps has been inferred, after light propagation through 250 m of SMF for an

injection current of 155 mA (see fig. 3.2d). This corresponds to a laser GDD on the order of 5.5 ps^2, for a fiber GVD of -0.022 ps^2/m.
Although this method of estimating pulse GDD is rather approximate, we will show in sec. 3.2 that this approach may enable a more accurate assessment of GDD when used in combination with FROG technique.

3.1.3 InAs/InP (100) quantum dash lasers at 1.55 µm

The material most widely investigated in this work are InAs QDashes on InP. To highlight the main features of QDash based lasers, we consider here an 890-µm-long BRS device with repetition frequency of about 48 GHz and as-cleaved facets. The laser, issued from a 9 DBAR structure with modal gain of ≈ 50 cm^{-1} and internal loss of ≈ 18 cm^{-1}, exhibits a light-current characteristic and an evolution of the central wavelength and spectrum FWHM, shown respectively in fig. 3.4a and (b). The device features a threshold current of about 10 mA and a

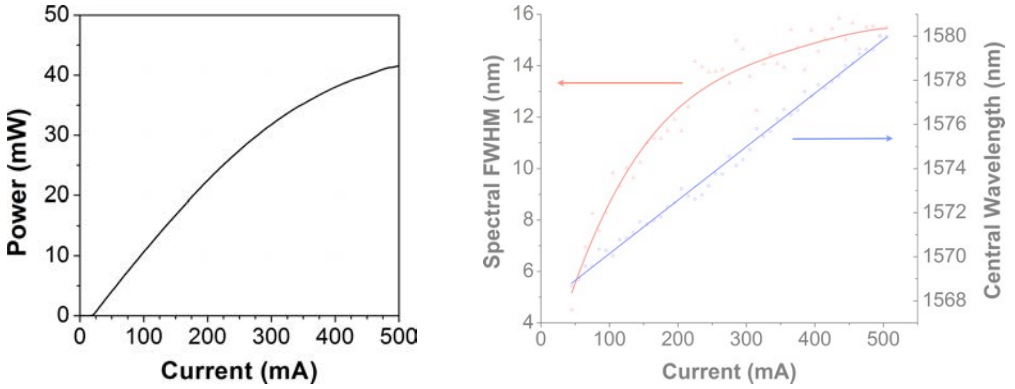

(a) (b)

Figure 3.4 – (a) Light-current characteristic and (b) evolution of central wavelength and spectral FWHM as a function of current for the 890-µm-long single-section QDash MLL at 20 °C.

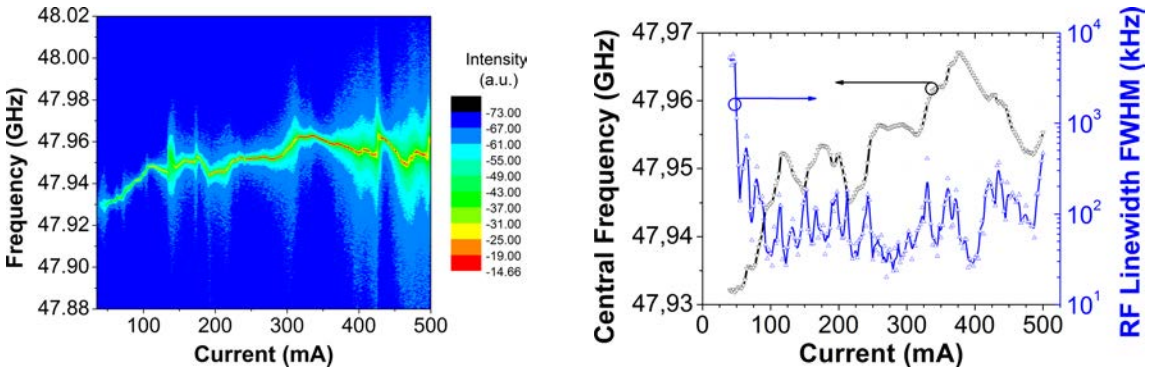

(a) (b)

Figure 3.5 – (a) RF spectrum mapping and (b) central frequency and linewidth FWHM evolution as a function of current for the 890-µm-long single-section QDash MLL at 20 °C.

maximum output power of ≈ 40 mW. Moreover, broad and flat emission spectra with FWHM

in excess of 15 nm are observed for high injection current. This unique feature makes QDash lasers especially interesting for the generation of frequency combs for optical communications. To identify mode-locking regions as a function of injection current, the longitudinal mode beating of the laser is studied in the RF domain. A mapping of the RF spectrum and RF central frequency and linewidth FWHM vs. bias current is shown in fig. 3.5. It can be observed that, unlike the QW device, a clear supermode competition takes place in the QDash laser, as abrupt changes of the central frequency with current are accompanied by increasing RF linewidth. Nonetheless, the low values of RF linewidth (few tens of kHz) measured for the present device demonstrate effective ML characteristics and highlight the potential of QDashes for low-timing-jitter applications.

As in the case of QW lasers, short pulse trains from QDash devices can be generated by propagating the laser signal through suitable lengths of standard SMF-28. This fact, already reported by several authors [7, 82, 111, 112], is studied in more detail for the 48 GHz device under test using SHG-FROG. Retrieved shape and GDD of generated pulses can then be found in sec. 3.2.

3.1.4 InAs/InP (311)B quantum dot lasers at 1.55 µm

Another material system proposed for operation at 1.55 µm is InAs QDs grown on InP (311)B substrates at INSA Rennes, already introduced in sec. 2.2.2 [149, 150]. To evaluate their ML characteristics, we consider a 1-mm-long, single-section ridge waveguide laser with as-cleaved facets. Light-current characteristics and optical spectrum evolution with current for this device are shown, respectively, in fig. 3.6a and 3.6b. As it can be noticed, the laser exhibits a relatively high threshold current of 56 mA, probably due to the large inhomogeneous broadening of the QD ensemble leasing to a reduced modal gain (cf. sec. 2.2.2). Moreover, early output power saturation occurs around 170 mA, most likely induced by junction heating. The latter may be caused by a sub-optimal doping profile for the laser structure, resulting in a large series resistance of 10 Ω measured for the device.
Yet, a flat optical spectrum with FWHM growing with current from 1.5 nm up to 4 nm is observed. Furthermore, strong phase correlation between the longitudinal modes is indicated by narrow RF linewidths and pulse trains with FWHM down to 1.5 ps can be achieved after light propagation through 220 m of SMF-28 (see fig. 3.6c and 3.6d). This study, carried out in collaboration with K. Klaime as part of his PhD thesis, constitutes to the best of our knowledge the first observation of mode-locking regime in single-section lasers based on InAs QDs on InP (311)B [e].

3.1.5 InAs/GaAs quantum dot lasers at 1.3 µm

In addition to lasers operating at 1.55 µm, in our study we have also investigated the well-known InAs/GaAs QD material system for emission at 1.3 µm. In order to describe its main

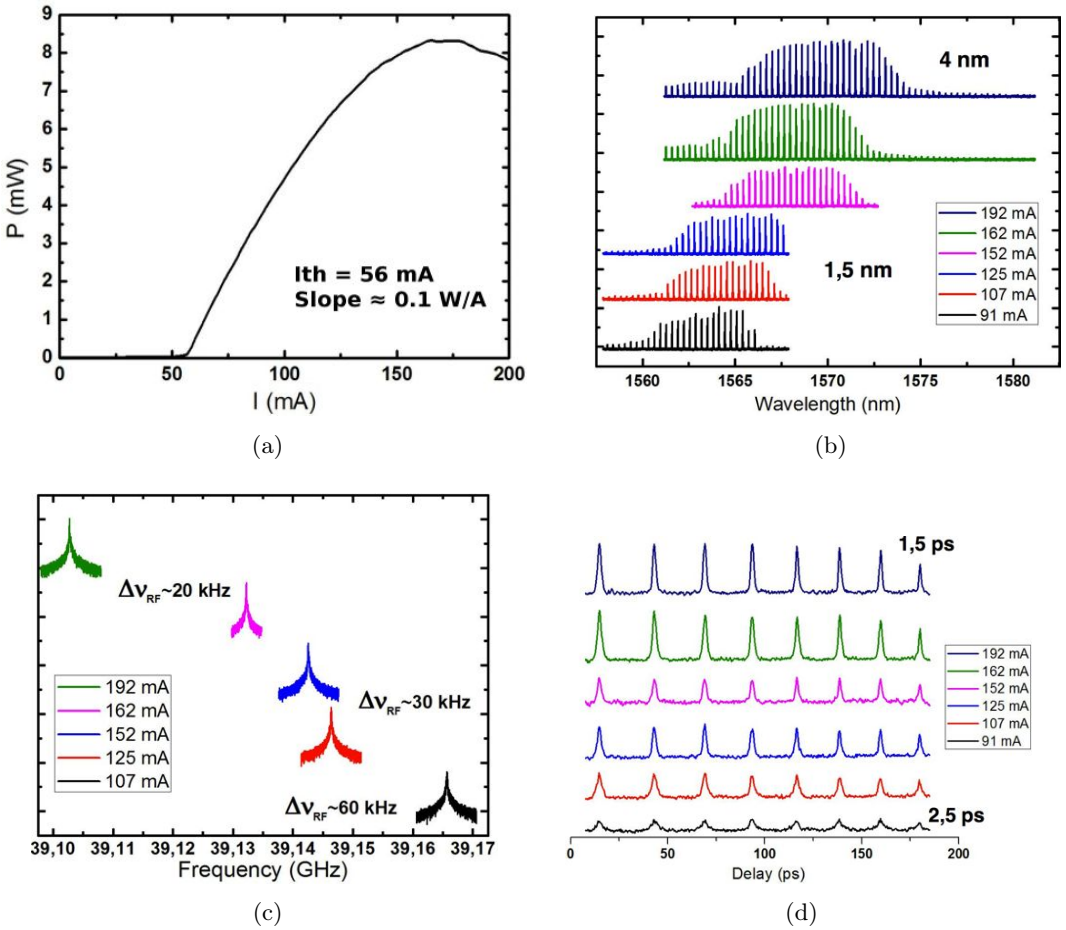

Figure 3.6 – (a) Light-current characteristic and (b)-(d) mode-locking properties of the 1-mm-long, single-section InAs/InP (311)B QD laser for different values of the bias current: (b) optical spectrum, (c) RF spectrum and (d) pulse autocorrelation.

ML characteristics, we consider here a 1.4-mm-long ridge waveguide laser with as-cleaved facets, issued from the commercial structure described in sec. 2.2.1. The device has a threshold current of 60 mA and a maximum output power of 36 mW at saturation, as shown in the light-current characteristics in fig. 3.7.

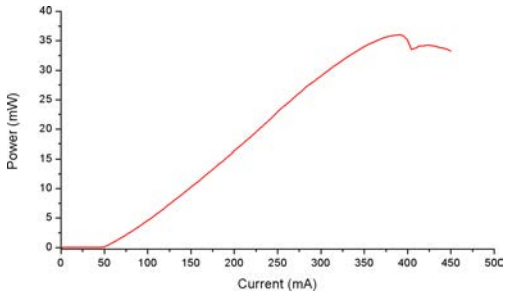

Figure 3.7 – Light-current characteristic for the 1.4-mm-long, single-section InAs/GaAs QD laser.

Also for this component, a mapping of the optical spectrum and the RF spectrum as a function of injection current is carried out under CW operation and the corresponding results are reported in fig. 3.8. From this mapping, we have found a strong correlation between the

shape of the spectrum envelope and the laser phase noise. More specifically, whenever a single lobe is observed in the output spectrum, broad RF line shapes occur. On the other hand, as the laser emits light on two distinct wavelength sub-bands for current ranges around 180 and 310 mA, noise reduction takes place. Noise performances are further improved for injection currents above 450 mA, where stable lasing from both ground state (GS) and excited state (ES) of dots is observed. These findings can be interpreted in terms of supermode

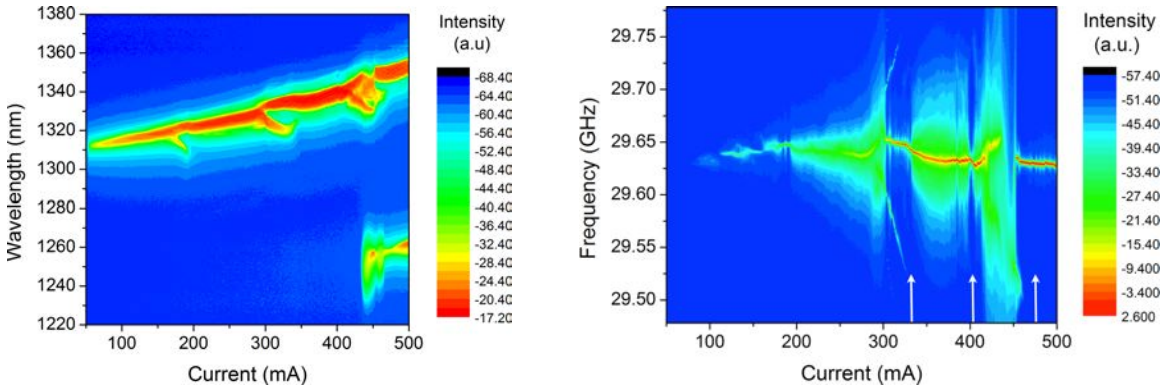

(a) (b)

Figure 3.8 – (a) Optical spectrum and (b) RF spectrum mapping as a function of current for the 1.4-mm-long, single-section InAs/GaAs QD laser. Efficient mode-locking regions are highlighted by the arrows.

theory [45], by speculating that a severe supermodes competition takes place for current values below 450 mA. This competition, resulting in large RF linewidths, is slightly reduced when spectrum splitting occurs, as the latter induces a wavelength separation of the supermodes involved. Alternatively, a more physical explanation for the large phase noise in the laser may be given by the pronounced carrier scattering among the energy levels of the dots. Carrier capture and escape processes in the QD states, in fact, may be responsible for a large dephasing of the modal fields. Lasing from both GS and ES, on the other hand, may reduce this scattering mechanism, as carriers are more efficiently evacuated from the dots through radiative recombination.

Although these conjectures are not supported by suitable theoretical models as yet, carrier dynamics have been indicated as possible cause for specific experimental observations in QD laser. Emission from distinct GS sub-bands, for example, has been attributed to the redistribution of the carriers from the center of the lasing spectrum to the outer modes through the homogeneous broadening of QD ensemble [75, 131]. This last phenomenon, in particular, seems to be a specific feature of quantum dots [105, 115], especially those based on the InAs/GaAs material system [75, 131, 166–168]. Indeed, splitting and merging of GS sub-bands, accompanied by large RF linewidths, has been observed for all the InAs/GaAs QD structures investigated during this thesis. We have, therefore, associated this occurrence to poor ML performances in single-section lasers based on this material system.

Inferior noise performances in free-running single-section InAs/GaAs QD laser are accompanied by the absence of self-pulsation, despite any attempt of GDD compensation. On the

other hand, for operating points where narrow RF linewidths occur, short pulse can be generated after suitable compression. For the device under test, RF linewidths down to ≈ 30 kHz have been measured for injection currents above 450 mA (see fig. 3.9a). Moreover, because at these currents the emission spectrum lies above the zero-dispersion point of standard SMF-28, the anomalous GVD of the latter can be used to compensate the blue chirp of the laser signal. Following this procedure, self-starting pulses with FWHM down to about 4 ps have been measured by background-free autocorrelation for the single section device after light propagation through 2.1 km of SMF, as shown in fig. 3.9b.

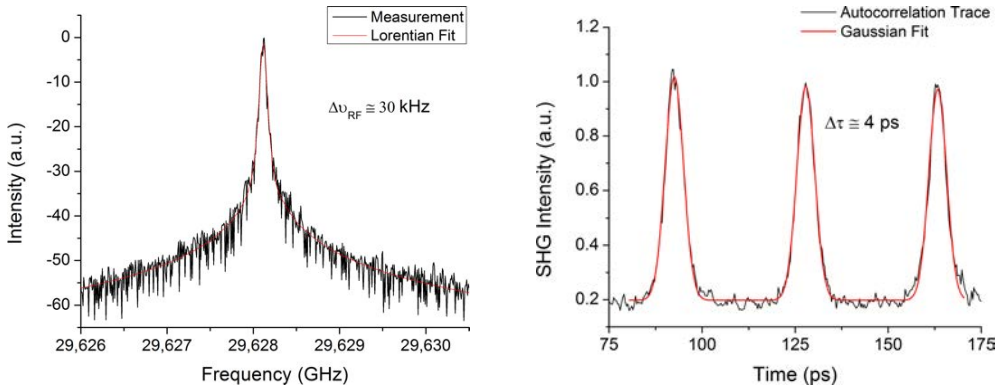

(a) (b)

Figure 3.9 – (a) RF linewidth and (b) autocorrelation trace measured for an injection current of 463 mA after propagation through 2.1 km of SMF for the 1.4-mm-long, single-section InAs/GaAs QD laser.

3.1.6 Discussion

The preceding investigations on single-section lasers based on QW, QDash and QD active regions allow us to draw some general conclusions regarding the material dependence of ML characteristics in these devices. First of all, we have noticed that different evolution of the emission spectrum with current takes place in the studied systems. While for QW lasers the spectrum FWHM does not significantly increase with injection current, for QDash and QD material at 1.55 µm a regular broadening is observed. QDash lasers, in particular, have demonstrated a spectrum FWHM as large as 15 nm. This trend, already highlighted in previous works on QDash lasers [7, 109–112, 116], has been attributed to band filling effects in combination with junction heating, although the origin of spectrum broadening in QD/QDash material at 1.55 µm is still unclear. As opposed to devices based on InP here investigated, a unique spectrum evolution is exhibited by InAs/GaAs QD lasers, with frequent splitting and merging of ground state sub-bands accompanied by large phase noise.

Regarding phase noise, narrow RF linewidths have been observed for nearly all of the low-confinement-factor structures investigated. However, depending on the material system, different dynamics are found. Wider and more regular regions of low phase noise occur in InP devices compared to GaAs ones. RF linewidth in lasers operating at 1.55 µm is shown to

decrease with current, reaching typical values of few tens of kHz for bias currents of few times the threshold. Minimum linewidth value achievable for QDash and QD material is generally lower than that of QW devices, even though wider regions of instability are observed for the first, probably due to increased nonlinear gain and/or carrier scattering effects.
As broad, phase-locked spectra are highly interesting for optical frequency combs for telecommunications, in the following we focus mostly on QDash MLLs. This material, allowing for best ML performances and highest average power among the investigated InP-based structures, appears to be a well-suited candidate for many of the applications reported in sec. 1.1.2.

3.2 Frequency-resolved optical gating measurement of single-section MLL pulses

For applications employing short MLL pulses, knowledge of pulse shape and chirp is very important to assess system performances. In this section we aim at investigating the pulse generation capabilities of single-section QDash lasers by means of second harmonic generation frequency-resolved optical gating (SHG-FROG) [65]. The technique, unlike standard autocorrelation (AC), allows getting access to both intensity and phase information of ultrashort pulses by retrieving the complex electric field and, therefore, constitutes a valuable tool for the detailed investigation of semiconductor MLLs [35, 111]. In addition, it has been proven to be more robust against pulse shape instabilities than AC and SPIDER [169].
Use of FROG for the study of duration and timing jitter of pulses generated by single-section FP lasers based on InAs/InP QDashes has been already demonstrated, respectively, in [111] and [112]. However, in these studies, the use of Erbium-doped fiber amplifier (EDFA) and filter to get a sufficiently high power for the FROG measurement has not allowed to draw conclusion on the actual chirp of the laser signal, in addition of being a source of distortion for the signal to be characterized. As a consequence the stepped heterodyne technique, a linear method based on fast electronics, has become the preferred tool to get access to the phase information of single-section QDash MLLs [7, 170].

Here we show how GDD information of highly chirped pulses from single-section MLLs can be deduced using SHG-FROG in combination with pulse compression by means of standard SMF-28. FROG characterizations, carried out in collaboration with Prof. Bimberg's group at TU Berlin, are presented for the 890-µm-long device considered in sec. 3.1.3. In the following, after a brief introduction to the technique, we discuss the role of fiber dispersion compensation in the measurements and we study the pulse GDD as function of laser bias conditions. Specific capabilities and limitations of FROG technique for our purposes are also highlighted.

3.2.1 Frequency-resolved optical gating technique

SHG-FROG is a pulse characterization technique that allows retrieving full information in terms of intensity and phase profile, without any assumptions on the pulse shape, as it

is commonly done for SHG-AC [65]. As anticipated in sec. 1.3.1, the technique is based on the detection of a convoluted, spectrally resolved autocorrelation. The recorded FROG spectrogram shows the frequency resolved convoluted intensity of the pulse as a function of time delay. Extracting the intensity and phase profile from the spectrogram represents a two-dimensional phase retrieval problem, which can be solved by an iterative algorithm. A FROG retrieval error ϵ is used as a figure of merit of the quality of the retrieval process [65]. The pulse profile so obtained, however, suffers from a time direction ambiguity, arising from the inherent delay direction symmetry of SHG-FROG. This ambiguity can be resolved through the comparison between the result of an additional measurement with the introduction of a known amount of dispersion and the simulation of the propagation of the previously retrieved pulse through a medium with the same dispersion. A SHG-FROG setup consisting of a SHG-AC stage, followed by a monochromator and a highly sensitive charge-coupled device (CCD), described in more detail in [35], was used.

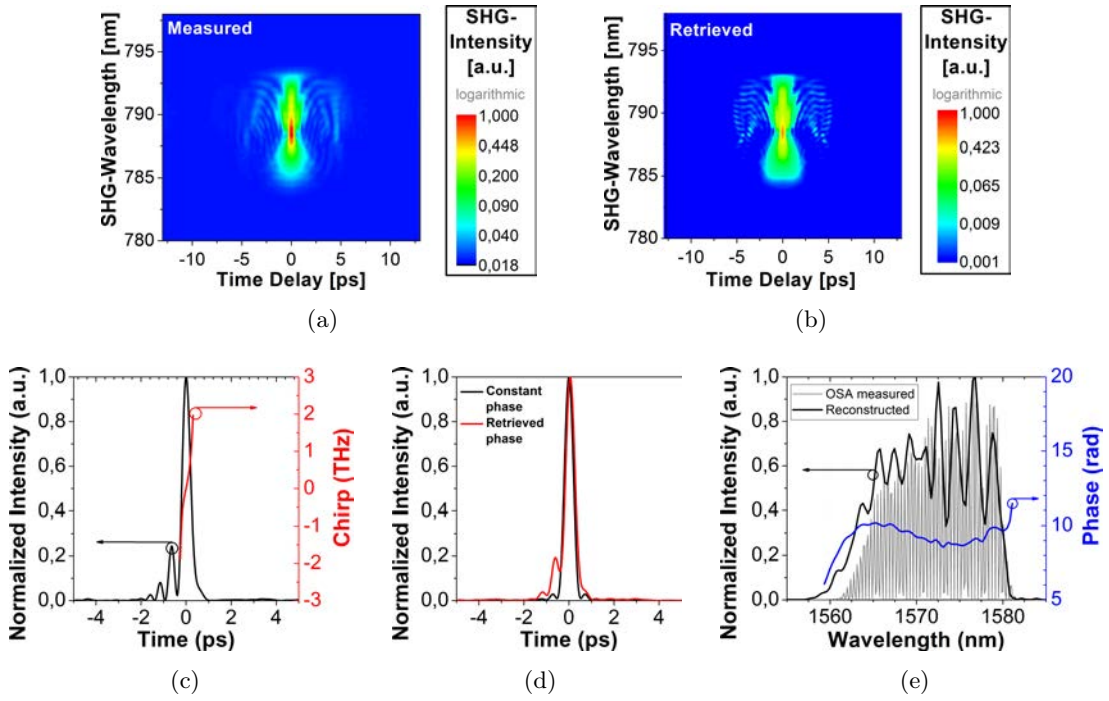

Figure 3.10 – FROG measurement of pulses generated by the 890-µm-long single-section QDash MLL for a bias current of 300 mA, after signal propagation through 66 m of SMF-28. (a) Measured and (b) retrieved FROG spectrogram, (c) reconstructed pulse intensity and chirp, (d) simulated pulse shapes for constant phase profile and for the retrieved phase profile and (e) retrieved spectral phase and intensity in comparison with optical spectrum measured using an optical spectrum analyzer.

Fig. 3.10 shows an example of FROG measurement on the laser under investigation for an injection current of 300 mA, after signal propagation through 66 m of SMF-28 for dispersion compensation. For these operating conditions, a minimum pulse FWHM of 423 fs and pulse peak power of about 100 mW have been measured for an average input power in the FROG setup of about 0.6 mW. A pulse retrieval error of 0.0061 for a retrieval grid size of 256×256 measurement points and the agreement between measured and reconstructed FROG trace,

but also between the retrieved pulse spectral envelope and the laser spectrum measured with an OSA confirm the reliability of the measurement. Comparison between the spectra shows also that all the longitudinal modes are phase-locked and contribute to the pulse formation, in agreement with recent results demonstrating phase coherence across a 1.5 THz spectral bandwidth for analogous devices [171].

3.2.2 Pulse duration dependence on SMF-28 length

In order to resolve the time direction ambiguity of the measured pulses and to determine the fiber length that minimizes the pulse duration, the pulse profile has been studied as a function of the SMF-28 length. For all measurements, a nearly quadratic temporal phase is observed, indicating that the chirp is essentially linear. The linear spectral chirp coefficient (in units of ps/nm) commonly used in practice [35, 87, 105] has been extracted from the retrieved temporal and spectral phases by calculating the fiber dispersion needed to fully compress the pulse. This has been carried out by simulating the pulse propagation over SMF-28 by means of the Split-Step Fourier Method, described in [172].
It is observed that, as the length of SMF-28 introduced compensates the pulse chirp, the retrieved pulse shape approaches the profile calculated from the power spectrum measured by an optical spectrum analyzer, assuming an equal spectral phase for all the modes. Deviations from such a shape are due to the nonlinear component of the chirp not compensated by the SMF-28 (see fig. 3.10d). Conversely, a few tens of meters deviation from the optimal linear chirp compensating fiber length induces severe broadening and distortion of the pulse shape, due to the wide emission spectrum of the laser. This trend is in agreement with the model on chirped pulse propagation through fiber reported in [172] and can be accurately predicted with the Split-Step Fourier Method, used here to deduce the correct time direction.

It is worth to remark that for pulse broadenings such that the full pulse duration becomes larger than half of the pulse repetition interval T_r, the FROG autocorrelation trace tends to overlap with the neighboring cross-correlation traces at the edges of the spectrogram (time delay values around $-T_r/2$ and $-T_r/2$). This condition implies non-zero intensity at the edges of the spectrogram, unlike what required by the reconstruction algorithm to perform inverse Fourier transformations [65], leading to large retrieval errors [173, 174]. In this case, simple truncation of the spectrogram between $-T_r/2$ and $-T_r/2$ and use of noise subtraction functions before pulse retrieval may be performed to improve the convergence of the retrieval algorithm. However, the retrieved pulse will significantly differ from the real one, since a non-negligible fraction of the pulse energy will lie outside the reconstruction grid. This is the reason why the highly chirped signal emitted by the single-section QDash MLL is characterized by FROG after compression by suitable lengths of SMF-28.
The issue described above becomes more severe for short cavity lengths than for long ones, as the condition on the full pulse duration becomes more stringent for increasing repetition rates. Using this technique, pulses generated from single-section devices with repetition

frequencies up to 60 GHz could be successfully characterized, while for repetition rates larger than 100 GHz large reconstruction errors have been observed.

3.2.3 Pulse duration dependence on injection current

In order to study the dependence of the intensity and phase profile on the operating condition of the laser, FROG measurements have been performed at 20 °C for different values of injection current. The SMF-28 length was kept to 66 m for all the measurements. Figure 3.11 shows the retrieved pulse intensity and phase as well as extracted pulse FWHM and GDD data for injection currents of 100, 200, 300 and 400 mA. The pulse GDD is given by the second derivative of the spectral phase $\varphi(\omega)$ with respect to angular frequency ω (cf. eq. 1.24), while the dispersion introduced by the 66 m of SMF-28 is calculated using the formula for the dispersion parameter reported in [175], taking into account the shift of central emission wavelength with current.

Pulse Intensity and Phase	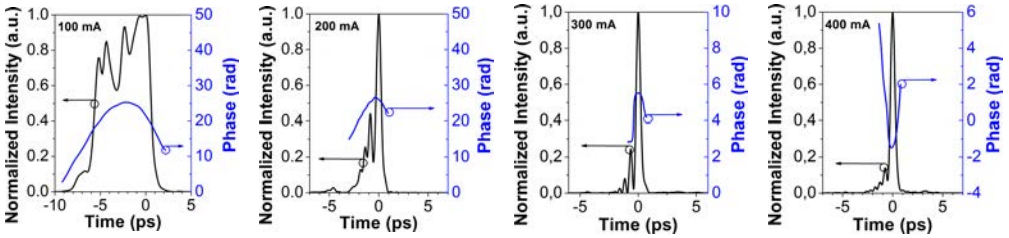			
$\Delta\tau$	6.188 ps	576 fs	423 fs	519 fs
ε	0.0297	0.0095	0.0061	0.0088
λ_c	1561.39 nm	1566.89 nm	1575.0 nm	1582.81 nm
$\Delta\lambda_{FWHM}$	9.32 nm	12.45 nm	13.76 nm	14.65 nm
GDD_p	0.65 ps^2	0.16 ps^2	0.01 ps^2	-0.12 ps^2
GDD_{SMF-28}	-1.43 ps^2	-1.46 ps^2	-1.52 ps^2	-1.57 ps^2
GDD_{tot}	2.08 ps^2	1.62 ps^2	1.53 ps^2	1.45 ps^2
$\Delta\tau_{min}$	567 fs	439 fs	423 fs	374 fs

Figure 3.11 – Reconstructed pulse intensity and phase for injection currents (from left to right) of 100, 200, 300 and 400 mA. The values of pulse width $\Delta\tau$, FROG reconstruction error ε, central wavelength λ_c, spectral FWHM $\Delta\lambda_{FWHM}$, pulse, fiber-induced and total group delay dispersion GDD_p, GDD_{SMF-28} and GDD_{tot} and minimum pulse width achievable $\Delta\tau_{min}$, are reported for each measurement.

It can be observed that the GDD of the pulse passes from positive values (corresponding to normal dispersion) for currents values below 300 mA, to negative values (anomalous dispersion) for larger currents. This trend in part is due to the increase of the anomalous dispersion introduced by the fiber, but mostly depends on variations of the laser cavity dispersion with carrier injection. The total GDD of the signal emitted at the laser facet can be estimated with good approximation by adding the absolute value of the GDD introduced by the SMF-28 to that calculated for the retrieved pulses, neglecting the dispersion of the FROG measurement system itself (N-BK7 lenses and fiber collimators with a total length below 8 mm; $LiNbO_3$ SHG crystal with effective thickness below 1.5 mm). The values obtained are in agreement

with measurements on analogous devices performed with the stepped-heterodyne technique [7] and confirm a monotonic decrease of the GDD as a function of injection current.

In addition, it is worth to notice that the minimum pulse FWHM achievable for each bias point (calculated using the Split-Step Fourier Method by propagating the measured pulse through a length of fiber that exactly compensates the linear chirp) is observed to decrease with current. This fact is attributed to the increase with current of the optical spectrum FWHM and, thus, of the number of longitudinal modes contributing to pulse formation. For the sake of comparison, we remind that for standard two-section MLLs, pulses tend to broaden with injection current for the same reverse bias on the absorber [91], although this increase of pulse width is often imputable to excess of chirp [35].
Analogous trends for the GDD and the minimum pulse width are observed for devices with different cavity length, with increasing values of GDD for larger cavity lengths in agreement with measurements performed by stepped-heterodyne [7]. Also in these cases, the retrieved pulses feature asymmetric shapes with satellite peaks produced by the nonlinear chirp not compensated by the SMF-28. Nonetheless, the good match between the measured and the retrieved FROG traces confirms the stability of pulse generation and the mode-locking capabilities of single-section QDash devices.

3.3 Frequency stability and optical linewidth of single-section MLLs

The broad and flat emission spectrum of QDash based MLLs is especially interesting for frequency domain applications of OFCs. In these applications, optical and timing phase noise, as well as pulse repetition frequency stability assume a particular importance and merit more attention. In this section, after a presentation of the typical short term and long term stability performances of single-section QDash MLLs, we consider the impact on optical and RF linewidth of characterization setup, concentrating in particular on short distance feedback from coupling fiber. As similar behavior is observed for all the devices examined in this thesis work, in our discussion we do not focus just on one specific laser. Instead, every time a particular phenomenon is considered, we make reference to a device for which the latter is more easily noticeable.

3.3.1 Stability performances of single-section MLLs

A systematic investigation on the stability of the optical frequency combs generated by QDash Fabry-Perot lasers has been initiated at LPN by K. Merghem. Here, in order to illustrate the typical timing jitter and long term stability performance of these devices, we report the most salient results of the work presented in [d]. The device considered in this study is a 890-µm-long single-section BRS device issued from a 9 DBAR structure. For technical noise reduction, a low noise, battery-based current source is used (cf. sec. 3.1.1). As typical for

single-section QDash MLLs, the linewidth of mode beatings (on the order of few tens of kHz) is observed to be much narrower than the optical linewidths of the different modes (> 10 MHz), indicating strong phase coherence between the modes [171]. Also, a parabolic dependence of the optical linewidth as function of optical frequency is found, due to the timing jitter of the MLL output, as discussed in sec. 1.2.2.

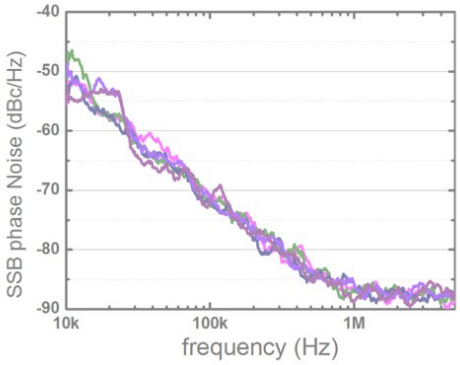

Figure 3.12 – single sideband phase noise (SSBPN) curves recorded every ≈ 30 s for a central frequency of 47.54 GHz.

The jitter is determined from the single sideband phase noise (SSBPN) spectra $\mathcal{L}(f) = S_{\varphi_t}^{\mathrm{SSB}}(f)/2$, measured over a frequency interval ranging from 10 kHz to 5 MHz, using a 50-GHz-bandwidth photodiode and an ESA. Phase noise curves recorded every ≈ 30 s for the laser biased at 220 mA are shown in fig. 3.12. The repeatability of the curves indicates good phase noise stability over time. Moreover, all traces exhibit a clear roll-off with a slope of -20 dBc/Hz per decade over the considered frequency range, representative of the f^{-2} dependence of $S_{\varphi_t}^{\mathrm{SSB}}(f)$. This suggests that the major source of short-term instability of single-section MLLs is spontaneous emission coupled to lasing modes, as anticipated in chapter 1. The rms timing jitter is on the order of 1.3 ps, as calculated from eq. 1.29 on page 26 by integrating SSBPN spectra from 10 kHz to 1 MHz, point at which the phase noise trace reaches the thermal noise floor of the ESA. This value is comparable to that reported in previous investigations on QDash devices [82] and demonstrate good stability performances for free-running MLLs based on this material system, owing to its reduced dimensionality.

Another quantity of interest for optical frequency combs from MLLs is the long-term stability of the laser free spectral range, that is evaluated in [d] by recording the beat-note between the longitudinal modes during one hour using an electrical spectrum analyzer in frequency count mode. Additionally, in order to assess the possible correlation between the frequency drift and the heat-sink temperature, also the thermistor reading is registered at each time instant. The measurement performed with a gate time of 1 s during 3602 s are shown in fig. 3.13a. Experimental observations indicate a stability of 1.7 mK over one hour for our temperature controller, while RF frequency exhibits an excursion of less than 86 kHz around the mean value of 47.540 GHz during the whole experiment. Moreover, inspection of the recorded time-series does not reveal any significant correlation between the temperature fluctuations and the RF frequency drift. As a measure of the stability of the generated

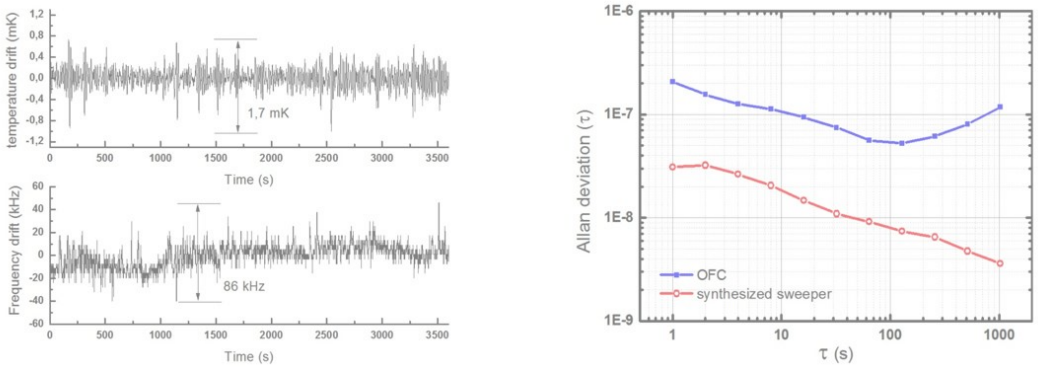

(a) (b)

Figure 3.13 – (a) Measured temperature fluctuation and residual RF frequency drift (RBW = 1 kHz) over one hour and (b) fractional frequency instability (overlapping Allan deviation) based on the measured time-series in fig. 3.13a.

comb, the overlapping Allan deviation is computed from the frequency time-series reported in fig. 3.13a (cf. sec. 1.3.4) and results are reported in fig. 3.13b. For the sake of comparison, the figure also shows the Allan deviation of the reference synthesized sweeper used in the experiment, calculated to ascertain the calibration of the equipment. It can be observed that, as expected, the synthesized sweeper has a better long-term stability compared to the device under test, therefore it can be used to evaluate the stability of the QDash MLL. The latter follows similar trends to that of other free running oscillators: first decreasing to a certain value, then increasing again for larger averaging times [51]. Indeed, starting at 2×10^{-7} for 1 s, the Allan deviation reaches 5×10^{-8} at 100 s averaging time, before returning to the 10^{-7} level at 1000 s.

As anticipated in sec. 1.3.4, this increase of frequency instability can be attributed to a random walk change of the optical cavity length, induced by mechanical or thermal environmental fluctuations. Variations of the optical feedback from coupling optics and/or fluctuations of the room temperature may be possible causes of instability. Yet, the slow timescale of frequency drift shown in fig. 3.13b indicates that the latter can be easily compensated with relatively slow feedback loops. For example, knowing the rate of change of repetition frequency with current around a given operating point, a PID controller can be implemented to restore the quantum noise limited regime for the MLL, as demonstrated in [o]. Alternatively, more complex techniques for enhanced stability can be adopted, such as synchronization with optical frequency standard [176] or Pound-Drever-Hall stabilization [22].

3.3.2 Cavity length fluctuations in single-section MLLs

As introduced in chapter 1, cavity length variations may strongly impact on the optical phase noise and the timing jitter of a laser. In this section we study in more detail the effect of these fluctuations. In particular, we focus on the effects of short-distance optical feedback induced by the coupling optics and we discuss the possible approaches to reduce them.

Effect of short-distance feedback

Light emitted from the laser facet, reflected at the air/silica interface of the lensed fiber and, then, coupled back into the laser cavity can significantly perturb the device dynamics. The effects of short-distance feedback induced by laser-to-fiber coupling have been studied in detail in 1982 by Bludau and Rossberg [164]. They have shown that the feedback from fiber can be suitably modeled by introducing a compound laser facet reflectivity R_c given by:

$$R_c(d) = [\sqrt{R_1} - (1 - R_1)\sqrt{R_e}]^2 + 4(1 - R_1)\sqrt{R_e R_1}\sin^2\delta, \tag{3.1}$$

where d is the coupling distance, R_1 is the laser facet reflectivity, R_e is the effective reflectivity of the fiber and $\delta = 2\pi d/\lambda$.
This reflectivity varies sinusoidally with the coupling distance d, with period equal to one half of the laser wavelength λ. Accordingly, also the photon lifetime in the laser cavity τ_p, defined by

$$\tau_p^{-1} = \frac{c}{n_r}\left[\alpha_i + \frac{1}{2L}\log\left(\frac{1}{R_1 R_2}\right)\right], \tag{3.2}$$

is expected to change periodically with d. As τ_p determines the number of photons present in the cavity and, thus, the level of carrier population inversion, different laser dynamics can take place for different coupling distances. This results in feedback-dependent output power [164], optical spectra and RF spectra.

To clarify this point, let us consider the RF spectra of the full comb and the amplitude noise spectra of a single line, recorded for a 54 GHz single-section MLL for different laser-to-fiber positions and shown in fig. 3.14a and 3.14b. The device, based on the same QDash structure considered in sec. 3.3.1, exhibits static characteristics similar to those shown in fig. 3.4 and has been selected on the basis of the FSR for simultaneous measurements using two electrical spectrum analyzers. The measurements reported in fig. 3.14a and 3.14b indicate that, depending on the coupling distance d, conditions of reduced or enhanced amplitude and phase noise can be found. In particular, looking at the shape of the curves in fig. 3.14a and 3.14b, amplitude and timing phase fluctuations seem to be strongly correlated, confirming our expectation that larger relative intensity noise (RIN) is accompanied by increased phase noise (cf. sec. 1.2.2).
Conditions leading to larger intensity noise are also responsible for broadening and distortion of the optical line shape. This fact is confirmed through additional characterizations carried out in collaboration with III-V Lab, using a high-resolution (5 MHz) optical spectrum analyzer from APEX Technologies. Measurement of a single comb line performed for different coupling distances on the same 54 GHz device at the same bias, but on a different setup, are shown in fig. 3.14c. It can be noticed that for some fiber distances a pronounced shoulder appears in the optical lineshape and larger linewidths result for more prominent side peaks. For the same conditions, analogous features are observed on all the lines of the spectrum, indicating a collective behavior of the phase-locked modes. This observation is in agreement with RF characterization shown in fig. 3.14a and 3.14b and demonstrate the impact of short-distance

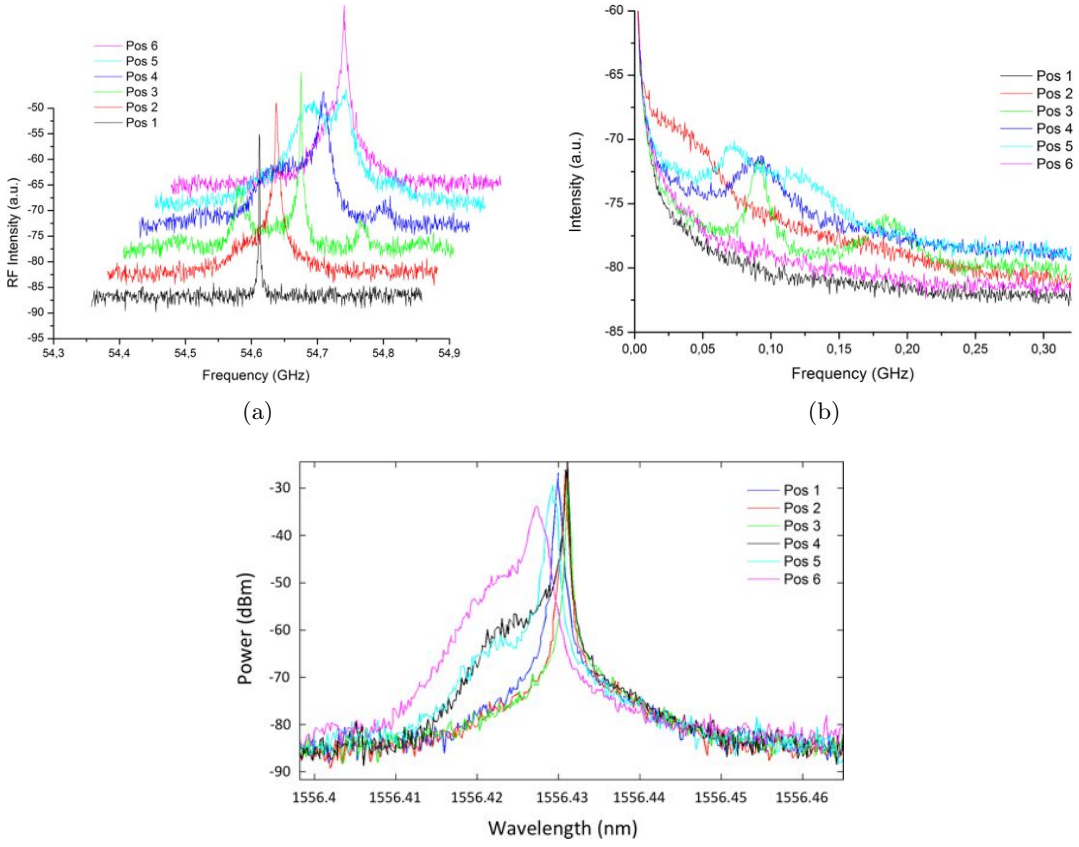

Figure 3.14 – (a) RF spectra, (b) amplitude noise spectra and (c) optical line shapes measured for different laser-to-fiber coupling distances d within one oscillation period for d, for a 54 GHz single-section QDash MLL at $I = 180$ mA.

feedback on laser dynamics.

For the sake of precision, we aim at stressing that optical feedback from coupling fiber, by itself, is not necessarily a detrimental effect. Indeed, depending on the laser bias current and operating temperature, it can even improve noise performances. This can be recognized by looking, for example, at black curves in fig. 3.14a and 3.14b. On the other hand, if feedback is coupled with random mechanical vibration, the resulting fluctuation of the compound facet reflectivity R_c will give rise to unstable laser dynamics. In this case, RF and optical linewidth fluctuations will be imposed by technical noise.

Experimental observations on single-section devices also indicate that, for the same variation of coupling distance d, more severe changes in the RF and optical spectrum take place for the bias current values at which supermodes competition occur. In these regions, in fact, laser dynamics appears to be more sensitive to the photon density in the cavity and situations like the one depicted in fig. 3.14 may be found. Conversely, if the laser operates in a stable region, slow fluctuations of the coupling distance merely result in a small variation of the cavity refractive index, with consequent changes in the repetition frequency on the order of few hundreds of kHz.

Reduction of feedback effects

As time-varying feedback from coupling optics has a detrimental impact on the noise properties of MLLs, the reduction of its effects is of fundamental importance. A solution in this sense can be making the coupling stage more stiff, so as to reduce its sensitivity to mechanical fluctuations. In addition, one can engineer the coupling optics and/or the laser to be more tolerant to feedback effects.

If this last approach is followed, one can deduce from eq. 3.1 that the most effective way of minimizing the reflectivity change due to feedback is decreasing R_e. From the derivation reported in [164], this quantity can be written as $R_e(d) = R_f\epsilon(d)$, where R_f is the Fresnel reflection of the fiber facet and $\epsilon(d)$ is the fraction of reflected power that couples back into the laser cavity. For typical lensed fiber used for laser diode coupling, the effective reflectivity R_e is on the order of 10^{-5}-10^{-6} and $\epsilon(d)$ is approximately constant around the focal point of the fiber lens. However, as shown before, even such small values of R_e cannot prevent laser dynamics variations due to feedback.

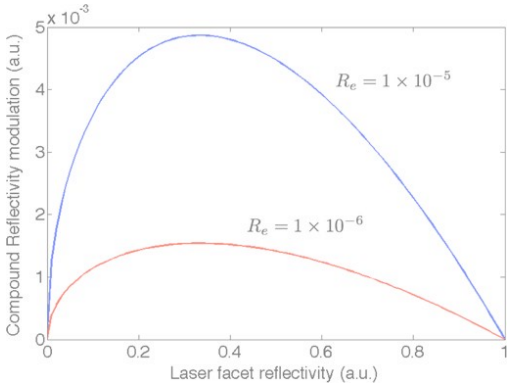

Figure 3.15 – Compound reflectivity modulation $A(R)$ as function of laser facet reflectivity R for different values of effective reflectivity R_e of coupling optic.

In order to decrease the dependence of compound reflectivity R_c on the coupling distance d, one can change the laser reflectivity R_1 through a suitable facet coating, rather than acting on R_e. To identify the optimal values for R_1 that allow to minimize the amplitude of sinusoidal variations of R_c with d, in fig. 3.15 we plot this amplitude $A(R_1) = 4(1 - R_1)\sqrt{R_eR_1}$ as function of R_1 for different values of R_e. We can observe that this amplitude is reduced either for an antireflection (AR) or for a high reflection (HR) coating. Of course, to maximize the power coupled into fiber an AR coating is preferable, although this may produce also an increase of laser threshold.

Very often it is not possible or convenient to make use of facet coatings. In this case, for reliable characterization coupling optics should be optimized. A desirable feature for this optics to induce the least amount of feedback is a large working distance. In this way, laser light impinging on the coupling component and backscattered by the latter can travel further away from the core part of the laser waveguide, resulting in a reduced value of $\epsilon(d)$.

In our study on feedback, in addition to lensed fiber, we have taken advantage of a particular

custom-made SELFOC lens with working distance of ≈ 700 µm, endowed with a 70 dB isolation stage. Owing to the large coupling distance and to the high-quality AR coating present on the lens, feedback effects are strongly reduced. Indeed, regardless on laser bias current, little RF spectrum variations are observed when finely changing the lens position. This can be appreciated from the measurements performed on a 20-GHz-repetition-rate 9 DBAR BRS QDash MLL, reported in fig. 3.16. Here, in addition to the RF spectra recorded for different self-focusing lens positions, we report a mapping of the RF spectrum as function of current. We can notice that, also for these reduced feedback measurement conditions, operating regions showing large RF linewidths can be still identified. These instability regions, attributed in previous works to random fluctuations of fiber coupling [155], are in reality intrinsic to laser dynamics and probably attributable to gain nonlinearity. In these conditions, changes of slope (and sometimes sudden hops) of the repetition frequency are accompanied by broad optical line shapes, possibly including pronounced side peaks, as in fig. 3.14b. In all cases, strong correlation is observed between the RF spectrum of the optical line shapes, therefore for single-section MLL the first constitutes a highly sensitive tool to predict the properties of the latter.

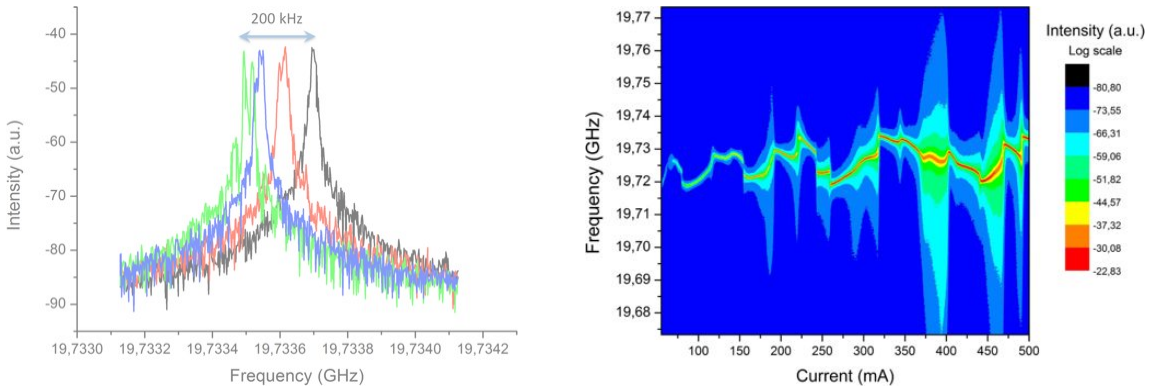

(a) (b)

Figure 3.16 – (a) RF spectra recorded for different positions of coupling optic (SELFOC lens) for a 2-mm-long QDash MLL: maximum shift of central frequency is on the order of 200 kHz. (b) RF spectrum mapping as a function of current for the same device under reduced feedback measurement conditions.

3.4 QDash Fabry-Pérot lasers for photonic integrated circuits

Besides pulse generation and stability, other important aspects of frequency combs generated by monolithic semiconductor MLLs are the possibility of using these components in photonic integrated circuits (PICs) and the precise control of lines spacing. These problematics are often addressed in literature by resorting to ring laser geometries, for which cavity length is lithographically defined and the emitted light is directly coupled into an output waveguide [177, 178]. Ring lasers, however, are less compact than standard Fabry-Perot (FP) design and typically require complex fabrication steps for active/passive device integration [23].

An alternative solution can be using distributed Bragg reflectors DBRs to close the laser cavity and, thus, produce FP-MLLs suitable for photonic integration on InP. With this approach, the laser cavity length can be defined with lithographic precision provided that both cleaved facet mirrors are replaced by DBRs. Also, fine tuning of the free spectral range to comply with standardized wavelength grids for telecommunications can be achieved by means of current injection in the DBR section(s) [36].

Use of DBRs in combination with QDash active material may be very promising for the generation of THz-wide frequency combs on-chip. Yet, because DBR gratings are wavelength selective structures, suitable designs with large reflectivity bandwidths are needed to allow for laser amplification of such wide spectra. Moreover, the impact of DBR mirrors on the noise properties of the generated combs has to be evaluated, since grating dispersion may compromise the equidistance between longitudinal modes [179].
First investigations on these aspects are carried out in collaboration with Alcatel-Lucent-Thales III-V Lab. In this preliminary study, we consider an FP QDash laser with just a single broadband DBR, monolithically integrated with a QDash semiconductor optical amplifier (SOA). The device, designed and fabricated at III-V Lab, is characterized using the setup described in sec. 3.1.1. In this section, after a brief description of the device, we discuss its mode-locking performances and the role of SOA amplification on the latter.

Single-section QDash DBR laser for photonic integration

The investigated device is a 1-mm-long FP laser based on a 6 DBAR InAs/InP QDash structure. The component, shown in fig. 3.17, consists of three section, the two leftmost of which are connected together and constitute the actual laser, while the third one is a 1000-µm-long integrated SOA, terminated with a tilted taper and an anti-reflection coated facet. An optimized DBR with effective length of 25 µm is included on the right-hand side of the middle section, in order to close the laser cavity. The DBR grating, fabricated using a deep etch process and MOCVD regrowth according to BRS technology, is designed to have a large AC coupling coefficient [179] of about $\kappa = 400$ cm^{-1}, yielding a nominal reflectivity of 60% over a bandwidth of ≈10 nm. This pass band for the DBR is large enough to accommodate the full emission spectrum of an FP laser with as cleaved facet taken from the same material, with a measured FWHM of about 6 nm. Further information regarding the design of this structure and static characteristics of the device can be found in [b].

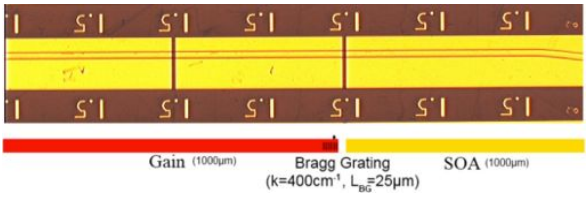

Figure 3.17 – Micrograph picture of the DBR laser integrated with a tapered SOA (Courtesy of S. Joshi, III-V Lab).

Mode-locking performances of single-section QDash DBR laser

In order to evaluate the impact of DBR on the mode-locking performances of single-section lasers, we compare the RF spectrum of the generated comb with that measured for an FP laser with as cleaved facets and similar cavity length, issued from the same QDash structure. The result of this comparison is shown fig. 3.18. In this measurement, light from the DBR laser is coupled from the left facet of the component (see fig. 3.17) and the SOA is reverse biased in order to suppress of any possible perturbations from this section. It can be observed that the RF spectrum evolution with current features wide regions of low noise in the ranges 250-360 mA and 410-480 mA, with some instability points commonly exhibited by this material. The RF linewidth in the low-noise regions is on the order of few tens to hundreds of kHz, demonstrating that the use of a broadband DBR does not compromise phase-locking in the device [b]. Also, looking at the RF mappings in fig. 3.18, similar trends for the repetition rate and linewidth are found for the FP laser with as cleaved facets, with low-noise regions just occurring at lower current than in the DBR laser. This fact indicates that these characteristics essentially depend on the specific laser material.

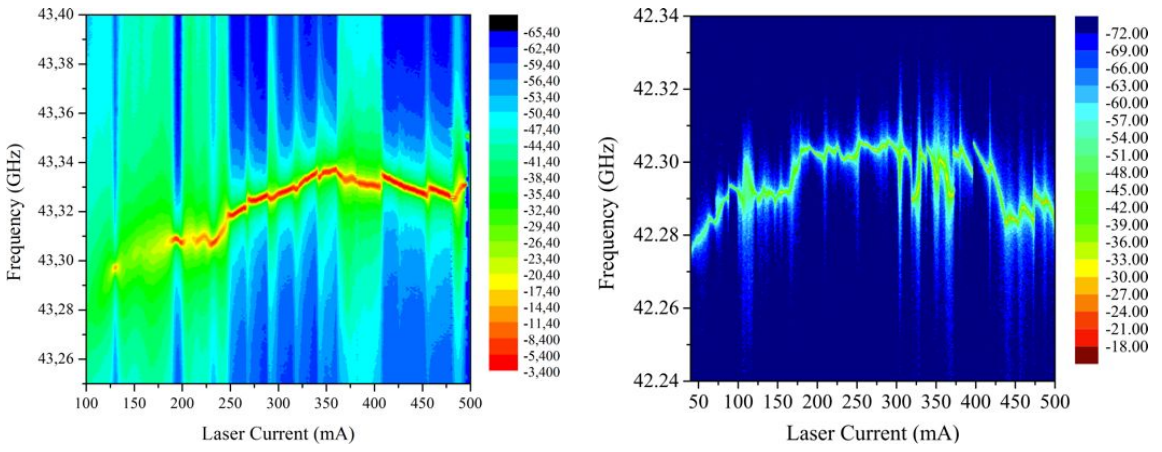

Figure 3.18 – RF spectrum mappings as a function of injection current for the DBR laser (a) and for a 1-mm-long Fabry-Perot laser with as cleaved facets from the same epitaxial structure (b).

The comb spectrum generated by the DBR laser can be amplified on-chip using the integrated SOA. To study the impact of this process, we operate the laser at 300 mA, point at which a narrow RF linewidth of ≈ 30 kHz is found, and we look at the RF spectrum as function of bias current in the SOA, as reported in fig. 3.19a. It can be noticed that both laser repetition rate and noise characteristics experience significant change upon current injection in the SOA section. This effect is attributed to the interaction of the laser emission with the ASE coming from the SOA section, in addition to chip heating due to amplifier biasing. Yet regions of effective mode-locking with narrow RF linewidth can still be found (see fig. 3.19b). For example, experimental observation indicate that, at gain saturation of the SOA for a bias current of 200 mA, low noise performances are exhibited for laser current ranges in excess of

50 mA.

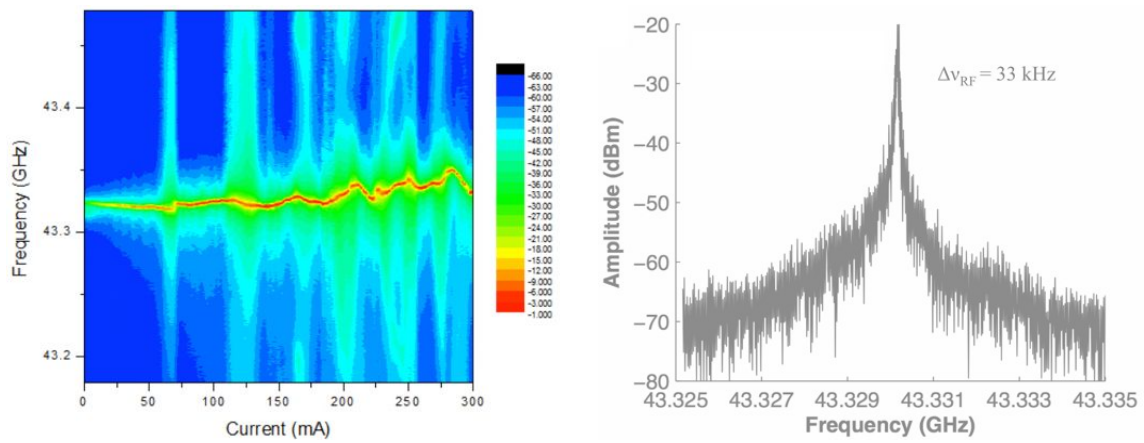

(a) (b)

Figure 3.19 – (a) RF spectrum mapping as a function of injection current in the SOA section, for a laser bias current of 300 mA; (b) RF linewidth measured for a DBR laser current of 300 mA and SOA bias of 150 mA.

Despite previous demonstration of quantum well MLLs integrated with SOAs [180, 181], these results show for the first time the generation and amplification on-chip of optical frequency combs from single-section QDash-based MLLs. Moreover, the use of DBR gratings to lithographically define the cavity length paves the way for single-section MLLs integration in PICs and makes possible additional functionalities such as the tunability of the repetition frequency [36] and the compensation of the laser intracavity dispersion if suitable DBR chirping is adopted [47, 180].

Chapter 4

Components characterization using Optical Frequency-Domain Reflectometry

In the previous chapter, we have seen that, in the absence of external compression, very broad optical pulses are emitted by single-section MLLs. Pulse broadening in these devices has been attributed by several authors to the non-negligible group velocity dispersion (GVD) of the laser cavity [4, 125], impacting also on the stability of the output pulse train [55, 182]. In order to verify whether chromatic dispersion in the laser is responsible for the large GDD values reported in sec. 3.2, this chapter is entirely devoted to GVD measurement in optical and optoelectronic components.
Because GVD is expected to play a key role in lasers, but also in other optical systems such as optical fibers [172] or microresonators [25], the problem of determining this quantity acquires a rather general significance. Suitable tools are, thus, required for the precise characterization of phase features, together with the amplitude response of optical components.

Interferometric methods, owing to their unrivaled sensitivity and versatility, appear to be the best candidates this purpose. Indeed, techniques such as white light interferometry [183] and optical low-coherence reflectometry (OLCR) [184] have already proven to be effective in determining the dispersion of both active [185–187] and passive devices [184, 188, 189]. In these approaches, phase information can be extracted from the interference fringes recorded from a Michelson interferometer with the device under test (DUT) and a scanning mirror on its arms, upon illumination by an incoherent light source. However, the need of precise alignment of free-space optical components and the use of mechanical translation stages to provide variable optical delays pose severe limitations in terms of setup flexibility and acquisition speed. To overcome these shortcomings, swept-wavelength interferometric techniques have been developed [190, 191]. Among these, optical frequency-domain reflectometry (OFDR) has proven to be a highly sensitive and flexible tool for devices characterization, as it employs a

tunable laser source (TLS) and standard fiber optics components [192, 193]. The technique has been widely used for the detection of discrete reflections and defects in optical fibers [194] and integrated optical devices [190], although few studies have been reported so far on the measurement of dispersion by OFDR [192, 195].

In this chapter, after an introduction to OFDR presented in sec. 4.1, in sec. 4.2 we investigate the spectral phase measurement capabilities of the technique by evaluating the smallest dispersion values measurable. For this purpose, and because of the unavailability of group delay dispersion (GDD) or optical phase references, we retrieve the response of a commercially available optical filter (Finisar Waveshaper 1000 S/X), for which the amplitude and phase transfer function can be precisely controlled in the C+L band (1530–1625 nm). In this study, carried out at Télécom SudParis, we show that the smallest phase features measurable by OFDR are ultimately limited by parasitic phase fluctuations, induced by environmental vibrations. Specific signatures and measurement ambiguities associated with these fluctuation are studied in more detail in sec. 4.3 in order to understand their impact on the measurements. Finally, once spectral phase characterization using OFDR is validated, in sec. 4.4 we apply this technique to the measurement of chromatic dispersion of a QDash based SOA.

4.1 Principles of Optical Frequency-Domain Reflectometry

Optical frequency-domain reflectometry OFDR is a characterization technique that consists in probing an optical component, located on one of the arms of an interferometer, with the light from a linearly tunable laser source (TLS). Interference fringes recorded by a square-law detector at the output of the system are, then, post-processed to extract information about the device under test (DUT). As this technique involves a certain number of design issues in terms of optical setup, signal processing and compensation of possible sweep nonlinearity of the TLS, these aspects are treated in more detail below.

4.1.1 OFDR setup

An implementation of an OFDR setup using fiber optic components is sketched in fig. 4.1a. The setup is essentially composed of two parts: a core part constituted by a measurement Michelson interferometer, with the device under test (DUT) in one of its arms, and an auxiliary reference Mach-Zehnder interferometer used for triggering data acquisition purposes. The light from a TLS constitutes the input of the system. In this configuration, the DUT acts as a mirror and discrete reflections from its input and output facets, as well as from any backscattering element possibly included, give rise to signal components in the detected fringes.

Alternatively, the DUT can be probed in transmission configuration using a Mach-Zehnder interferometer for the measurement path, as shown in fig. 4.1b. In this case, the technique

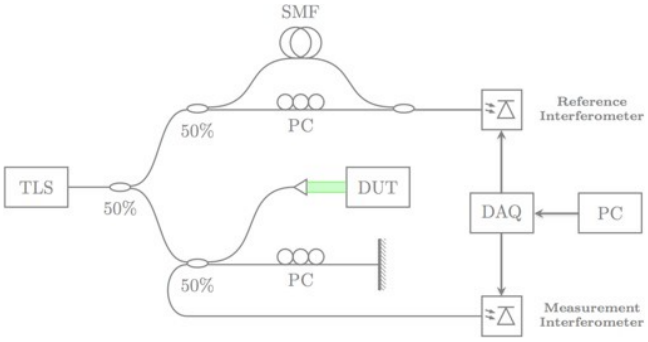

(a) optical frequency-domain reflectometry (OFDR)

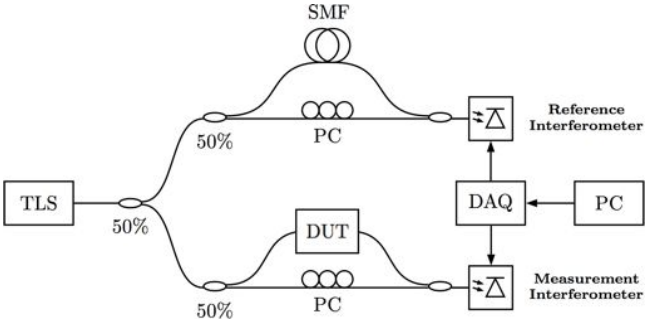

(b) optical frequency-domain interferometry (OFDI)

Figure 4.1 – Setup for optical frequency-domain reflectometry (OFDR) (a) and optical frequency-domain interferometry (OFDI) (b) using with fiber optic components.

is referred to as optical frequency-domain interferometry (OFDI). In order to gain insight into the principles of the measurement, let us consider for simplicity this last configuration. Differences with respect to the reflection configuration will be discussed further on in this section.

Assuming a time-linear frequency sweep $\nu(t) = \nu_0 + \gamma t$ of the optical source, the electric field of the laser output can be written as:

$$\mathbf{E}(t) = E_0 \, \mathrm{e}^{\mathrm{i}\,\phi(t)} \boldsymbol{\varrho} = E_0 \, \mathrm{e}^{\mathrm{i}\,2\pi[\nu_0 + (\gamma/2)t]t} \boldsymbol{\varrho}, \tag{4.1}$$

where E_0 is a constant amplitude, $\boldsymbol{\varrho}$ is a unit polarization vector, and γ is the tuning rate of the instantaneous optical frequency $\nu(t) = (1/2\pi)(\mathrm{d}\phi/\mathrm{d}t)$. After propagation through the measurement interferometer, the optical fields in the two paths of group delays τ_1 and τ_2, lead to a detector voltage given by:

$$\begin{aligned} U(t) &= U_0 \left| \mathrm{e}^{\mathrm{i}\,\phi(t-\tau_1)} + H(\nu) \, \mathrm{e}^{\mathrm{i}\,\phi(t-\tau_2)} \right|^2 \\ &= U_0 \left[1 + |H(\nu)|^2 + 2\,\mathbf{Re}\left\{ H(\nu) \, \mathrm{e}^{\mathrm{i}(2\pi\gamma\tau_0 t + \varphi)} \right\} \right] \\ &= U_0 \left[1 + A(\nu)^2 + 2A(\nu)\cos(2\pi\gamma\tau_0 t + \Phi(\nu) + \varphi) \right], \end{aligned} \tag{4.2}$$

where $\tau_0 = \tau_2 - \tau_1$, φ is a phase constant, $H(\nu) = A(\nu) \, \mathrm{e}^{\mathrm{i}\,\Phi(\nu)}$ is the transfer function of the DUT, $U_0 = \sigma E_0^2/2$ and σ depends on the detector sensitivity. Here, for the sake of clarity, assumptions have been made on the co-polarization of the optical fields from the two interferometer paths and on the polarization independence of the transfer function of

the DUT. Although these assumptions are, in general, quite strong, they are reasonable for the setup in exam. In fact, co-polarization of the interfering signals can be achieved over a wide wavelength range of several nm by adjusting the fringe visibility by means of the fiber polarization controller on one of the interferometer arms. If the two signals are not co-polarized, polarization fading of the interference fringes occurs. However, polarization-diverse detection can be used to avoid it [190, 192].

Since in eq. 4.2, the DC term $U_0(1 + A(\nu)^2)$ does not carry any useful information, it is typically neglected and fringe equation is more conveniently written as a function of the instantaneous optical frequency $\nu(t)$ as:

$$\tilde{U}(\nu) = 2U_0 A(\nu) \cos(2\pi\nu\tau_0 + \Phi(\nu) + \xi), \tag{4.3}$$

with $\xi = \varphi - 2\pi\nu_0\tau_0$. In other words, the interference fringes recorded at the output of the measurement interferometer are amplitude modulated by the amplitude transfer function of the DUT and phase modulated by its phase transfer function. By sampling fringes at constant frequency spacing $\delta\nu$ and applying fast Fourier transform (FFT) to the sampled signal, one can obtain a reflectogram with a positive frequency peak centered at the time delay τ_0. This peak contains all the information on the DUT. Additionally, a negative frequency peak at $-\tau_0$ will be present because of the hermitian properties of the FFT applied on a real signal.

If light travels along multiple paths with different lengths in the measurement arm of the interferometer, different peaks will appear in the reflectogram at the corresponding time delays. A sum of multiple sinusoids at different delay-frequencies, in fact, will be present in eq. 4.3. In addition, because of square-law photodetection (cf. eq. 4.2), beat-note terms of these sinusoids may be found, resulting in spurious peaks in the reflectogram. Their appearance is a well-known ambiguity of the technique. However, judicious choice for the reference arm of the measurement interferometer can be made to distinguish DUT signatures from these spurious peaks [190].
Occurrence of multiple peaks in the reflectogram is typical for the reflection configuration of OFDR, since at least the signals corresponding to the input and output facets of the DUT will be found. While the first signal specifies only the position of the DUT with respect to the reference mirror, the second carries information about the optical length and the amplitude and phase transfer function of the component after one round-trip. This feature can, then, be used to fully characterize the DUT, provided that information encoded in the interference fringes is suitably extracted.

4.1.2 Digital signal processing for information extraction

Given the reflectogram for the recorded fringes, digital signal processing (DSP) is performed in order to retrieve the amplitude and phase response of the DUT. For this purpose, as first step, the negative frequencies part of the reflectogram is suppressed by setting the corresponding data points to zero (or, equivalently, after an Hilbert transform). Then, assuming that the

DUT peak is localized at τ_0 (in time domain), a digital band pass filter centered at τ_0 is applied both to isolate the peak and to reduce as much as possible the white noise (shot-noise plus dark-noise contribution) generated by the detector. Finally, the filtered data set is inverse Fourier transformed and extraction of $A(\nu)$ and $\Phi(\nu)$ can be performed from the analytic signal of the fringes.
It is worth noting that the employed digital filter width and shape influence, in the spectral domain, both the sharpness and the noise level of the retrieved amplitude and phase transfer functions: the larger the filter width, the sharper and noisier the transfer functions will be, and vice-versa.

Concerning the retrieval of amplitude transfer function of the DUT, this does not present particular difficulties and it is achieved by extracting the envelope of the fringe analytic signal. On the other hand, spectral phase response extraction starting from the argument of the analytic signal is more delicate and requires additional signal processing. In fact, since the DUT signal is centered at τ_0 in time domain, a rapidly growing linear phase profile is expected for the computed $\Phi(\nu)$. This is a direct consequence of the Shift Theorem of the Fourier transform, which states that a translation in the time domain corresponds to a linear phase factor in the frequency domain. Therefore, subtraction from the unwrapped phase data of the first-order polynomial fit to the data, corresponding to this linear phase factor, is performed in order to isolate the phase response of the DUT.

Furthermore, for the sake of precision, it is important to remark that not only the phase response of the DUT is encoded in the fringes, but also the GDD of the optical components that constitute the measurement setup itself. So, in order to precisely determine the phase transfer function of the DUT, the GDD of the setup should be estimated and subtracted from the measured phase profile.
For OFDI characterizations in transmission configuration (cf. fig. 4.1b), this can be done by performing a two step measurement: one with the DUT and the other without, and extracting the setup GDD and the overall phase profile using the procedure described above. For measurements in reflection configuration, instead, only one acquisition step is needed. In this case, reflection peaks in the reflectogram corresponding to the input and the output facet of the DUT can be separately used, respectively, to determine the setup contribution and the overall phase profile for one round-trip in the DUT.

4.1.3 Nonlinear frequency sweep of the tunable laser source

In deriving the equations governing OFDR/OFDI and the signal processing procedure used to extract amplitude and phase information, assumptions have been made concerning the time-linear frequency sweep of the TLS and interferogram sampling at constant frequency spacing. In practice, the frequency sweep of TLSs may strongly deviate from linearity, so ad hoc techniques are introduced to ensure interferogram sampling at constant frequency spacing. Methods typically adopted for this purpose involve the use of an auxiliary interferometer

to estimate the time-dependent sweep rate of the laser $\gamma(t)$ and compensate for its effect (see Fig. 4.1b). The simplest and most popular way of doing that consists in using the frequency-periodic output of the auxiliary interferometer (cf. eq. 4.3) as trigger signal for sampling the fringe pattern from the measurement interferometer [190, 192]. This technique allows for fast data acquisition and real-time analysis. However, it is commonly admitted that this method is not necessarily the best choice when measuring phase features [195].
In alternative, a different technique consists in sampling with a standard time-domain sampler the output of both interferometers and subsequently performing a numerical resampling at constant frequency spacing of the measurement interferogram, based on the time dependent sweep rate $\gamma(t)$ measured from the auxiliary interferometer fringe pattern [196]. Compared to the first method, this approach offers a better control of phase information, at the expense of an oversampling of the interferograms and a heavier digital signal processing of the acquired data and it is preferred for our purposes.

4.2 Spectral phase measurement by Optical Frequency-Domain Interferometry

We observe from the previous sections that a large number of filtering steps are to be applied before data exploitation. As their impact on device characterization has not been fully studied in literature yet, here we aim at determining what are the smallest phase features accurately measurable by OFDI and which factors actually limit the measure. For this purpose, we avail ourselves of a high sensitivity OFDI setup, developed at Télécom SudParis, and we use as DUT a commercial optical filter, the Finisar Waveshaper 1000 S/X, programmable in attenuation and phase over the C+L band. Retrieval of the complex transfer function of the filter will, then, be used to qualify the measurement capabilities of OFDI.
Accordingly, in this section we describe the working principle of the programmable filter and the measurement strategy adopted for our purposes. Next, we discuss the spectral phase measurement capabilities of OFDI, focusing in particular on parabolic profiles corresponding to nonzero group delay dispersion.

4.2.1 Use of programmable optical filter as phase reference

The programmable optical filter Finisar Waveshaper 1000 S/X, used as reference DUT in the OFDI setup, is a commercial device that can produce user-defined filter shapes with arbitrary amplitude and phase profiles with resolution down to 1 GHz and minimum filter bandwidth down to 20 GHz. Its operating principle is based on the concept of *4-f Pulse Shaper*, first introduced by Froehly, *et al.* in 1983 [197] and depicted in Fig. 4.2. The latter consists in angularly separating the spectral components of the incoming signal by a first grating and focusing each of them to small diffraction spots in the Fourier plane by a lens. In this plane, a suitably patterned mask can be used to induce optical path length and/or optical density

changes for the spatially dispersed spectral components. Shaping of the output waveform is, then, achieved by recombining the spectral components by a second lens and grating. Such a waveform will result from the mapping of the Fourier transform of the mask pattern onto the output spectrum.

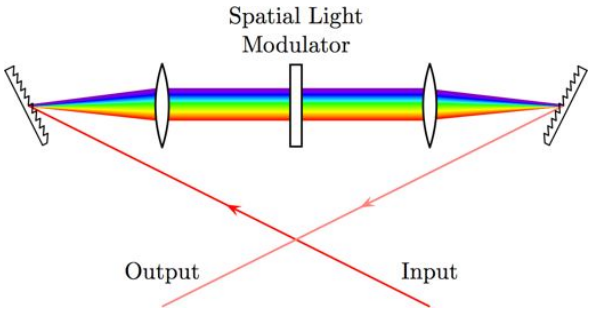

Figure 4.2 – Schematic of the *4-f Pulse Shaper* concept.

In the optical filter under consideration, the spatial mask is implemented using a programmable liquid crystal modulator array on a silicon substrate (LCoS – Liquid Crystal on Silicon) providing independent control over spectral amplitude and phase profiles. A polarization diverse optics is used to separate and align the orthogonal polarization states of input field to match the high efficiency *s*-polarization state of the diffraction grating and, thus, reduce the polarization-dependent loss of the device. For more details about the implementation and the application in optical fiber communications of this class of LCoS programmable optical processors, the interested reader is referred to [198] and [199].

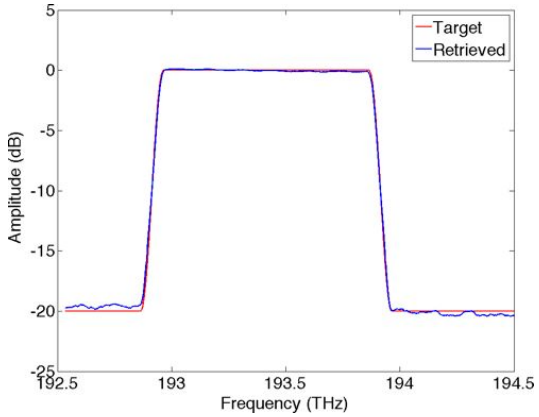

Figure 4.3 – Measured transfer function of a 1 THz bandwidth bandpass filter generated with the Waveshaper (blue), in comparison with the programmed filter shape (red).

In the present study, we take advantage of the capabilities of the Waveshaper by programming suitable filter transfer functions and by retrieving them using the DSP procedure described in sec. 4.1. More specifically, we use 1 THz bandwidth bandpass filters having a parabolic phase response only in the pass-band. OFDI performances are, then, evaluated in terms of the minimum slope of the parabola detectable.
The amplitude profile of the filters programmed on the Waveshaper, compared with that

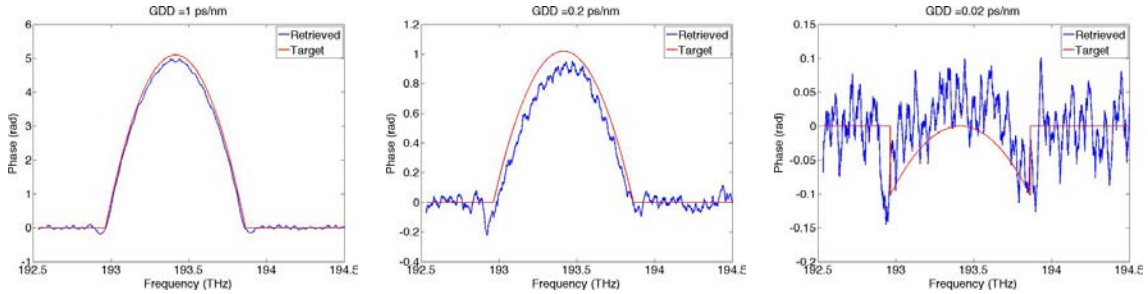

(a) GDD = 1 ps/nm (b) GDD = 0.2 ps/nm (c) GDD = 0.02 ps/nm

Figure 4.4 – Examples of group delay dispersion measurements for different values of GDD.

measured by OFDI, is shown in fig. 4.3. This comparison is used here to estimate the instantaneous optical frequency of the TLS along the fringes, since no other calibration tools were available at the time of the measurement. Yet, despite the inaccuracy of this approach compared to more advanced calibration methods [191, 193], valuable conclusion can be drawn regarding spectral phase characterization, as it is shown in the following.

4.2.2 Measurement of group delay dispersion

The capability of OFDI of measuring group delay dispersion is here evaluated using the bandpass optical filters described above. As outlined in sec. 4.1, the phase response of the filters is retrieved from the argument of the fringes analytic signal after a number of processing steps. First of all, the cumulated delay (or, equivalently, the linear phase factor) due to light propagation in measurement interferometer is systematically cancelled out. Then, estimation and compensation of the setup group delay dispersion by means of polynomial fit to the phase data set corresponding to the filter stop-band is performed. Finally, the measured phase profile is compared with that programmed on the Waveshaper.
The result of this comparison for GDD values of 1, 0.2 and 0.02 ps/ns is shown in fig. 4.4. It can be noticed that for large values of dispersion the retrieved phase profile accurately reproduces the programmed one. On the other hand, when the dispersion decreases the impact of noise on the measurement becomes more important. Yet, small GDD values down to 20 fs/nm can be measured over a relatively narrow optical bandwidth of 1 THz.

As the shallowest parabolic phase profile observed over a given bandwidth depends on the level of noise encoded in the fringes, special attention is paid to this quantity. We observe, in particular, that even though the noise can be reduced by using a narrower digital filter to isolate the DUT peak in the reflectogram, a wider oscillatory behavior will occur for the retrieved phase response, as a result of the tighter filtering. Also, we notice that, for digital filters exhibiting the best tradeoff in terms of noise rejection and phase distortion, fluctuations impacting on dispersion measurements are not white. Indeed, a periodical oscillation seems to be superimposed to the parabolic phase related to the programmed GDD, as shown for example in fig. 4.4. As this behavior plays an important role in GDD measurement, the origin

of these fluctuations needs to be be more carefully identified and this is studied in the next section.

4.3 Dynamical aspects of OFDI measurements

4.3.1 Experimental facts

In order to gain more insight into the physical properties of the fluctuation observed in the measurements reported in the previous section, further OFDI characterizations have been performed as a function of the TLS sweep rate. Figure 4.5 shows the phase profiles and the reflectograms recorded for an all-pass filter shape with a flat phase response, at nominal sweep rates of 10 and 20 nm/s.

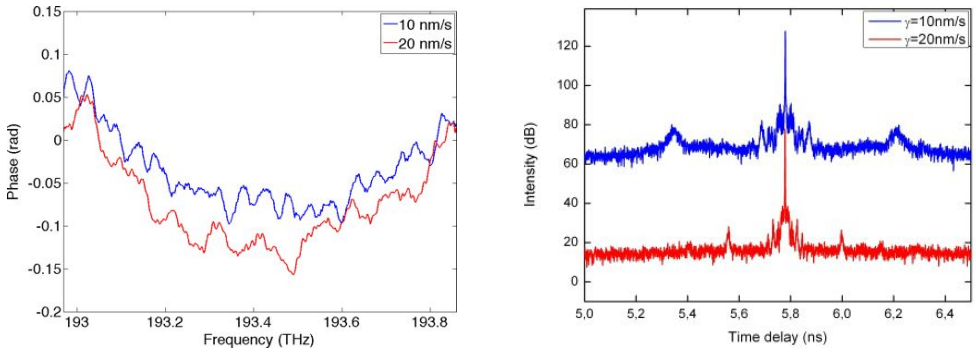

Figure 4.5 – (a) Spectral phase measurements and (b) corresponding reflectograms for nominal sweep rates of 10 and 20 nm/s.

From fig. 4.5 two main features can be observed. First of all, the average phase variation over the optical frequency range of the measurement is parabolic. This can be attributed to GDD of the OFDI setup, as explained in sec. 4.1. In the second instance, the fluctuations superimposed on the parabolic phase profile (see fig. 4.5a) seem to be almost periodical. More importantly, their periods manifest to be highly dependent on the TLS tuning rate. At the same time, two symmetric sidebands are observed on both side of the main peak on the corresponding reflectograms (see fig. 4.5b). Their positions are influenced by the tuning rate of the TLS, with a separation relatively to the central peak that decreases when the sweep rate γ is increased.

These experimental results suggest that the sidebands observed in time-domain as well as the period of the recorded phase fluctuations in spectral domain are closely related one another. Furthermore, since their different characteristics depend on the TLS tuning rate, and consequently, on the time needed to perform an OFDI data acquisition, it becomes clear that the experimental conditions are changing over the data acquisition.

4.3.2 Theoretical interpretation

A phase modulation of light during its transmission through the DUT is a possible hypothesis that can explain the previous observations. To clarify this affirmation, and in complement to usual assumptions that are implicitly imposed when analyzing OFDR signals, we consider in the following the situation in which the DUT, or part of the OFDI setup, has characteristics that may vary over time. In other words, dynamical aspects occurring during the OFDI data measurement are here specifically addressed.
To do so, eq. 4.2 is reviewed assuming now that the time delay $\tau = \tau_2 - \tau_1$ is not constant anymore but it can change over time. In particular, we consider

$$\tau(t) = \tau_0 + \Delta\tau(t), \tag{4.4}$$

where τ_0 is the time delay of the OFDI measurement interferometer in the absence of perturbations, while $\Delta\tau(t) \ll \tau_0$ is a perturbation term that represents the time deviation from the static condition needed for the light to propagate in the OFDI measurement interferometer.

This formulation is quite general and well-suited to describe the effect induced by different physical phenomena, such as the refractive index variations due to temperature or strain fluctuations in the fibered interferometer, or coupling of mechanical perturbations to the DUT properties. In order to simplify the mathematical study of this situation, a DUT with a flat phase $\Phi(\nu)$ and amplitude $A(\nu)$ response is considered. This choice corresponds to a device that introduces neither extra time-delay nor amplitude distortion (in agreement with experimental conditions of measurements reported in fig. 4.5). Following the derivation reported in eq. 4.2 and using the definition in eq. 4.4, the interference fringes become,

$$\tilde{U}(t) = 2AU_0 \cos\left[2\pi\gamma\tau_0 t + 2\pi(\nu_0 + \gamma t)\Delta\tau(t) + \varphi\right], \tag{4.5}$$

where φ is the same phase constant as in equation 4.2. If we rearrange equation 4.5 to take into account the impact of variations of $\tau(t)$ with time by further considering $\nu_0 \gg \gamma t \gg \gamma\tau_0$, as we only address the case of a perturbation, equation 4.5 becomes:

$$\tilde{U}(t) = 2AU_0 \cos(2\pi\gamma\tau_0 t + \Phi_m(t) + \varphi), \tag{4.6}$$

where

$$\Phi_m(t) = 2\pi\nu_0\Delta\tau(t) = 2\pi\frac{\nu_0}{c}x(t) \tag{4.7}$$

and $x(t)$ represents the optical path change caused by external perturbations.

A close examination of the phase of equation 4.6 reveals two distinct physical contributions. The first one (i.e. the term that varies linearly with time) corresponds to the relative time delay caused by the propagation of light in the OFDI interferometer under static conditions. The second term ($\Phi_m(t)$) corresponds to dynamical contribution of the interferometer. It is important to remark that, since the optical path difference of the two arms of the interferometer is not constant by definition, light passing through the interferometer will be affected by Doppler effect and the time-varying instantaneous optical frequency of the TLS will experiences an

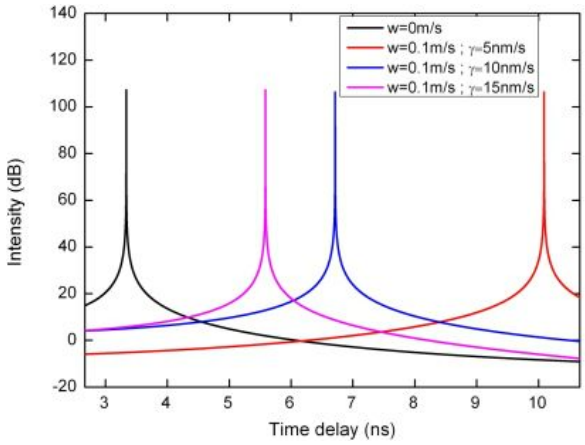

Figure 4.6 – Reflectograms simulated in the case of constant increase of the optical path length difference with a speed of $w = 0.1$ m/s for TLS sweep rates of 5,10, and 15 nm/s.

additional spectral shift. Using eq. 4.7, the signatures of Doppler effect on OFDI measurement can be conveniently modeled and studied.

4.3.3 Constant Doppler effect during OFDI data acquisition

In this section, we consider the most common situation when dealing with Doppler effect, that is when the optical path length linearly changes over the measurement time. In this case, a constant Doppler frequency shift is expected for the light that propagates through the measurement interferometer of the OFDI setup. This situation is modeled by imposing that $x(t)$ in eq. 4.7 varies linearly with t, i.e. $x(t) = wt$, where w is the rate of change of the optical path length, expressed in m/s.

Figure 4.6 shows the simulated reflectograms, obtained for two different values of the velocity w and four different tuning rates γ of the TLS, after Fourier transformation of eq. 4.6 and 4.7. In the simulations, the parameter τ_0 is set to 3.3 ns, as can be observed from the curve for $w = 0$. It can be noticed that, when Doppler effect is introduced in the simulations (by setting here $w = 0.1$ m/s), the position of the reflectometer peak is shifted from its nominal position by an amount that strongly depends on the tuning rate parameter γ. In particular, the higher the tuning rate, the lower the shift of the reflectogram peak. From the analytical expression in eq. 4.6, the peak shift is calculated to be $\Delta = \nu_0 w/c\gamma$.

The simulations reported in fig. 4.6 show that ambiguities on the optical path length can be encountered when exploiting the OFDI/OFDR reflectogram data. Indeed, in addition to the ambiguities already identified in [190], we note that a full exploitation of reflectogram abscissa requires some extra knowledge on possible Doppler effects present when the measurements are performed. In particular, when the DUT is subject to dynamical phase variation (as, for example, in the case of phase modulators), special care must be taken when exploiting its signature in OFDR reflectogram.

4.3.4 Non-constant Doppler effect during OFDI data acquisition

In this section, we examine the most general situation where Doppler effect is not constant during OFDR data acquisition. To this end, let us consider a pure harmonic perturbation described by setting in eq. 4.7 $x(t) = x_m \sin(2\pi\nu_m t)$, where x_m is the amplitude of the phase perturbation and ν_m its frequency. In this case, by applying the Jacobi-Angers identity

$$e^{i\,x\sin\phi} = \sum_{n=-\infty}^{+\infty} J_n(x)\, e^{i\,n\phi} \tag{4.8}$$

to eq. 4.6 written in complex form as

$$\tilde{u}(t) = 2AU_0\, e^{i(2\pi\gamma\tau_0 t+\varphi)}\, e^{i\,\frac{2\pi\nu_0}{c}x_m \sin(2\pi\nu_m t)} \tag{4.9}$$

and taking the real part, the temporal evolution of the signal recorded by the detector can be expressed with a series of Bessel functions of the first kind, as:

$$\tilde{U}(t) = 2AU_0 \sum_{n=-\infty}^{+\infty} J_n\left(\frac{2\pi x_m}{\lambda_0}\right) \cos\left[2\pi(\gamma\tau_0 + n\nu_m)t + \varphi\right], \tag{4.10}$$

where $\lambda_0 = c/\nu_0$ is the wavelength of the TLS. In fig. 4.7a the reflectogram obtained after a Fourier transform of eq. 4.10 and simulated for different values of γ are shown. It can be noticed that, when x_m is set to 0 (i.e. no Doppler effect is simulated), only one peak is present in the reflectogram. On the other hand, when $x_m \neq 0$ (i.e. in the case of pure harmonic perturbation), multiple side-peaks, regularly spaced from the main central peak are observed in the simulated OFDI reflectograms. More precisely, the position of the n-th peak is separated from the central peak by $n\nu_m/\gamma$ and its intensity is proportional to $J_n(2\pi x_m/\lambda_0)$, as indicated by eq. 4.10. When OFDI data are represented in the spectral domain, i.e. after an inverse Fourier Transform of the reflectogram, the retrieved phase profile appears to be frequency-modulated, with a modulation period that strongly depends on the tuning rate of the TLS, as shown in fig. 4.7b.

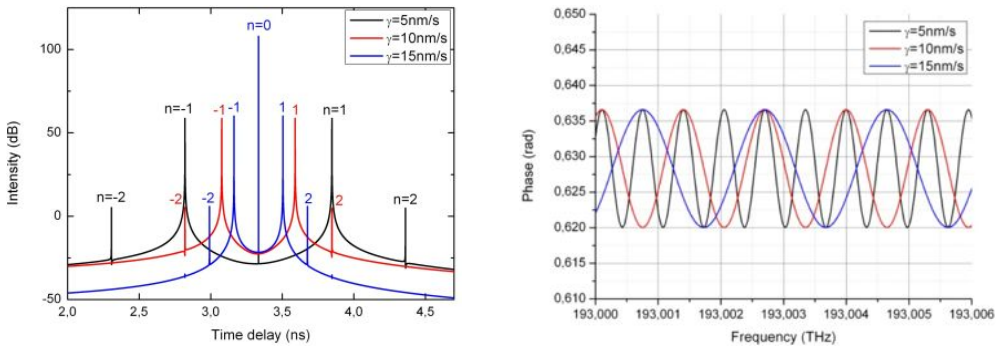

Figure 4.7 – (a) Reflectograms and (b) spectral phase profiles simulated in the case of sinusoidal variation of the optical path difference with amplitude $x_m = 1$ nm and frequency $\nu_m = 1$ kHz, for TLS sweep rates of 5,10, and 15 nm/s.

It is worth to note that, although the previous formulation may appear very specific and

restricted to the case of pure harmonic modulation, it is indeed very general and it can be easily extended to the case of non-periodic modulation by virtue of the spectral decomposition by means of the Fourier transform.

We would like to stress that, because of the high sensitivity S and dynamic range D of OFDI measurements (in our case evaluated at $S = -125$ dB and $D = 80$ dB, respectively) and because of Bessel functions properties, phase perturbation of extremely low amplitude x_m (compared to the TLS wavelength) or faint temporal evolution the phase of the DUT can be detected by OFDI. We also further insist on the fact that, without any precise knowledge on the temporal phase characteristics of the DUT, the interpretation of reflectogram peaks, as well as their phase, can be ambiguous. In fact, without any a priori assumption on the nature of the reflectogram peaks, the different side peaks observed in experimental results or simulations can be attributed either to specific reflections in the DUT or to Doppler effect. Nonetheless, the symmetric structure of the modulation sidebands with respect to a central, main peak and the tuning rate dependence of the position of the sidebands allow for an easy and fast discrimination of Doppler effect related peaks and reflections in the DUT. This feature enables new applications of OFDR/OFDI for the characterization of the dynamical properties of devices. In addition, as independent fluctuations acting on different reflectors along the beam path will give rise to different modulation sidebands on both sides of the respective reflection peaks in the reflectogram, OFDR allows the characterization of the temporal phase of multiple target in the direction of the probe beam.

We finally note that the simulations carried out are well suited to interpret the experimental results reported in fig. 4.5. In particular, they show that one or more sources of technical noise, inducing phase fluctuations on the OFDI measurement by virtue of the Doppler effect, was present in the environment of the setup or in proximity to the optics of the programmable filter, during the experiments. We believe that the vibrations induced by the cooling fan of the Waveshaper may be responsible for the fluctuation observed, as noise sidebands as those shown in fig. 4.5b disappear when the component is not present. Still, the amplitude of the variation of optical path difference between the two arms of the OFDR measurement interferometer is rather small, as indicated by the relative amplitude of the modulation sidebands with respect to the main reflectogram peak. These measurements confirm the potential of OFDR/OFDI technique for the characterization of microscopic optical path length variation and of the dynamical properties of devices.

4.4 Dispersion measurement of a quantum dash based semiconductor optical amplifier

Once the dispersion measurement capabilities of OFDR/OFDI are verified and its limitation identified, the technique is applied to the characterization of the chromatic dispersion of a QDash based semiconductor optical amplifier (SOA). The component is preferred to a laser

diode with the same material as the light emitted from the latter and coupled into the OFDR setup can potentially perturb the measurement. Additionally, the injection of the TLS light into the laser cavity would modify its properties, leading to results that would be difficult to interpret. Yet conclusions on the role of material dispersion on the chirp of single-section MLLs can be drawn, based on the GDD values measured by OFDR for the QDash SOA.

4.4.1 SOA characterization by OFDR

A 2-mm-long semiconductor optical amplifier based on a 9 DBAR InAs/InP QDash structure is characterized using OFDR setup in reflection configuration (see fig. 4.1a). The component, fabricated at III-V lab using BRS technology, consists of a buried ridge waveguide, tilted by $\approx 7^{\circ}$ with respect to the cleaved facets and terminated on both sides by integrated tapers for efficient light coupling. Antireflection (AR) coatings on the SOA facets are used to prevent laser emission from the device at large injection currents. As usual, the sample is mounted on a copper base for thermal management purposes and wire bonded for ease of testing.
The device, sitting on a copper heat sink temperature controlled at 20°C, is operated under CW current injection using a commercial current source (Keithley 2400). Coupling of light into and from the SOA is achieved using a hemisphere-lensed fiber, as described in sec. 3.1.1 although this time no automated alignment control system was employed. Indeed, the fast acquisition of OFDR does not require such a feedback loop and, more importantly, the coupling fluctuations associated with this system may impact on spectral phase retrieval.
Owing to the setup sensitivity to environmental vibration, noisy electronic equipments are physically separated from the optical setup, placed on a floating table. For SOA characterization the TLS sweep rate is set to 20 nm/s and the start wavelength to 1520 nm, as the maximum of ASE spectrum of the device occurs around 1530 nm. Under these conditions, 1.3 millions of samples from the interference fringes produced at the photodetectors of both measurement and auxiliary interferometers are recorded using a 700 kSa/s sampler. Digital resampling of the main interferometer fringes is, finally, performed for compensation of TLS sweep nonlinearity prior to signal exploitation.

The reflectograms obtained for different values of the injection current into the SOA are shown in fig. 4.8. It can be noticed that all the measurements include three main peaks, indicated in fig. 4.8 by arrows. The two leftmost of them have a constant intensity in all curves and correspond to discrete reflections from the coupling fiber, as we have verified with measurements in the absence of the SOA, like the one shown in fig. 4.9. More specifically, while the second peak is associated with the tip of the coupling fiber, the first is most likely due to light scattering from the fusion splicing used by the producer to include the hemisphere lens. As for the third peak, this is associated to the output facet of the SOA and contains all the information regarding round-trip light propagation into the component. Indeed, one can observe that its intensity increases with current, indicating TLS light amplification in the device.

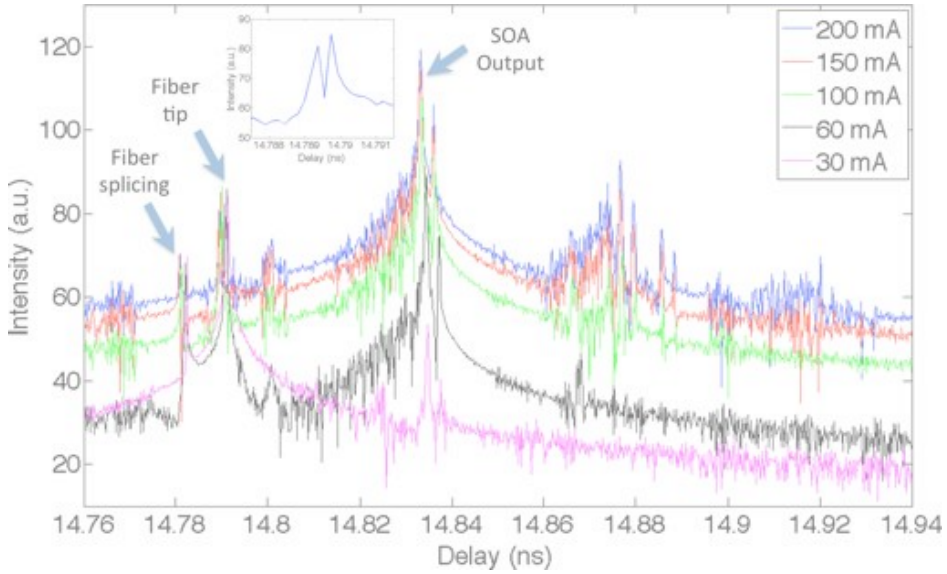

Figure 4.8 – Reflectograms measured for the QDash based SOA as function of injection current. Peaks corresponding to fiber splicing, lensed fiber tip and SOA output facet are indicated by arrows. In the inset: magnification of the reflectogram curve for $I = 150$ mA around the peaks corresponding to lensed fiber tip. A second peak representative of the SOA input facet is readily identifiable.

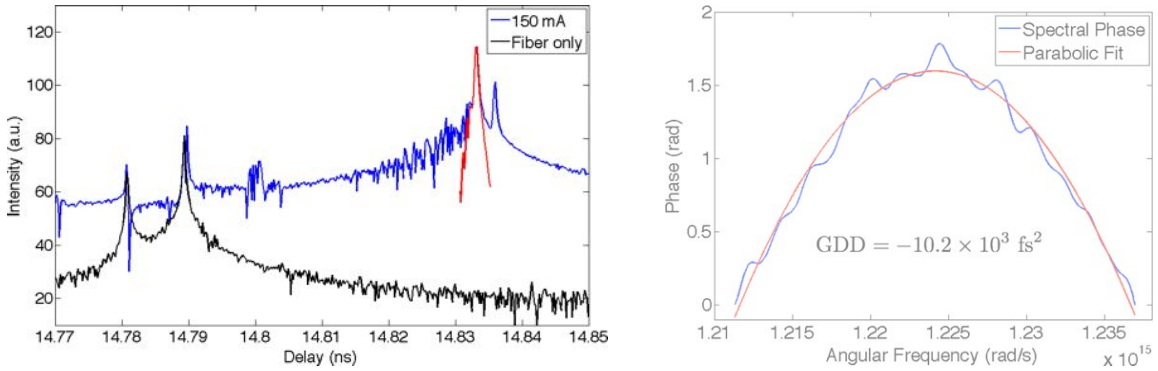

Figure 4.9 – Example of GDD extraction for SOA current of 150 mA. (a) Reflectograms measured with (blue) and without (black) the SOA. Peak filtering using Hamming window is highlighted in red. (b) Retrieved phase response plus parabolic fitting for GDD extraction.

A close inspection of the reflectograms also allows to identify the peak corresponding to the input facet of the SOA. This is located in the close proximity of the second peak, representative of the reflection from the tip of the lensed fiber, as shown in the inset of fig. 4.8. Additionally, on the right hand side of the reflectogram, some broad features are noticeable. These are most likely imputable to the combined effect of multiple round-trips into the SOA and AR facet coatings. Although valuable information can, in principle, be extracted from these features, in the following we focus on the three main peaks discussed above for our study on dispersion.

In order to evaluate the GDD arising after a round-trip into the SOA, one should subtract the parabolic spectral phase profile encoded in the input peak from that included in the output peak. However, we have observed that the phase profile extracted from the input peak is far from being parabolic. In fact, in all measurements, a prominent phase shift is present

in the middle of the trace, probably because of the air/device interface. Therefore, instead of referring the phase response of the SOA to its input facet, we calculate it with respect to the phase profile encoded in the first peak of the reflectogram. Then, in order to deduce the actual GDD of the SOA, we determine and subtract the spectral phase resulting from round-trip light propagation in the segment comprised from the splicing to the fiber tip. For that we use a reference measurement carried out without the component.
An example of GDD extraction for an SOA current of 150 mA is shown in fig. 4.9. As highlighted in fig. 4.9a, the SOA and fiber peaks are individually filtered in the digital domain using N-points Hamming window functions

$$w(n) = \alpha - \beta \cos\left(\frac{2\pi n}{N-1}\right), \tag{4.11}$$

with $\alpha = 0.54$, $\beta = 1 - \alpha = 0.46$, as they provide a good tradeoff between resolution and spectral leakage. Phase profiles are then deduced from the respective analytic signals. The DUT phase response, calculated as described above, is fitted to a parabolic curve and GDD is measured from the second derivative of the spectral phase with respect to angular frequency (cf. eq. 1.24). For all the SOA currents considered here, a negative concavity is observed for the parabolic phase response of the device, indicating anomalous dispersion. In all the measurements a GDD of about -10×10^3 fs^2 is found, with no significant trend as function of injection current. This corresponds to an anomalous group velocity dispersion (GVD) of about -2.5×10^3 fs^2/mm for the QDash material in exam.

4.4.2 Discussion

The GDD value of -10×10^3 fs^2 measured after a round-trip light propagation in the QDash SOA compares well with data reported in literature for other semiconductor materials [187,200]. On the other hand, the anomalous dispersion in QDash material suggests that chromatic dispersion cannot be the cause of the large normal GDD observed for the signal emitted by single-section MLLs. Also, even assuming that positive GVD occur in semiconductor materials, values on the order of that reported here are too small to produce pulse broadenings like those described in chapter 3.
Concerning research on single-section MLLs, our results indicate that the origins of large blue-chirp in these components should be searched into the specific laser dynamics, rather than in material dispersion. Conversely, from the instrumentation point of view, these findings indicate that small spectral phase features can be identified and characterized by OFDR/OFDI. The technique appears well suited for accurate characterization of passive, as well as active optical components. Moreover its sensitivity to Doppler effect open the way for new device characterization possibilities.

Chapter 5

Single-section mode-locked lasers for high capacity transmission links

Extending the capacity of optical networks with minimal increase of costs and energy consumption has become a high-priority task in order to support the current growth of Internet traffic. As transmission bottlenecks approach data centers and metro/access networks, use of wavelength division multiplexing (WDM) and advanced modulation formats in these systems appears to be more and more attractive [201]. Yet the need of tens of single-frequency, wavelength-stabilized distributed feedback (DFB) lasers to produce optical carriers for WDM constitutes a severe limitation for the deployment of this technology. A promising solution to this problem consists in replacing a multitude of DFB lasers with a single optical frequency comb (OFC) generator, providing many equally-spaced wavelength channels [33]. Using OFCs from solid-state mode-locked lasers and nonlinear microresonators, multiple terabit per seconds data transmissions have been achieved with advanced modulation techniques [30, 202, 203]. The technologies employed in these experiments, however, appear too complex to be practically implemented in cost and power consumption sensitive systems, such as for example data centers.
For these communication scenari, competitive technologies capable of high data rate transmissions over relatively short links (tens of kilometers down to hundreds of meters) are needed. In this sense, intensity modulation of laser light and direct detection are preferable over complex electric field modulation and coherent detection. The latter, in fact, despite their high sensitivity, pose stringent requirements on the optical linewidth and require a separate laser at the receiver side to act as local oscillator for optical amplitude and phase retrieval.

In this chapter, we study the use of direct detection orthogonal frequency division multiplexing (DD-OFDM) modulation in combination with OFCs from single-section MLLs for optical interconnects. Orthogonal frequency division multiplexing (OFDM) technique for optical communications, having received particular attention in recent years owing to its high spectral efficiency and its tolerance to chromatic dispersion, is introduced in sec. 5.1. Then, transmission experiments carried out in the framework of the EU BIG PIPES project in

collaboration with Dublin City University (DCU) are presented in sec. 5.2. Overall capacities up to 400 Gb/s using QW lasers and in excess of 2 Tb/s (with a potential for 4 Tb/s and more) using QDash MLLs are demonstrated.

5.1 Orthogonal Frequency Division Multiplexing for optical communications

OFDM is a nowadays established modulation technique, widely employed in both wired and wireless communication systems (WiFi, WiMAX, LTE, UWB, ADSL), as well as in radio and television broadcasting standards (DAB+, DVB). In this section we provide a brief introduction to OFDM technique and its use in optical telecommunications. A more detailed presentation of the subject can be found e.g. in [204, 205].

5.1.1 OFDM basics

Orthogonal frequency division multiplexing is a modulation scheme that consists in transmitting data on multiple carrier frequencies simultaneously. Although the basic principle of this technique is analogous to that of frequency division multiplexing (FDM) or its optical counterpart WDM, the concept behind OFDM is fundamentally different. While in FDM/WDM the spectra of signals modulated on different carriers are not allowed to overlap and suitable guard bands have to be envisaged for analog filtering, in OFDM carrier frequencies are selected to be mathematically orthogonal among them, so that spectral overlapping can be used to improve bandwidth efficiency (see fig. 5.1). Digital filtering at the receiver can then be used to demodulate each channel without interference.
Orthogonality among frequency carriers can be obtained by imposing that the latter are integer multiples of a fundamental frequency $f_0 = 1/T_0$. In this case, in fact, the following relation holds true for any $m, n \in \mathbb{Z}$, with $m \neq n$:

$$\frac{1}{T_0} \int_{-\frac{T_0}{2}}^{\frac{T_0}{2}} \sin(2\pi m f_0 t) \cdot \sin(2\pi n f_0 t)\, \mathrm{d}t = 0, \tag{5.1}$$

indicating that crosstalk among subcarriers can be eliminated.

The most efficient way of generating orthogonal subcarriers for OFDM is to take advantage of the fast Fourier transform (FFT) algorithm. In most OFDM system, an inverse FFT (IFFT) is implemented at the transmitter to modulate data, while forward FFT is used at the receiver for demodulation. Denoting with N the size of FFT/IFFT and with X_k, $k = 0, \ldots, N-1$ the Fourier coefficients, the time-domain OFDM signal generated at the transmitter side can be written as:

$$x_l = \frac{1}{\sqrt{N}} \sum_{k=0}^{N-1} X_k \exp\left(\frac{j2\pi kl}{N}\right) \qquad \text{for } l = 0, \ldots, N-1. \tag{5.2}$$

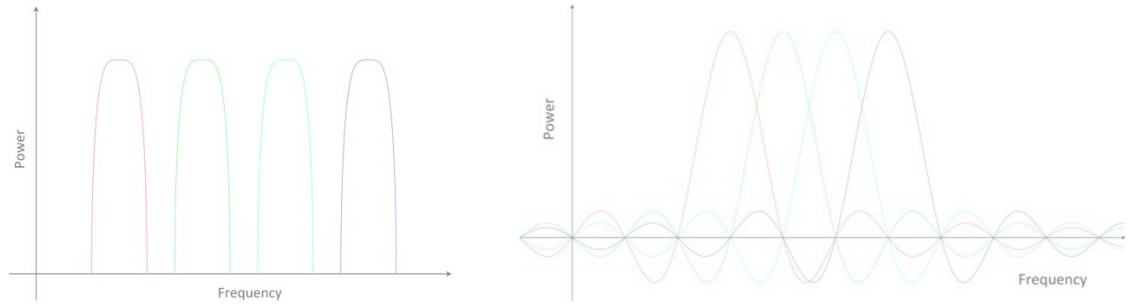

(a) FDM (b) OFDM

Figure 5.1 – Modulated spectra of (a) frequency division multiplexing (FDM) and (b) orthogonal frequency division multiplexing (OFDM).

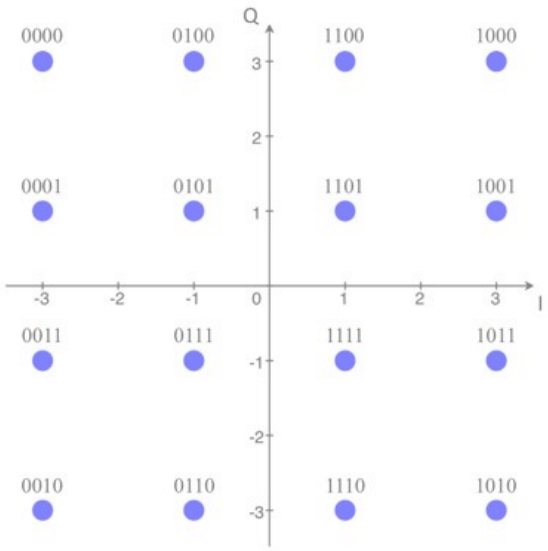

Figure 5.2 – Example of mapping between groups of bits and numbers in the complex plane for 16-QAM modulation format. Gray code is used in the 16-QAM constellation to facilitate error correction at the receiver.

The X_k in eq. 5.2 are complex number associated with the data to be transferred. In case quadrature amplitude modulation (QAM) is used, as typical for OFDM, suitable mapping between groups of bits and complex numbers is performed prior to IFFT computation, as illustrated in fig. 5.2 for 16-QAM. Eq. 5.2 shows that data encoded in the X_k symbols are transmitted simultaneously over N orthogonal frequencies at multiples of $1/N$. Each time-domain sample x_l, in fact, is constructed from N samples associated with the X_k symbols and transmission of the latter is completed only after the N-th sample is sent. This means that, if symbols X_k are generated at a rate R_{sym}, OFDM symbols $\boldsymbol{x} = [x_0, x_1, \cdots, x_{N-1}]^T$ are transmitted at a rate $R_{\text{ofdm}} = R_{\text{sym}}/N$. Therefore, for the same total data rate, lower symbol rates are found for OFDM compared to standard serial modulation techniques, such as for example non-return-to-zero (NRZ).

This last feature allows for a significant simplification of equalization functions needed to eliminate the ISI caused by channel dispersion, as in typical OFDM systems the latter influences at most one symbol [204]. The standard way of compensating for dispersive effects

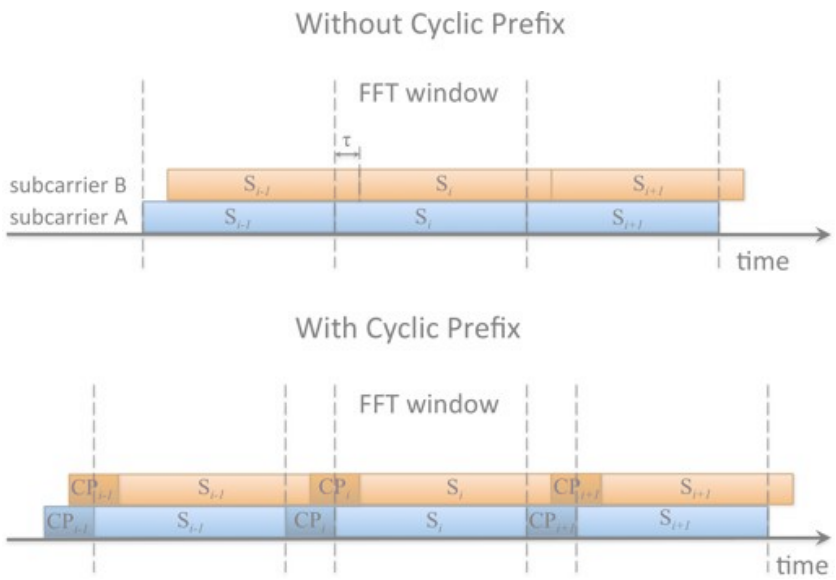

Figure 5.3 – Role of OFDM cyclic prefix at the receiver side. The relative delay τ between different subcarriers within the same OFDM symbol S_i causes inter-symbol interference (ISI) in the absence of cyclic prefix, while it is compensated with the introduction of such a guard interval.

in OFDM is to use a cyclic prefix (CP) before each symbol. This prefix consists of a certain number of samples from the end of the time-domain symbol $\boldsymbol{x}$, that are attached to the beginning of $\boldsymbol{x}$ before transmission. Its role at the receiver side is highlighted in fig. 5.3. By effect of dispersion, OFDM subcarriers travelling along the channel at different velocities are detected with different time delays. In the absence of cyclic prefix, these delays will cause the FFT block at the receiver to consider, at each symbol period, time-domain samples associated with different OFDM symbols, giving rise to ISI. On the other hand, when CP is present, ISI is avoided and the received OFDM subcarrier is just a time-shifted version of the transmitted one. This time shift corresponds in the spectral domain to a phase shift that can be readily balanced out for each subcarrier by digital signal processing (DSP) through a complex multiplication.
As one would expect, the maximum amount of dispersion that can be compensated for depends on the length of the cyclic prefix. However, the latter can be suitably designed to cancel out the effect of any arbitrary amount of dispersion, at the expenses of larger overhead.

Compensation of dispersion and other channel-induced impairments, such as frequency-selective fading, is particularly easy in OFDM as this is carried out in the frequency domain by digital signal processing (DSP). This consists in multiplying the symbols Y_k, recorded at the receiver after removal of cyclic prefix, by the inverse transfer function of the channel H_k^{-1}, in order to retrieve the transmitted symbols X_k. The operation, known as *single tap equalization*, relies on the assumption that the channel is linear, i.e. transmission impairments on one subcarrier do not depend on other subcarriers.
The transfer function of the channel, which is not known a priori, can be estimated with the use of *training sequences*, i.e. specific OFDM symbols sent out regularly by the transmitter and known at the receiver. Channel response is evaluated from the ratio $\hat{H}_k = Y_k/X_k$ between

the received and transmitted sequences. Then, based on this estimation, equalization is performed on the subsequent OFDM symbols, prior to bit demapping from the modulation constellation received for each subcarrier.

At the receiver, the constellation diagrams of the different subcarriers will be affected by amplitude and phase noise arising from the channel, as well as from system imperfections. This noise will lead to a certain spread of the detected constellation points around their nominal value, possibly resulting in wrong decision during symbol-to-bit de-mapping. A common measure of the performance of a digital transmission system is the root-mean-square error vector magnitude (EVM) [206]. This quantity can be defined as:

$$EVM_{rms} = \sqrt{\frac{\frac{1}{N}\sum_{n=1}^{N}|S_{m,n} - S_{i,n}|^2}{\frac{1}{N}\sum_{n=1}^{N}|S_{i,n}|^2}}, \tag{5.3}$$

where $S_{m,n}$ and $S_{i,n}$ are, respectively, the measured and the ideal symbols of the n-th point of a constellation of size N. In practice, signal voltages are used to represent constellation point, therefore in order to compute EVM_{rms} from eq. 5.3 both the transmitted and the received constellation are normalized so that the mean symbol power is one. Also, the EVM is typically indicated as the percentage of the mean power of constellation symbols. For the sake of precision, we note that the definition of EVM given here and commonly used in the case of multi-carrier modulations like OFDM [207], differs from that adopted for single carrier modulations, according to which the normalization is carried out, by convention, with respect to the power of the outermost point in the signal constellation.
In digital communications systems, the EVM is inherently related to another important measure of performances, the bit error rate (BER), quantifying the number of bit errors over the total transferred bits occurring during a given time interval [205, 206]. The BER is often specified as a design parameter in communication systems. Accordingly, performance optimization in these systems typically consists in the increase of capacity and the reduction of energy per bit required for data transmission for a given BER level. This level is generally chosen on the basis of the threshold value above which data recovery using forward error correction (FEC) becomes not possible. In current optical communication systems based on OFDM, such a BER limit is on the order of $3 - 4 \times 10^{-3}$ for FEC with 7% overhead and can reach values of $1 - 2 \times 10^{-2}$ with 20% overhead [208].

5.1.2 OFDM-based system architectures for optical communications

Owing to its potential for high spectral efficiency, its resilience to channel dispersion and the simplification of complex equalization functions through the use of DSP, OFDM technique has received particular attention for optical communications. Fiber optic systems employing OFDM as modulation formats are typically divided in two main classes, known respectively as *Optical OFDM* and *All-optical OFDM*. The latter are discussed in more detail in the following.

Optical OFDM

In Optical OFDM, the signal generated digitally with the procedure described in sec. 5.1 is directly modulated onto an optical carrier provided by a laser source. If the OFDM signal is used to modulate only the intensity of the optical field, low-cost components can be employed across the system and direct detection can be performed at the receiver. On the other hand, if both amplitude and phase of the complex electric field of the laser are used to encode the data, a coherent receiver is needed for demodulation.
Depending on whether coherent detection is used or not, the optical modulation technique is referred to as coherent optical OFDM or opto-electrical OFDM [205]. The architecture of both systems is shown in fig. 5.4. It can be observed that both schemes rely on the same building blocks in order to modulate and demodulate data into and from OFDM symbols. The main difference between the two approaches resides essentially in the transmitter and receiver front-ends, that are much simpler in the case of opto-electrical OFDM as compared to coherent optical OFDM.

In both architectures the laser source at the transmitter side may be either a DFB laser or a comb source. In the latter case, suitable selection of the comb line by optical filtering has to be performed prior to modulation. If coherent detection is intended to be used, the optical linewidth of the laser source needs to be at most on the order of few hundreds of kHz. On the contrary, no such limitation exist with opto-electrical OFDM. Also, in this last scheme, direct current modulation of a DFB lasers with the OFDM signal can be used to further simplify the system.
Owing to its ease of implementation and its potential for low cost, opto-electrical OFDM appears well-suited for next generation access networks [201, 208] and inter- and intra-data

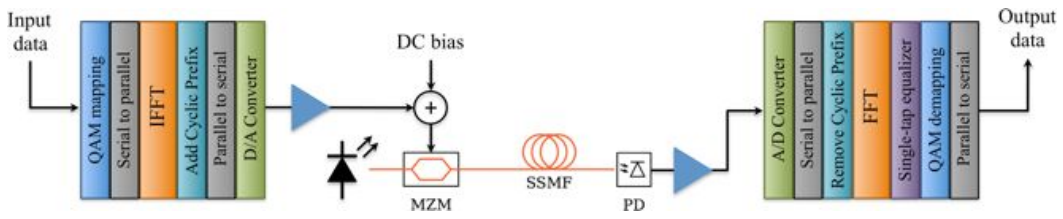

(a) Opto-electrical OFDM

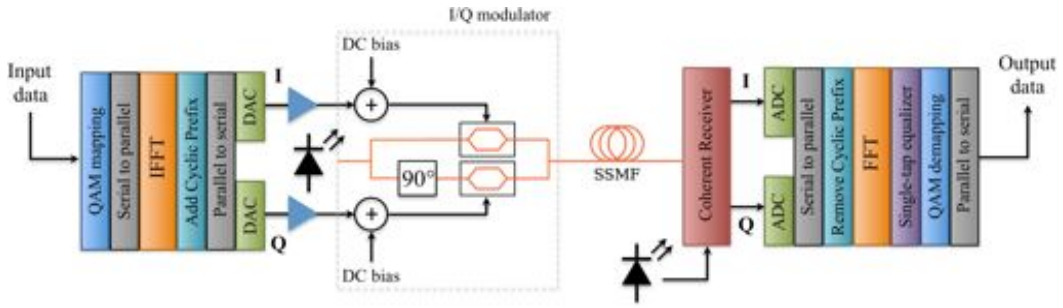

(b) Coherent optical OFDM

Figure 5.4 – System architectures for (a) opto-electrical OFDM and (b) coherent optical OFDM.

center communications [209]. On the other hand, coherent optical OFDM, providing better sensitivity at the expenses of a more complex architecture, may be more attractive for metropolitan networks and long-haul transmissions.

All-optical OFDM

Another widely investigated system architecture is All-optical OFDM [31, 202], which consists in employing the spectral lines produced by a frequency comb generator as orthogonal frequency subcarriers for OFDM. Accordingly, each comb line is modulated in amplitude and phase at a rate equal to the carrier spacing, as in standard OFDM, and multiplexing is performed prior to fiber optic transmission. Coherent detection is, then, used at the receiver side for data demodulation, as shown in fig. 5.5.

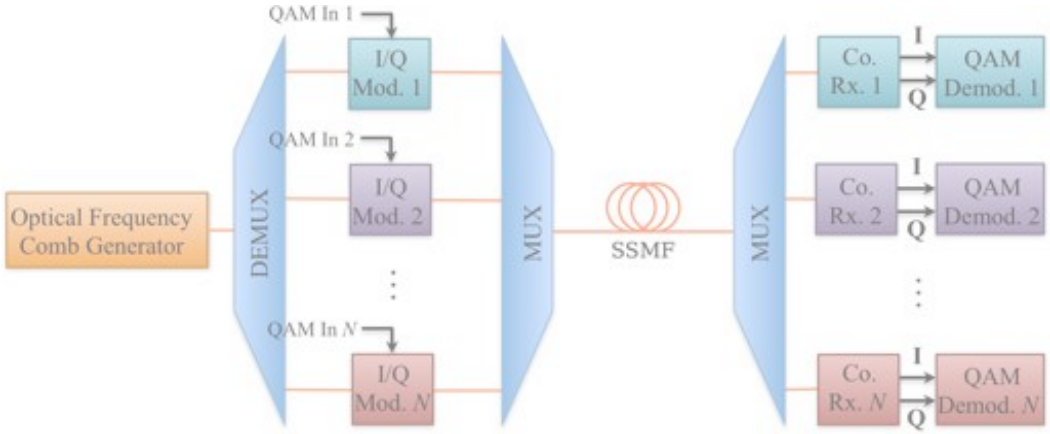

Figure 5.5 – System architectures for all-optical OFDM.

In All-optical OFDM systems, QAM modulation is generally employed. Also, depending on the particular implementation, FFT-like all-optical signal processing can be implemented by means of optical splitters, phase shifters and delay lines, in order to separate individual subcarriers [202, 210]. With this approach a record transmission capacity of 26 Tb/s has been reported in [202], demonstrating the inherent advantages of this technology. However, the system complexity and the number of components involved practically limit the applicability of all-optical OFDM to long-haul communications.

5.2 High-capacity communications with single-section mode-locked lasers and direct detection OFDM

For future access networks and data center communications, short-reach transmission systems providing high capacity at low cost are needed. Based on previous discussions, direct detection OFDM (DD-OFDM) in combination with optical frequency combs appears to be a promising solution for these systems. In DD-OFDM, intensity modulation of laser light typically results in a double sideband (DSB) signal, with spectral component lying symmetrically

around the carrier. This fact, besides reducing the spectral efficiency, may render the system more vulnerable to dispersion-induced power fading. For this reason, extensive research has been carried out in recent years on the application of single sideband (SSB) modulation to DD-OFDM [211].
Among different SSB techniques, compatible SSB modulation has received particular attention [212] owing to the possibility of tailoring the OFDM waveform so as to eliminate the guard band between the optical carrier and the modulated signal [213]. Recently, Vujicic *et al.* from DCU have adopted this technique to modulate at 12.75 Gb/s and transmit over 87 km of standard single mode fiber (SMF) 10 comb lines from an actively mode-locked laser [208]. Here, based on such an expertise on optical OFDM, we investigate the use of single-section MLLs as comb source for WDM data transmission employing 25 Gb/s compatible SSB OFDM modulation.

In this section, after a description of the DD-OFDM setup used at DCU for transmission experiment, we present the system performances of single-section MLLs based on single QW and QDash material discussed in chapter 3. As the modulation scheme adopted is particularly vulnerable to intensity noise due to its inherently high carrier-to-signal ratio [214], special attention is devoted to the relative intensity noise (RIN) of the comb source. Then performance comparison is carried out on the basis of device characteristics.

5.2.1 Experimental setup for direct detection OFDM

In our work, we have considered five different Fabry-Perot lasers: the single QW device presented in sec. 3.1.2 and four QDash lasers with free spectral range of 83, 44.7, 22.7 and 10.8 GHz, taken from the same 9 DBAR structure. System experiments are carried out using the setup shown in fig. 5.6. The comb generated by the semiconductor MLL is amplified with a low noise-figure (NF = 3.8 dB) Erbium-doped fiber amplifier (EDFA) and filtered with a waveshaper to select the desired number of lines. Then, all carriers are modulated simultaneously with a single dual-drive Mach-Zehnder modulator (DD-MZM). In practical installations, each wavelength channel would be separated by a demultiplexer and individually modulated. The DD-MZM is biased at the quadrature point, where the minimum of modulator transfer function occurs, and electrically driven with amplified SSB OFDM signal waveforms. The latter are derived from an arbitrary waveform generator (AWG) operating at 25 GSa/s and constructed as reported in [213].
For the experiment involving QW device the OFDM signal is comprised of 80 subcarriers and has an overall bandwidth of $\approx$ 7.8 GHz with a raw data rate of $\approx$ 31.25 Gb/s. For QDash lasers, instead, depending on the overhead assumed for FEC (7 or 20%), a 28.2 Gb/s or 33.6 Gb/s SSB OFDM signal is used, respectively. The 28.2 Gb/s signal is composed of 72 subcarriers and has a total bandwidth of about 7 GHz, while the 33.6 Gb/s signal consists of 86 subcarriers with an overall bandwidth of 8.3 GHz. Each subcarrier has a bandwidth 97.65 MHz and is encoded with 16-QAM modulation, resulting in a total subcarrier data rate of

390.6 Mb/s. In order to reduce the impact of low-frequency intensity noise in the vicinity of the carrier, a frequency offset of 800 MHz from the carrier frequency is applied.
In addition to FEC, the OFDM signal includes the following overheads: 10 training sequences and cyclic prefix of 6.25% of the IFFT size (which has 256 inputs). After overhead subtraction, the net data rate of each OFDM channel is 25 Gb/s for the QW laser and 24.5 Gb/s for QDash devices.

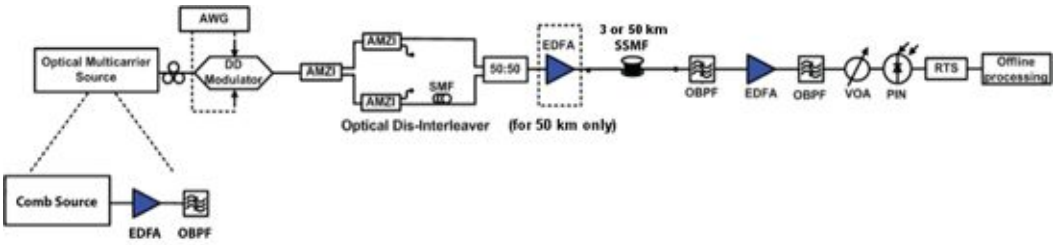

Figure 5.6 – Schematic of the experimental setup for direct detection SSB OFDM transmission (Courtesy of V. Vujicic, DCU).

Because we modulate all the comb lines simultaneously, in order to correctly determine the BER at the receiver side, adjacent channels have to be decorrelated. For that, odd and even sub-channels are split with tunable cascaded disinterleavers based on asymmetric Mach-Zehnder interferometers (AMZI). The even channels are then passed through a 5 m fiber patchcord, prior to be recombined with the odd channels. The overall signal is subsequently amplified with an EDFA operated in constant power mode and transmitted over 3 or 50 km of standard SMF, depending on the experiment.
At the receiver side, the individual wavelength channels are selected at a pre-amplified filtered stage consisting of a tunable optical bandpass filter (OBPF), an EDFA and a second tunable OBPF with 10 GHz bandwidth. Each filtered channel is detected with a 10 GHz receiver composed of a PIN photodiode and an integrated trans-impedance amplifier (TIA) and the signal is recorded using a real-time scope (RTS) with a sampling rate of 50 GSa/s. Digital processing of the received signal and BER calculation is then performed offline using Matlab. For each device considered in this study, BER results are interpreted on the basis of the relative intensity noise (RIN) of the laser modes, i.e. the laser power fluctuation normalized to the average power level. The one-sided RIN PSD of the individually filtered laser lines and of the full comb are measured in the electrical domain using a photodiode and an ESA, starting from the AC noise on the detector output and the electrical DC power, as illustrated in [215]. In all the measurements, the optical power is kept constant at about 1 mW by amplifying the laser signal using an EDFA and attenuating it prior to photodetection. With the available equipments, RIN characterizations are most likely limited by the noise of the ESA, approaching that of the MLLs, especially when the RIN of the full comb is investigated.

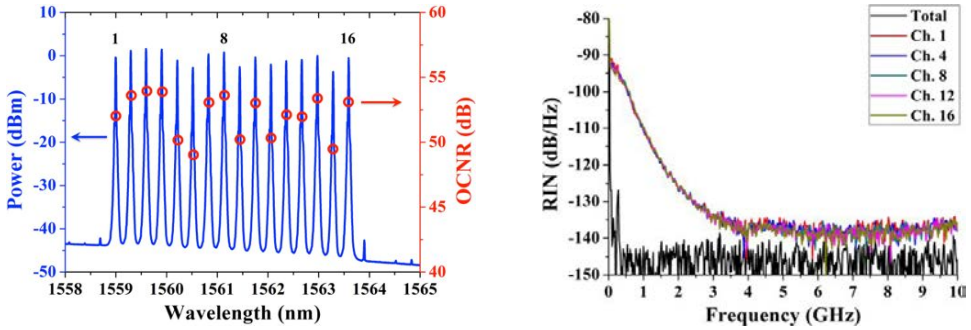

(a) (b)

Figure 5.7 – (a) Filtered comb after amplification: optical carrier-to-noise ratio (OCNR) before EDFA is indicated with red circles, modes are numbered with increasing wavelength. (b) Relative intensity noise spectra (0-10 GHz) for the overall comb and for a number of comb lines (Ch. 1, 4, 8, 12, 16).

5.2.2 Quantum well MLL system performances

Among the devices employed in the present study, we have selected the single quantum well laser discussed in sec. 3.1.2 owing to its relatively high output power, comparable to that of QDash devices, distributed over a narrow bandwidth of about 5 nm. The device is operated at a bias current of 155 mA, which provides an average power in the fiber of $\approx$ 8 dBm. The optical and RF spectra at this bias point are shown in fig. 3.2 on page 56.
For transmission experiments, the output of the MLL is amplified to 23 dBm using a low-noise EDFA (NF = 3.8 dB) and an OBPF is used to select 16 comb lines spaced by 37.6 GHz as WDM optical carriers. Figure 5.7a shows the filtered lines, numbered with increasing wavelength, together with the corresponding optical carrier-to-noise ratio (OCNR) measured prior to amplification. For all comb lines the OCNR is found to be greater than 49 dB, owing to the limited spectrum FWHM of the device. To further characterize the intensity noise of the different wavelength channels, we measure the RIN spectra over the band 0-10 GHz for the full spectrum and for a given set of individual comb lines (Ch. 1, 4, 8, 12, 16). Results shown in fig. 5.7b indicate the presence of significant mode partition noise, typical of passively mode-locked semiconductor lasers [216], as the RIN of individual modes is on average -131.2 dB/Hz while that of the full comb is -145.6 dB/Hz. The comb lines exhibit analogous intensity noise spectra, with a pronounced RIN component at frequencies below 2 GHz. These features may have a detrimental effect on system performances at low frequencies, even for a high OCNR of 50 dB.

After data transmission over 50 km of SMF using the setup shown in fig. 5.6, the BER performance of the 16 channels determined by error-counting is shown in fig. 5.8a. For all the channels, the BER is below the 7% FEC limit of 4.4×10^{-3} (shown as the red line). The inset of fig. 5.8a shows the 16-QAM constellation diagram representative of all the 80 OFDM subcarriers for channel number 10, exhibiting a BER of 3×10^{-3}. Also, for the sake of comparison, the transmission performance of a single-channel external cavity laser (ECL) through the test bed, is indicated with a green line at 1.3×10^{-3}. The higher BER exhibited

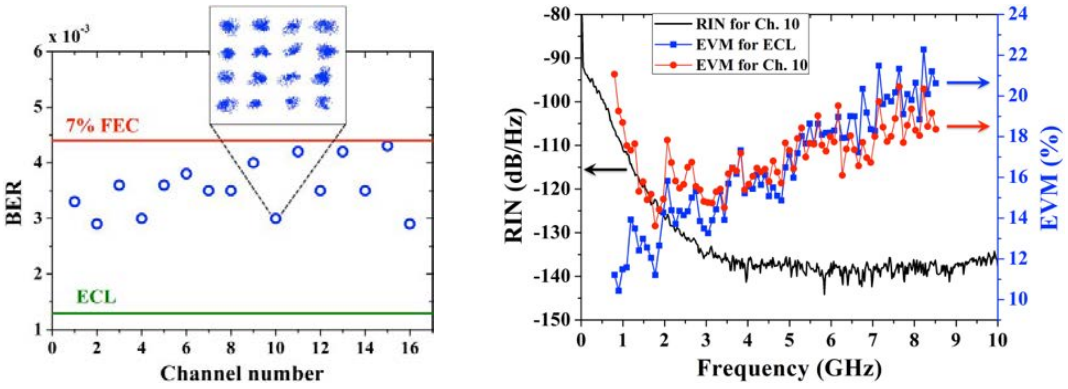

(a) (b)

Figure 5.8 – (a) Bit error rate (BER) performances for the QW sub-channels compared to that of a single-channel external cavity laser (ECL). In the inset: 16-QAM constellation diagram of all the 80 OFDM sub-carriers for sub-channel number 10. (b) Error-vector magnitude (EVM) of the 16-QAM constellations of the 80 OFDM sub-carriers for QW sub-channel number 10 and ECL. RIN spectrum of Ch. 10 is also included for comparison.

by the QW MLL compared to the ECL is attributed to larger RIN of the comb source, due to mode partition noise on the filtered comb lines.

The effect of RIN on system performance is made clear when the EVM of the 16-QAM constellations of the 80 OFDM subcarriers is investigated more closely. Figure 5.8b compares the EVM performance of channel number 10 (red circles) and the single-channel ECL (blue squares). The best achievable performance for the test bed, as indicated by the ECL, shows that the EVM degrades linearly with increasing frequency (i.e. increasing subcarrier number). This is due to the non-linear phase shift among OFDM subcarriers introduced by the data amplifiers used after the AWG to drive the DD-MZM. This effect, coupled with a large amount of dispersion from the SMF, significantly impairs the ability to correctly reconstruct the OFDM signal at higher frequencies, as the linear single-tap equalizer at the receiver cannot properly compensate for it. At frequencies above 2 GHz, the EVM performance of Ch. 10 is similar to that of the ECL, however below 2 GHz the EVM performance decreases with decreasing frequency (or decreasing OFDM subcarrier number) for Ch 10. Figure 5.8b also shows the RIN spectrum of Ch. 10, and it is clear that as the intensity noise increases at the lower frequencies, the EVM increases accordingly. By comparison, the average RIN of the ECL is -140 dB/Hz, with a flat power spectrum. This indicates that low-frequency intensity fluctuations are the main cause of performance degradation when using semiconductor passively MLLs as comb sources for IM/DD SSB OFDM transmission. Yet the sufficiently high power per line exhibited by this QW device allows for successful data transmission over 50 km of SMF with a net aggregate data rate of 400 Gb/s in a single polarization and a spectral efficiency (SE) of 0.66 bit/s/Hz [a].

Using the approach described here, the overall capacity and spectral efficiency can be further improved by using Fabry-Perot lasers with lower free-spectral ranges and larger spectrum FWHM. Also, RIN reduction by suitable selection of the laser material may result in better

BER performances. These solutions are investigated in the following for QDash material, having promising characteristics in this regard.

5.2.3 Quantum dash MLL system performances

Quantum dash lasers, exhibiting emission spectra as large as 15 nm, appear to be ideal candidates for high capacity WDM systems using DD-OFDM. Here we consider four BRS lasers with ridge width of 1.5 µm, issued from the same 9 DBAR QDash structure. The devices have free spectral ranges of 83, 44.7, 22.7 and 10.8 GHz and as-cleaved facets. For transmission experiments, all the devices are temperature controlled at 25°C and biased so as to yield the maximum power coupled in fiber, given the limit of 500 mA for the current source employed. For all the lasers, this power is on the order of 6-8 dBm, which means that the power per comb line and, therefore, the OCNR decreases for longer cavity lengths. Indeed, for lower FSRs, the total output power is divided over a larger number of modes assuming, with reason, that the spectrum FWHM remains the same [155]. Also, for such an increased number of lasing modes a higher mode partition noise is expected. Therefore, also in the case of QDash devices, RIN measurements assume a particular importance.

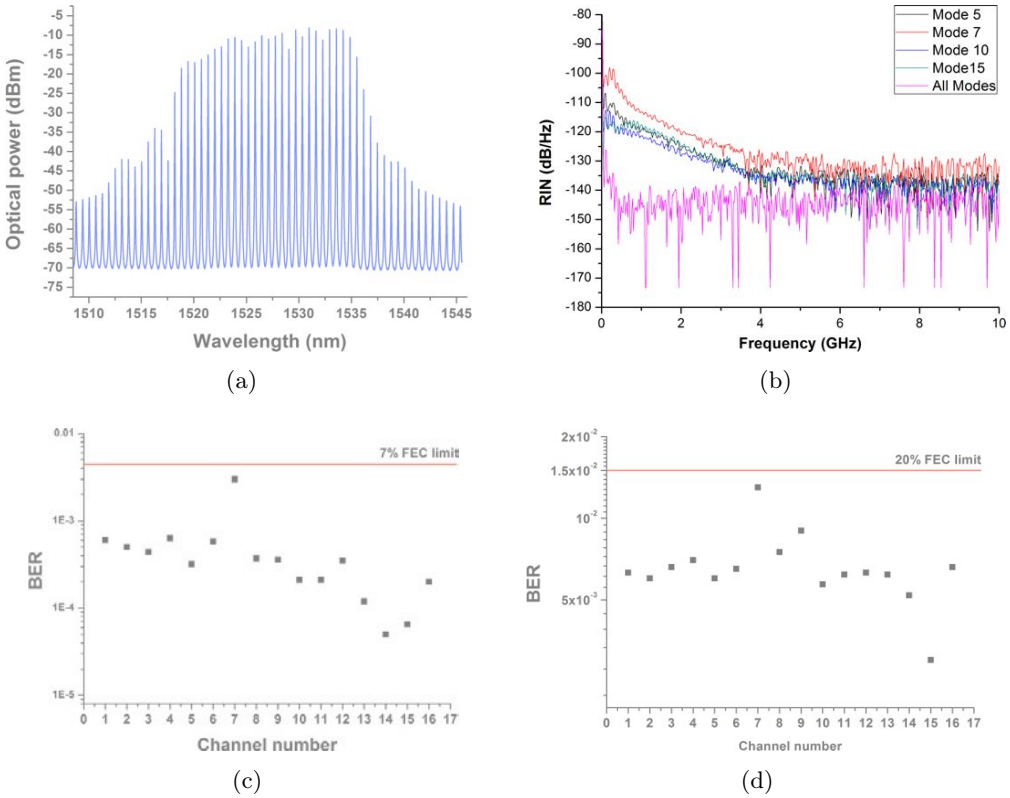

Figure 5.9 – (a) Emission spectrum of the 83 GHz laser at 300 mA, (b) RIN spectra (0-10 GHz) for the overall comb and for a number of modes (Ch. 5, 7, 10, 15), and BER performances after transmission over (c) 3 km and (d) 50 km of standard SMF.

The first device considered in our study is the 83 GHz repetition rate QDash MLL. As in the case of the QW laser, 16 comb lines from the phase locked spectrum of the QDash device

are selected and used for data transmission with the setup described in sec. 5.2.1. In fig. 5.9, we report the emission spectrum of the laser biased at 300 mA, the RIN measurement for selected modes, as well as BER performances of the 16 wavelength channels after 3 and 50 km of standard SMF. It can be noticed that also for this device mode partition noise is present, as indicated by the larger RIN of individual lines with respect to that of the full comb. Yet, the RIN observed for the QDash laser at frequencies below 2 GHz is much lower than that of the QW device over the same bandwidth (cf. fig. 5.7b). This indicates that the better noise characteristics of QDash material can somehow compensate for the reduced power per comb line.
Transmission performance indicate that the BER is well below the 7% FEC limit for communications over 3 km of SMF and below the 20% FEC limit for 50 km transmissions. The non-uniformity of BER values across the 16 channels is due to the more or less marked dips in the optical spectrum, resulting in lower OCNR. On the other hand, the performance degradation after transmission over 50 km compared to the case when the signal is transmitted over 3 km of SMF can be associated with the phase shift among subcarriers introduced by the data drivers which have nonlinear phase transfer characteristics. The introduced phase shift in combination with chromatic dispersion cause penalties, as the linear equalizer cannot properly compensate for this degradation. Increasing the length of the cyclic prefix, in this case, has little effect on system performances.
Using the 83 GHz QDash MLL, the net aggregate data rate achievable is 392 Gb/s with a spectral efficiency of about 0.3 bit/s/Hz. Such a low SE, arising from the large laser FSR, is unsuitable for next generation communication. Also, no practical advantages with respect to the QW MLL system performances discussed in sec. 5.2.2 are remarked when using QDash devices with such a large FSR.

The situation is significantly changed when QDash devices with longer cavity lengths are considered, such as the above-mentioned FP lasers with free spectral range of 44.7 and 22.7 GHz. Figure 5.10 shows the optical spectra, the RF spectra and the RIN of individual comb lines, measured for the 44.7 GHz laser biased at 380 mA and for the 22.7 GHz device at 350 mA. The detected RF spectra revealed narrow linewidths of 91 kHz and 200 kHz, respectively for the 44.7 GHz and the 22.7 GHz lasers, indicating strong passive mode-locking as typical for QDash material. Measured RIN spectra on the bandwidth 0-10 GHz manifest more severe mode partition noise than in the case of the 83 GHz device, owing to the larger number of lasing modes. However, the behavior of the intensity noise at frequencies below 2 GHz is comparable.
Transmission results obtained for the two devices are reported in fig. 5.11. More specifically, fig. 5.11a-d show the channels selected for data transmission, the BER and RIN performances as function of channel number, as well as the constellation diagram of the central channel after transmission over 3 km of SMF for the 44.7 GHz laser, while fig. 5.11e-h displays the same quantities for the 22.7 GHz device. It can be observed that all the 40 channels from the 44.7 GHz QDash MLL exhibit performance far below the 7% FEC limit (BER= 4×10^{-3})

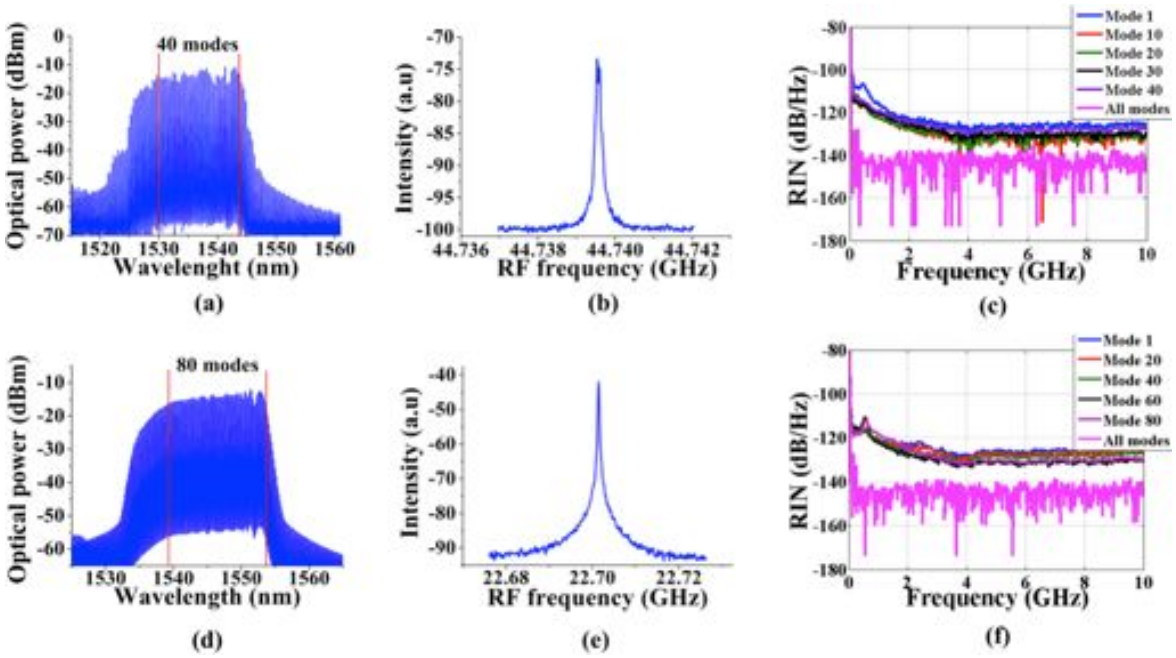

Figure 5.10 – (a) Optical spectrum, (b) RF spectrum, and (c) RIN for selected filtered modes and all modes for the 44.7 GHz QDash laser. (d-f) Same quantities as in (a-c), but for the QDash MLL with 22.7 GHz free spectral range.

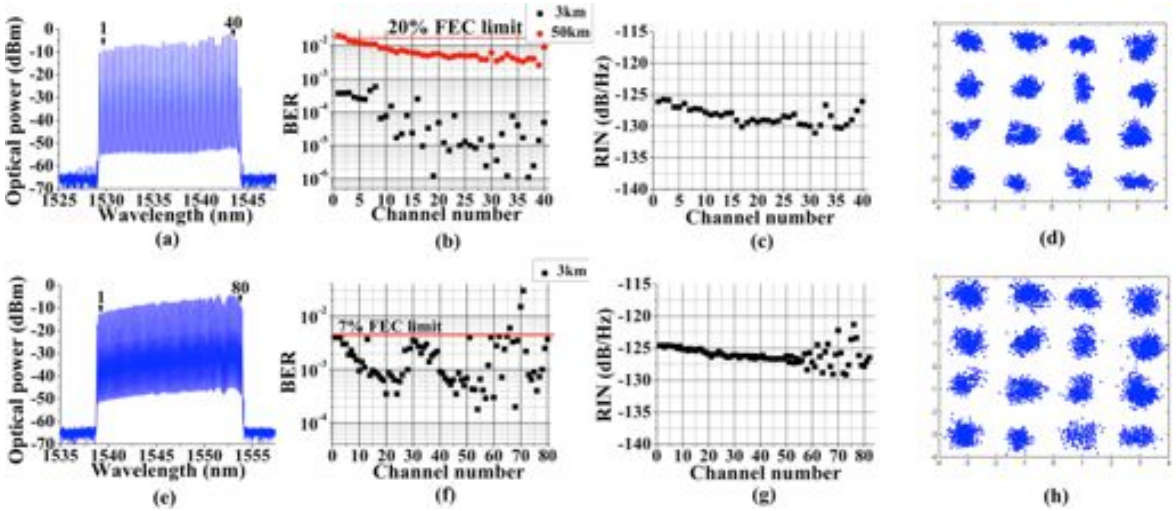

Figure 5.11 – (a) Filtered optical spectrum of the QDash MLL with 44.7 GHz channel spacing, (b) measured BER of the 28.2 Gb/s (black squares) and 33.6 Gb/s (red circles) SSB OFDM data for each channel number, over 3 and 50 km of SMF, (c) measured average RIN (0-10 GHz) for all modes, and (d) measured constellation diagrams for the central channel after 3 km of SMF. (e-h) Same results as in (a-d), but for the QDash MLL with 22.7 GHz channel spacing.

after transmission over 3 km of SMF. On the other hand, for signal propagation through the 50 km of SMF, the BER is compatible with the 20% FEC limit (BER= 1.5×10^{-2}), with the exception of the two leftmost channels which display slightly worse performance. Once again the performance degradation is associated with the nonlinearity of electrical amplifier used to drive the DD-MZM, while for each measurement the trend of BER vs. channel number is related to the OCNR and the RIN of each mode. This fact can be readily observed when

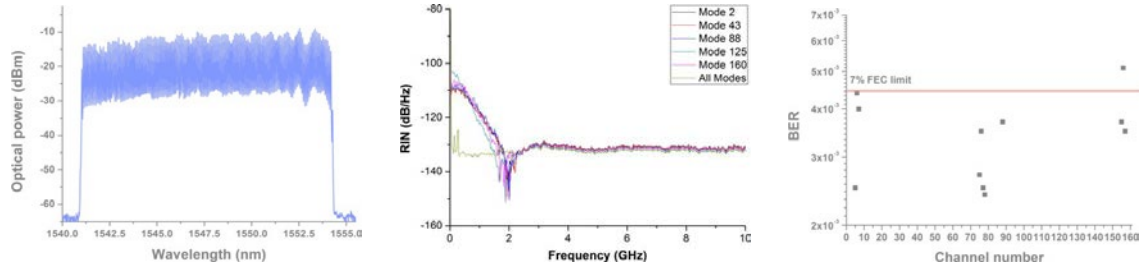

(a) (b) (c)

Figure 5.12 – (a) Filtered optical spectrum of the 10.8 GHz laser at 500 mA, (b) RIN spectra (0-10 GHz) for the overall comb and for a number of modes (Ch. 2, 43, 88, 125, 160), and (c) BER performances after transmission over 3 km of SMF for selected modes in the center and on the sides of the comb spectrum.

moving from higher towards lower wavelength channels, where transmission performance vary in accordance with the shape of the optical spectrum envelope, as well as the channels RIN ranging from -125 dB/Hz to -132 dB/Hz

Analogous conclusions can be drawn for the 22.7 GHz laser, for which data transmission is carried out only over 3 km of SMF. In this case, BER performance are compatible with the 7% FEC limit for all the wavelength channels, except three lines corresponding to the wavelength region where a dip in the spectrum of the laser is found. The higher BER measured for the 22.7 GHz device with respect to the 44 GHz one is due to the higher RIN of the first, ranging from -122 dB/Hz to -129 dB/Hz. Yet for both lasers the large number of modes distributed over a spectrum FWHM in excess of 15 nm, allows for terabit-per-second capable data transmissions. Indeed, the gross aggregate capacities achieved with the 44.7 GHz QDash MLL using IM/DD SSB OFDM are 1.128 Tb/s (40×28.2 Gb/s) and 1.344 Tb/s (40×33.6 Gb/s), while the total data rate obtained with the 22.7 GHz device is 2.256 Tb/s (80×28.2 Gb/s). The highest SE of 1.25 bit/s/Hz is obviously achieved for the 22.7 GHz MLL, but given the small bandwidth of the SSB OFDM signal (≈ 7-8 GHz), QDash lasers with narrower FSR can be used to increase the SE.

In order to verify the feasibility of this approach, we have evaluated the performance of few selected modes from the lasing spectrum of a 10.8 GHz repetition rate QDash MLL biased at 500 mA. The filtered wavelength channels, the RIN spectra, together with the BER measured for a number of modes in the center and on the sides of the comb are shown in fig. 5.12. It can be noticed that, as expected, the RIN spectra in fig. 5.12 exhibit larger low-frequency components compared to those reported in fig. 5.9 and 5.10, due to the more severe mode partition effects. However, the BER of the considered wavelength channels is still below, or slightly above, the 7% FEC limit after transmission over 3 km of SMF. Therefore, assuming that the performance of all the 160 channels are relatively homogeneous, as in the case of the devices examined above, we can infer for this 10.8 GHz laser an aggregate data rate in excess of 4 Tb/s, with SE of about 2.6 bit/s/Hz. Still, for the sake of completeness, we remark that with such a small FSR the narrow filter bandwidth required to separate the different wavelength channels imposes more stringent requirement in terms of comb wavelength stability

in order to prevent random fluctuation of the performances.

5.2.4 Discussion

From the results presented above, single-section MLLs based on single InGaAsP/InP quantum well and on InAs/InP QDash material appear to be suitable comb sources for WDM data transmissions based on DD-OFDM. Using the system architecture described in sec. 5.2.1, we have observed that the maximum aggregate capacity, as well as the BER performance obtained for a given length of the optical link, strongly depend on the FSR and on the intensity noise of the laser. In particular, because the maximum laser output power does not necessarily scale with cavity length and mode partition noise becomes more severe for longer devices, inferior system performances are to be expected for low-FSR MLLs. In this case, the reduced resilience of the transmission system to intensity noise would directly impact on the maximum transmission distance achievable. In fact, the noise introduced by booster amplifiers along the transmission line needed to increase the reach of the link, would severely degrade the OFDM signal quality. Nevertheless, terabit-per-second communications have been demonstrated over distances compatible with inter- and intra-data center networking scenarios using single-section QDash MLLs with FSR down to 10.8 GHz.

For this particular application, depending on the specific system requirements, either QW or QDash lasers may be the preferred choice. Single QW lasers, being mature from a manufacturing point of view and providing large output power over a relatively narrow bandwidth, are good candidates for optical interconnects, especially for transmission distances of tens of kilometers. Because they can be operated with adequate performances at lower currents with respect to QDash devices, QW lasers may also be interesting in a perspective of reduction of power consumption. On the other hand, QDash MLLs, providing much wider and flatter frequency combs with reduced intensity noise and enhanced stability [d], appear more attractive for substantial increase of transmission capacity.
Both QW and QDash based single-section MLLs are promising candidates for hybrid integration on the emerging silicon photonics platform, owing to their compact size and the capability of generating tens of comb lines at relatively low injection currents. Also, the possibility of lithographically defining the FSR by means of distributed Bragg reflectors (cf. sec. 3.4), would make these devices more compatible with existing off-the-shelf component and telecommunication standards.
Finally, the use of DD-OFDM in combination with OFCs generators is particularly advantageous for data center networks owing to the inherent properties of this modulation format. DD-OFDM technique, in fact, allows to use low-cost electronic components in the system, besides addressing complex equalization functions in the digital domain, rather than in the analog one. With OFDM, dispersion compensation is strongly simplified, provided that nonlinearities of the system are reduced. Otherwise, if dispersive effects are too severe, adaptive modulation techniques can be use to mitigate channel effects [205]. Moreover, the use of low-frequency

RF subcarriers provides the system with fine granularity for bandwidth allocation, a highly desirable quality for efficient spectrum utilization in data center networks [209].

Conclusions and future perspectives

The increasing demand for communication bandwidth in the current optical networks requires new technological solutions to provide high capacity at low costs. Optical frequency combs (OFCs), generating tens of optical carriers from a single laser source, are very attractive for next-generation telecommunications. Their use in wavelength division multiplexing (WDM) systems in combination with advanced optical modulation formats, in fact, opens the way for unprecedented transmission capacities.

In this thesis, we have investigated the optical frequency combs generated by single-section mode-locked lasers (MLLs) based on low-dimensional semiconductor nanostructures. These devices, owing to their compactness and their potential for low manufacturing costs and low jitter performances, appear to be particularly suitable for optical communication applications over other OFCs technologies discussed in chapter 1. In the present work, a systematic comparison of different laser active materials has been carried out. More specifically, we have focused our attention on laser structures based on InAs quantum dots and dashes grown on InP, on InAs QDs on GaAs, as well as on the conventional InGaAsP quantum well material on InP. The structures, optimized for light emission in the fiber optic transmission windows around 1.55 µm and 1.3 µm, are described in chapter 2, while mode-locking performances of single-transverse mode ridge waveguide lasers based on those are presented in chapter 3.

Our study has shown that in the single-section configuration, quantum dot and QDash lasers on InP outperform QD devices based on GaAs in terms of optical spectrum full width at half maximum (FWHM) and timing phase noise. InAs/GaAs QD lasers at 1.3 µm, in fact, are observed to exhibit broad RF beatings and irregular optical spectra with laser emission on multiple wavelength sub-bands. On the other hand, all the lasers at 1.55 µm based on InP considered in this work display narrow RF linewidth of few tens of kHz and square-shaped optical spectra over large injection current ranges several tens of mA. The spectrum FWHM of InAs quantum dot lasers on InP (311)B and of InAs quantum dash devices on InP (100), in particular, is observed to steadily increase with current, reaching values as large as 15 nm for QDash material. This property, appearing to be specific to QDs and QDashes grown on InP, is very attractive for wide comb and short pulse generation from the MLLs.

Concerning this last aspect of single-section lasers, narrow optical pulses with ps and sub-ps durations can be obtained for devices emitting at 1.55 µm after compensation of the positive chirp of the laser signal. This can be easily carried out by means of light propagation through

suitable lengths of standard single mode fiber SMF-28, whose dispersion can readily used as a measure of the pulse chirp. The same procedure can be applied to compress the chirped waveforms emitted by InAs/GaAs QD lasers at 1.3 µm, provided that the optical spectrum lies above the zero-dispersion point of SMF-28. However, pulse generation from these devices is found to be achievable only over limited operating regions of the lasers, for which narrow RF linewidths and square-shaped optical spectra occur.

As superior mode-locking performances are exhibited by QDash lasers, their unique properties in terms of pulse generation and optical frequency comb stability are studied in more detail. Frequency-resolved optical gating FROG characterization of pulses compressed with SMF-28 carried out at TU Berlin has allowed to gain insight into the group delay dispersion (GDD) of the emitted signal. The GDD, as well as the minimum pulse duration, are found to decrease with injection current, in agreement with previous studies on analogous components [155]. These results indicate that QDash devices are most suitably operated at high currents in order to favor pulse formation and, at the same time, increase the output power. More importantly, the agreement between pulse spectrum measured by FROG and that recorded with a standard optical spectrum analyzer, suggests that the full comb emitted by the laser contribute to pulse formation. In addition, the good match between the measured and retrieved FROG traces reveals adequate stability for the generated pulses.
The stability of the combs produced by QDash based MLLs and especially that of the beat-note frequency are also investigated in depth. The optical lineshape, as well as the frequency and linewidth of the laser longitudinal modes beating appears to be particularly affected by environmental fluctuations. In particular, the short distance feedback variation from coupling optics has been recognized as the main source of instability. However, suitable coupling optics and device engineering techniques have been identified for the reduction of feedback effects. This has allowed us to distinguish the intrinsic behavior of the devices from the effects attributable to random fluctuations of the laser-to-fiber coupling.

Because one of the main limiting factors for the use of multimode Fabry-Perot (FP) laser in optical communications is the incertitude on their free spectral range (FSR) determined by cleaving precision, in this work we have also investigated the possibility of lithographically defining the cavity length by means of distributed Bragg reflectors (DBRs). In a preliminary study initiated by III-V Lab, we have shown that a DBR with sufficiently large reflectivity bandwidth can be used to close the laser cavity without compromising the optical spectrum and RF linewidth of QDash MLLs. This approach, besides allowing to control the laser FSR and enabling photonic integration on the InP platform, can also be applied in the future to compensate for the GDD of laser pulses on-chip by suitably chirping the DBR.
In this regard, understanding the origin of the large pulse chirp observed for single-section MLLs would be highly desirable for the design of structures for dispersion compensation. As this GDD is often attributed to the chromatic dispersion of the laser active material [4,125], in our work we have tested this hypothesis by determining the dispersion of the QDash gain medium. For this purpose, we have employed the optical frequency-domain reflectometry (OFDR) technique that,

owing to its swept-wavelength nature, allows for fast component characterization and enables the study of the dynamical properties of the devices through the analysis of Doppler effects. As few studies on the measurement of dispersion by OFDR have been previously reported in literature [192, 195], in chapter 4 we have first validated the technique systematically by retrieving the amplitude and phase response of a programmable optical filter in the C+L band. Then, having observed that the minimum dispersion measurable by OFDR is much smaller than the values expected for semiconductor materials, we have applied the technique to the study of a semiconductor optical amplifier based on QDash active region. The measurements have revealed that the small anomalous dispersion of the semiconductor material is unlikely to be the cause of the large normal GDD of MLLs pulses. The reason for the latter may be looked into the specific laser dynamics and suitable modeling is required to gain more insight into these mode-locking phenomena.

Despite the chirp of the signal emitted by single-section MLLs, the combs generated by these devices can be effectively employed in high-capacity WDM systems. In a study carried out in collaboration with Dublin City University and presented in chapter 5, we have demonstrated successful data transmission at 25 Gbit/s using direct detection orthogonal frequency division multiplexing (DD-OFDM) modulation format. Fiber optic transmissions over 50 km of standard SMF with aggregate capacities up to 400 Gb/s using InGaAsP/InP QW lasers and over 3 km of SMF with data rates in excess of 2 Tb/s (with a potential for 4 Tb/s and more) using QDash MLLs have been achieved. The performances appear to be limited only by the low frequency behavior of the RIN of the different laser modes and by nonlinearities possibly present in the system. Yet, the followed approach appears to be very promising to obtain multi-terabit per second capacities at minimal costs in short distance optical interconnects and intra- and inter-data center communication scenari.

Owing to the variety of subjects investigated, a number of perspectives for the present work have been identified. Assessment and improvement of the wavelength and/or RF frequency stability of the combs generated by single-section MLLs would be particularly useful for spectroscopy applications and for the development of stabilized sources for telecommunications. For this purpose, the use of techniques common to frequency metrology research would be particularly advantageous. Regarding the application of single-section devices in optical communication, a substantial increase of transmission capacity is expected from the use of advanced amplitude and phase modulation formats and coherent optical detection. In this case, optical linewidth reduction of the comb lines (or a consistent fraction thereof), required for coherent systems, can be carried out by means of feed-forward control schemes [m,217] or optical phase-locked loops [218]. Integration of single-section MLLs in photonic integrated circuits based on the InP or Si platform would also be interesting to perform complex (de)multiplexing and (de)modulation functions on the comb lines with compact optical modules. Additionally, the chirped waveforms emitted by single-section MLLs and, above all, the possibility of easily controlling the chirp by signal propagation through SMF may find application in ultrahigh-speed swept-wavelength interferometric systems and OFDR. In these systems, in fact, the

linear variation of the instantaneous optical frequency over the periodic MLL waveforms may be used to simulate the wavelength sweep of mechanically tunable laser sources [219].
With respect to OFDR, the high sensitivity of the technique to optical path length variations during the measurement may be employed for the characterization of the dynamic properties of optical components, such as the linewidth enhancement factor of SOAs or electro-absorption modulators. The same feature opens the way for a wide range of sensing applications based on the principles of swept-wavelength interferometry.

Bibliography

[1] E. Avrutin, J. Marsh, and E. L. Portnoi, "Monolithic and multi-gigahertz mode-locked semiconductor lasers: constructions, experiments, models and applications," Optoelectronics, IEE Proceedings - **147**(4), 251–278 (2000).

[2] K. A. Williams, M. G. Thompson, and I. H. White, "Long-wavelength monolithic mode-locked diode lasers," New Journal of Physics **6**, 179–179 (2004).

[3] E. U. Rafailov, M. A. Cataluna, and W. Sibbett, "Mode-locked quantum-dot lasers," Nature Photonics **1**(7), 395–401 (2007).

[4] K. Sato, "Optical pulse generation using Fabry-Pérot lasers under continuous-wave operation," IEEE Journal of Selected Topics in Quantum Electronics **9**(5), 1288–1293 (2003).

[5] Y. Nomura, S. Ochi, N. Tomita, K. Akiyama, T. Isu, T. Takiguchi, and H. Higuchi, "Mode locking in Fabry-Pérot semiconductor lasers," Physical Review A **65**(4) (2002).

[6] J. Renaudier, G.-H. Duan, P. Landais, and P. Gallion, "Phase Correlation and Linewidth Reduction of 40 GHz Self-Pulsation in Distributed Bragg Reflector Semiconductor Lasers," IEEE Journal of Quantum Electronics **43**(2), 147–156 (2007).

[7] R. Rosales, S. G. Murdoch, R. T. Watts, K. Merghem, A. Martinez, F. Lelarge, A. Accard, L. P. Barry, and A. Ramdane, "High performance mode locking characteristics of single section quantum dash lasers," Optics Express **20**(8), 8649–8657 (2012).

[8] T. Udem, R. Holzwarth, and T. W. Hänsch, "Optical frequency metrology," Nature **416**(6877), 233–237 (2002).

[9] T. Udem, J. Reichert, R. Holzwarth, and T. W. Hänsch, "Accurate measurement of large optical frequency differences with a mode-locked laser," Optics Letters **24**(13), 881–883 (1999).

[10] D. J. Jones, S. A. Diddams, J. K. Ranka, A. Stentz, R. S. Windeler, J. L. Hall, and S. T. Cundiff, "Carrier-Envelope Phase Control of Femtosecond Mode-Locked Lasers and Direct Optical Frequency Synthesis," Science **288**(5466), 635–639 (2000).

[11] J. Ye, H. Schnatz, and L. Hollberg, "Optical frequency combs: From frequency metrology to optical phase control," IEEE Journal of Selected Topics in Quantum Electronics **9**(4), 1041–1058 (2003).

[12] J. Ye, L.-S. Ma, T. Daly, and J. L. Hall, "Highly selective terahertz optical frequency comb generator," Optics Letters **22**(5), 301–303 (1997).

[13] S. Bennett, B. Cai, E. Burr, O. Gough, and A. Seeds, "1.8-THz bandwidth, zero-frequency error, tunable optical comb generator for DWDM applications," IEEE Photonics Technology Letters **11**(5), 551–553 (1999).

[14] S. Fukushima, C. Silva, Y. Muramoto, and A. Seeds, "Optoelectronic millimeter-wave synthesis using an optical frequency comb Generator, optically injection locked lasers, and a unitraveling-carrier photodiode," Journal of Lightwave Technology **21**(12), 3043–3051 (2003).

[15] R. Wu, V. R. Supradeepa, C. M. Long, D. E. Leaird, and A. M. Weiner, "Generation of very flat optical frequency combs from continuous-wave lasers using cascaded intensity and phase modulators driven by tailored radio frequency waveforms," Optics Letters **35**(19), 3234–3236 (2010).

[16] R. Zhou, S. Latkowski, J. O'Carroll, R. Phelan, L. P. Barry, and P. Anandarajah, "40 nm wavelength tunable gain-switched optical comb source," Optics Express **19**(26), B415–B420 (2011).

[17] P. Anandarajah, "The Pilot Photonics Optical Wavelength Comb Source and its Expansion," White paper, Pilot Photonics Ltd (2012).

[18] H. A. Haus, "Mode-locking of lasers," Selected Topics in Quantum Electronics, IEEE Journal of **6**(6), 1173–1185 (2000).

[19] R. Ell, U. Morgner, F. X. Kärtner, J. G. Fujimoto, E. P. Ippen, V. Scheuer, G. Angelow, T. Tschudi, M. J. Lederer, A. Boiko, and B. Luther-Davies, "Generation of 5-fs pulses and octave-spanning spectra directly from a Ti:sapphire laser," Optics Letters **26**(6), 373–375 (2001).

[20] A. Bartels, D. Heinecke, and S. A. Diddams, "10-GHz Self-Referenced Optical Frequency Comb," Science **326**(5953), 681–681 (2009).

[21] F. Quinlan, C. Williams, S. Ozharar, S. Gee, and P. Delfyett, "Self-Stabilization of the Optical Frequencies and the Pulse Repetition Rate in a Coupled Optoelectronic Oscillator," Journal of Lightwave Technology **26**(15), 2571–2577 (2008).

[22] J. Davila-Rodriguez, I. Ozdur, M. Bagnell, P. Delfyett, J. Plant, and P. Juodawlkis, "Ultralow Noise, Etalon Stabilized, 10-GHz Optical Frequency Comb Based on an SCOW Amplifier," IEEE Photonics Technology Letters **24**(23), 2159–2162 (2012).

[23] P. R. A. Binetti, M. Lu, E. J. Norberg, R. S. Guzzon, J. S. Parker, A. Sivananthan, A. Bhardwaj, L. A. Johansson, M. J. Rodwell, and L. A. Coldren, "Indium Phosphide Photonic Integrated Circuits for Coherent Optical Links," IEEE Journal of Quantum Electronics **48**(2), 279–291 (2012).

[24] D. Liang and J. E. Bowers, "Recent progress in lasers on silicon," Nature Photonics **4**(8), 511–517 (2010).

[25] T. J. Kippenberg, R. Holzwarth, and S. A. Diddams, "Microresonator-Based Optical Frequency Combs," Science **332**(6029), 555–559 (2011).

[26] T. Herr, K. Hartinger, J. Riemensberger, C. Y. Wang, E. Gavartin, R. Holzwarth, M. L. Gorodetsky, and T. J. Kippenberg, "Universal formation dynamics and noise of Kerr-frequency combs in microresonators," Nature Photonics **6**(7), 480–487 (2012).

[27] J. Riemensberger, K. Hartinger, T. Herr, V. Brasch, R. Holzwarth, and T. J. Kippenberg, "Dispersion engineering of thick high-Q silicon nitride ring-resonators via atomic layer deposition," Optics Express **20**(25), 27,661–27,669 (2012).

[28] J. S. Levy, A. Gondarenko, M. A. Foster, A. C. Turner-Foster, A. L. Gaeta, and M. Lipson, "CMOS-compatible multiple-wavelength oscillator for on-chip optical interconnects," Nature Photonics **4**(1), 37–40 (2009).

[29] S. T. Cundiff, "Metrology: New generation of combs," Nature **450**(7173), 1175–1176 (2007).

[30] J. Pfeifle, V. Brasch, M. Lauermann, Y. Yu, D. Wegner, T. Herr, K. Hartinger, P. Schindler, J. Li, D. Hillerkuss, R. Schmogrow, C. Weimann, R. Holzwarth, W. Freude, J. Leuthold, T. J. Kippenberg, and C. Koos, "Coherent terabit communications with microresonator Kerr frequency combs," Nature Photonics **8**(5), 375–380 (2014).

[31] S. Chandrasekhar and X. Liu, "OFDM Based Superchannel Transmission Technology," Journal of Lightwave Technology **30**(24), 3816–3823 (2012).

[32] S. T. Cundiff and A. M. Weiner, "Optical arbitrary waveform generation," Nature Photonics **4**(11), 760–766 (2010).

[33] P. Delfyett, S. Gee, M.-T. Choi, H. Izadpanah, W. Lee, S. Ozharar, F. Quinlan, and T. Yilmaz, "Optical frequency combs from semiconductor lasers and applications in ultrawideband signal processing and communications," Journal of Lightwave Technology **24**(7), 2701–2719 (2006).

[34] A. Stöhr, A. Akrout, R. Buß, B. Charbonnier, F. van Dijk, A. Enard, S. Fedderwitz, D. Jäger, M. Huchard, F. Lecoche, J. Marti, R. Sambaraju, A. Steffan, A. Umbach, and M. Weiß, "60 GHz radio-over-fiber technologies for broadband wireless services," Journal of Optical Networking **8**(5), 471–487 (2009).

[35] H. Schmeckebier, G. Fiol, C. Meuer, D. Arsenijevic, and D. Bimberg, "Complete pulse characterization of quantum dot mode-locked lasers suitable for optical communication up to 160 Gbit/s," Optics express **18**(4), 3415–3425 (2010).

[36] I. Ogura, H. Kurita, T. Sasaki, and H. Yokoyama, "Precise operation-frequency control of monolithic mode-locked laser diodes for high-speed optical communication and all-optical signal processing," Optical and Quantum Electronics **33**(7-10), 709–725 (2001).

[37] J. Luo, N. Calabretta, J. Parra-Cetina, S. Latkowski, R. Maldonado-Basilio, P. Landais, and H. J. S. Dorren, "320 Gb/s all-optical clock recovery and time de-multiplexing after transmission enabled by single quantum dash mode-locked laser," Optics Letters **38**(22), 4805–4808 (2013).

[38] P. Delfyett, D. Hartman, and S. Ahmad, "Optical clock distribution using a mode-locked semiconductor laser diode system," Journal of Lightwave Technology **9**(12), 1646–1649 (1991).

[39] G. Berrettini, A. Bogoni, F. Fresi, G. Meloni, and L. Potì, "Evolution of Optical Sampling," in *Advances in Lasers and Electro Optics*, InTech ed., pp. 289—314 (Nelson Costa and Adolfo Cartaxo, 2010).

[40] M. Shirane, Y. Hashimoto, H. Yamada, and H. Yokoyama, "A compact optical sampling measurement system using mode-locked laser-diode modules," IEEE Photonics Technology Letters **12**(11), 1537–1539 (2000).

[41] O. Svelto and D. C. Hanna, *Principles of lasers* (Springer, New York, 2010).

[42] K. Sala, G. Kenney-Wallace, and G. Hall, "CW autocorrelation measurements of picosecond laser pulses," IEEE Journal of Quantum Electronics **16**(9), 990–996 (1980).

[43] S. Arahira, S. Kutsuzawa, Y. Matsui, D. Kunimatsu, and Y. Ogawa, "Generation of synchronized subterahertz optical pulse trains by repetition-frequency multiplication of a subharmonic synchronous mode-locked semiconductor laser diode using fiber dispersion," Photonics Technology Letters, IEEE **10**(2), 209–211 (1998).

[44] M. Xia, C. H. Kwok, M. G. Thompson, R. V. Penty, I. H. White, F. V. Dijk, A. Enard, F. Lelarge, and G.-H. Duan, "270 GHz, 580 fs optical pulse generation from a single-section quantum-dash Fabry-Pérot laser using frequency multiplication," in *International Quantum Electronics Conference* (2009).

[45] I. Kim and K. Lau, "Frequency and timing stability of mode-locked semiconductor lasers-passive and active mode locking up to millimeter wave frequencies," IEEE Journal of Quantum Electronics **29**(4), 1081–1090 (1993).

[46] S. Arahira, S. Kutsuzawa, Y. Matsui, and Y. Ogawa, "Higher order chirp compensation of femtosecond mode-locked semiconductor lasers using optical fibers with different

group-velocity dispersions," Selected Topics in Quantum Electronics, IEEE Journal of **2**(3), 480–486 (1996).

[47] M. J. Strain, P. M. Stolarz, and M. Sorel, "Passively Mode-Locked Lasers With Integrated Chirped Bragg Grating Reflectors," IEEE Journal of Quantum Electronics **47**(4), 492–499 (2011).

[48] D. Marcuse, "Computer simulation of laser photon fluctuations: Theory of single-cavity laser," IEEE Journal of Quantum Electronics **20**(10), 1139–1148 (1984).

[49] D. Marcuse, "Computer simulation of laser photon fluctuations: Single-cavity laser results," IEEE Journal of Quantum Electronics **20**(10), 1148–1155 (1984).

[50] C. Henry, "Phase noise in semiconductor lasers," Journal of Lightwave Technology **4**(3), 298–311 (1986).

[51] E. Rubiola, *Phase noise and frequency stability in oscillators*, The Cambridge RF and microwave engineering series (Cambridge University Press, Cambridge, UK; New York, 2009).

[52] R. Paschotta, A. Schlatter, S. Zeller, H. Telle, and U. Keller, "Optical phase noise and carrier-envelope offset noise of mode-locked lasers," Applied Physics B **82**(2), 265–273 (2005).

[53] R. Paschotta, "Derivation of the Schawlow - Townes Linewidth of Lasers," (2013).

[54] R. Paschotta, "Noise of mode-locked lasers (Part I): numerical model," Applied Physics B **79**(2), 153–162 (2004).

[55] R. Paschotta, "Noise of mode-locked lasers (Part II): timing jitter and other fluctuations," Applied Physics B **79**(2), 163–173 (2004).

[56] A. Demir, A. Mehrotra, and J. Roychowdhury, "Phase noise in oscillators: a unifying theory and numerical methods for characterization," Circuits and Systems I: Fundamental Theory and Applications, IEEE Transactions on **47**(5), 655–674 (2000).

[57] D. Eliyahu, R. A. Salvatore, and A. Yariv, "Effect of noise on the power spectrum of passively mode-locked lasers," Journal of the Optical Society of America B **14**(1), 167–174 (1997).

[58] F. Kéfélian, S. O'Donoghue, M. T. Todaro, J. G. McInerney, and G. Huyet, "RF Linewidth in Monolithic Passively Mode-Locked Semiconductor Laser," IEEE Photonics Technology Letters **20**(16), 1405–1407 (2008).

[59] M. Osinski and J. Buus, "Linewidth broadening factor in semiconductor lasers – An overview," IEEE Journal of Quantum Electronics **23**(1), 9–29 (1987).

[60] T. Habruseva, S. O'Donoghue, N. Rebrova, F. Kéfélian, S. P. Hegarty, and G. Huyet, "Optical linewidth of a passively mode-locked semiconductor laser," Optics letters **34**(21), 3307–3309 (2009).

[61] R. Rosales, K. Merghem, A. Martinez, F. Lelarge, A. Accard, and A. Ramdane, "Timing jitter from the optical spectrum in semiconductor passively mode locked lasers," Optics Express **20**(8), 9151–9160 (2012).

[62] E. Martin, R. Watts, L. Bramerie, A. Shen, H. Gariah, F. Blache, F. Lelarge, and L. Barry, "Terahertz-bandwidth coherence measurements of a quantum dash laser in passive and active mode-locking operation," Optics letters **37**(23), 4967–4969 (2012).

[63] G. P. Agrawal and R. Roy, "Effect of injection-current fluctuations on the spectral linewidth of semiconductor lasers," Physical Review A **37**(7), 2495–2501 (1988).

[64] L. D. Turner, K. P. Weber, C. J. Hawthorn, and R. E. Scholten, "Frequency noise characterisation of narrow linewidth diode lasers," Optics communications **201**(4), 391–397 (2002).

[65] R. Trebino, *Frequency-resolved optical gating: the measurement of ultrashort laser pulses* (Kluwer Academic, 2000).

[66] E. W. Van Stryland, "The effect of pulse to pulse variation on ultrashort pulsewidth measurements," Optics Communications **31**(1), 93–96 (1979).

[67] C. Iaconis and I. Walmsley, "Spectral phase interferometry for direct electric-field reconstruction of ultrashort optical pulses," Optics Letters **23**(10), 792–794 (1998).

[68] P. Kockaert, M. Peeters, S. Coen, P. Emplit, M. Haelterman, and O. Deparis, "Simple amplitude and phase measuring technique for ultrahigh-repetition-rate lasers," IEEE Photonics Technology Letters **12**(2), 187–189 (2000).

[69] M. Kwakernaak, R. Schreieck, A. Neiger, H. Jackel, E. Gini, and W. Vogt, "Spectral phase measurement of mode-locked diode laser pulses by beating sidebands generated by electrooptical mixing," IEEE Photonics Technology Letters **12**(12), 1677–1679 (2000).

[70] Z. Jiang, D. Leaird, and A. Weiner, "Optical arbitrary waveform generation and characterization using spectral line-by-line control," Journal of Lightwave Technology **24**(7), 2487–2494 (2006).

[71] C. Dorrer and I. Kang, "Simultaneous temporal characterization of telecommunication optical pulses and modulators by use of spectrograms," Optics Letters **27**(15), 1315 (2002).

[72] B. Szafraniec, A. Lee, J. Law, W. McAlexander, R. Pering, T. Tan, and D. Baney, "Swept coherent optical spectrum analysis," IEEE Transactions on Instrumentation and Measurement **53**(1), 203–215 (2004).

[73] T. Habruseva, S. O'Donoghue, N. Rebrova, D. Reid, L. Barry, D. Rachinskii, G. Huyet, and S. Hegarty, "Quantum-Dot Mode-Locked Lasers With Dual-Mode Optical Injection," IEEE Photonics Technology Letters **22**(6), 359–361 (2010).

[74] D. A. Reid, S. G. Murdoch, and L. P. Barry, "Stepped-heterodyne optical complex spectrum analyzer," Optics express **18**(19), 19,724–19,731 (2010).

[75] M. Sugawara, K. Mukai, Y. Nakata, H. Ishikawa, and A. Sakamoto, "Effect of homogeneous broadening of optical gain on lasing spectra in self-assembled $In_xGa_{1-x}As/GaAs$ quantum dot lasers," Physical Review B **61**(11), 7595–7603 (2000).

[76] T. Okoshi, K. Kikuchi, and A. Nakayama, "Novel method for high resolution measurement of laser output spectrum," Electronics Letters **16**(16), 630–631 (1980).

[77] M. Kourogi and M. Ohtsu, "Novel optical frequency discriminator for FM noise reduction of semiconductor lasers," Optics Communications **81**(3-4), 204–208 (1991).

[78] D. Von der Linde, "Characterization of the noise in continuously operating mode-locked lasers," Applied Physics B **39**(4), 201–217 (1986).

[79] L. A. Jiang, M. E. Grein, H. A. Haus, and E. P. Ippen, "Noise of mode-locked semiconductor lasers," Selected Topics in Quantum Electronics, IEEE Journal of **7**(2), 159–167 (2001).

[80] H. A. Haus and A. Mecozzi, "Noise of mode-locked lasers," Quantum Electronics, IEEE Journal of **29**(3), 983–996 (1993).

[81] L. Jiang, S. Wong, M. Grein, E. Ippen, and H. Haus, "Measuring timing jitter with optical cross correlations," IEEE Journal of Quantum Electronics **38**(8), 1047–1052 (2002).

[82] J. P. Tourrenc, A. Akrout, K. Merghem, A. Martinez, F. Lelarge, A. Shen, G. H. Duan, and A. Ramdane, "Experimental investigation of the timing jitter in self-pulsating quantum-dash lasers operating at 1.55 µm," Optics Express **16**(22), 17,706–17,713 (2008).

[83] S. Dawkins, J. McFerran, and A. Luiten, "Considerations on the measurement of the stability of oscillators with frequency counters," IEEE Transactions on Ultrasonics, Ferroelectrics, and Frequency Control **54**(5), 918–925 (2007).

[84] IEEE, "IEEE Standard Definitions of Physical Quantities for Fundamental Frequency and Time Metrology – Random Instabilities," IEEE Std 1139-2008 (Revision of IEEE Std 1139-1999) pp. 1–50 (2009).

[85] M. J. Heck, E. J. Salumbides, A. Renault, E. Bente, Y.-S. Oei, M. K. Smit, R. van Veldhoven, R. Nötzel, K. S. Eikema, and W. Ubachs, "Analysis of hybrid mode-locking

of two-section quantum dot lasers operating at 1.5 µm," Opt. Express17 (20) pp. 18,063–18,075 (2009).

[86] G. Carpintero, M. Thompson, R. Penty, and I. White, "Low Noise Performance of Passively Mode-Locked 10-GHz Quantum-Dot Laser Diode," IEEE Photonics Technology Letters **21**(6), 389–391 (2009).

[87] M. S. Tahvili, L. Du, M. J. R. Heck, R. Nötzel, M. K. Smit, and E. Bente, "Dual-wavelength passive and hybrid mode-locking of 3, 4.5 and 10 GHz InAs/InP (100) quantum dot lasers," Optics Express **20**(7), 8117–8135 (2012).

[88] T. Habruseva, D. Arsenijevic, M. Kleinert, D. Bimberg, G. Huyet, and S. P. Hegarty, "Optimum phase noise reduction and repetition rate tuning in quantum-dot mode-locked lasers," Applied Physics Letters **104**(2), 021,112 (2014).

[89] E. Sooudi, S. Sygletos, A. D. Ellis, G. Huyet, J. G. McInerney, F. Lelarge, K. Merghem, R. Rosales, A. Martinez, A. Ramdane, and S. Hegarty, "Optical Frequency Comb Generation Using Dual-Mode Injection-Locking of Quantum-Dash Mode-Locked Lasers: Properties and Applications," IEEE Journal of Quantum Electronics **48**(10), 1327–1338 (2012).

[90] H. A. Haus, "Modelocking of Semiconductor Laser Diodes," Japanese Journal of Applied Physics **20**(6), 1007 (1981).

[91] M. Thompson, A. Rae, M. Xia, R. Penty, and I. White, "InGaAs Quantum-Dot Mode-Locked Laser Diodes," IEEE Journal of Selected Topics in Quantum Electronics **15**(3), 661–672 (2009).

[92] A. Vladimirov and D. Turaev, "Model for passive mode locking in semiconductor lasers," Physical Review A **72**(3) (2005).

[93] D. I. Nikitichev, Y. Ding, M. A. Cataluna, E. U. Rafailov, L. Drzewietzki, S. Breuer, W. Elsaesser, M. Rossetti, P. Bardella, T. Xu, I. Montrosset, I. Krestnikov, D. Livshits, M. Ruiz, M. Tran, Y. Robert, and M. Krakowski, "High peak power and sub-picosecond Fourier-limited pulse generation from passively mode-locked monolithic two-section gain-guided tapered InGaAs quantum-dot lasers," Laser Physics **22**(4), 715–724 (2012).

[94] R. Scollo, H. J. Lohe, F. Robin, D. Erni, E. Gini, and H. Jackel, "Mode-Locked InP-Based Laser Diode With a Monolithic Integrated UTC Absorber for Subpicosecond Pulse Generation," IEEE Journal of Quantum Electronics **45**(4), 322–335 (2009).

[95] I. Kulkova, D. Larsson, E. Semenova, and K. Yvind, "Individual optimization of InAlGaAsP-InP sections for 1.55 µm passively mode-locked lasers," in *Semiconductor Laser Conference (ISLC), 2012 23rd IEEE International*, pp. 133–134 (2012).

[96] K. Yvind, D. Larsson, J. Mørk, J. M. Hvam, M. Thompson, R. Penty, and I. White, "Low-noise monolithic mode-locked semiconductor lasers through low-dimensional structures," in *Proceedings of SPIE*, A. A. Belyanin and P. M. Smowton, eds., vol. 6909, pp. 69,090A–69,090A–9 (2008).

[97] J. Mee, M. Crowley, D. Murrell, R. Raghunathan, and L. Lester, "Temperature Performance of Monolithic Passively Mode-Locked Quantum Dot Lasers: Experiments and Analytical Modeling," IEEE Journal of Selected Topics in Quantum Electronics **19**(4), 1101,110–1101,110 (2013).

[98] E. A. Viktorov, P. Mandel, A. G. Vladimirov, and U. Bandelow, "Model for mode locking in quantum dot lasers," Applied Physics Letters **88**(20), 201,102 (2006).

[99] A. G. Vladimirov, U. Bandelow, G. Fiol, D. Arsenijevic, M. Kleinert, D. Bimberg, A. Pimenov, and D. Rachinskii, "Dynamical regimes in a monolithic passively mode-locked quantum dot laser," JOSA B **27**(10), 2102–2109 (2010).

[100] M. Rossetti, P. Bardella, and I. Montrosset, "Time-Domain Travelling-Wave Model for Quantum Dot Passively Mode-Locked Lasers," IEEE Journal of Quantum Electronics **47**(2), 139–150 (2011).

[101] M. Radziunas, A. G. Vladimirov, E. A. Viktorov, G. Fiol, H. Schmeckebier, and D. Bimberg, "Pulse Broadening in Quantum-Dot Mode-Locked Semiconductor Lasers: Simulation, Analysis, and Experiments," IEEE Journal of Quantum Electronics **47**(7), 935–943 (2011).

[102] E. A. Viktorov, T. Habruseva, S. P. Hegarty, G. Huyet, and B. Kelleher, "Coherence and Incoherence in an Optical Comb," Physical Review Letters **112**(22), 224,101 (2014).

[103] R. Rosales, K. Merghem, A. Martinez, A. Akrout, J.-P. Tourrenc, A. Accard, F. Lelarge, and A. Ramdane, "InAs/InP Quantum-Dot Passively Mode-Locked Lasers for 1.55 µm Applications," IEEE Journal of Selected Topics in Quantum Electronics **17**(5), 1292–1301 (2011).

[104] C. Y. Lin, Y. C. Xin, Y. Li, F. L. Chiragh, and L. F. Lester, "Cavity design and characteristics of monolithic long-wavelength InAs/InP quantum dash passively mode-locked lasers," Opt. Express **17**(22), 19,739–19,748 (2009).

[105] M. Heck, A. Renault, E. Bente, Y.-S. Oei, M. Smit, K. Eikema, W. Ubachs, S. Anantathanasarn, and R. Nötzel, "Passively Mode-Locked 4.6 and 10.5 GHz Quantum Dot Laser Diodes Around 1.55 µm With Large Operating Regime," IEEE Journal of Selected Topics in Quantum Electronics **15**(3), 634–643 (2009).

[106] L. Tiemeijer, P. I. Kuindersma, P. Thijs, and G. Rikken, "Passive FM locking in InGaAsP semiconductor lasers," IEEE Journal of Quantum Electronics **25**(6), 1385–1392 (1989).

[107] S. Chinn and E. Swanson, "Passive FM locking and pulse generation from 980-nm strained-quantum-well Fabry-Pérot lasers," IEEE Photonics Technology Letters **5**(9), 969–971 (1993).

[108] W. Yang, "Single-Section Fabry-Pérot Mode-Locked Semiconductor Lasers," Advances in OptoElectronics **2011**, 1–11 (2011).

[109] C. Gosset, K. Merghem, A. Martinez, G. Moreau, G. Patriarche, G. Aubin, A. Ramdane, J. Landreau, and F. Lelarge, "Subpicosecond pulse generation at 134GHz using a quantum-dash-based Fabry-Pérot laser emitting at 1.56 µm," Applied Physics Letters **88**(24), 241,105 (2006).

[110] K. Merghem, A. Akrout, A. Martinez, G. Aubin, A. Ramdane, F. Lelarge, and G.-H. Duan, "Pulse generation at 346 GHz using a passively mode locked quantum-dash-based laser at 1.55 µm," Applied Physics Letters **94**(2), 021,107–021,107–3 (2009).

[111] S. Latkowski, R. Maldonado-Basilio, and P. Landais, "Sub-picosecond pulse generation by 40-GHz passively mode-locked quantum-dash 1-mm-long Fabry-Pérot laser diode," Optics Express **17**(21), 19,166–19,172 (2009).

[112] R. Maldonado-Basilio, J. Parra-Cetina, S. Latkowski, and P. Landais, "Timing-jitter, optical, and mode-beating linewidths analysis on subpicosecond optical pulses generated by a quantum-dash passively mode-locked semiconductor laser," Optics letters **35**(8), 1184–1186 (2010).

[113] J. Renaudier, R. Brenot, B. Dagens, F. Lelarge, B. Rousseau, F. Poingt, O. Legouezigou, F. Pommereau, A. Accard, P. Gallion, and G.-H. Duan, "45 GHz self-pulsation with narrow linewidth in quantum dot Fabry-Pérot semiconductor lasers at 1.5 µm," Electronics Letters **41**(18), 1007 (2005).

[114] Z. G. Lu, J. R. Liu, S. Raymond, P. J. Poole, P. J. Barrios, and D. Poitras, "312-fs pulse generation from a passive C-band InAs/InP quantum dot mode-locked laser," Opt. Express **16**(14), 10,835–10,840 (2008).

[115] J. Liu, Z. Lu, S. Raymond, P. J. Poole, P. J. Barrios, and D. Poitras, "Dual-wavelength 92.5 GHz self-mode-locked InP-based quantum dot laser," Optics letters **33**(15), 1702–1704 (2008).

[116] F. Lelarge, B. Dagens, J. Renaudier, R. Brenot, A. Accard, F. Van Dijk, D. Make, O. Le Gouezigou, J. Provost, F. Poingt, J. Landreau, O. Drisse, E. Derouin, B. Rousseau, F. Pommereau, and G.-H. Duan, "Recent Advances on InAs/InP Quantum Dash Based Semiconductor Lasers and Optical Amplifiers Operating at 1.55 μm," IEEE Journal of Selected Topics in Quantum Electronics **13**(1), 111–124 (2007).

[117] K. Shore and W. M. Yee, "Theory of self-locking FM operation in semiconductor lasers," Optoelectronics, IEE Proceedings J **138**(2), 91–96 (1991).

[118] P. Landais, J. Renaudier, P. Gallion, and G.-H. Duan, "Analysis of self-pulsation in a distributed Bragg reflector laser based on four-wave mixing," in *Integrated Optoelectronic Devices 2004*, pp. 262–270 (2004).

[119] G. Gray and G. Agrawal, "Importance of self-induced carrier-density modulation in semiconductor lasers," IEEE Photonics Technology Letters **4**(11), 1216–1219 (1992).

[120] A. Bogatov, P. Eliseev, and B. Sverdlov, "Anomalous interaction of spectral modes in a semiconductor laser," Quantum Electronics, IEEE Journal of **11**(7), 510–515 (1975).

[121] M. Alalusi and B. Darling, "Effects of nonlinear gain on mode-hopping in semiconductor laser diodes," IEEE Journal of Quantum Electronics **31**(7), 1181–1192 (1995).

[122] M. Ahmed and M. Yamada, "Influence of instantaneous mode competition on the dynamics of semiconductor lasers," IEEE Journal of Quantum Electronics **38**(6), 682–693 (2002).

[123] W. Yang, "Picosecond Dynamics of Semiconductor Fabry-Pérot Lasers: A Simplified Model," IEEE Journal of Selected Topics in Quantum Electronics **13**(5), 1235–1241 (2007).

[124] Y. Wang, Y. Mao, Y. Chen, X. Wang, and H. Su, "Random Population Model for Self Pulsation in Single-Section Quantum-Dot Lasers," IEEE Photonics Technology Letters **25**(4), 389–392 (2013).

[125] Z. Jiao, R. Zhang, X. Zhang, J. Liu, and Z. Lu, "Modeling of Single-Section Quantum Dot Mode-Locked Lasers: Impact of Group Velocity Dispersion and Self Phase Modulation," IEEE Journal of Quantum Electronics **49**(12), 1008–1015 (2013).

[126] Y. Arakawa and H. Sakaki, "Multidimensional quantum well laser and temperature dependence of its threshold current," Applied Physics Letters **40**(11), 939–941 (1982).

[127] M. Asada, Y. Miyamoto, and Y. Suematsu, "Gain and the threshold of three-dimensional quantum-box lasers," Quantum Electronics, IEEE Journal of **22**(9), 1915–1921 (1986).

[128] D. Deppe, H. Huang, and O. Shchekin, "Modulation characteristics of quantum-dot lasers: the influence of p-type doping and the electronic density of states on obtaining high speed," IEEE Journal of Quantum Electronics **38**(12), 1587–1593 (2002).

[129] P. Borri, S. Schneider, W. Langbein, and D. Bimberg, "Ultrafast carrier dynamics in InGaAs quantum dot materials and devices," Journal of Optics A: Pure and Applied Optics **8**(4), S33–S46 (2006).

[130] M. Gioannini, "Numerical Modeling of the Emission Characteristics of Semiconductor Quantum Dash Materials for Lasers and Optical Amplifiers," IEEE Journal of Quantum Electronics **40**(4), 364–373 (2004).

[131] M. Sugawara, N. Hatori, H. Ebe, M. Ishida, Y. Arakawa, T. Akiyama, K. Otsubo, and Y. Nakata, "Modeling room-temperature lasing spectra of 1.3 µm self-assembled InAs/GaAs quantum-dot lasers: Homogeneous broadening of optical gain under current injection," Journal of Applied Physics **97**(4), 043,523 (2005).

[132] M. Gioannini, "Analysis of the Optical Gain Characteristics of Semiconductor Quantum-Dash Materials Including the Band Structure Modifications Due to the Wetting Layer," IEEE Journal of Quantum Electronics **42**(3), 331–340 (2006).

[133] H. Dery and G. Eisenstein, "Self-consistent rate equations of self-assembly quantum wire lasers," IEEE Journal of Quantum Electronics **40**(10), 1398–1409 (2004).

[134] M. Gioannini and I. Montrosset, "Numerical Analysis of the Frequency Chirp in Quantum-Dot Semiconductor Lasers," IEEE Journal of Quantum Electronics **43**(10), 941–949 (2007).

[135] D. Bimberg, N. Kirstaedter, N. N. Ledentsov, Z. I. Alferov, P. S. Kop'ev, and V. M. Ustinov, "InGaAs-GaAs quantum-dot lasers," Selected Topics in Quantum Electronics, IEEE Journal of **3**(2), 196–205 (1997).

[136] W. Chow, M. Lorke, and F. Jahnke, "Will Quantum Dots Replace Quantum Wells As the Active Medium of Choice in Future Semiconductor Lasers?" IEEE Journal of Selected Topics in Quantum Electronics **17**(5), 1349–1355 (2011).

[137] I. I. Novikov, N. Y. Gordeev, L. Y. Karachinskii, M. V. Maksimov, Y. M. Shernyakov, A. R. Kovsh, I. L. Krestnikov, A. V. Kozhukhov, S. S. Mikhrin, and N. N. Ledentsov, "Effect of p-doping of the active region on the temperature stability of InAs/GaAs QD lasers," Semiconductors **39**(4), 477–480 (2005).

[138] M. van der Poel, J. Mørk, A. Somers, A. Forchel, J. P. Reithmaier, and G. Eisenstein, "Ultrafast gain and index dynamics of quantum dash structures emitting at 1.55 µm," Applied Physics Letters **89**(8), 081,102 (2006).

[139] H. S. Djie, C. L. Tan, B. S. Ooi, J. C. M. Hwang, X.-M. Fang, Y. Wu, J. M. Fastenau, W. K. Liu, G. T. Dang, and W. H. Chang, "Ultrabroad stimulated emission from quantum-dash laser," Applied Physics Letters **91**(11), 111,116 (2007).

[140] J. P. Reithmaier, A. Somers, S. Deubert, R. Schwertberger, W. Kaiser, A. Forchel, M. Calligaro, P. Resneau, O. Parillaud, S. Bansropun, M. Krakowski, R. Alizon, D. Hadass, A. Bilenca, H. Dery, V. Mikhelashvili, G. Eisenstein, M. Gioannini, I. Montrosset, T. W. Berg, M. v. d. Poel, J. Mørk, and B. Tromborg, "InP based lasers and optical amplifiers with wire-/dot-like active regions," Journal of Physics D: Applied Physics **38**(13), 2088–2102 (2005).

[141] M. Sugawara, *Self-assembled InGaAs/GaAs quantum dots* (Academic, San Diego, CA; London, 1999).

[142] D. Bimberg, M. Grundmann, and N. N. Ledentsov, *Quantum dot heterostructures* (John Wiley, Chichester [England]; New York, 1999).

[143] J. J. Plant, J. T. Gopinath, B. Chann, D. J. Ripin, R. K. Huang, and P. W. Juodawlkis, "250 mW, 1.5 µm monolithic passively mode-locked slab-coupled optical waveguide laser," Optics Letters **31**(2), 223–225 (2006).

[144] M. Silver and E. O'Reilly, "Optimization of long wavelength InGaAsP strained quantum-well lasers," IEEE Journal of Quantum Electronics **31**(7), 1193–1200 (1995).

[145] N. N. Ledentsov, "Quantum dot laser," Semiconductor Science and Technology **26**(1), 014,001 (2011).

[146] D. Bimberg and U. W. Pohl, "Quantum dots: promises and accomplishments," Materials Today **14**(9), 388–397 (2011).

[147] Innolume GmbH, http://www.innolume.com/technology/quantum_dots.htm.

[148] QD Laser, Inc., http://www.qdlaser.com.

[149] C. Paranthoen, N. Bertru, O. Dehaese, A. L. Corre, S. Loualiche, B. Lambert, and G. Patriarche, "Height dispersion control of InAs/InP quantum dots emitting at 1.55 µm," Applied Physics Letters **78**(12), 1751–1753 (2001).

[150] P. Caroff, C. Paranthoen, C. Platz, O. Dehaese, H. Folliot, N. Bertru, C. Labbé, R. Piron, E. Homeyer, A. L. Corre, and S. Loualiche, "High-gain and low-threshold InAs quantum-dot lasers on InP," Applied Physics Letters **87**(24), 243,107 (2005).

[151] A. Lenz, F. Genz, H. Eisele, L. Ivanova, R. Timm, D. Franke, H. Künzel, U. W. Pohl, and M. Dähne, "Formation of InAs/InGaAsP quantum-dashes on InP(001)," Applied Physics Letters **95**(20), 203,105 (2009).

[152] S. C. Heck, S. Osborne, S. B. Healy, E. P. O'Reilly, F. Lelarge, F. Poingt, O. Le Gouezigou, and A. Accard, "Experimental and Theoretical Study of InAs/InGaAsP/InP Quantum Dash Lasers," IEEE Journal of Quantum Electronics **45**(12), 1508–1516 (2009).

[153] K. Merghem, R. Rosales, A. Martinez, G. Patriarche, A. Ramdane, N. Chimot, F. Van Dijk, Y. Moustapha-Rabault, F. Poingt, and F. Lelarge, "Improvement of modal gain of InAs/InP quantum-dash lasers," in *Compound Semiconductor Week (CSW/IPRM), 2011 and 23rd International Conference on Indium Phosphide and Related Materials*, pp. 1–4 (2011).

[154] O. Mollet, A. Martinez, K. Merghem, S. Joshi, J.-G. Provost, F. Lelarge, and A. Ramdane, "Dynamic characteristics of undoped and p-doped Fabry-Perot InAs/InP quantum dash based ridge waveguide lasers for access/metro networks," Applied Physics Letters **105**(14), 141,113 (2014).

[155] R. Rosales, "InAs/InP quantum dash mode-locked lasers for optical communications," Ph.D. thesis, Université Pierre et Marie Curie (2012).

[156] G. P. Agrawal and N. K. Dutta, *Semiconductor Lasers* (Springer US, Boston, MA, 1995).

[157] A. R. Adams, I. P. Marko, N. F. Mass, and S. J. Sweeney, "Effect of non-pinned carrier density above threshold in InAs quantum dot and quantum dash lasers," IET Optoelectronics **8**(2), 88–93 (2014).

[158] P. M. Smowton and P. Blood, "On the determination of internal optical mode loss of semiconductor lasers," Applied Physics Letters **70**(18), 2365–2367 (1997).

[159] H. Dery, "On the nature of quantum dash structures," Journal of Applied Physics **95**(11), 6103 (2004).

[160] D. Bimberg and C. Ribbat, "Quantum dots: lasers and amplifiers," Microelectronics Journal **34**(5-8), 323–328 (2003).

[161] S. Bouchoule, S. Azouigui, S. Guilet, G. Patriarche, L. Largeau, A. Martinez, L. L. Gratiet, A. Lemaitre, and F. Lelarge, "Anisotropic and Smooth Inductively Coupled Plasma Etching of III-V Laser Waveguides Using HBr-O_2 Chemistry," Journal of The Electrochemical Society **155**(10), H778–H785 (2008).

[162] L. Gatilova, S. Bouchoule, S. Guilet, and P. Chabert, "Investigation of InP etching mechanisms in a Cl_2/H_2 inductively coupled plasma by optical emission spectroscopy," Journal of Vacuum Science & Technology A **27**(2), 262–275 (2009).

[163] I. Ladany, "Laser to single-mode fiber coupling in the laboratory," Applied Optics **32**(18), 3233–3236 (1993).

[164] W. Bludau and R. Rossberg, "Characterization of laser-to-fiber coupling techniques by their optical feedback," Applied Optics **21**(11), 1933–1939 (1982).

[165] S. Pralgauskaitė, V. Palenskis, J. Matukas, B. Šaulys, V. Kornijčuk, and V. Verdingovas, "Analysis of mode-hopping effect in Fabry-Pérot multiple-quantum well laser diodes via low frequency noise investigation," Solid-State Electronics **79**, 104–110 (2013).

[166] F. Kéfélian, S. O'Donoghue, M. T. Todaro, J. McInerney, and G. Huyet, "Experimental investigation of different regimes of mode-locking in a high repetition rate passively mode-locked semiconductor quantum-dot laser," Optics Express **17**(8), 6258–6267 (2009).

[167] C. Mesaritakis, C. Simos, H. Simos, S. Mikroulis, I. Krestnikov, and D. Syvridis, "Pulse width narrowing due to dual ground state emission in quantum dot passively mode locked lasers," Applied Physics Letters **96**(21), 211,110 (2010).

[168] C. Mesaritakis, C. Simos, H. Simos, I. Krestnikov, and D. Syvridis, "Dual ground-state pulse generation from a passively mode-locked InAs/InGaAs quantum dot laser," Applied Physics Letters **99**(14), 141,109–141,109 (2011).

[169] J. Ratner, G. Steinmeyer, T. C. Wong, R. Bartels, and R. Trebino, "Coherent artifact in modern pulse measurements," Opt. Lett. **37**(14), 2874–2876 (2012).

[170] S. G. Murdoch, R. T. Watts, Y. Q. Xu, R. Maldonado-Basilio, J. Parra-Cetina, S. Latkowski, P. Landais, and L. P. Barry, "Spectral amplitude and phase measurement of a 40 GHz free-running quantum-dash modelocked laser diode," Optics Express **19**(14), 13,628–13,635 (2011).

[171] R. Watts, R. Rosales, F. Lelarge, A. Ramdane, and L. Barry, "Mode coherence measurements across a 1.5 THz spectral bandwidth of a passively mode-locked quantum dash laser," Optics Letters **37**(9), 1499–1501 (2012).

[172] G. Agrawal, *Nonlinear Fiber Optics*, Optics and Photonics (Elsevier Science, 2001).

[173] L. Xu, E. Zeek, and R. Trebino, "Measuring very complex ultrashort pulses using Frequency-Resolved Optical Gating (FROG)," in *Lasers and Electro-Optics, 2008 and 2008 Conference on Quantum Electronics and Laser Science. CLEO/QELS 2008. Conference on*, pp. 1–2 (2008).

[174] K. DeLong, D. Fittinghoff, and R. Trebino, "Practical issues in ultrashort-laser-pulse measurement using frequency-resolved optical gating," IEEE Journal of Quantum Electronics **32**(7), 1253–1264 (1996).

[175] Corning Incorporated, *Corning® SMF-28e+™ Optical Fiber with NexCor® Technology Product Information* (2006).

[176] D. J. Jones, K. W. Holman, M. Notcutt, J. Ye, J. Chandalia, L. A. Jiang, E. P. Ippen, and H. Yokoyama, "Ultralow-jitter, 1550-nm mode-locked semiconductor laser synchronized to a visible optical frequency standard," Optics Letters **28**(10), 813–815 (2003).

[177] A. Criado, C. De Dios, P. Acedo, G. Carpintero, and K. Yvind, "Comparison of Monolithic Optical Frequency Comb Generators Based on Passively Mode-Locked Lasers for Continuous Wave mm-Wave and Sub-THz Generation," Journal of Lightwave Technology **30**(19), 3133–3141 (2012).

[178] J. S. Parker, A. Bhardwaj, P. R. A. Binetti, Y.-J. Hung, and L. A. Coldren, "Monolithically Integrated Gain-Flattened Ring Mode-Locked Laser for Comb-Line Generation," IEEE Photonics Technology Letters **24**(2), 131–133 (2012).

[179] T. Erdogan, "Fiber grating spectra," Journal of Lightwave Technology **15**(8), 1277–1294 (1997).

[180] K. Sato, A. Hirano, and H. Ishii, "Chirp-compensated 40-GHz mode-locked lasers integrated with electroabsorption modulators and chirped gratings," IEEE Journal of Selected Topics in Quantum Electronics **5**(3), 590–595 (1999).

[181] J. Akbar, L. Hou, M. Haji, M. Strain, J. Marsh, A. Bryce, and A. Kelly, "High-Power AlGaInAs Mode-Locked DBR Laser With Integrated Tapered Optical Amplifier," IEEE Photonics Technology Letters **25**(3), 253–256 (2013).

[182] M. Schell, M. Tsuchiya, and T. Kamiya, "Chirp and stability of mode-locked semiconductor lasers," IEEE Journal of Quantum Electronics **32**(7), 1180–1190 (1996).

[183] S. Diddams and J.-C. Diels, "Dispersion measurements with white-light interferometry," JOSA B **13**(6), 1120–1129 (1996).

[184] C. Palavicini, Y. Jaouën, G. Debarge, E. Kerrinckx, Y. Quiquempois, M. Douay, C. Lepers, A.-F. Obaton, and G. Melin, "Phase-sensitive optical low-coherence reflectometry technique applied to the characterization of photonic crystal fiber properties," Optics Letters **30**(4), 361–363 (2005).

[185] K. Naganuma, "Semiconductor laser cavity dispersion measurement based on interferometric crosscorrelation of amplified spontaneous emission," Applied Physics Letters **64**(3), 261–263 (1994).

[186] C. Palavicini, G. Campuzano, B. Thedrez, Y. Jaouën, and P. Gallion, "Analysis of optical-injected distributed feedback lasers using complex optical low-coherence reflectometry," IEEE Photonics Technology Letters **15**(12), 1683–1685 (2003).

[187] M. Bagnell, J. Davila-Rodriguez, A. Ardey, and P. J. Delfyett, "Dispersion measurements of a 1.3 µm quantum dot semiconductor optical amplifier over 120 nm of spectral bandwidth," Applied Physics Letters **96**(21), 211,907 (2010).

[188] Y. Gottesman, E. V. K. Rao, H. Sillard, and J. Jacquet, "Modeling of optical low coherence reflectometry recorded Bragg reflectograms: Evidence to a decisive role of Bragg spectral selectivity," Journal of Lightwave Technology **20**(3), 489–493 (2002).

[189] A. Parini, P. Hamel, A. De Rossi, S. Combrie, N.-V.-Q. Tran, Y. Gottesman, R. Gabet, A. Talneau, Y. Jaouën, and G. Vadala, "Time-Wavelength Reflectance Maps of Photonic Crystal Waveguides: A New View on Disorder-Induced Scattering," Journal of Lightwave Technology **26**(23), 3794–3802 (2008).

[190] U. Glombitza and E. Brinkmeyer, "Coherent frequency-domain reflectometry for characterization of single-mode integrated-optical waveguides," Journal of Lightwave Technology **11**(8), 1377–1384 (1993).

[191] E. D. Moore, "Advances in Swept-Wavelength Interferometry for Precision Measurements," Ph.D. thesis, University of Colorado (2011).

[192] B. J. Soller, D. K. Gifford, M. S. Wolfe, and M. E. Froggatt, "High resolution optical frequency domain reflectometry for characterization of components and assemblies," Optics Express **13**(2), 666–674 (2005).

[193] E. D. Moore and R. R. McLeod, "Phase-sensitive swept-source interferometry for absolute ranging with application to measurements of group refractive index and thickness," Optics Express **19**(9), 8117–8126 (2011).

[194] Z. Ding, T. Liu, Z. Meng, K. Liu, Q. Chen, Y. Du, D. Li, and X. S. Yao, "Note: Improving spatial resolution of optical frequency-domain reflectometry against frequency tuning nonlinearity using non-uniform fast Fourier transform," Review of Scientific Instruments **83**(6), 066,110–066,110–3 (2012).

[195] T.-J. Ahn, Y. Jung, K. Oh, and D. Y. Kim, "Optical frequency-domain chromatic dispersion measurement method for higher-order modes in an optical fiber," Optics Express **13**(25), 10,040–10,048 (2005).

[196] T.-J. Ahn, J. Y. Lee, and D. Y. Kim, "Suppression of nonlinear frequency sweep in an optical frequency-domain reflectometer by use of Hilbert transformation," Applied Optics **44**(35), 7630 (2005).

[197] C. Froehly, B. Colombeau, and M. Vampouille, "II Shaping and Analysis of Picosecond Light Pulses," in *Progress in Optics*, E. Wolf, ed., vol. Volume 20, pp. 63–153 (Elsevier, 1983).

[198] M. F. Roelens, S. Frisken, J. Bolger, D. Abakoumov, G. Baxter, S. Poole, and B. Eggleton, "Dispersion Trimming in a Reconfigurable Wavelength Selective Switch," Journal of Lightwave Technology **26**(1), 73–78 (2008).

[199] Finisar, "WaveShaper 1000S Programmable Optical Filter," http://www.finisar.com/products/optical-instrumentation/WaveShaper-1000S (2013).

[200] K. Naganuma and H. Yasaka, "Group delay and α-parameter measurement of 1.3 µm semiconductor traveling-wave optical amplifier using the interferometric method," IEEE Journal of Quantum Electronics **27**(6), 1280–1287 (1991).

[201] N. Cvijetic, "OFDM for Next-Generation Optical Access Networks," Journal of Lightwave Technology **30**(4), 384–398 (2012).

[202] D. Hillerkuss, R. Schmogrow, T. Schellinger, M. Jordan, M. Winter, G. Huber, T. Vallaitis, R. Bonk, P. Kleinow, F. Frey, M. Roeger, S. Koenig, A. Ludwig, A. Marculescu, J. Li, M. Hoh, M. Dreschmann, J. Meyer, S. Ben Ezra, N. Narkiss, B. Nebendahl, F. Parmigiani, P. Petropoulos, B. Resan, A. Oehler, K. Weingarten, T. Ellermeyer, J. Lutz, M. Moeller, M. Huebner, J. Becker, C. Koos, W. Freude, and J. Leuthold, "26 Tbit s^{-1} line-rate super-channel transmission utilizing all-optical fast Fourier transform processing," Nature Photonics **5**(6), 364–371 (2011).

[203] D. Hillerkuss, R. Schmogrow, M. Meyer, S. Wolf, M. Jordan, P. Kleinow, N. Lindenmann, P. Schindler, A. Melikyan, X. Yang, S. Ben-Ezra, B. Nebendahl, M. Dreschmann, J. Meyer, F. Parmigiani, P. Petropoulos, B. Resan, A. Oehler, K. Weingarten, L. Altenhain, T. Ellermeyer, M. Moeller, M. Huebner, J. Becker, C. Koos, W. Freude, and J. Leuthold, "Single-Laser 32.5 Tbit/s Nyquist WDM Transmission," Journal of Optical Communications and Networking **4**(10), 715–723 (2012).

[204] J. Armstrong, "OFDM for Optical Communications," Journal of Lightwave Technology **27**(3), 189–204 (2009).

[205] C. Browning, "Orthogonal Frequency Division Multiplexing for Next Generation Optical Networks," Ph.D. thesis, Dublin City University (2013).

[206] R. Shafik, S. Rahman, R. Islam, and N. Ashraf, "On the error vector magnitude as a performance metric and comparative analysis," in *International Conference on Emerging Technologies, 2006. ICET '06*, pp. 27–31 (2006).

[207] M. D. McKinley, K. A. Remley, M. Myslinski, J. S. Kenney, D. Schreurs, and B. Nauwelaers, "EVM calculation for broadband modulated signals," in *64th ARFTG Conf. Dig*, pp. 45–52 (2004).

[208] V. Vujicic, P. Anandarajah, C. Browning, and L. Barry, "WDM-OFDM-PON Based on Compatible SSB Technique Using a Mode Locked Comb Source," IEEE Photonics Technology Letters **25**(21), 2058–2061 (2013).

[209] P. Ji, D. Qian, K. Kanonakis, C. Kachris, and I. Tomkos, "Design and Evaluation of a Flexible-Bandwidth OFDM-Based Intra-Data Center Interconnect," IEEE Journal of Selected Topics in Quantum Electronics **19**(2), 3700,310–3700,310 (2013).

[210] A. Sano, H. Masuda, E. Yoshida, T. Kobayashi, E. Yamada, Y. Miyamoto, F. Inuzuka, Y. Hibino, Y. Takatori, K. Hagimoto, T. Yamada, and Y. Sakamaki, "30 x 100-Gb/s all-optical OFDM transmission over 1300 km SMF with 10 ROADM nodes," in *2007 33rd European Conference and Exhibition of Optical Communication - Post-Deadline Papers (published 2008)*, pp. 1–2 (2007).

[211] B. Schmidt, A. Lowery, and J. Armstrong, "Experimental Demonstrations of Electronic Dispersion Compensation for Long-Haul Transmission Using Direct-Detection Optical OFDM," Journal of Lightwave Technology **26**(1), 196–203 (2008).

[212] M. Schuster, S. Randel, C. A. Bunge, S. Lee, F. Breyer, B. Spinnler, and K. Petermann, "Spectrally Efficient Compatible Single-Sideband Modulation for OFDM Transmission With Direct Detection," IEEE Photonics Technology Letters **20**(9), 670–672 (2008).

[213] Z. Xu, M. O'Sullivan, and R. Hui, "OFDM system implementation using compatible SSB modulation with a dual-electrode MZM," Optics Letters **35**(8), 1221–1223 (2010).

[214] Y. Zhang, M. O'Sullivan, and R. Hui, "Theoretical and experimental investigation of compatible SSB modulation for single channel long-distance optical OFDM transmission," Optics Express **18**(16), 16,751–16,764 (2010).

[215] Eagleyard Photonics GmbH, "Relative Intensity Noise of Distributed Feedback Lasers," URL http://www.eagleyard.com.

[216] Y. Ben M'Sallem, Q. T. Le, L. Bramerie, Q.-T. Nguyen, E. Borgne, P. Besnard, A. Shen, F. Lelarge, S. LaRochelle, L. Rusch, and J. C. Simon, "Quantum-Dash Mode-Locked Laser as a Source for 56-Gb/s DQPSK Modulation in WDM Multicast Applications," IEEE Photonics Technology Letters **23**(7), 453–455 (2011).

[217] R. Watts, S. G. Murdoch, and L. Barry, "Spectral linewidth reduction of single-mode and mode-locked lasers using a feed-forward heterodyne detection scheme," in *CLEO: 2014*, OSA Technical Digest (online), p. STh3O.8 (Optical Society of America, 2014).

[218] J. Parker, M. Lu, H. Park, A. Sivananthan, E. Bloch, Z. Griffith, L. Johansson, M. Rodwell, and L. Coldren, "Highly-Stable Integrated InGaAsP/InP Mode-Locked Laser and Optical Phase-Locked Loop," IEEE Photonics Technology Letters **25**(18), 1851–1854 (2013).

[219] T.-J. Ahn, Y. Park, and J. Azaña, "Ultrarapid Optical Frequency-Domain Reflectometry Based Upon Dispersion-Induced Time Stretching: Principle and Applications," IEEE Journal of Selected Topics in Quantum Electronics **18**(1), 148–165 (2012).

List of Publications

Peer-reviewed Journals

[a] **C. Calò**, V. Vujicic, R. Watts, C. Browning, K. Merghem, V. Panapakkam, F. Lelarge, A. Martinez, B.-E. Benkelfat, A. Ramdane, and L. P. Barry, "Single-section quantum well mode-locked laser for 400 Gbit/s SSB-OFDM transmission," *Submitted to Optics Express* (2015).

[b] S. Joshi, **C. Calò**, N. Chimot, M. Radziunas, R. Arkhipov, S. Barbet, A. Accard, A. Ramdane, and F. Lelarge, "Quantum dash based single section mode locked lasers for photonic integrated circuits," *Optics Express* Vol. 22, Issue 9, pp. 11254-11266 (2014).

[c] **C. Calò**, H. Schmeckebier, K. Merghem, R. Rosales, F. Lelarge, A. Martinez, D. Bimberg and A. Ramdane, "Frequency resolved optical gating characterization of sub-ps pulses from single-section InAs/InP quantum dash based mode-locked lasers," *Optics Express*, Vol. 22, Issue 2, pp. 1742-1748 (2014).

[d] K. Merghem, **C. Calò**, R. Rosales, X. Lafosse, G. Aubin, A. Martinez, F. Lelarge and A. Ramdane, "Stability of Optical Frequency Comb Generated with InAs/InP Quantum-Dash-Based Passive Mode-Locked Lasers," *IEEE Journal of Quantum Electronics*, Vol. 50, Issue 4, pp. 275-280 (2014).

[e] K. Klaime, **C. Calò**, R. Piron, C. Paranthoen, D. Thiam, T. Batte, O. Dehaese, J. Le Pouliquen, S. Loualiche, A. Le Corre, K. Merghem, A. Martinez, and A. Ramdane, "23 and 39 GHz low phase noise monosection InAs/InP (113)B quantum dots mode-locked lasers," *Optics Express*, Vol. **21**, Iss. 23, pp. 29000-29005 (2013).

[f] R. Rosales, K. Merghem, **C. Calò**, G. Bouwmans, I. Krestnikov, A. Martinez, and A. Ramdane, "Optical pulse generation in single section InAs/GaAs quantum dot edge emitting lasers under continuous wave operation," *Applied Physics Letters* **101**, 221113 (2012).

Invited International Conferences

[g] A. Martinez, **C. Calò**, R. Rosales, R. T. Watts, K. Merghem, A. Accard, F. Lelarge, L. P. Barry, A. Ramdane, "Quantum dot mode locked lasers for coherent frequency comb

generation," Invited talk at the *SPIE Photonics West Conference 2014*, San Francisco, 1-6$^{\text{th}}$ February (2014).

[h] R.T. Watts, R. Rosales, C. Browning, E. Martin, K. Merghem, **C. Calò**, A. Martinez, A. Ramdane, and L.P. Barry, "Generation and Characterization of Optical Frequency Comb for Photonic Systems," Invited talk at the *International Conference on Fiber Optics and Photonics (Photonics 2012)*, Madras, 9-12$^{\text{th}}$ December (2012).

[i] R. Rosales, R. T. Watts, K. Merghem, **C. Calò**, A. Martinez, A. Accard, F. Lelarge, L.P. Barry, and A. Ramdane, "Quantum Dash Mode Locked Lasers as Optical Comb Sources for OFDM Superchannels," Invited talk at the *European Conference on Optical Communication (ECOC 2012)*, Amsterdam, 17-20$^{\text{th}}$ September (2012).

[j] R. Rosales, R. T. Watts, K. Merghem, **C. Calò**, A. Martinez, L. P. Barry, and A. Ramdane, "1.55 µm InAs/InP quantum dash based mode locked lasers for coherent optical frequency combs," Invited talk at *Nonlinear Dynamics in Semiconductor Lasers (NDSL 2012)*, 12-14$^{\text{th}}$ September (2012).

[k] R. Rosales, R.T. Watts, K. Merghem, **C. Calò**, A. Martinez, L.P. Barry, A. Ramdane, "Quantum Dot Mode Locked Lasers for OFDM Applications," Invited talk at the *International Nano-Optoelectronics Workshop (i-NOW 2012)*, Berkeley and Stanford, 7-15$^{\text{th}}$ August (2012).

[l] R. Rosales, R. T. Watts, K. Merghem, **C. Calò**, A. Martinez, A. Accard, F. Lelarge, L. P. Barry, and A. Ramdane, "Quantum dot mode locked lasers for coherent frequency comb generation," Invited talk at the *15$^{\text{th}}$ International Conference of Laser Optics (LO2012)*, St. Petersburg, 25-29$^{\text{th}}$ June, WeR3-28 (2012).

International Conferences

[m] J. Pfeifle, R. Watts, I. Shkarban, S. Wolf, V. Vujicic, P. Landais, N. Chimot, S. Joshi, K. Merghem, **C. Calò**, M. Weber, A. Ramdane, F. Lelarge, L. Barry, W. Freude, and C. Koos, "Simultaneous Phase Noise Reduction of 30 Comb Lines from a Quantum-Dash Mode-Locked Laser Diode Enabling Coherent Tbit/s Data Transmission," Talk at the Optical Fiber Communication Conference (OFC 2015), Los Angeles, 22-26$^{\text{th}}$ March (2015).

[n] V. Vujicic, **C. Calò**, R. Watts, F. Lelarge, C. Browning, K. Merghem, A. Martinez, A. Ramdane, and L. P. Barry, "Quantum Dash Passively Mode-Locked Lasers for Tbit/s Data Interconnects," Talk at the Optical Fiber Communication Conference (OFC 2015), Los Angeles, 22-26$^{\text{th}}$ March (2015).

[o] K. Merghem, **C. Calò**, A. Martinez, F. Lelarge and A. Ramdane, "10 GHz Monolithic Optical Frequency Combs using InAs/InP Quantum-Dash-Based Passively Mode-Locked

Lasers stabilized to the 10^{-9} Level," Talk at the *24*$^{\text{th}}$ *IEEE International Semiconductor Laser Conference (ISLC 2014)*, Palma de Mallorca, 7-10$^{\text{th}}$ September (2014).

[p] K. Merghem, **C. Calò**, R. Rosales, X. Lafosse, G. Aubin, A. Martinez, F. Lelarge and A. Ramdane, "Optical Frequency Comb Generation using InAs/InP Quantum-Dash-Based Passive Mode-Locked Lasers," Talk at the *26*$^{\text{th}}$ *International Conference on Indium Phosphide and Related Materials (IPRM 2014)*, Montpellier, 11-15$^{\text{th}}$ May (2014).

[q] **C. Calò**, B. Robillart, Y. Gottesman, A. Fall, F. Lamare, K. Merghem, A. Martinez, A. Ramdane, and B.-E. Benkelfat, "Spectral and temporal phase measurement by Optical Frequency-Domain Reflectometry," Poster at the *26*$^{\text{th}}$ *International Conference on Indium Phosphide and Related Materials (IPRM 2014)*, Montpellier, 11-15$^{\text{th}}$ May (2014).

[r] B. Robillart, **C. Calò**, A. Fall, F. Lamare, Y. Gottesman, B.-E. Benkelfat, "Spectral and temporal phase measurement by Optical Frequency-Domain Reflectometry," Poster at the *SPIE Photonics West Conference 2014*, San Francisco, 1-6$^{\text{th}}$ February (2014).

[s] **C. Calò**, K. Merghem, R. Rosales, E. Galopin, O. Moustapha, A. Lemaître, I. Krestnikov, G. Bouwmans, A. Martinez and A. Ramdane, "Mode-locking and Optical pulse generation from single-section InAs/GaAs quantum dot edge-emitting lasers," Poster at the *International Nano-Optoelectronics Workshop (i-NOW 2013)*, Cargèse, 19-30$^{\text{th}}$ August (2013).

[t] **C. Calò**, K. Merghem, R. Rosales, E. Galopin, O. Moustapha, A. Lemaître, I. Krestnikov, G. Bouwmans, A. Martinez and A. Ramdane, "Optical pulse generation from single-section InAs/GaAs quantum dot edge-emitting lasers", Talk at the *International Conference on Lasers and Electro-Optics (CLEO 2013)*, San Jose, 9-14$^{\text{th}}$ June (2013).

[u] **C. Calò**, H. Schmeckebier, K. Merghem, R. Rosales, F. Lelarge, A. Martinez, D. Bimberg and A. Ramdane, "Frequency resolved optical gating measurement of sub-ps pulses from InAs/InP quantum dash based mode-locked lasers", Talk at the *25*$^{\text{th}}$ *International Conference on Indium Phosphide and Related Materials (IPRM 2013)*, Kobe, 19-23$^{\text{th}}$ May (2013).

[v] K. Klaime, **C. Calò**, R. Piron, C. Paranthoen, D. Thiam, T. Batte, O. Dehaese, J. Le Pouliquen, S. Loualiche, A. Le Corre, K Merghem, A. Martinez and A. Ramdane, "InAs/InP quantum dot mode-locked lasers grown on (113)B InP substrate", Poster at the *25*$^{\text{th}}$ *International Conference on Indium Phosphide and Related Materials (IPRM 2013)*, Kobe, 19-23$^{\text{th}}$ May (2013).

[w] **C. Calò**, K. Klaime, K. Merghem, A. Martinez, A. Ramdane, R. Piron, O. Dehaese, S. Loualiche and A. Le Corre, "Self Pulsation in Quantum Dot lasers operating at 1.55 µm based on (311)B substrates," Poster at the *International Nano-Optoelectronics Workshop (i-NOW 2012)*, Berkeley and Stanford, 7-15$^{\text{th}}$ August (2012).

List of Acronyms

AC	autocorrelation
AFM	atomic force microscopy
AOM	acousto-optic modulator
ASE	amplified spontaneous emission
AWG	arbitrary waveform generator
BA	broad area
BER	bit error rate
BRS	buried ridge stripe
CB	conduction band
CBE	chemical beam epitaxy
CCD	charge-coupled device
CCP-RIE	capacitively coupled plasma reactive ion etching
CDM	carrier density modulation
CH	carrier heating
CO-OFDM	coherent optical OFDM
CW	continuous wave
DBAR	dash-in-a-barrier
DBR	distributed Bragg reflector
DD-OFDM	direct detection OFDM
DD-MZM	dual-drive Mach-Zehnder modulator
DFB	distributed feedback

DOS	density of states
DSH	delayed self-heterodyne
DSP	digital signal processing
DUT	device under test
DWELL	dash-in-a-well
ECL	external cavity laser
EDFA	Erbium-doped fiber amplifier
ES	excited state
ESA	electrical spectrum analyzer
EVM	error vector magnitude
FEC	forward error correction
FFT	fast Fourier transform
FP	Fabry-Perot
FROG	frequency-resolved optical gating
FSR	free spectral range
FWHM	full width at half maximum
FWM	four wave mixing
GD	group delay
GDD	group delay dispersion
GS	ground state
GSMBE	gas source molecular beam epitaxy
GVD	group velocity dispersion
LEF	linewidth enhancement factor
LNA	Low Noise Amplifier
IBE	ion beam etching
ICP-RIE	inductively coupled plasma reactive ion etching
ISI	inter-symbol interference

LO local oscillator

MAN metropolitan area network

MBE molecular beam epitaxy

ML mode-locking

MLL mode-locked laser

MOCVD metal-organic chemical vapor deposition

MPRE multi-population rate equations

MZ Mach-Zehnder

OBPF optical bandpass filter

OCDMA optical code-division multiple access

OCNR optical carrier-to-noise ratio

OCT optical coherence tomography

OFCs optical frequency combs

OFDI optical frequency-domain interferometry

OFDM orthogonal frequency division multiplexing

OFDR optical frequency-domain reflectometry

OLCR optical low-coherence reflectometry

OOK on-off keying

OSA optical spectrum analyzer

OTDM optical time-division multiplexing

PECVD plasma-enhanced chemical vapor deposition

PICs photonic integrated circuits

PL photoluminescence

PLL phase-locked loop

PSD power spectral density

QAM quadrature amplitude modulation

QD quantum dot

QDash	quantum dash
QW	quantum well
QWR	quantum wire
RF	radio frequency
RIN	relative intensity noise
RoF	radio over fiber
RTA	rapid thermal annealing
SA	saturable absorber
SCH	separate confinement heterostructure
SE	spectral efficiency
SEM	scanning electron microscopy
SHB	spectral hole burning
SHG	second harmonic generation
S-K	Stranski-Krastanov
SMF	single mode fiber
SNR	signal-to-noise ratio
SOA	semiconductor optical amplifier
SPIDER	spectral phase interferometry for direct electric-field reconstruction
SSB	single sideband
SSBPN	single sideband phase noise
S-T	Schawlow-Townes
TBP	time bandwidth product
TEM	transmission electron microscopy
TLS	tunable laser source
VB	valence band
WDM	wavelength division multiplexing
WL	wetting layer
XC	cross-correlation